

EVOLUTION OF KANTOWSKI-SACHS UNIVERSE WITH RENYI HOLOGRAPHIC DARK ENERGY

 T. Chinnappalanaidu^a,  S. Srivani Madhu^a,  M. Vijaya Santhi^b,  N. Sri Lakshmi Sudha Rani^{b,c},
 A. Krishna Rao^d

^aDepartment of Mathematics, Vignan's Institute of Information Technology (Autonomous), Visakhapatnam 530049, India

^bDepartment of Applied Mathematics, Andhra University, Visakhapatnam 530003, India

^cDepartment of Humanities and Sciences, Teegala Krishna Reddy Engineering College, Hyderabad-500097, India

^dDepartment of Mathematics, Government Degree College, Chodavaram, Andhrapradesh, 531036, India

*Corresponding Author e-mail: chinnappalanaidu.tadi@gmail.com

Received January 1, 2025; revised April 25, 2025; in final form May 14, 2025; accepted May 18, 2025

By considering generalized scalar tensor theory, as the gravitational theory, we have investigated the dynamical evolution of the homogeneous and anisotropic Kantowski-Sachs space in the presence of Renyi holographic dark energy. To obtain the solution for this model, we have derived the field equations and we have also analyzed the various physical and geometrical parameters of the model, such as deceleration, jerk, EoS, EoS plane, statefinder pair, density, squared speed of sound and the Om-diagnostic. It is shown from these parameters that the model is very much stable, projecting a quintessence nature and also, obtained model depicts the Λ CDM model. Our observations and conclusions from the constructed model are in good agreement with the recent studies.

Keywords: Kantowski-Sachs metric; Anisotropic models; General scalar-tensor theory; Renyi holographic dark energy; Dark energy

PACS: 98.80.-k; 95.36.+x

1. INTRODUCTION

The Universe we see today is around 46 billion light years in radius [1]. The formation of planets, stars and galaxies that keep changing over time, constitute the evolution of the cosmos. The American astronomer Edwin Powell Hubble has observed and deciphered that, from each direction, the distant stars and galaxies are moving away from Earth; and further, this rapid recession increases as the distance increases, implying that the Universe is expanding. Moreover, many repeated measurements have established these findings of Hubble ever since his discovery. Hubble's hypothesis of Universe expansion suggests that, all the presently observed matter and energy of the cosmos were more condensed as an infinitely small hot mass in the past, and later, a huge explosion called the "BIG BANG" has scattered the matter and energy in every direction. The Cosmic Microwave Background (CMB) explorer has confirmed that the background radiation field has the exact spectrum that is predicted by the Big Bang theory which prevails all the cosmological models and elucidates the Universe's initial development that begun 13.798 ± 0.037 billion years ago [2]. And, this hypothesis deduces that, in the deep space, the temperatures today, should be much more than the absolute zero. However, the modern astronomy is the consequence of Galileo's bequest of scientific knowledge of the space, and they understand that the present Universe has been made up of matter and vacuum. This view is widely held and appears to be common. Further experiments and observations made by the astronomers, the astrophysicists and, finally by particle physicists suggests that the Universe is much more beautiful and complicated than it was first believed. Additionally, general relativity tells that the past and as well the future of the Universe is depends on the aggregate of energy and matter contained therein. Hence, the study of exploded massive old stars has ascertained the existence of "dark matter (DM)" and the mysterious component called the "dark energy (DE)" which is neither related to matter nor energy and is clearly distinct from DM. These suggests that the space is being governed by the same physical laws all over its extent and history.

The observations from supernovae reveal that there is an expanding Universe at an accelerating rate [3, 4]. Also, the Coma galaxy cluster mass [5, 6] along with the study of the galaxy rotation curve (1970) [7] that have been provided by the "Viral theorem" (1930's) has uncovered the most important aspects of cosmology: the dark sector (DM & DE), which is particularly accountable for rapid cosmic expansion and helps us to understand the nature of the cosmos. In terms of theological understanding, one of the most challenging issues is the concept of dark sectors [8]. For a standard cosmological scenario, the DM is called as cold dark matter (CDM), and DE as the cosmological constant (Λ). As a result of the combination of radiation and baryons, the Λ CDM model captures the dark component of the Universe. However, this is much of hypothetical nature, despite of Λ CDM having an impressive observational achievements [9, 10]. Taking some inspiration from the holographic principle [11–17], the idea of holographic dark energy (HDE) has been proposed by Li [18] to elucidate the phenomenon of rapid expansion of the Universe, in the year 2004. Consequently, the most complete generalization including the mostly known HDE models were suggested by Nojiri and Odintsov [19] and later

on, covariant theories different from Li's HDE have been discussed by Nojiri-Odintsov HDE [20]. Recently, a number of entropies have been formalized and are used to explore the various cosmological models. Among all those which are developed, namely Sharma Mittal HDE [21], Tsallis holographic dark energy (THDE) [22], Renyi holographic dark energy (RHDE) models [23] have proved to be more stable, based on non-interactions among the cosmic regions [24]. Current observations have suggested that Bekenstein entropy ($S = \frac{A}{4}$) is nothing but Tsallis entropy [25–31] that ultimately lead to the following expression, for the ease of Renyi entropy [32] as,

$$S = \frac{1}{8} \log \left(\frac{\delta}{4} A + 1 \right). \quad (1)$$

On applying equation (1), with the assumption $\rho_{de} dV \propto T dS$ [23], we acquire RHDE as

$$\rho_{de} = \frac{3c^2 H^2}{8\pi \left(\frac{\pi\delta}{H^2} + 1 \right)}, \quad (2)$$

where c^2 is a numerical constant. To obtain this we use relations that are reasonable in FLRW flat Universe [33], $T = \frac{H}{2\pi}$ and $A = \frac{4\pi}{H} = 4\pi \left(\frac{3V}{4\pi} \right)^{\frac{2}{3}}$. It is clear that without δ , we obtain $\rho_{de} = \frac{3c^2 H^2}{8\pi}$, that agrees with the original HDE.

The RHDE models have been studied with various IR cut-offs [34, 35]. Furthermore, Sharma et al. [36, 37] have investigated how the RHDE model can be distinguished from the Λ CDM model using different diagnostic tools. More recently, Dubey and Sharma [38] have compared the holographic and THDE models with the RHDE model using the (r - s) diagnostic. These studies highlight the importance of examining the interaction between dark energy (DE) and dark matter (DM). Additionally, constraints on the strength and nature of this interaction under different model setups have been explored in the literature [39–41]. Once again, the RHDE model in FLRW Universe has been investigated by Sharma and Dubey [42] by considering the interaction between the DM and DE. Also, RHDE model in a scalar tensor theory studied by Santhi and Naidu [43]. Very recently, Santhi et al., [44] have examined the RHDE model with two IR cutoffs in Saez-Ballester scalar tensor theory with marder type Universe.

It is assumed by many physicists that, at the emergence of the galaxies, the gravitational interactions responsible for the dynamics of the cosmos were quantized and its geometry should have been like a foam, resonating among the various configurations [45], which is of course, much different from what it is today. This raises the question on the validity of the “cosmological principle” which says that the Universe is homogeneous and isotropic, at sufficiently large scales [46]. Supposing that at the initial stages, the cosmological principle is not validated by the Universe i.e., the cosmos is inhomogeneous and anisotropic; and later it subsequently transformed to homogeneous and isotropic state as we understand it today. Since CMB radiation is almost uniformly distributed in all the directions with little variability, this transformation must have occurred before the matter and radiation got separated [47]. In a very transient period of time, cosmological inflation has caused the isotropization and homogenization of the primordial Universe, and later on with the initial singularity, the accelerated cosmic expansion has taken place and the size of the Universe has increased by many folds [48]. Physicists have worked on the proposition of inhomogeneous and anisotropic cosmos, turning into a homogeneous and isotropic one [49]. Most of these works are related to the initial time, where the Universe is homogeneous and anisotropic. However, one is left with many other possibilities to contribute for the choice of such a particular space-time. One such space time is the Kantowski-Sachs (KS) [50]. Therefore, the space-time S^2R spatial topology (or S^2S^1 , when the real line is compactified because of identifications), has only two scale factors to describe the spherical symmetry. For this space-time we have constants and positives curvatures of the spatial slices. The KS space-time may also elucidate the Schwarzschild black hole in detail [50]. Many studies have been performed on this Universe by theorists, of which few have been mentioned here. The possibility of having a nonsingular KS-type static state has been evaluated by Ghorani and Heydarzade by considering four and five dimensional models [51]. The KS space time in the presence of strange quark matter cosmological models attached to string cloud in $f(R)$ theory of gravity has been examined by Santhi and Naidu [52]. A dynamical evolution of a homogeneous and anisotropic KS cosmological model has been studied by Oliveira-Neto in the presence of general relativity [53]. Observational constraints on RHDE in KS Universe has been studied by Prasanthi and Aditya [54]. The geometric properties of the generalized KS space-time, has been examined by Shaikh and Chakraborty [55], in a warped product of 2-dimensional base and fibre. Harmonic metrics with respect to generalized KS type space-times have been dealt with Altunbas [56]. The KS metric has been parameterized in a traditional way as:

$$ds^2 = dt^2 - A^2 dr^2 - B^2 (d\theta^2 + \sin^2 \theta d\phi^2), \quad (3)$$

where the arbitrary functions of time are taken as $A(t)$ and $B(t)$; and $r \in [0, +\infty)$ is the radial coordinate and θ, ϕ are the spherical angular coordinates that vary in $[0, \pi]$, $[0, 2\pi]$ ranges respectively.

Hence, the following article has been divided into various sections for better understanding. Section (2) mentions about the general scalar tensor theory and the field equations, along with some physical quantities. Section (3) mainly deals

with the physical and geometrical properties of the cosmological model that are ascertained with the help of corresponding graphs w.r.t $'z'$ (where z is the redshift defined through $1+z = \frac{a_0}{a_1}$ setting the current value of the scale factor to $a_0 = 1$). In the last section the obtained results have been concluded.

2. FIELD EQUATIONS FOR GENERAL SCALAR-TENSOR THEORY

Nordtvedt [57] has suggested the scalar tensor gravitational theories of a general class, where the Brans-Dicke theory parameter ω is an arbitrary (positive definite) function of the scalar field as $\omega \rightarrow \omega(\varphi)$. Schwinger [58] has attracted a lot of work by considering a specific case of Nordtvedt's theory to evaluate the scalar field cosmological models. Also, the theories of Jordan [59] and, Brans and Dicke [60] have been taken as a special case in the general class of scalar-tensor gravitational theories. This theory has been considered by some of the researchers [61–64] to understand the Universe. Higher-derivative operators and effective field theory for general scalar-tensor theories have been considered by Solomon and Trodden [65]. Huang et al. [66], have analyzed the stability of Einstein static Universes in general scalar-tensor theory with non-minimal derivative coupling by analyzing scalar and tensor perturbations. Also, much recently a simplified approach to general scalar-tensor theories has been made by Bloomfield [67]. López et al. [68] have studied a chaotic inflation and reheating in generalized scalar-tensor gravity.

The proposed field equations by Nordtvedt are given by,

$$R_{\mu\nu} - \frac{1}{2}g_{\mu\nu}R = -8\pi\phi^{-1}T_{\mu\nu} - \omega\phi^{-2}(\phi_{;\mu}\phi_{;\nu} - \frac{1}{2}g_{\mu\nu}\phi_{;k}\phi^{;k}) - \phi^{-1}(\phi_{\mu;\nu} - g_{\mu\nu}\phi_{;k}^{;k}), \quad (4)$$

$$\phi_{;k}^{;k} = \frac{1}{3+2\omega}\left(8\pi T - \frac{d\omega}{d\phi}\phi_{;\mu}\phi^{;\mu}\right), \quad (5)$$

where $R_{\mu\nu}$ & R is the Ricci tensor and scalar curvature respectively; and $T_{\mu\nu}$ is the stress energy tensor of the matter, T is the trace of $T_{\mu\nu}$ and comma and semicolon represent the partial and covariant differentiation respectively. Also, from field Eqs. (4) and (5) we get the conservation equation is given as,

$$T^{\mu\nu}{}_{;\mu} = 0. \quad (6)$$

The DE and pressureless matter combinedly constitutes the cosmos, which can be defined as,

$$T_{\mu\nu} = \rho_m u_\mu u_\nu, \quad (7)$$

$$\& \quad \bar{T}_{\mu\nu} = (\rho_{de} + p_{de})u_\mu u_\nu - p_{de}g_{\mu\nu}, \quad (8)$$

where p_{de} is the pressure of RHDE; whereas, ρ_m and ρ_{de} are the matter energy density and the energy density of RHDE. The presumption of taking the anisotropic DE, whose energy-momentum tensor, $T_{\mu\nu}$ as given below, determines the study of present cosmic accelerated expansion,

$$\bar{T}_{\mu\nu} = [1, -\omega_r, -\omega_\theta, -\omega_\phi]\rho_{de} = [1, -\omega_{de}, -\omega_{de}, -\omega_{de}]\rho_{de}, \quad (9)$$

where the directional EoS parameters: $\omega_r = -\omega_{de}$, $\omega_\theta = -\omega_{de}$ and $\omega_\phi = -\omega_{de}$ are along r , θ and ϕ respectively.

Hence, we obtain the following field equations from the equations (4), (5) and (9) as follows:

$$\frac{2\ddot{B}}{B} + \frac{\dot{B}^2}{B^2} + \frac{1}{B^2} - \frac{\omega\dot{\phi}^2}{2\phi^2} - \frac{\ddot{\phi}}{\phi} - \frac{2\dot{B}\dot{\phi}}{B\phi} = -\frac{8\pi\omega_{de}\rho_{de}}{\phi}, \quad (10)$$

$$\frac{\ddot{A}}{A} + \frac{\ddot{B}}{B} + \frac{\dot{A}\dot{B}}{AB} - \frac{\omega\dot{\phi}^2}{2\phi^2} - \frac{\ddot{\phi}}{\phi} - \frac{\dot{\phi}}{\phi}\left(\frac{\dot{A}}{A} + \frac{\dot{B}}{B}\right) = -\frac{8\pi\omega_{de}\rho_{de}}{\phi}, \quad (11)$$

$$2\frac{\dot{A}\dot{B}}{AB} + \frac{\dot{B}^2}{B^2} + \frac{1}{B^2} + \frac{\omega\dot{\phi}^2}{2\phi^2} - \frac{\dot{\phi}}{\phi}\left(\frac{\dot{A}}{A} + \frac{2\dot{B}}{B}\right) = -\frac{8\pi(\rho_m + \rho_{de})}{\phi}, \quad (12)$$

$$\& \quad \ddot{\phi} + \dot{\phi}\left(\frac{\dot{A}}{A} + \frac{2\dot{B}}{B}\right) = \frac{8\pi[3\omega_{de}\rho_{de} - \rho_m - \rho_{de}]}{3+2\omega} - \frac{1}{3+2\omega}\frac{d\omega}{d\phi}\dot{\phi}^2. \quad (13)$$

The transformation $dt = AB^2d\tau$, can be used to rewrite the above field equations (10)-(13) as,

$$\frac{1}{A^2B^4}\left[\frac{2B''}{B} - \frac{3B'^2}{B^2} - \frac{2A'B'}{AB} + A^2B^2 - \frac{\omega\phi'^2}{2\phi^2} - \frac{\phi''}{\phi} + \frac{A'\phi'}{A\phi}\right] = \frac{-8\pi\omega_{de}\rho_{de}}{\phi}, \quad (14)$$

$$\frac{1}{A^2B^4}\left[\frac{A''}{A} + \frac{B''}{B} - \frac{A'^2}{A^2} - \frac{2B'^2}{B^2} - \frac{2A'B'}{AB} - \frac{\omega\phi'^2}{2\phi^2} - \frac{\phi''}{\phi} + \frac{B'\phi'}{B\phi}\right] = \frac{-8\pi\omega_{de}\rho_{de}}{\phi}, \quad (15)$$

$$\frac{1}{A^2 B^4} \left[\frac{2A'B'}{AB} + \frac{B'^2}{B^2} + A^2 B^2 + \frac{\omega \phi'^2}{2\phi^2} - \frac{\phi'}{\phi} \left(\frac{A'}{A} + \frac{2B'}{B} \right) \right] = -\frac{8\pi(\rho_{de} + \rho_m)}{\phi}, \quad (16)$$

$$\& \quad (3 + 2\omega)\phi'' = 8\pi[3\omega_{de}\rho_{de} - \rho_m - \rho_{de}](A^2 B^4) - \frac{d\omega}{d\phi}\phi'^2. \quad (17)$$

Here the overhead dot (.) denotes differentiation w.r.t 't', the overhead dash (') denotes differentiation w.r.t τ and the field equations (14)-(17) corresponds to KS-Universe.

Therefore, from equations (14)-(17), we have obtained,

$$(3 + 2\omega)\phi'' + \frac{d\omega}{d\phi}\phi'^2 = 2\phi \left[\frac{A''}{A} - \frac{A'^2}{A^2} - \frac{2A'B'}{AB} + \frac{2B''}{B} - \frac{3B'}{B} + A^2 B^2 \right] + 3\phi'' + \frac{\omega \phi'^2}{\phi^2}. \quad (18)$$

There are four field equations (14)-(17) and six unknowns - A , B , ϕ , ρ_{de} , ρ_m and ω_{de} that are to be determined. As a specific case proposed by Schwinger [58] in the following form,

$$3 + 2\omega(\phi) = \frac{1}{\lambda\phi}, \quad \lambda = \text{constant}, \quad (19)$$

we have obtained Nordtvedt's general scalar tensor cosmic model in the framework of RHDE.

Hence, from equations (18) and (19) we obtain,

$$\frac{1}{\lambda} \left[\frac{\phi''}{\phi} - \frac{\phi'^2}{\phi^2} \right] + \frac{3\phi'^2}{2\lambda\phi} - 3\phi'' = 2\phi \left[\frac{A''}{A} - \frac{A'^2}{A^2} - \frac{2A'B'}{AB} + \frac{2B''}{B} - \frac{3B'}{B} + A^2 B^2 \right]. \quad (20)$$

The preceding equation has been solved by the condition of proportionality between the shear scalar and the expansion scalar as,

$$A = B^n, \quad n > 1. \quad (21)$$

From equations (20) and (21) we get,,

$$\phi = e^{k_1\tau + k_2}, \quad (22)$$

$$\text{and} \quad \frac{B''}{B} - \frac{3(n+1)}{n+2} \frac{B'^2}{B^2} = -\frac{1}{n+2} B^{n+2} - \frac{3}{n+2} k_1^2, \quad (23)$$

where k_1 and k_2 represent the arbitrary constants. And, on solving equation (23) we obtain the metric potentials as:

$$A = \left(\frac{\beta_1}{\beta_2} \operatorname{sech}(\beta_1(n+1)\tau) \right)^{\frac{n}{n+1}}, \quad (24)$$

$$B = \left(\frac{\beta_1}{\beta_2} \operatorname{sech}(\beta_1(n+1)\tau) \right)^{\frac{1}{n+1}}. \quad (25)$$

Firstly, we have studied various physical parameters, like volume (V), scale factor ($a(t)$), Hubble parameter (H), expansion scalar (ϑ), shear scalar (σ^2) and the anisotropic parameter (\mathcal{A}_h) whose expressions are given respectively as,

$$V = \left(\frac{\beta_1}{\beta_2} \operatorname{sech}(\beta_1(n+1)\tau) \right)^{\frac{n+2}{n+1}}, \quad (26)$$

$$a = \left(\frac{\beta_1}{\beta_2} \operatorname{sech}(\beta_1(n+1)\tau) \right)^{\frac{n+2}{3n+3}}, \quad (27)$$

$$H = \frac{-(n+2)\beta_1 \tanh(\beta_1(n+1)\tau)}{3}, \quad (28)$$

$$\vartheta = -(n+2)\beta_1 \tanh(\beta_1(n+1)\tau), \quad (29)$$

$$\sigma^2 = \frac{(n-1)^2 \beta_1^2 \tanh^2(\beta_1(n+1)\tau)}{3}, \quad (30)$$

$$\& \quad \mathcal{A}_h = \frac{2(n-1)^2}{(n+2)^2}. \quad (31)$$

For the RHDE, the energy density takes the value,

$$\rho_{de} = \frac{d^2 \beta_1^4 \sinh^4(\beta_1(n+1)\tau)(n+2)^4}{3 \left(\left((n+2)^2 \beta_1^2 + 9\pi\delta \right) \cosh^2(\beta_1(n+1)\tau) - (n+2)^2 \beta_1^2 \right) \cosh^2(\beta_1(n+1)\tau)}, \quad (32)$$

and the energy density of matter has the following expression

$$\rho_m = \frac{e^{\tau k_1 + k_2}}{8\pi} \left(\frac{\beta_1}{\beta_2} \operatorname{sech}(\beta_1(n+1)\tau) \right)^{\frac{-2n-4}{n+1}} \frac{\operatorname{sech}^2(\beta_1(n+1)\tau)}{2\beta_2^2} \left(-4 \times \right. \\ \left. \left(\left(n + \frac{1}{2} \right) \beta_1^2 - \frac{\omega k_1^2}{4} \right) \beta_2^2 \cosh^2(\beta_1(n+1)\tau) + 2k_1 \beta_1 \beta_2^2 (n+2) \times \right. \\ \left. \sinh(\beta_1(n+1)\tau) \cosh(\beta_1(n+1)\tau) + 4\beta_1^2 \left(\frac{-1}{2} + \left(n + \frac{1}{2} \right) \beta_2^2 \right) \right) - \rho_{de} \quad (33)$$

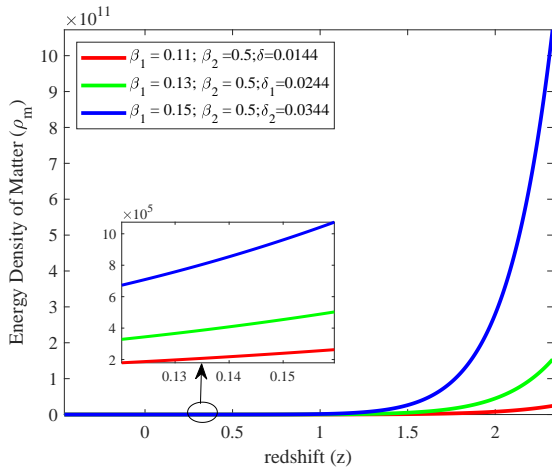


Figure 1. Illustration of energy density matter (ρ_m) against redshift (z)

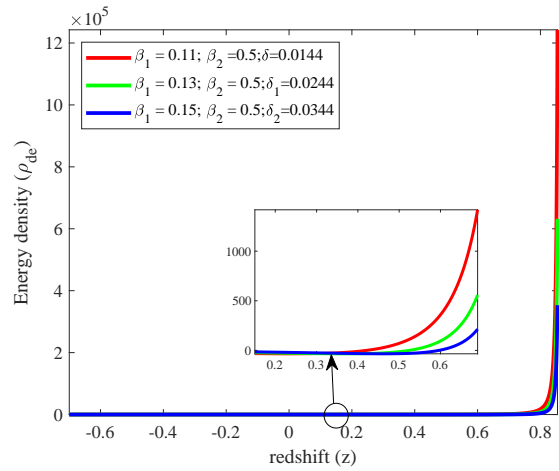


Figure 2. Illustration of energy density of DE (ρ_{de}) against redshift (z)

Thus, Eq. (3) becomes,

$$ds^2 = -dt^2 + \left(\frac{\beta_1}{\beta_2} \operatorname{sech}(\beta_1(n+1)\tau) \right)^{\frac{2n}{n+1}} dr^2 + \left(\frac{\beta_1}{\beta_2} \operatorname{sech}(\beta_1(n+1)\tau) \right)^{\frac{2}{n+1}} (d\theta^2 + \sin^2 \theta d\varphi^2). \quad (34)$$

For various β_1 , β_2 and δ values, the energy density of matter (ρ_m) and RHDE (ρ_{de}) have been constructed against redshift (z) in Figs. (1) and (2) respectively. It can be seen from their graphical course that the trajectories vary in positive region decreasing against redshift (z), which indicates rapid cosmic expansion. From the equation (26) it can be noticed that, at initial periods of the cosmos formation i.e., at $\tau = 0$, the volume (V) and scale factor (a) of the Universe is constant, but as time $\tau \rightarrow \infty$ the Universe has been expanding i.e., $V \rightarrow \infty$. Also, from equations (28)-(30), we can categorically say that, at the initial time phase ($\tau = 0$), all the parameters H , ϑ and σ vanish and as τ increases these parameters increase, illustrating an inflationary scenario of the Universe, expanding at a constant rate. From equation (31), we observe that $\mathcal{A}_h \neq 0$ throughout the evolution of the Universe, and our model (34) is an anisotropic model.

3. PHYSICAL AND GEOMETRICAL INTERPRETATIONS OF THE MODEL

The parameters such as EoS (ω_{de}), EoS plane ($\omega_{de} - \omega'_{de}$), deceleration parameter (q), stability (v_s^2), density (Ω_{de}), jerk (j), Om(z) and statefinder ($r - s$) have been studied in this particular section to understand the constructed model of the Universe in a better way.

- **Equation of state parameter (ω_{de}):** Study of the Universe has always been a mysterious task, and with the mysterious component, so called the DE, it has been more difficult to understand the nature of the cosmos. However, the EoS parameter might help us to evaluate the nature of the Universe to some extent. ω_{de} is used to study the acceleration of the cosmos and the phase change from deceleration to acceleration, and is defined as,

$$\omega_{de} = \frac{p_{de}}{\rho_{de}}. \quad (35)$$

For the model, we get the EoS parameter as

$$\omega_{de} = \frac{3\Psi_1}{8\pi d^2 \beta_2^2 \beta_1^4 \sinh^4(\beta_1(n+1)\tau)(n+2)^4}, \quad (36)$$

$$\text{where } \Psi_1 = \left(\frac{\beta_1}{\beta_2} \operatorname{sech}(\beta_1(n+1)\tau) \right)^{\frac{-2n-4}{n+1}} \left(\left((n^2 - 4n - 2)\beta_1^2 + \frac{k_1^2}{2}(4+\omega) \right) \times \right. \\ \left. \beta_2^2 \cosh^2(\beta_1(n+1)\tau) + \beta_1 \beta_2^2 ((k_1 + 1)n + k_1) \sinh(\beta_1(n+1)\tau) \times \right. \\ \left. \cosh(\beta_1(n+1)\tau) - 2\beta_1^2 \left(\frac{-1}{2} + (n^2 + \frac{1}{2})\beta_2^2 \right) \right) e^{\tau k_1 + k_2} \left(\left((n+2)^2 \times \right. \right. \\ \left. \left. \beta_1^2 + 9\pi\delta \right) \cosh^2(\beta_1(n+1)\tau) - (n+2)^2 \beta_1^2 \right).$$

The EoS (ω_{de}) parameter has been plotted against redshift (z), for different values of δ . It is observed from Fig. (3), the model starts its evolution from the quintessence region as ω_{de} lies in the range $(-1, 1/3)$, then crosses the phantom divide line at $\omega_{de} = -1$ behaving like a non-relativistic matter, and finally reaches the phantom region, as $\omega_{de} < -1$. Such a behavior of the model is called as quintessence like nature.

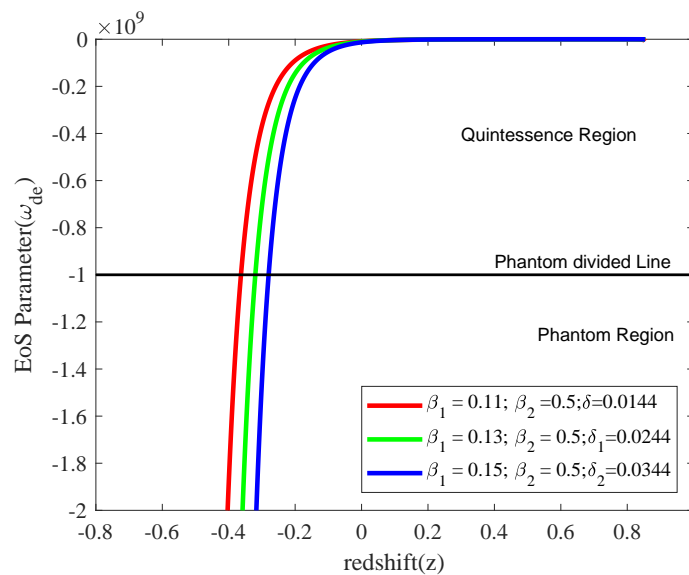


Figure 3. Illustration of EoS parameter (ω_{de}) against redshift (z)

- **EoS plane ($\omega_{de} - \omega'_{de}$):** As proposed by Cadwell and Linder [69] the $\omega_{de} - \omega'_{de}$ plane describes the various regions of Universe's expansion which evaluates the quintessence scalar field. For the values of ω_{de} and ω'_{de} , such as $\omega_{de} < 0$, $\omega'_{de} > 0$ and $\omega_{de} < 0$, $\omega'_{de} < 0$ the EoS plane is characterized into thawing region and freezing region respectively. The EoS plane for the model is given by,

$$\omega'_{de} = \frac{-9\Psi_2}{4\beta_2^2(n+2)^5\beta_1^5 \sinh^6(\beta_1(n+1)\tau)\pi d^2}, \quad (37)$$

$$\begin{aligned}
 \text{where } \Psi_2 = & \left(\beta_1 \left((n^3 - 2n^2 - 10n - 4)\beta_1^2 + \frac{k_1}{2} \left(\left(1 + (\omega + 5)k_1 \right) n + k_1(2\omega + 9) \right) \right) \times \right. \\
 & \left((n+2)^2\beta_1^2 + 9\pi\delta \right) \beta_2^2 \cosh^6(\beta_1(n+1)\tau) + \frac{3}{2} \left(\left((k_1 + \frac{2}{3})n^2 + \left(\frac{2k_1}{3} \right. \right. \right. \\
 & \left. \left. \left. + \frac{4}{3} \right) n + \frac{7k_1}{3} \right) \beta_1^2 + \frac{k_1^3}{6}(4+\omega) \right) \left((n+2)^2\beta_1^2 + 9\pi\delta \right) \beta_2^2 \sinh(\beta_1(n+1)\tau) \times \\
 & \cosh^5(\beta_1(n+1)\tau) - 3 \left((n+2)^2 \left(\frac{-1}{3} + \left(n^3 - \frac{5n^2}{3} - \frac{26n}{3} - 3 \right) \beta_2^2 \right) \beta_1^4 \right. \\
 & + \left(\left(\left(\frac{\omega}{2} + \frac{7}{3} \right) k_1^2 + \frac{k_1}{3} + 9\pi\delta \right) n^3 + \left(\left(\frac{17\omega}{6} + 13 \right) k_1^2 + \frac{4k_1}{3} - 18\pi\delta \right) n^2 \right. \\
 & + \left(\left(\frac{16\omega}{3} + 24 \right) k_1^2 + \frac{4k_1}{3} - 66\pi\delta \right) n + \left(\frac{44}{3} + \frac{10\omega}{3} \right) k_1^2 - 21\pi\delta \Big) \beta_2^2 - 3\pi\delta \Big) \beta_1^2 \\
 & + \frac{9\pi\delta}{2} \left(\left(\frac{1}{3} + (\omega + \frac{13}{3})k_1 \right) n + \frac{4}{3} \left(\omega + \frac{17}{4} \right) k_1 \right) \beta_2^2 \delta k_1 \Big) \beta_1 \cosh^4(\beta_1(n+1)\tau) \\
 & - 4\beta_1^2 \left(\left(\left((k_1 + \frac{5}{8})n^2 + \left(\frac{5k_1}{4} + \frac{9}{8} \right) n + k_1 \right) \beta_2^2 - \frac{k_1}{8} \right) (n+2)^2\beta_1^2 + \left(\left(\frac{\omega}{16} + \frac{1}{4} \right) k_1^3 \right. \right. \\
 & + \frac{63\pi\delta k_1}{8} + \frac{45\pi\delta}{8} \Big) n^2 + \left(\left(\frac{\omega}{4} + 1 \right) k_1^3 + \frac{27\pi\delta k_1}{2} + \frac{63\pi\delta}{8} \right) n + \left(\frac{\omega}{4} + 1 \right) k_1^3 + 9\pi\delta k_1 \Big) \beta_2^2 \\
 & - \frac{9\pi\delta k_1}{8} \Big) \sinh(\beta_1(n+1)\tau) \cosh^3(\beta_1(n+1)\tau) + 4\beta_1^3 \left((n+2)^2 \left(n^3 + \frac{n^2}{4} - \frac{15n}{4} \right. \right. \\
 & - \frac{3}{4} \Big) \beta_2^2 - \frac{n}{4} - \frac{3}{4} \beta_1^2 + \left(\left(\frac{9}{8} + \frac{\omega}{4} \right) k_1^2 + \frac{k_1}{8} + 9\pi\delta \right) n^3 + \left(\left(\frac{49}{8} + \frac{11\omega}{8} \right) k_1^2 + \frac{k_1}{2} \right. \\
 & + \frac{27\pi\delta}{2} \Big) n^2 + \left(\left(11 + \frac{5\omega}{2} \right) k_1^2 + \frac{k_1}{2} + \frac{9\pi\delta}{2} \right) n + \left(\frac{3\omega}{2} + \frac{13}{2} \right) k_1^2 + \frac{27\pi\delta}{4} \Big) \beta_2^2 \\
 & - \frac{9\pi}{2} \left(n + \frac{3}{2} \right) \delta \Big) \cosh^2(\beta_1(n+1)\tau) + \frac{5}{2} \beta_1^4 (n+2)^2 \left(\left((k_1 + \frac{3}{5})n^2 + \left(\frac{8k_1}{5} + 1 \right) n \right. \right. \\
 & + \frac{6k_1}{5} \Big) \beta_2^2 - \frac{k_1}{5} \Big) \sinh(\beta_1(n+1)\tau) \cosh(\beta_1(n+1)\tau) - 2\beta_1^5 (n+2)^3 \left(\frac{-1}{2} \right. \\
 & \left. \left. + \left(n^2 + \frac{1}{2} \right) \beta_2^2 \right) \right) \left(\frac{\beta_1}{\beta_2} \operatorname{sech}(\beta_1(n+1)\tau) \right)^{\frac{-2n-4}{n+1}} e^{k_1\tau+k_2} \Big).
 \end{aligned}$$

As depicted from the Fig. (4), $\omega_{de} - \omega'_{de}$ plane has been taken against redshift (z) for different values of δ . Here, the trajectories varies in the negative region, characterizing the freezing region as $\omega_{de} < 0$ and $\omega'_{de} < 0$. These observations are in correspondence with the recent observations.

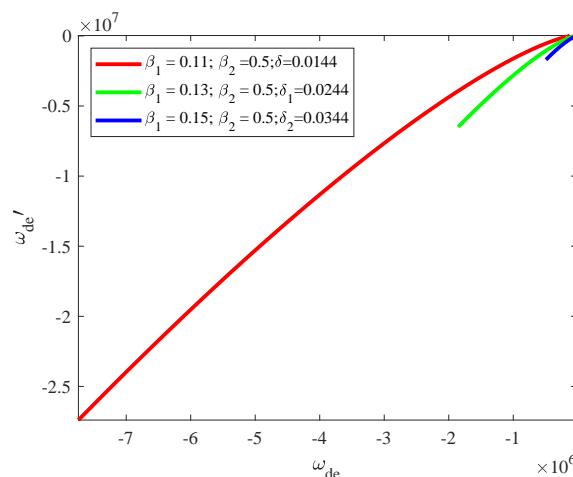


Figure 4. Illustration of EoS plane

- **Deceleration Parameter (q):** The deceleration parameter (q), more explicitly, the signature of q determines the nature of accelerating expansion of the cosmos. Whenever, $q > 0$ the Universe shows decelerating expansion and when $q < 0$ there is rapid expansion of the cosmos. Here, the deceleration parameter (q) is defined as,

$$q = -1 + \frac{d}{dt} \left(\frac{1}{H(t)} \right). \quad (38)$$

The deceleration parameter for our model is given by,

$$q = \frac{(-n-2) \cosh^2(\beta_1(n+1)\tau) + 4n+5}{(n+2) \sinh^2(\beta_1(n+1)\tau)}. \quad (39)$$

Therefore, we can observe from the Fig. (5) that deceleration parameter (q) has been constructed against redshift (z) for distinct estimates of β_1 and β_2 . The trajectories of q projects that the Universe travels previously from decelerated phases to the current accelerating phase. The model basically shows exponential or the de-Sitter expansion, as it is observed that $q = -1$.

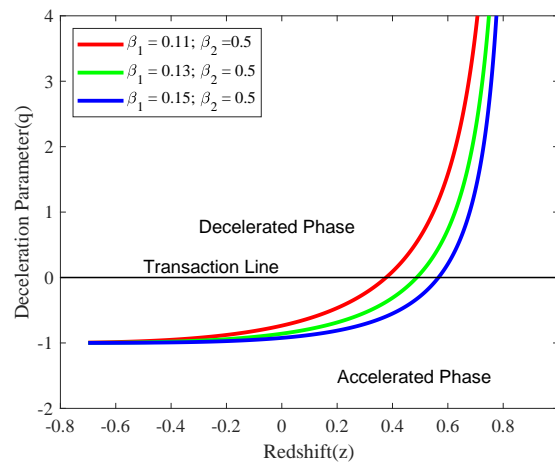


Figure 5. Illustration of deceleration parameter (q) against redshift (z)

- **Analysis of Model's Stability:** The squared speed of sound has a vital role in analyzing the stability of any model. The model exhibits a stable behavior whenever $v_s^2 > 0$ and shows an unstable behavior when $v_s^2 < 0$. The model's stability can be determined with the help of following mathematical formula:

$$v_s^2 = \frac{\dot{p}_{de}}{\dot{\rho}_{de}}. \quad (40)$$

The squared speed of the sound for the obtained model is given by,

$$v_s^2 = \frac{\Psi_3}{\Psi_4}, \quad (41)$$

$$\text{where } \Psi_3 = \frac{9}{16} \left(\left(\frac{\beta_1}{\beta_2} \operatorname{sech}(\beta_1(n+1)\tau) \right)^{\frac{-2n-4}{n+1}} e^{k_1\tau+k_2} \left(\left((n+2)^2\beta_1^2 + 9\pi\delta \right) \cosh^2(\beta_1(n+1)\tau) - (n+2)^2\beta_1^2 \right)^2 \left(\left(\left(k_1 + \frac{2}{3} \right) n^2 + \left(\frac{2k_1}{3} + \frac{4}{3} \right) n + \frac{2k_1}{3} \right) \beta_1^2 + \frac{k_1^3(4+\omega)}{6} \right) \beta_2^2 \times \right. \\ \left. \cosh^3(\beta_1(n+1)\tau) + \frac{2}{3} \left((n^3 - 2n^2 - 10n - 4)\beta_1^2 + \frac{k_1}{2} \left(\left(1 + (\omega+5)k_1 \right) n + k_1(2\omega+9) \right) \right) \beta_1\beta_2^2 \sinh(\beta_1(n+1)\tau) \cosh^2(\beta_1(n+1)\tau) - \beta_1^2 \left(\left(k_1 + \frac{1}{3} \right) n^2 + \left(\frac{4k_1}{3} + 1 \right) n + \frac{4k_1}{3} \right) \beta_2^2 - \frac{k_1}{3} \right) \cosh(\beta_1(n+1)\tau) - \frac{4}{3} \left(\frac{-1}{2} + \left(n^2 + \frac{1}{2} \right) \right) \beta_2^2 \times \right. \\ \left. \beta_1^3 \sinh(\beta_1(n+1)\tau) \right),$$

$$\text{and } \Psi_4 = \left(\pi \left(\left((n+2)^2 \beta_1^2 + 18\pi\delta \right) \cosh^2 (\beta_1(n+1)\tau) - (n+2)^2 \beta_1^2 \right) d^2 \beta_1^5 (n+1) \beta_2^2 (n+2)^4 \sinh^3 (\beta_1(n+1)\tau) \right) \cdot \right\}$$

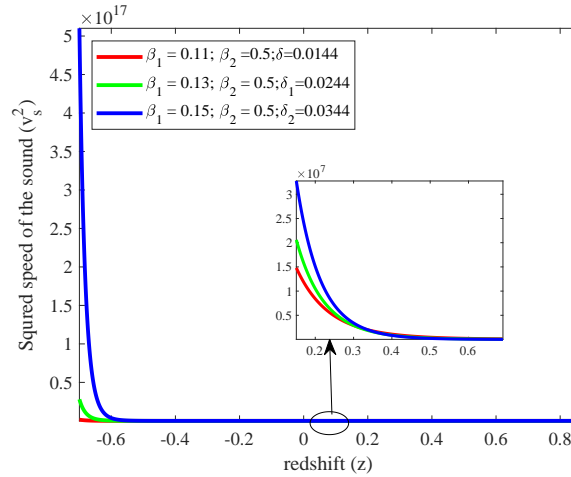


Figure 6. Squared speed of sound (v_s^2) against redshift (z)

From the Fig. (6) it is observed that v_s^2 is plotted against z to understand the model's stability. Here, trajectories are completely varying positive region for several values of δ . This illustrates Universe's stable behavior.

- **Density Parameter:** For a DE model, the density parameter has been defined as

$$\Omega_{de} = \frac{\rho_{de}}{3H^2}.$$

The density parameter for our model is obtained as,

$$\Omega_{de} = \frac{d^2 \beta_1^2 \sinh^2 (\beta_1(n+1)\tau) (n+2)^2}{\left((n+2)^2 \beta_1^2 + 9\pi\delta \right) \cosh^2 (\beta_1(n+1)\tau) - (n+2)^2 \beta_1^2}. \quad (42)$$

In order to analyze the behavior of the density parameter Ω_{de} we have the graphical representation of Ω_{de} against redshift (z) for various values of δ in the Fig. (7). It can be observed that the trajectories are varying in the positive region, decreasing against redshift.

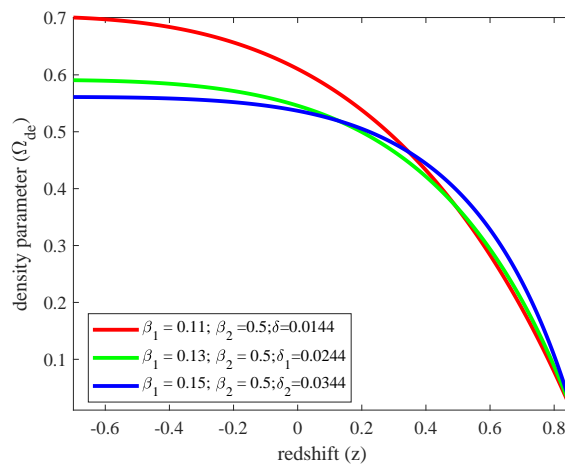


Figure 7. Illustration of density parameter (Ω_{de}) against redshift (z)

- **Jerk Parameter (j):** In an cosmic evolution, the jerk parameter is defined as,

$$j = \frac{\ddot{a}}{aH^3}, \quad (43)$$

where a and H are the cosmic scale factor and the Hubble parameter. Here, the scale factor has been differentiated w.r.t. the cosmic time. The jerk parameter (j) happens to be the 4^{th} expression of a_0 in a Taylor series expansion:

$$\frac{a(t)}{a_0} = 1 + H_0(t - t_0) - \frac{1}{2}q_0H_0^2(t - t_0)^2 + \frac{1}{6}j_0H_0^3(t - t_0)^3 + O[(t - t_0)^4], \quad (44)$$

where a_0 denotes the present value. The jerk parameter for our model is obtained as,

$$j = \frac{(n+2)^2 \cosh^2(\beta_1(n+1)\tau) - 28n^2 - 67n - 40}{\sinh^2(\beta_1(n+1)\tau)(n+2)^2}. \quad (45)$$

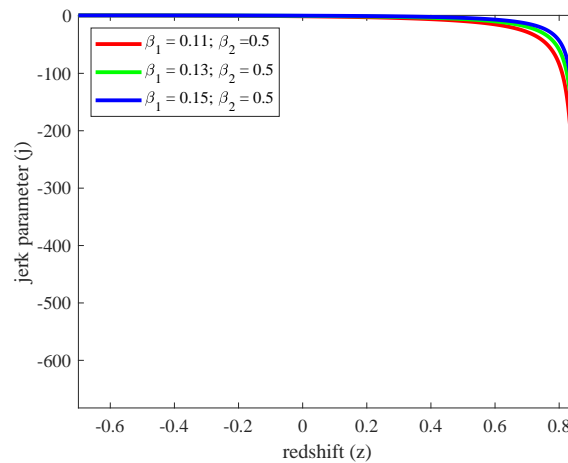


Figure 8. Illustration of jerk parameter (j) against redshift (z)

Fig. (8) depicts the construction of jerk parameter (j) against redshift (z). It is clearly observed that the curves of j are completely varying in the negative region for all the values of β_1 and β_2 and approaches to unity in late times.

- **Om(z)- diagnostic:** Om-diagnostics is an another tool discovered by Sahni et al. [70] other than statefinder plane, to differentiate the various phases of the Universe. A positive path of the curve indicates that the model corresponds to phantom DE and the path of the curve oriented in the negative region indicates a quintessence DE. The Om(z) in terms of $H(z)$ function is defined as,

$$Om(z) = \frac{H^2(z) - H_0^2}{H_0^2[(1+z)^3 - 1]}, \quad (46)$$

where,

$$H(z) = \frac{-\beta_1(n+2)}{3} \sqrt{1 - \frac{\beta_2^2}{\beta_1^2} \left(\frac{a_0}{1+z} \right)^{\frac{6n+6}{n+2}}}. \quad (47)$$

We can depict that in the Fig. (9) the path of the Om(z), as taken against redshift(z) differs in negative region, thus having a quintessence behavior.

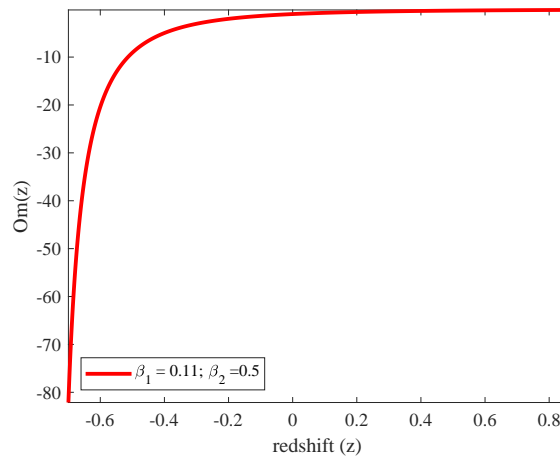


Figure 9. Illustration of $Om(z)$ against redshift (z)

- **Statefinder Pair (r, s):** The study and discrimination of essential DE models can be done with a sensitive and a geometrical diagnostic pair- (r, s) that had been developed by Sahni et al. [71] and Alam et al. [72]. This helps us to understand the process of Universe's acceleration. The statefinder pair (r, s) that purely depends on scale factor (a) and is defined as

$$r = \frac{\ddot{a}}{aH^3} \quad \& \quad s = \frac{r-1}{3(q-1/2)}.$$

For the constructed model, we have

$$r = \frac{(n+2)^2 \cosh^2(\beta_1(n+1)\tau) - 28n^2 - 67n - 40}{\sinh^2(\beta_1(n+1)\tau)(n+2)^2}, \quad (48)$$

$$\& \quad s = \frac{1}{(n+2)^3 \sinh(\beta_1(n+1)\tau)^4} \left\{ (n+2)^3 \cosh(\beta_1(n+1)\tau)^4 + (-200n^3 - 714n^2 - 852n - 340) \cosh(\beta_1(n+1)\tau)^2 + 280n^3 + 978n^2 + 1137n + 440 \right\}.$$

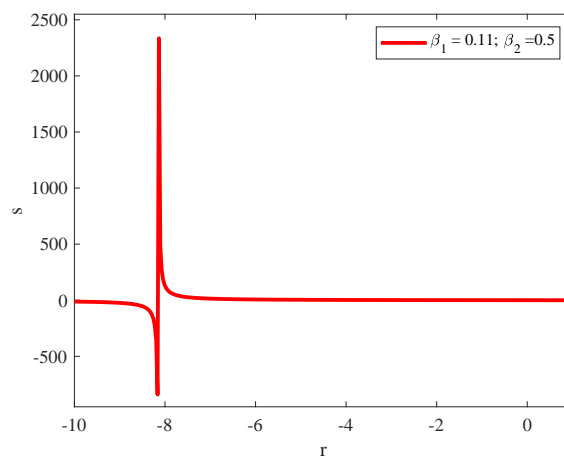


Figure 10. Illustration of $r-s$ plane

From the Fig. (10), which is the construction of $r-s$ plane, it can be interpreted that, the Universe begins its evolution from the quintessence and phantom region and finally reaches the Λ CDM region for $r = 1, s = 0$.






4. CONCLUSIONS

It has been many decades by now, that the scientists have started the process of figuring out the puzzling component: the DE and finding out the causes for the accelerated expansion of the cosmos. In such an attempt, we have built a model that helps us to understand these things. The constructed model describes the KS-Universe in the backdrop of RHDE in a general scalar tensor theory. It is observed that the Universe is homogeneous and anisotropic with a continuous expansion. Because of positive and decreasing energy density of matter (ρ_m) and as well as DE (ρ_{de}), the cosmos shows a rapid expansion. Also, a quintessence nature of the space is projected by the EoS parameter (ω_{de}); and the Universe is mainly characterized by freezing region, as $\omega_{de} < 0$ and $\omega'_{de} < 0$. The deceleration parameter (q) suggests that the Universe has a transition from erstwhile deceleration to present acceleration and shows a de-Sitter expansion at $q = -1$. The stability of the model has been examined with the help of squared speed of sound, which describes a stable behavior for the cosmos. The density parameter (Ω_{de}) varies in the positive region, decreasing against redshift (z) and where as the jerk parameter (j) approaches to unity as the time passes, while differing in the negative region. The $Om(z)$ parameter depicts the quintessence behavior of the cosmos, as the parameter is varying in the negative region. And, finally the statefinder plane ($r-s$) evolves from quintessence and phantom region and reaches the Λ CDM region for $r = 1$ and $s = 0$. Our observations are in concurrent with the recent studies and various experiments, and thus holding the sustainability of the model.

Acknowledgments

MVS acknowledges Department of Science and Technology (DST), Govt of India, New Delhi for financial support to carry out the Research Project [No. EEQ/2021/000737, Dt. 07/03/2022].

ORCID

 **T. Chinnappalanaidu**, <https://orcid.org/0000-0001-6902-2820>;  **S. Srivani Madhu**, <https://orcid.org/0009-0002-2640-3011>;  **M. Vijaya Santhi**, <https://orcid.org/0000-0002-0050-3033>;  **N. Sri Lakshmi Sudha Rani**, <https://orcid.org/0009-0009-9593-954X>;  **A. Krishna Rao**, <https://orcid.org/0000-0003-2786-9526>

REFERENCES

- [1] I. Bars, and J. Terning, *Extra Dimensions in Space and Time*, (Springer, NY, 2010). <https://doi.org/10.1007/978-0-387-77638-5>
- [2] P.A.R. Ade, *et al.*, *Astronomy & Astrophysics*, **571**, A16 (2014). <https://doi.org/10.1051/0004-6361/201321591>
- [3] S. Perlmutter, *et al.*, *Astrophys. J.* **517**, 565 (1999). <https://doi.org/10.1086/307221>
- [4] A.G. Riess, *et al.*, *Astron. J.* **116**, 1009 (1998). <https://doi.org/10.1086/300499>
- [5] F. Zwicky, *Astrophys. J.* **83**, 23 (1936). <https://doi.org/10.1086/143697>
- [6] F. Zwicky, *Astrophys. J.* **86**, 217 (1937). <https://doi.org/10.1086/143864>
- [7] V.C. Rubin, and W.K. Ford, *Astrophys. J.* **159**, 379 (1970). <https://doi.org/10.1086/150317>
- [8] R.V. Marttens, *et al.*, *Phys. Dark Uni.* **28**, 100490 (2020). <https://doi.org/10.1016/j.dark.2020.100490>
- [9] N. Aghanim, *et al.*, *Astro. Astrophys.* **641**, A6 (2020). <https://doi.org/10.1051/0004-6361/201833910>
- [10] S. Alam, *et al.*, *Astronomical Society*, **470**, 2617 (2017). <https://doi.org/10.1093/mnras/stx721>
- [11] P. Horava, and D. Minic, *Phys. Rev.Lett.* **85**, 1610 (2000). <https://doi.org/10.1103/PhysRevLett.85.1610>
- [12] S.D. Thomas, *Phys. Rev. Lett.* **89**, 081301 (2002). <https://doi.org/10.1103/PhysRevLett.89.081301>
- [13] S.D.H. Hsu, *Phys. Lett. B*, **594**, 13 (2004). <https://doi.org/10.1016/j.physletb.2004.05.020>
- [14] S. Wang, *et al.*, *Phys. repo.* **696**, 1 (2017). <https://doi.org/10.1016/j.physrep.2017.06.003>
- [15] A.G. Cohen, *et al.*, *Phys. Rev. Lett.* **82**, 4971 (1999). <https://doi.org/10.1103/PhysRevLett.82.4971>
- [16] B. Guberina, *et al.*, *J. Cosm. Astro. Phys.* **2007**, 012 (2007). <https://doi.org/10.1088/1475-7516/2007/01/012>
- [17] L. Susskind, *J. Math.Phys.* **36**, 6377 (1995). <https://doi.org/10.1063/1.531249>
- [18] M. Li, *Phys. Lett. B*, **603**, 1 (2004). <https://doi.org/10.1016/j.physletb.2004.10.014>
- [19] S. Nojiri, and S.D. Odintsov, *Gen. Rel. Grav.* **38**, 1285 (2006). <https://doi.org/10.1007/s10714-006-0301-6>
- [20] S. Nojiri, and S.D. Odintsov, *Eur. Phys. J. C*, **77**, 528 (2017). <https://doi.org/10.1140/epjc/s10052-017-5097-x>
- [21] A.S. Jahromi, *et al.*, *Phys. Lett. B*, **780**, 21 (2018). <https://doi.org/10.1016/j.physletb.2018.02.052>
- [22] C. Tsallis, and L.J.L. Cirto, *Eur. Phys. J. C*, **73**, 2487 (2013). <https://doi.org/10.1140/epjc/s10052-013-2487-6>
- [23] H. Moradpour, *et al.*, *Eur. Phys. J. C*, **78**, 829 (2018). <https://doi.org/10.1140/epjc/s10052-018-6309-8>
- [24] M. Tavayef, *et al.*, *Phys. Lett. B*, **781**, 195 (2018). <https://doi.org/10.1016/j.physletb.2018.04.001>
- [25] H. Moradpour, *et al.*, *Phys. Lett. B*, **783**, 82 (2018). <https://doi.org/10.1016/j.physletb.2018.06.040>
- [26] S. Abe, *Phys. Rev. E*, **63**, 061105 (2001). <https://doi.org/10.1103/PhysRevE.63.061105>
- [27] A. Majhi, *Phys. Lett. B*, **775**, 32 (2017). <https://doi.org/10.1016/j.physletb.2017.10.043>

- [28] T.S. Biro, and V.G. Czimmer, Phys. Lett. B, **726**, 861 (2013). <https://doi.org/10.1016/j.physletb.2013.09.032>
- [29] V.G. Czimmer, and H. Iguchi, Phys. Lett. B, **752**, 306 (2016). <https://doi.org/10.1016/j.physletb.2015.11.061>
- [30] N. Komatsu, Eur. Phys. J. C, **77**, 229 (2017). <https://doi.org/10.1140/epjc/s10052-017-4800-2>
- [31] H. Moradpour, *et al.*, Phys. Rev. D, **96**, 123504 (2017). <https://doi.org/10.1103/PhysRevD.96.123504>
- [32] A. Renyi, "On Measures of Entropy and Information," in: *Proceedings of the Fourth Berkeley Symposium on Mathematical Statistics and Probability*, (Berkley, 1961). pp. 547-561.
- [33] R.G. Cai, *et al.*, Class. Quantum Grav. **26**, 155018 (2009). <https://doi.org/10.1088/0264-9381/26/15/155018>
- [34] S. Chunlen, and P. Rangdee, (2020). <https://arxiv.org/abs/2008.13730>
- [35] U.Y.D. Prasanthi, and Y. Aditya, Res.Phys. **17**, 103101 (2020). <https://doi.org/10.1016/j.rinp.2020.103101>
- [36] U.K. Sharma, and V.C. Dubey, New Astronomy, **80**, 101419 (2020). <https://doi.org/10.1016/j.newast.2020.101419>
- [37] V.C. Dubey, *et al.*, Astrophys. Space Sci. **365**, 129 (2020). <https://doi.org/10.1007/s10509-020-03846-x>
- [38] V.C. Dubey, and U.K. Sharma, New Astronomy, **86**, 101586 (2021). <https://doi.org/10.1016/j.newast.2021.101586>
- [39] A.A. Mamon, *et al.*, Eur. Phys.J. C, **80**, 974 (2020). <https://doi.org/10.1140/epjc/s10052-020-08546-y>
- [40] A.A. Mamon, *et al.*, Eur. Phys. J. **136**, 134 (2021). <https://doi.org/10.1140/epjp/s13360-021-01130-7>
- [41] U.K. Sharma, *et al.*, Int. J. Mod.Phys. D, **30**, 2150021 (2021). <https://doi.org/10.1142/S0218271821500218>
- [42] U.K. Sharma, and V.C. Dubey, Int. J.Mod.Phys. D, **19**, 2250010 (2022). <https://doi.org/10.1142/S0219887822500104>
- [43] M.V. Santhi, and T. Chinnappalanaidu, New Astronomy, **92**, 101725 (2022). <https://doi.org/10.1016/j.newast.2021.101725>
- [44] M.V. Santhi, *et al.*, Ind. J. Phys. **98**, 3393 (2024). <https://doi.org/10.1007/s12648-023-03051-w>
- [45] C.W. Misner, *et al.*, *Gravitation*, (W.H. Freeman and Company, New York, 1973).
- [46] R.D. Inverno, *Introducing Einstein's Relativity*, (Oxford University Press, Oxford, 1998).
- [47] A.R. Liddle, *An Introduction to Modern Cosmology*, (Wiley and Sons, Chichester, 2015).
- [48] A.R. Liddle, and D.H. Lyth, *Cosmological Inflation and Large-Scale Structure*, (Cambridge University Press, Cambridge, 2000). <https://doi.org/10.1017/CBO9781139175180>
- [49] C.W. Misner, Astrophys. J. **151** 431 (1968). <https://doi.org/10.1086/149448>
- [50] R.K. Kantowski, and R.K. Sachs, J. Math. Phys. **7**, 443 (1966). <https://doi.org/10.1063/1.1704952>
- [51] E. Ghorani, and Y. Heydarzade, Eur.Phys. J. C, **81**, 557 (2021). <https://doi.org/10.1140/epjc/s10052-021-09355-7>
- [52] M.V. Santhi, and T.C. Naidu, Indian J. Phys. **96**, 953 (2022). <https://doi.org/10.1007/s12648-020-01983-1>
- [53] G. Oliveira-Neto, *et al.*, Brazil. J. Phys. **52**, 130 (2022). <https://doi.org/10.1007/s13538-022-01137-0>
- [54] U.Y.D. Prasanthi, and Y. Aditya, Phys. Dark Uni. **31**, 100782 (2021). <https://doi.org/10.1016/j.dark.2021.100782>
- [55] A.A. Shaikh, and D. Chakraborty, J. Geom. Phys. **160**, 103970 (2021). <https://doi.org/10.1016/j.geomphys.2020.103970>
- [56] M. Altunbas, J. Geom. **113**, 40 (2022). <https://doi.org/10.1007/s00022-022-00655-1>
- [57] K.J. Nordtvedt, Astrophys J. **161**, 1059 (1970). <https://doi.org/10.1086/150607>
- [58] J. Schwinger, *Particles, Sources and Fields*, (Addison-Wesley, Reading, 1970). <https://archive.org/details/particleessources0001schw>
- [59] P. Jordan, in: *Schwerkraft und Weltall*, (Friedrich Vieweg and Sohn, Braunschweig, 1955). pp.207-213.
- [60] C.H. Brans, and R.H. Dicke, Phys. Rev. **124**, 925 (1961). <https://doi.org/10.1103/PhysRev.124.925>
- [61] V.U.M. Rao, and D. Neelima, Iran. J.Phys. Res. **14**(3), 35 (2014). https://ijpr.iut.ac.ir/article_1085_a67b4dc9c472767d094a4c561fd7475f.pdf?lang=en
- [62] V. U. M. Rao., D. Neelima, *Int. Sch. Res. Notices*. **2013**, 174741 (2013). <http://dx.doi.org/10.1155/2013/174741>
- [63] V.U.M. Rao, and D. Neelima, *Int. Sch. Res. Notices*. **2013**, 759274 (2013). <https://doi.org/10.1155/2013/759274>
- [64] V.U.M. Rao, and D. Neelima, *J. Theor. Appl. Phys.* **7**, 50 (2013). <https://doi.org/10.1186/2251-7235-7-50>
- [65] A.R. Solomon, and M. Trodden, *J. Cosmo. Astro. Phys.* **02**, 031 (2018). <https://doi.org/10.1088/1475-7516/2018/02/031>
- [66] Q. Huang, *et al.*, Anna. Phys. **399**, 124 (2018). <https://doi.org/10.1016/j.aop.2018.09.014>
- [67] J. Bloomfield, J. Cosmol. Astropart. Phys. **12**, 044 (2013). <https://doi.org/10.1088/1475-7516/2013/12/044>
- [68] M. López, *et al.*, J. Cosmo. Astro. Phys. **2021**, (2021). <https://doi.org/10.1088/1475-7516/2021/10/021>
- [69] R. Caldwell, and E.V. Linder, Phys. Rev. Lett. **95**, 141301 (2005). <https://doi.org/10.1103/PhysRevLett.95.141301>
- [70] M.V. Sahni, *et al.*, Phys. Rev. D, **78**, 103502 (2008). <https://doi.org/10.1103/PhysRevD.78.103502>
- [71] M.V. Sahni, *et al.*, J. Exp.Theor. Phys. Let. **77**(5), 201 (2003). <https://doi.org/10.1134/1.1574831>
- [72] U. Alam, *et al.*, Mon. Not. R. Astron.Soc. **344**(4), 1057 (2003). <https://doi.org/10.1046/j.1365-8711.2003.06871.x>

ЕВОЛЮЦІЯ ВСЕСВІТУ КАНТОВСЬКОГО-САКСА З ГОЛОГРАФІЧНОЮ ТЕМНОЮ ЕНЕРГІЄЮ РЕНІ Т. Чиннаппаланайду^a, С. Шривані Мадху^a, М. Віджая Санті^b, N. Шрі Лакшмі Судха Рані^{b,c}, А. Крішна Рао^d

^aКафедра математики, Інститут інформаційних технологій Віньяна (автономний), Вішакхапатнам 530049, Індія

^bКафедра прикладної математики, Університет Андхра, Вішакхапатнам 530003, Індія

^cКафедра гуманітарних наук та природничих наук, Інженерний коледж Тігала Крішна Редді, Хайдерабад 500097, Індія.

^dКафедра математики, Державний коледж, Чодаварам, Андхрапрадеш, 531036, Індія

Розглядаючи узагальнену скалярно-тензорну теорію як гравітаційну теорію, ми дослідили динамічну еволюцію однорідного та анізотропного простору Кантовського-Сакса за наявності голографічної темної енергії Реньї. Щоб отримати розв'язок для цієї моделі, ми вивели рівняння поля, а також проаналізували різні фізичні та геометричні параметри моделі, такі як уповільнення, ривок, EoS, площа EoS, пара statefinder, густина, квадрат швидкості звуку та Om-діагностика. Ці параметри показують, що модель є дуже стабільною, проектує квінтесенційну природу, а також отримана модель відображає модель Λ CDM. Наші спостереження та висновки з побудованої моделі добре узгоджуються з нещодавніми дослідженнями.

Ключові слова: метрика Кантовського-Сакса; анізотропні моделі; загальна скалярно-тензорна теорія; голографічна темна енергія Реньї; темна енергія

FEASIBILITY OF NUCLEAR FUSION OF ${}^1_1\text{H} + {}^7_3\text{Li}$ FOR GENERATION OF ELECTRIC POWER IN TCT FUSION REACTOR

 B.M. Dyavappa

Department of Physics, Government First Grade College, Chikkaballapura, India

**Corresponding Author e-mail: dyavappabm@gmail.com*

Received February 14, 2025; revised April 21, 2025; accepted May 15, 2025

The feasibility of nuclear fusion reaction ${}^1_1\text{H} + {}^7_3\text{Li} \rightarrow 2{}^4_2\text{He}$ (17.5 MeV), for generation of electric power in nuclear reactors is presented. The fusion cross-section of nuclear reaction for the projectile beam of ${}^1_1\text{H}$ whose energy ranges from 1 keV to 1×10^4 keV in the centre-of-mass frame is computed with the aid of GEMINI⁺⁺ statistical decay model. The Maxwellian average of the product of the fusion cross-section and the relative velocity of projectile and target $\langle \sigma v \rangle$ gives the fusion reaction rate. The fusion reaction rate should be sufficiently high to produce more nuclear fusion electric power. The energy multiplication factor (ζ) of nuclear fusion is defined as the ratio of nuclear fusion energy (E_F) generated to injected energy of projectile beam (E_P), i.e., $\zeta = E_F/E_P$. The lower energy loss rate and higher fusion reaction rate should contribute higher value of the energy multiplication factor (ζ). The Energy multiplication factor (ζ) for nuclear fusion of ${}^1_1\text{H} + {}^7_3\text{Li}$, variation with projectile beam energy is presented. The energy multiplication factor can be enhanced by clamping (or fixing) of projectile beam energy at a suitable value. The clamping of the projectile beam energy defers slowing down process of projectile beam and compensates the Coulomb drag by the bulk plasma, thus the energy multiplication factor increases. The variation of the Energy multiplication factor (ξ) for nuclear fusion of ${}^1_1\text{H} + {}^7_3\text{Li}$, with projectile beam energy clamping (or fixing) is also presented.

Keywords: Proton-Lithium fusion; TCT reactor; Energy multiplication factor; Projectile beam energy clamping

PACS: 24.00, 25.00, 28.00

1. INTRODUCTION

In the future world enormous amount of electric power energy can be generated by nuclear fusion in nuclear reactors. The energy distribution of the ions of the plasma consists of two components in Two-component torus (TCT) fusion reactor, which is the torus type plasma-containment nuclear fusion reactor [1-3]. In TCT nuclear fusion reactor high energy ion beam is shot into target plasma, to cause the nuclear fusion reaction between the ions, electrons of the target plasma and the injected beam. The ions and electrons of plasma possess thermal energy and it can be converted into electrical energy with high efficiency in nuclear fusion reactor. The energy multiplication factor is an important parameter to optimise nuclear fusion reactions for the commercial production of electrical power energy. When energy multiplication factor $\zeta = 1$, the fusion power is equal to the thermal power to cause fusion and it is known as breakeven, and the plasma will not be cooled down without any external heating. If $\zeta > 1$, self-heating causes the process to become self-sustaining and ignition occurs at the high temperature. The high value of energy multiplication factor ζ is essential for commercially possible practical TCT fusion reactor. The fusion power density in a TCT fusion reactor can be much more than in thermal reactor of the same pressure. The most favourable injection energy of incident beam for nuclear fusion to occur is the energy which gives maximum energy multiplication factor ζ , as it yields maximum output energy.

Researchers studied the feasibility of energy multiplication factor of the ${}^2_1\text{H} + {}^3_1\text{H}$ nuclear fusion reaction in detail [4-8]. K. Ogawa et.al studied the ${}^1_1\text{H} + {}^{11}_5\text{B}$ fusion reaction in the fusion reactor [9]. J. Bahmani studied the parameters related to the energy multiplication factor of ${}^3_2\text{He} + {}^6_3\text{Li}$ for two-component torus fusion plasma [10]. The energy multiplication factor should be high to produce nuclear electric power economically. The fusion reaction rate, the energy confinement time, the beam containment time, the impurities present in the target plasma, the beam energy clamping and the plasma density, influence the energy multiplication factor. In the present work, I have studied the feasibility of the fusion reaction of ${}^1_1\text{H} + {}^7_3\text{Li}$ in nuclear fusion reactor for the commercial production of electric power to meet the demand in the future.

2. THEORY

2.1 The fusion cross section

The fusion cross-section at the centre-of-mass of ${}^1_1\text{H}$ projectile and ${}^7_3\text{Li}$ target system is given by [11]

$$\sigma(E) = \frac{\pi R^2(E)}{E} \int_0^E \frac{dE'}{1 + \exp\left[2\left(\frac{A_1}{E'} - A_2 E' + A_3\right)\right]} \quad (1)$$

Here $\sigma(E)$ is fusion cross-section for projectile and target, E is projectile beam energy, $R(E)$ is the effective radius of the projectile and target system, A_1 , A_2 , A_3 are constants.

2.2 The Rate of Nuclear fusion reaction

The rate of nuclear fusion reaction evaluated as the Maxwellian average of the product of the fusion cross-section and the relative velocity between projectile and target which is given by [12,13]

$$\langle \sigma v \rangle = \left(\frac{8}{\pi}\right)^{1/2} \left(\frac{\mu}{k_B T_i}\right)^{3/2} \frac{1}{m_p^2} \int_0^E E \sigma(E) \exp\left[-\left(\frac{\mu E}{m_p k_B T_i}\right)\right] dE \quad (2)$$

Here v is the relative velocity between 1_1H projectile and 7_3Li target, μ is reduced mass of projectile and target, k_B is Boltzmann's constant, T_i is temperature of ion plasma, m_p is the mass of projectile, E is the energy of projectile beam.

2.3 Injected beam energy transfer to target plasma

When energetic injected 1_1H beam collides with ions and electrons of 7_3Li target plasma, the energy of injected beam is transferred to ions and electrons through Coulomb interactions, until thermal equilibrium is reached. The mean rate of energy loss of injected 1_1H beam by all thermal electrons and ions of 7_3Li target plasma is determined using Fokker-Planck slowing down model of Sivukhin as [14-17]

$$\left\langle \frac{dE}{dt} \right\rangle = \frac{4\pi n_T Z_P^2 Z_T^2 e^4 \Lambda}{v_p} \sqrt{\frac{m_P}{2E_P}} \sum_{T=i,e} F(x_T, \beta_{TP}) \quad (3)$$

Here n_T is the number density of ions or electrons of 7_3Li target plasma, Z_P and Z_T are charge states of ions or electrons of 1_1H projectile and 7_3Li target respectively, e is charge of electron, Λ is coulomb logarithm of 7_3Li target plasma, v_p is relative velocity of 1_1H projectile w.r.t 7_3Li target, m_P is mass of projectile, E_P is energy of projectile, $F(x_T, \beta_{TP})$ is related to the error function as

$$F(x_T, \beta_{TP}) = \phi(x_T) - (1 + \beta_{TP})\phi'(x_T) \quad (3a)$$

Here

$$\phi(x_T) = \frac{2}{\sqrt{\pi}} \int_0^{x_T} e^{-t^2} dt, \quad \beta_{TP} = \frac{m_T}{m_P}, \quad x_T = \beta_{TP} \frac{m_P}{2k_B T_T}$$

2.4 Energy Multiplication Factor (ζ) of Nuclear Fusion

When high energy projectile beam is injected into target plasma, nuclear fusion occurs. The energy multiplication factor of nuclear fusion is defined as the ratio of nuclear fusion energy (E_F) to injected energy of projectile beam (E_P) [12]

$$\zeta = \frac{E_{fusion}}{E_{projectile}} = \frac{Q n_T}{E_{1H}} \int_{E_{Th}}^{E_{1H}} \frac{\langle \sigma v \rangle}{\langle \frac{dE}{dt} \rangle} dE \quad (4)$$

Here, Q is fusion power gain of ${}^1_1H + {}^7_3Li$ nuclear fusion reaction, n_T is the number density of target plasma, E_{Th} is the threshold value of energy for fusion to occur and E_{1H} is the energy of 1_1H projectile beam.

2.5 Projectile beam energy clamping

One mode of two-component ${}^1_1H + {}^7_3Li$ nuclear fusion uses an auxiliary energy input to maintain the super-thermal ions of 7_3Li target at or near the injected energy of 1_1H projectile beam by energy clamping, as it defers slowing down process and compensates the Coulomb drag by the bulk plasma of 7_3Li target. The injected-ion energy is kept near the peak of the fusion cross section, when maximum fusion rate of nuclear reaction is achieved. The energy multiplication factor can be increased, even though the plasma temperature remains at the same value. The ions of plasma of 7_3Li target can be maintained at optimum values of high energies for nuclear fusion reactions to occur for longer periods of time. The energy multiplication factor for projectile energy clamping (or fixing) is given by [12]

$$\xi = Q n_T \frac{[\sigma v]_{E_0}}{[\frac{dE}{dt}]_{E_0}} \quad (5)$$

Here E_0 is clamped projectile beam energy.

3. Results and discussion

The fusion cross-section for ${}^1_1H + {}^7_3Li$ nuclear fusion is computed with the aid of GEMINI⁺⁺ statistical decay model [18]. I have computed fusion-cross-section in the centre-of-mass projectile beam energy ranging from 1 keV to 1×10^4 keV for ${}^1_1H + {}^7_3Li$ nuclear fusion. The calculations of the fusion cross section, the reactivity, the energy loss rate, the energy multiplication factor and the beam energy clamped energy multiplication factor of ${}^1_1H + {}^7_3Li$ fusion are shown in Table 1.

The variation of fusion cross section with the projectile beam energy is as shown in Figure 1, it is observed that the fusion cross section is $5.3 \times 10^{-21} \text{ cm}^2$ at 1 keV energy, decreases gradually to $0.53 \times 10^{-21} \text{ cm}^2$ at 10 keV energy and remains almost a constant at $0.0053 \times 10^{-21} \text{ cm}^2$ between $1 \times 10^2 \text{ keV} - 1 \times 10^3 \text{ keV}$ energy, beyond which it is

almost 10^{-25} cm^2 up to $1 \times 10^3 \text{ keV}$. The nuclear fusion reaction rate is measured as the Maxwellian average $\langle \sigma v \rangle$ of the product of the fusion cross-section and the relative velocity of ${}^1_1\text{H}$ projectile w.r.t ${}^7_3\text{Li}$ target. The fusion reaction rate of nuclear reaction is enhanced to produce more fusion energy.

Table 1. Fusion cross section, Reactivity, Energy loss rate of projectile beam due to collisions with ions, electrons and both ions and electrons, Energy multiplication factor and Beam energy clamped Energy multiplication factor of ${}^1_1\text{H} + {}^7_3\text{Li}$ nuclear fusion

$E_{p(\text{CM})}$ (keV)	σ (10^{-21} cm^2)	σv ($10^{-18} \text{ cm}^3 \text{ s}^{-1}$)	$\left[\frac{dE}{dt}\right]_i$	$\left[\frac{dE}{dt}\right]_e$	$\left[\frac{dE}{dt}\right]_{i+e}$	ζ	ξ
1	5.29E+00	2.12E-02	-3.11E+03	-2.62E+00	-3.12E+03	-1.19E-02	-1.19E-02
2	2.64E+00	4.21E-02	-2.88E+03	-2.66E+00	-2.88E+03	-2.47E-02	-2.55E-02
3	1.76E+00	6.29E-02	-2.67E+03	-2.59E+00	-2.67E+03	-3.84E-02	-4.12E-02
4	1.32E+00	8.35E-02	-2.47E+03	-2.58E+00	-2.47E+03	-5.32E-02	-5.92E-02
5	1.06E+00	1.04E-01	-2.28E+03	-2.56E+00	-2.28E+03	-6.91E-02	-7.96E-02
6	8.81E-01	1.24E-01	-2.11E+03	-2.54E+00	-2.11E+03	-8.63E-02	-1.03E-01
7	7.55E-01	1.44E-01	-1.95E+03	-2.52E+00	-1.95E+03	-1.05E-01	-1.30E-01
8	6.61E-01	1.64E-01	-1.80E+03	-2.51E+00	-1.80E+03	-1.25E-01	-1.60E-01
9	5.87E-01	1.84E-01	-1.66E+03	-2.49E+00	-1.66E+03	-1.46E-01	-1.94E-01
10	5.29E-01	2.03E-01	-1.52E+03	-2.47E+00	-1.53E+03	-1.70E-01	-2.33E-01
20	2.64E-01	3.83E-01	-6.27E+02	-2.31E+00	-6.29E+02	-7.02E-01	-1.06E+00
30	1.76E-01	5.47E-01	-1.92E+02	-2.12E+00	-1.94E+02	-2.35E+00	-4.93E+00
40	1.32E-01	6.97E-01	1.45E+01	-1.95E+00	1.25E+01	2.20E+01	9.75E+01
50	1.06E-01	8.35E-01	1.09E+02	-1.78E+00	1.07E+02	2.48E+01	1.36E+01
60	8.81E-02	9.61E-01	1.49E+02	-1.60E+00	1.48E+02	2.67E+01	1.14E+01
70	7.55E-02	1.08E+00	1.64E+02	-1.41E+00	1.63E+02	2.83E+01	1.16E+01
80	6.61E-02	1.18E+00	1.66E+02	-1.23E+00	1.65E+02	2.99E+01	1.25E+01
90	5.87E-02	1.28E+00	1.63E+02	-1.06E+00	1.62E+02	3.14E+01	1.38E+01
100	5.29E-02	1.37E+00	1.58E+02	-8.82E-01	1.57E+02	3.29E+01	1.52E+01
200	2.64E-02	1.74E+00	1.15E+02	8.84E-01	1.15E+02	4.61E+01	2.64E+01
300	1.76E-02	1.90E+00	9.35E+01	2.65E+00	9.62E+01	5.76E+01	3.45E+01
400	1.32E-02	1.96E+00	8.10E+01	4.41E+00	8.54E+01	6.77E+01	4.02E+01
500	1.06E-02	1.99E+00	7.25E+01	6.17E+00	7.86E+01	7.65E+01	4.42E+01
600	8.81E-03	2.00E+00	6.61E+01	7.94E+00	7.41E+01	8.44E+01	4.72E+01
700	7.55E-03	2.00E+00	6.12E+01	9.55E+00	7.08E+01	9.15E+01	4.95E+01
800	6.61E-03	2.01E+00	5.73E+01	1.15E+01	6.87E+01	9.78E+01	5.11E+01
900	5.87E-03	2.01E+00	5.40E+01	1.32E+01	6.72E+01	1.04E+02	5.22E+01
1000	5.29E-03	2.01E+00	5.12E+01	1.50E+01	6.62E+01	1.09E+02	5.30E+01
2000	2.64E-03	2.01E+00	3.62E+01	3.25E+01	6.87E+01	1.34E+02	5.11E+01
3000	1.76E-03	2.01E+00	2.96E+01	4.99E+01	7.94E+01	1.49E+02	4.42E+01
4000	1.32E-03	2.01E+00	2.56E+01	6.71E+01	9.27E+01	1.59E+02	3.79E+01
5000	1.06E-03	2.01E+00	2.29E+01	8.43E+01	1.07E+02	1.65E+02	3.28E+01
6000	8.81E-04	2.01E+00	2.09E+01	1.01E+02	1.22E+02	1.70E+02	2.87E+01
7000	7.55E-04	2.01E+00	1.94E+01	1.18E+02	1.38E+02	1.74E+02	2.55E+01
8000	6.61E-04	2.01E+00	1.81E+01	1.35E+02	1.53E+02	1.77E+02	2.29E+01
9000	5.87E-04	2.01E+00	1.71E+01	1.52E+02	1.69E+02	1.79E+02	2.08E+01
10000	5.29E-04	2.01E+00	1.62E+01	1.68E+02	1.85E+02	1.81E+02	1.90E+01

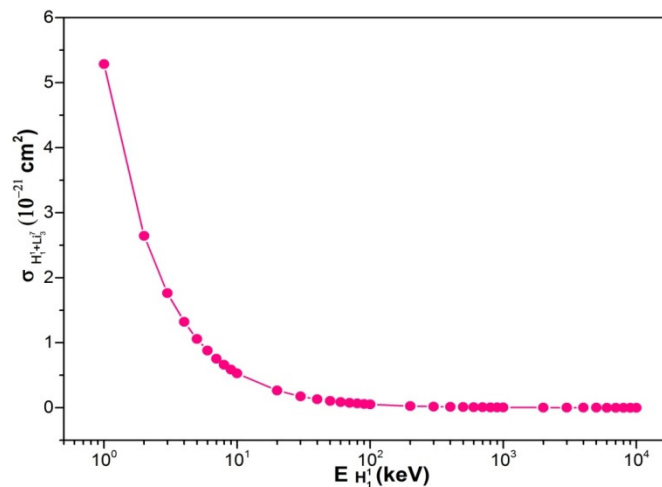


Figure 1. Fusion cross section of ${}^1_1\text{H} + {}^7_3\text{Li}$ as a function of ${}^1_1\text{H}$ projectile beam energy

The nuclear fusion ${}^1_1\text{H} + {}^7_3\text{Li}$ reaction rate is shown in the Figure 2, it is observed that the fusion reaction rate is $0.02 \times 10^{-17} \text{ cm}^3 \text{ s}^{-1}$ at 1 keV energy, increases gradually to $2.0 \times 10^{-17} \text{ cm}^3 \text{ s}^{-1}$ at $1 \times 10^3 \text{ keV}$ and remains almost a constant at $2.0 \times 10^{-17} \text{ cm}^3 \text{ s}^{-1}$ in the range $1 \times 10^3 \text{ keV} - 1 \times 10^4 \text{ keV}$ energy.

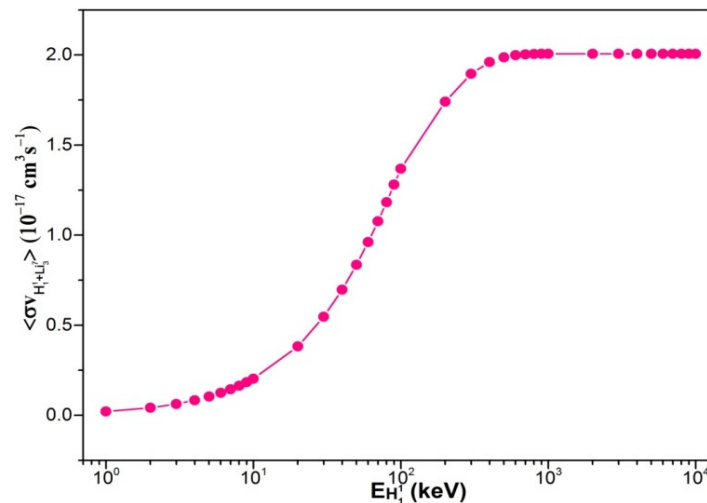


Figure 2. Fusion reaction rate of $^1H + ^7Li$ as a function of 1H projectile beam energy

The rate of total energy loss of $^1H + ^7Li$ nuclear fusion reaction is shown in the Figure 3, it is observed that the rate of energy loss of 1H projectile due to collisions with ions of 7Li target plasma is 158.36 keVs^{-1} at 100 keV , decreases sharply to 51.2 keVs^{-1} at $1 \times 10^3 \text{ keV}$, and decreases slowly from 36.2 keVs^{-1} to 16.2 keVs^{-1} in the energy range $2 \times 10^3 \text{ keV} - 1 \times 10^4 \text{ keV}$. The rate of energy loss of 1H projectile due to collisions with electrons of 7Li target plasma is 0.88 keVs^{-1} at 200 keV energy, increases linearly to 168.4 keVs^{-1} at $1 \times 10^4 \text{ keV}$ energy. Therefore, the rate of total energy loss of 1H projectile due to collisions with the ions and electrons of 7Li target plasma is 157.5 keVs^{-1} at 100 keV energy, decreases gradually to 66.2 keVs^{-1} at $1 \times 10^3 \text{ keV}$ energy, and increases linearly from 68.7 keVs^{-1} to 184.6 keVs^{-1} in the energy range $2 \times 10^3 \text{ keV} - 1 \times 10^4 \text{ keV}$. Thus, to generate more fusion power, the energy loss of the fusion reaction must be less.

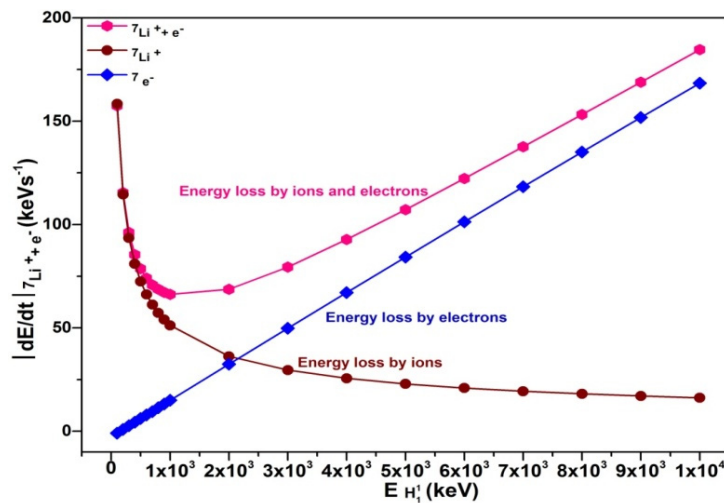


Figure3. Energy loss rates of ions and electrons of 7Li as functions of 1H projectile beam energy

The energy multiplication factor (ζ) of nuclear fusion is defined as the ratio of nuclear fusion energy (E_F) to injected energy of projectile beam (E_p). The energy multiplication factor (ζ) for $^1H + ^7Li$ nuclear fusion is shown in the Figure 4, it is observed that the energy multiplication factor increases sharply from 22.04 at 40 keV energy to 108.94 at $1 \times 10^3 \text{ keV}$ energy and it increases slowly from 134.5 at $2 \times 10^3 \text{ keV}$ to 180.75 at $1 \times 10^4 \text{ keV}$ projectile energy. The lesser the energy loss rate and more fusion reaction rate can contribute to higher value of the energy multiplication factor.

The energy multiplication factor of $^1H + ^7Li$ nuclear fusion reaction can be enhanced by clamping (fixing) of 1H projectile beam energy. The clamping of the 1H projectile beam energy, defers slowing down process and compensates the Coulomb drag by the bulk plasma of 7Li and consequently increases the energy multiplication factor (ξ). The variation of the energy multiplication factor with projectile beam energy being clamped is shown in Figure 5, it is observed that the energy multiplication factor with projectile beam energy clamping (ξ) for $^1H + ^7Li$ nuclear fusion increases sharply from 11.4 at 60 keV energy to 53.0 at 1000 keV energy and decreases gradually from 51.1 at 2000 keV energy to 19.02 at $1 \times 10^4 \text{ keV}$ projectile energy.

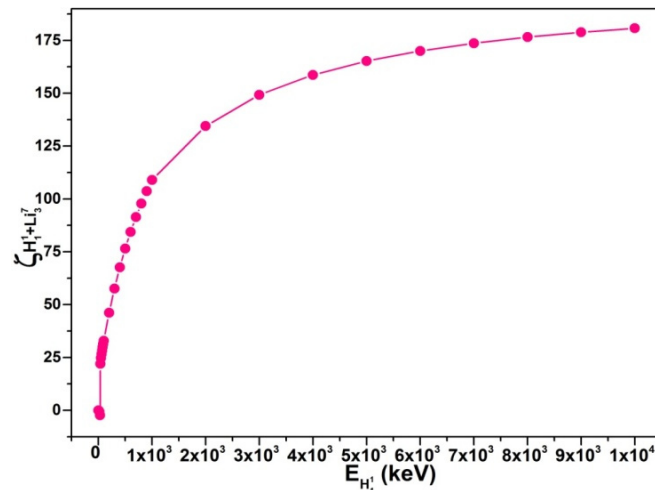


Figure 4. Energy multiplication factor of ${}^1_1\text{H} + {}^7_3\text{Li}$ as function of ${}^1_1\text{H}$ projectile beam energy

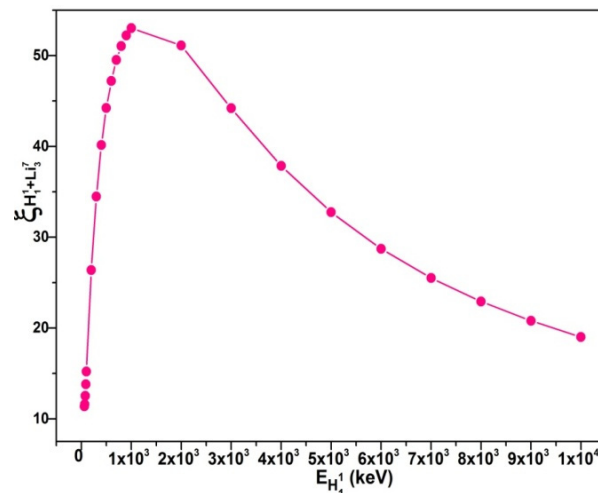


Figure 5. Energy multiplication factors of ${}^1_1\text{H} + {}^7_3\text{Li}$ as a function of projectile beam energy clamping

4. CONCLUSION

The nuclear fusion reaction ${}^1_1\text{H} + {}^7_3\text{Li} \rightarrow 2{}^4_2\text{He}$ (17.5 MeV) for generation of electric power in nuclear reactors has been studied. The fusion cross-section was computed with the aid of GEMINI⁺⁺ statistical decay model. I have computed fusion-cross-section in the centre-of-mass projectile beam energy range from 1 keV to 1×10^4 keV for ${}^1_1\text{H} + {}^7_3\text{Li}$ nuclear fusion. The fusion reaction rate is the Maxwellian average of the product of the fusion cross-section and the relative velocity of ${}^1_1\text{H}$ projectile and ${}^7_3\text{Li}$ target. The Energy multiplication factor (ξ) for ${}^1_1\text{H} + {}^7_3\text{Li}$ nuclear fusion variation with the projectile beam energy is presented. To generate more fusion power the fusion reaction rate should be higher, the energy loss rate due to collisions of the fusion reaction must be lower. The lower value of energy loss rate of projectile due to collisions with ions, electrons of plasma and more fusion reaction rate contribute higher value of the energy multiplication factor. The energy multiplication factor can be enhanced by clamping (fixing) of ${}^1_1\text{H}$ projectile beam energy. The clamping of the projectile beam energy defers slowing down process of fusing nuclei and compensates the Coulomb drag by the bulk plasma and consequently increases the energy multiplication factor. The variation of the Energy multiplication factor (ξ) with projectile beam energy clamping (fixing) also presented.

ORCID

©B.M. Dyavappa, <https://orcid.org/0000-0001-9326-4686>

REFERENCES

- [1] N. Inoue, and K. Yamazaki, "Reviews of TCT fusion reactor," Nippon Genshiryoku Gakkai-Shi, **18**, 189 (1976).
- [2] F. Tenney, "Reactor applications of two-component plasmas," IEEE Transactions on Plasma Science **4**, 157-161 (1976). <https://doi.org/10.1109/TPS.1976.4316957>
- [3] D. Meade, "Results and plans for the tokamak fusion test reactor in Fusion energy development", (Fusion Power Associates, 1987).
- [4] K. McGuire, H. Adler, P. Alling, C. Ancher, H. Anderson, J. Anderson, J.W. Anderson, *et al.*, "Review of deuterium-tritium results from the tokamak fusion test reactor," Physics of Plasmas, **2**, 2176-2188 (1995). <https://doi.org/10.1063/1.871303>

- [5] J. Team, *et al.*, "Fusion energy production from a deuterium-tritium plasma in the jet tokamak," Nuclear Fusion, **32**, 187 (1992). <https://doi.org/10.1088/0029-5515/32/2/I01>
- [6] M. Keilhacker, A. Gibson, C. Gormezano, P. Lo-mas, P. Thomas, M. Watkins, P. Andrew, *et al.*, "High fusion performance from deuterium-tritium plasmas in jet," Nuclear Fusion, **39**, 209 (1999). <https://doi.org/10.1088/0029-5515/39/2/306>
- [7] W. Lv, H. Duan, and J. Liu, "Enhanced deuterium-tritium fusion cross sections in the presence of strong electromagnetic fields," Physical Review C, **100**, 064610 (2019). <https://doi.org/10.1103/PhysRevC.100.064610>
- [8] M.A. Abdou, E. Vold, C. Gung, M. Youssef, and K. Shin, "Deuterium-tritium fuel self-sufficiency in fusion reactors," Fusion Technology, **9**, 250-285 (1986). <https://doi.org/10.13182/FST86-A24715>
- [9] K. Ogawa, M. Isobe, H. Nuga, R. Seki, S. Ohdachi, and M. Osakabe, "Evaluation of alpha particle emission rate due to $^1_1\text{H} + ^{11}_5\text{B}$ fusion reaction in the large helical device," Fusion Science and Technology, **78**, 175-185 (2022). <https://doi.org/10.1080/15361055.2021.1973294>
- [10] J. Bahmani, "Parameters affecting the energy multiplication factor of a $^2_1\text{H} + ^6_3\text{Li}$ two-component fusion plasma," IEEE Transactions on Plasma Science, **49**, 3108-3112 (2021). <https://doi.org/10.1109/TPS.2021.3109657>
- [11] M. Mahdavi, T. Koohrokhi, B. Kaleji, and B. Jalalee, "Calculation of fusion cross-section for $^3_2\text{He} + ^9_4\text{Li}$ system at near barrier energies," International Journal of Modern Physics E, **19**, 141-145 (2010). <https://doi.org/10.1142/S0218301310014686>
- [12] G.H. Miley, and H.H. Towner, "Reactivities for two-component fusion calculations", (Tech. Rep. Illinois Univ. Urbana, USA, 1975)
- [13] O.N. Oudah, and R.H. Majeed, "Fusion power density and radiation losses characteristics for tritium fusion reactions," Journal of Physics: Conference Series, **1234**, 012114(2019). <https://doi.org/10.1088/1742-6596/1234/1/012114>
- [14] D. Sivukhin, "Coulomb collisions in a fully ionized plasma", Rev. Plasma Phys. (USSR)(Engl. Transl.) **4**, (1966).
- [15] C. Chang, and H. Pecseli, "Estimations of the effect of alpha particles on a refuelling pellet", 378 (Risø National Laboratory, 1978).
- [16] V.T. Voronchev, Y. Nakao, and Y. Watanabe, "Model description of non-maxwellian nuclear processes in the solar interior," (2016). <https://arxiv.org/pdf/1606.00612>
- [17] R.C. Canfield, and C.R. Chang, "Ly-alpha and h-alpha emission by super thermal proton beams", The Astrophysical Journal, **295**, 275 (1985). <https://doi.org/10.1086/163371>
- [18] R. Charity, "GEMINI: a code to simulate the decay of a compound nucleus by a series of binary decays", Tech. Rep. (2008).

МОЖЛИВІСТЬ ЯДЕРНОГО СИНТЕЗУ $^1_1\text{H} + ^7_3\text{Li}$ ДЛЯ ГЕНЕРАЦІЇ ЕЛЕКТРОЕНЕРГІЇ У ТЕРМОЯДЕРНОМУ РЕАКТОРІ ТСТ

Б.М. Дьявappa

Кафедра фізики, державний коледж першого класу, Чиккабаллапура, Індія

Представлено можливість ядерної реакції синтезу $^1_1\text{H} + ^7_3\text{Li} \rightarrow 2^4_2\text{He}$ (17,5 MeV) для генерації електроенергії в ядерних реакторах. Перетин термоядерної реакції для пучка, що налітає ^1_1H , енергія якого в системі центру мас становить від 1 кеВ до 1×10^4 кеВ, обчислюється за допомогою статистичної моделі розпаду GEMINI++. Максвелловський середній твір перерізу синтезу та відносно швидкості атому що налітає та мішені $\langle \sigma v \rangle$ дає швидкість реакції синтезу. Швидкість реакції ядерного синтезу має бути досить високою, щоб виробляти більше електроенергії. Коефіцієнт множення енергії (ζ) ядерного синтезу визначається як відношення енергії ядерного синтезу (E_F), що генерується до інжектованої енергії пучка атомів (E_P), тобто $\zeta = E_F/E_P$. Нижча швидкість втрати енергії та більш висока швидкість реакції синтезу повинні вносити більш високе значення коефіцієнта множення енергії (ζ). Подано зміну коефіцієнта множення енергії (ζ) для ядерного синтезу $^1_1\text{H} + ^7_3\text{Li}$ залежно від енергії пучка атомів що налітають. Коефіцієнт множення енергії може бути збільшений шляхом фіксації (або фіксації) енергії пучка на відповідному значенні. Фіксація енергії снарядного пучка затримує процес уповільнення пучка атомів та компенсує кулонівський опір об'ємною плазмою, таким чином, коефіцієнт множення енергії збільшується. Також представлено зміну коефіцієнта множення енергії (ζ) для ядерного синтезу $^1_1\text{H} + ^7_3\text{Li}$ із затисканням (або фіксацією) енергії пучка що налітають.

Ключові слова: протонно-літєвий синтез; реактор ТСТ; коефіцієнт множення енергії; фіксація енергії пучка що налітає

THEORETICAL ANALYSIS OF INTERBAND SINGLE-PHOTON LIGHT ABSORPTION IN SEMICONDUCTORS: EFFECTS OF VALENCE-CONDUCTION BAND MIXING AND TEMPERATURE-DEPENDENT BANDGAP

✉ Rustam Y. Rasulov^a, ✉ Voxob R. Rasulov^{a*}, Nurillo U. Kodirov^a, Mardonbek Kh. Nasirov^c, Iqbol M. Eshboltaev^b

^a Fergana State University, Fergana, Uzbekistan

^b Kokand State pedagogical Institute, Kokand, Uzbekistan

^c Fergana Polytechnic Institute, Fergana, Uzbekistan

*Corresponding Author e-mail: vrrasulov83@gmail.com

Received December 28, 2024; revised February 15, 2025; accepted February 20, 2025

This study presents a theoretical analysis of the spectral and temperature dependence of the single-photon absorption coefficient for linearly and circularly polarized light in semiconductors with diamond and zinc blende lattice structures. Optical transitions involving subbands of light and heavy holes and the conduction band are examined, incorporating effects such as temperature-dependent bandgap, valence-conduction band state mixing, and coherent saturation. The findings indicate that heavy holes contribute approximately 10 times more than light holes to single-photon absorption. Furthermore, the relationship between linear-circular dichroism and light intensity is explored, emphasizing the role of coherent saturation effects.

Keywords: Semiconductor; Temperature dependence of the band gap; Mixing of valence band states with conduction band states; single-photon absorption; spectral-temperature dependence

PACS: 71.20. – b, 71.28. + d

INTRODUCTION

Today, the development of not only micro-, but also nanoelectronics requires knowledge of the band structure of semiconductors, to which many literatures are devoted (for example, [1-5]).

A number of optical phenomena in both bulk and low-dimensional semiconductors are determined by the states of current carriers in several zones, the energies of which are close in comparison with the energy distances to other zones [5, 6]. For example, in *InSb* the conduction band (*V*-band) and valence band (*c*-band) are located quite close, and the spin-orbit splitting subband (*SO*-band) is relatively far away (Fig. 1a). In *GaAs*, the *c*- and *V*-bands are located close, and the upper-perturbed conduction band (*c*-band) is far away (Fig. 1b) [7].

However, most of them do not pay attention to the spin-orbit interaction of bands, taking into account the substitution of conduction band states to the states of the valence band.

In this regard, below we will consider the interband single-photon (quantum) absorption of polarized radiation in semiconductors with a diamond and zinc blende lattice, taking into account the substitution of conduction band states to the valence band states and the temperature dependence of the band gap [8,9].

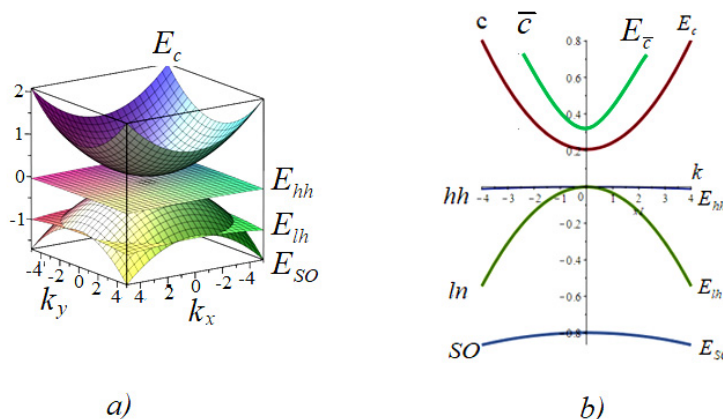


Figure 1. Multiband structure of indium antimonide: two (a) and multiband (b) approximation.

METHODS

The analysis is based on theoretical models that describe optical transitions in semiconductors with diamond and zinc blende lattice structures. The single-photon absorption coefficient was derived using the equilibrium distribution

function of charge carriers and the composite matrix element of optical transitions. The bandgap energy E_g , was modeled using the Varshni and Passler formulas to account for temperature variations. Effective masses of electrons and holes were treated as temperature-dependent parameters to reflect their variations with thermal energy. The Hamiltonian was developed to include terms representing the mixing of light and heavy hole states with conduction band states, ensuring that spin-orbit coupling effects were incorporated for enhanced accuracy in narrow-gap semiconductors. Additionally, the impact of light intensity on absorption coefficients was evaluated through the Rabi parameter, to quantify coherent saturation effects.

All calculations were conducted using computational tools such as “Maple”, with constants and material-specific parameters extracted from established databases and prior studies. This computational framework ensured consistency and reliability in deriving the temperature-dependent optical properties of the semiconductor materials under investigation.

INTERBAND AND INTRABAND MATRIX ELEMENTS OF THE MOMENTUM OPERATOR

Note that the probability of single-photon absorption (IPA) caused by the optical transition from state $|n, \vec{k}\rangle$ to state $|n', \vec{k}'\rangle$ is defined as [10-14]

$$W^{(1)} = \frac{2\pi}{\hbar} \left\langle \sum_{n, n', \vec{k}} \left| M_{n\vec{k}, n'\vec{k}}^{(1)} \right|^2 \right\rangle (f_{n\vec{k}} - f_{n'\vec{k}}) \delta(E_{n'}(\vec{k}) - E_n(\vec{k}) - \hbar\omega), \quad (1)$$

where $f_{n\vec{k}} (f_{n'\vec{k}})$ is the equilibrium distribution function of current carriers in the initial (final) state, $M_{n\vec{k}, n'\vec{k}}^{(1)}$ is the composite matrix element of a single-quantum optical transition, determined by the relation

$$M_{c,s; v, \Gamma_8, m}^{(1)} = \left(\frac{eA_0}{cm_0} \right) \vec{e} \cdot \vec{p}_{c,s; v, \Gamma_8, m}, \quad (2)$$

where $\vec{p}_{c,s; v, \Gamma_8, m} \frac{m_0}{\hbar} \frac{\partial}{\partial \vec{k}} [\hat{H}(\vec{k})]_{c,s; v, \Gamma_8, m}$ is the matrix element of the momentum operator, $A_0(\vec{e})$ - is the amplitude value of the potential vector (polarization vector) of the light wave, $\hat{H}(\vec{k})$ is the Hamiltonian of current carriers in crystals with a zinc blende lattice, taking into account the admixture of light and heavy hole (Γ_8) subband states in the lower conduction band (Γ_6) (two-zone approximation) which takes the form [15]

$$H(\Gamma_8) = E_{\Gamma_8}^0 + \frac{\hbar^2 k^2}{2m_0} - \frac{\hbar^2 |p_{eV}|^2}{m_0^2 E_g} \begin{bmatrix} \frac{k_z^2}{2} & -\frac{k_z k_-}{\sqrt{3}} & -\frac{k_z^2}{\sqrt{12}} & 0 \\ -\frac{k_z k_+}{\sqrt{3}} & \frac{2}{3} k_z^2 + \frac{k_+^2}{6} & 0 & -\frac{k_z^2}{\sqrt{12}} \\ -\frac{k_+^2}{\sqrt{12}} & 0 & \frac{2}{3} k_z^2 + \frac{k_+^2}{6} & \frac{k_z k_-}{\sqrt{3}} \\ 0 & -\frac{k_+^2}{\sqrt{12}} & \frac{k_z k_+}{\sqrt{3}} & \frac{k_+^2}{2} \end{bmatrix}, \quad (3)$$

where $p_{cV} = \langle S | p_z | Z \rangle$, $k_{\pm} = k_x \pm ik_y$. $E_{\Gamma_8}^0$ - is the extreme value of the valence band, which we further consider to be the starting point for the energy of current carriers.

Note that if we take into account the spin-orbit splitting (Γ_7) of the valence band with distant bands, then in semiconductors with a zinc blende lattice, the symmetry allows them to have terms linear in the wave vector in the effective Hamiltonian (3), however, but, as a rule, such terms are neglected.

According to Hamiltonian (3), the matrix elements of the momentum operator for optical transitions between subbands of the valence band can be written in the form of the following matrix:

$$\| \vec{e} \cdot \vec{p}_{m', m}^{(\Gamma_8)} \| = \hbar k \begin{bmatrix} e'_z & +\zeta_g \frac{e'_{-}}{\sqrt{3}} & 0 & 0 \\ +\zeta_g \frac{e'_{+}}{\sqrt{3}} & \left(1 - \frac{4}{3} \zeta_g\right) e'_z & 0 & 0 \\ 0 & 0 & \left(1 - \frac{4}{3} \zeta_g\right) e'_z & -\frac{\zeta_g e'_{-}}{\sqrt{3}} \\ 0 & 0 & -\frac{\zeta_g e'_{+}}{\sqrt{3}} & e'_z \end{bmatrix}. \quad (4)$$

and for interband optical transitions

$$\| \vec{e} \cdot \vec{p}_{c,s; v, \Gamma_8, m} \| = p_{c,v} \begin{bmatrix} -\frac{e'_{+}}{\sqrt{2}} & e'_z \sqrt{\frac{2}{3}} & \frac{e'_{-}}{\sqrt{6}} & 0 \\ 0 & -\frac{e'_{+}}{\sqrt{6}} & e'_z \sqrt{\frac{2}{3}} & \frac{e'_{-}}{\sqrt{2}} \end{bmatrix}, \quad (5)$$

Here $\zeta_g = \frac{|p_{c,V}|^2}{m_0 E_g}$ and it appears due to taking into account the admixture of the states of the valence band and the conduction band, $m', m = +3/2, +1/2, -1/2, -3/2$ eigenvalues of the angular momentum operator [5, 6], e'_x, e'_y, e'_z - \vec{e} projections of the polarization vector relative to the coordinate system $x', y', z' \parallel \vec{k}, \vec{k}$ - wave vector of current carriers, $p_{c,V}$ - Kane parameter and is determined in the following way

$$|p_{c,V}|^2 = \frac{3}{2} m_0 \frac{m_0 - m_c}{m_c} \frac{E_g(E_g + \Delta_{SO})}{2(E_g + \Delta_{SO}) + E_g}, \quad (6)$$

E_g - band gap, Δ_{SO} -spin-orbit splitting width. Then: $\zeta_g = \frac{3m_0}{4} \frac{m_{hh} - m_{lh}}{m_{hh} m_{lh}}$ and the effective mass of electrons in the conduction band is expressed as

$$\frac{1}{m_c} = \frac{1}{m_0} + \frac{2}{3m_0^2} |p_{c,V}|^2 \left(\frac{2}{E_g} + \frac{1}{E_g + \Delta_{SO}} \right), \quad (7)$$

We write the temperature dependence of the band gap ($E_g(T)$) in the form of the Varshni formula [8]

$$E_g(T) = E_g(T = 0) - \gamma_T \frac{T^2}{T + T_V}, \quad (8)$$

and Passner formulas [9]

$$E_g(T) = E_g(T = 0) - \frac{\alpha \theta_p}{2} \left[\left(1 + \left(\frac{2T}{\theta_p} \right)^p \right)^{1/p} - 1 \right]. \quad (9)$$

Here $\gamma_T, T_V, \alpha, \theta_p, p$ - are constant quantities, the numerical values of which are given in [8, 9].

In particular, we choose the temperature dependences of the effective masses of electrons ($m_c(T)$) in the conduction band and holes ($m_{SO}(T)$) in the spin-orbit splitting subband as follows (see, for example, [8]):

$$\frac{m_0}{m_{SO}(T)} = \gamma_1 - \frac{E_P \Delta_{SO}}{3E_g(E_g + \Delta_{SO})}, \quad \frac{m_0}{m_c(T)} = 1 + 2F + \frac{E_P(E_g + 2\Delta_{SO}/3)}{3E_g(E_g + \Delta_{SO})}. \quad (10)$$

Let us note here that with increasing temperature, $m_c(T)$ increases, and $m_{SO}(T)$ decreases, and this case has a noticeable effect, as shown below, on the frequency and temperature dependences of the light absorption coefficient.

From (4) and (5) it is clear that the composite matrix element depends on the type of single-photon optical transitions. In particular, for an optical transition from the heavy hole subband to the conduction band is determined by the relation

$$M_{c,\pm 1/2;hh,\pm 3/2}^{(1)} = \frac{1}{\sqrt{2}} \left(\frac{eA_0}{ch} \right) p_{c,V} \begin{bmatrix} -e'_- & 0 \\ 0 & e'_+ \end{bmatrix}; \quad (11)$$

from the subband of light holes to the conduction band:

$$M_{c,\pm 1/2;lh,\pm 1/2}^{(1)} = \frac{1}{\sqrt{6}} \left(\frac{eA_0}{ch} \right) p_{c,V}^* \begin{bmatrix} 2e'_z & -e'_- \\ e'_+ & 2e'_z \end{bmatrix}; \quad (12)$$

from the subzone of heavy holes to the subzone of heavy holes:

$$M_{hh,\pm 3/2;hh,\pm 3/2}^{(1)} = \left(\frac{eA_0}{ch} \right) \hbar k e'_z \begin{bmatrix} 1 & 0 \\ 0 & 1 \end{bmatrix}, \quad (13)$$

from the subzone of light holes to the subzone of light holes:

$$M_{lh,\pm 1/2;lh,\pm 1/2}^{(1)} = \frac{1}{3} \left(\frac{eA_0}{ch} \right) \hbar k (3 - 4\zeta_g) e'_z \begin{bmatrix} 1 & 0 \\ 0 & 1 \end{bmatrix}; \quad (14)$$

from the subzone of heavy holes to the subzone of light holes:

$$M_{lh,\pm 1/2;hh,\pm 3/2}^{(1)} = \frac{\zeta_g}{\sqrt{3}} \left(\frac{eA_0}{ch} \right) \hbar k \begin{bmatrix} e'_- & 0 \\ 0 & -e'_+ \end{bmatrix}. \quad (15)$$

Spectral dependence means that the interband absorption coefficient takes different values as the frequency of light (or photon energy) changes. The effect of temperature is mainly manifested through the following factors: Change in the energy gap between bands: As temperature increases, the bandgap of semiconductors narrows, which affects the absorption spectrum. Effect of phonons: With increasing temperature, the number of phonons (thermal vibrations) in the

crystal lattice increases, which influences the movement of electrons and holes. Optical absorption width: As temperature rises, the absorption spectrum may expand, or the absorption rate may decrease.

Coherent saturation is a phenomenon in which interband absorption decreases under the influence of intense light fields. In other words, under strong laser radiation or other optical excitations, the frequency and intensity of quantum transitions change in such a way that absorption decreases. This effect is of great importance in quantum mechanics and laser physics.

This concept describes the temporal variations of light absorption processes in semiconductors. The absorption rate and duration depend on the power of the light source, modulation frequency, and the physical properties of the material.

Note that the coefficient of single-quantum light absorption is determined by the expression (see, for example, [12])

$$K^{(1)} = \frac{2\pi\hbar\omega}{\hbar} \sum_{\vec{k}, L, m; L', m'} (f_{L', \vec{k}}^{(1)} - f_{L, \vec{k}}^{(1)}) |M_{L, m; L', m'}^{(1)}(\vec{k})|^2 \delta(E_{L', \vec{k}} - E_{L, \vec{k}} - \hbar\omega). \quad (16)$$

Here $L, m(L', m') = lh, m' = \pm 1/2 (hh, m' = \pm 3/2)$ - for heavy (light) holes), where their energy spectrum has the form $E_{L, \vec{k}} = -\hbar^2 k^2 / (2m_L)$, $L, m(L', m') = c, m' = \pm 1/2$ - for electrons in the conduction band, whose energy spectrum is: $E_{c, \vec{k}} = E_g + \hbar^2 k^2 / (2m_c)$. Then, taking into account relations (2)-(5) the light absorption coefficient:

a) for optical transitions from the heavy hole subband to the conduction band will be written as

$$K_{c, \pm 1/2; hh, \pm 3/2}^{(1)} = \frac{4\pi^2 e^2}{3\hbar n_{\omega} c} |p_{c, V}|^2 \frac{\mu_+^{(c, hh)} k_{c, lh}^{(\omega)}}{\hbar^2 \hbar \omega} \left\langle \frac{|e'_{\pm}|^2}{\sqrt{1 + \zeta_{hh} |e'_{\pm}|^2}} \right\rangle \cdot [f_c(k_{c, hh}^{(\omega)}) - f_{hh}(k_{c, hh}^{(\omega)})], \quad (17)$$

b) for optical transitions from the subband of light holes to the conduction band we have

$$K_{c, \pm 1/2; lh, \pm 1/2}^{(1)} = \frac{4\pi^2 e^2}{3\hbar n_{\omega} c} |p_{c, V}|^2 \frac{\mu_+^{(c, lh)} k_{c, lh}^{(\omega)}}{\hbar^2 \hbar \omega} \left\langle \frac{4e'_{\pm} z^2 + e'_{\pm}^2}{\sqrt{1 + \zeta_{lh} (4e'_{\pm} z^2 + e'_{\pm}^2)}} \right\rangle \cdot [f_c(k_{c, lh}^{(\omega)}) - f_{lh}(k_{c, lh}^{(\omega)})], \quad (18)$$

Here it is taken into account that $\left(\frac{eA_0}{\hbar c}\right)^2 = \frac{2\pi e^2}{n_{\omega} c} \frac{1}{(\hbar\omega)^2}$, $\zeta_{hh} = 4 \frac{\alpha_{\omega}}{\hbar^2 \omega^2} \left(\frac{eA_0}{\hbar c}\right)^2 |p_{c, V}|^2$, $\zeta_{lh} = \zeta_{hh}/3$, $\alpha_{\omega} = 6\omega^2 T_{hh}^{(1)} T_{lh}^{(1)} \frac{1}{I_0}$, $I_0 = \frac{cn_{\omega} \hbar^3 \omega^3}{2\pi |B|}$, $k_{c, L}^{(\omega)} = \sqrt{\frac{2\mu_+^{(c, L)}}{\hbar^2} (\hbar\omega - E_g)}$, $\mu_+^{(c, L)} = \frac{m_c m_L}{m_c + m_L}$ ($L = lh, hh$). $f_c(k_{c, lh}^{(\omega)}, T)$, $f_{hh}(k_{c, lh}^{(\omega)}, T)$ and $f_{lh}(k_{c, lh}^{(\omega)}, T)$ - distribution functions of electrons, light and heavy holes participating in optical transitions from subbands of the valence band to the conduction band; symbol $\langle \dots \rangle$ denotes averaging over solid angles of the wave vector.

Carrying out angular averaging over the solid angles of the wave vector of current carriers in (18, 19), we obtain that both the 1FP coefficient $K_{c, \pm 1/2; hh, \pm 3/2}^{(1)}(I)$ (Fig. 2 a) and the linear-circular dichroism coefficient $\eta_{c, \pm 1/2; hh, \pm 3/2}^{(1)}(I) = \frac{W_{c, \pm 1/2; hh, \pm 3/2}^{(1, circ)}(I)}{W_{c, \pm 1/2; hh, \pm 3/2}^{(1, linear)}(I)}$ (Fig. 2 b) decrease with increasing Rabi parameter $\zeta_{hh}(I)$ (light intensity) for optical transitions from the heavy hole subband to the conduction band in *InAs*. Calculations show that in *InSb* the light absorption coefficient $K_{c, \pm 1/2; hh, \pm 3/2}^{(1)}(\zeta_{hh} = 0)$ is approximately 5 times less than the light absorption coefficient due to optical transitions from the light hole subband to the conduction band, and the coefficient $\eta_{c, \pm 1/2; hh, \pm 3/2}^{(1)}(I) = \frac{W_{c, \pm 1/2; hh, \pm 3/2}^{(1, circ)}(I)}{W_{c, \pm 1/2; hh, \pm 3/2}^{(1, linear)}(I)}$ decreases by approximately 1.1 times.

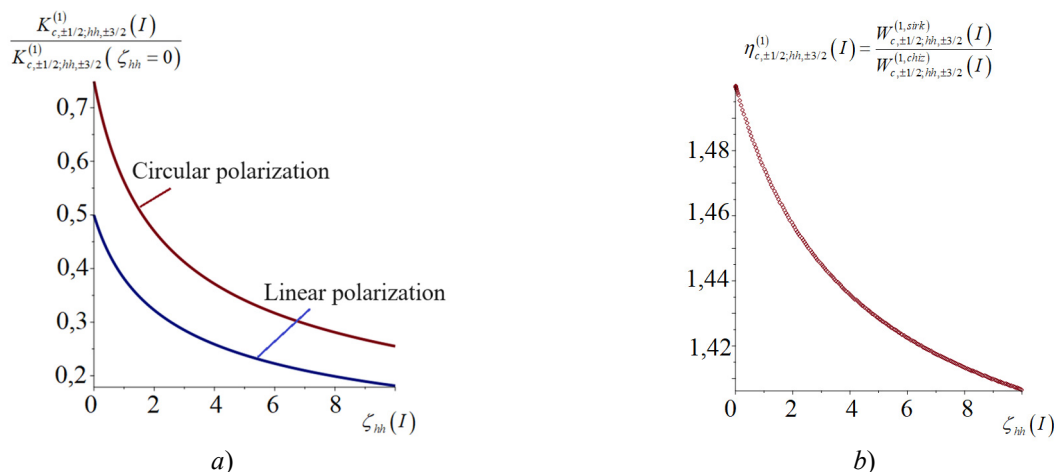


Figure 2. Dependence of the coefficients 1FA $K^{(1)}$ (a) and linear-circular dichroism $\eta_{c, \pm 1/2; hh, \pm 3/2}^{(1)}(I) = \frac{W_{c, \pm 1/2; hh, \pm 3/2}^{(1, circ)}(I)}{W_{c, \pm 1/2; hh, \pm 3/2}^{(1, linear)}(I)}$ (b) on the Rabi parameter $\zeta_{hh}(I)$ (on light intensity) for optical transitions from the heavy hole subband to the conduction band in *InAs*.

Thus, it was shown that the main contribution to the single quantum absorption coefficient of light comes from light holes participating in interband optical transitions from the subbands of the valence band to the conduction band.

Next, it is advisable to analyze the spectral-temperature dependences of the distribution functions of heavy ($f_{hh}(\omega, T)$) and light ($f_{lh}(\omega, T)$) holes (see Fig. 3), since $K^{(1)}(\omega, T)$ is determined by the spectral-temperature dependence $f_{hh}(\omega, T)$ and $f_{lh}(\omega, T)$ (see formula (18), (19). Calculations using spectral temperature dependences $f_{hh}(\omega, T)$ and $f_{lh}(\omega, T)$ (in the approximation of non-degenerate statistics [16] show that for *InSb*:

a) at a fixed frequency, with increasing temperature, the distribution functions increase, reach a maximum, and then decrease, since the distribution functions consist of the product of $T^{-3/2}$ and $\exp(-E^*/k_B T)$, where E^* -is the energy of photoexcited holes;

b) the maximum values of the distribution functions decrease with increasing frequency, the relative change of which depends on the band parameters of the crystal, for example, on $E_g(T)$. In particular, in narrow-gap crystals this value is greater than in wide-gap crystals: for example, in *InSb* it is approximately 5.4 times greater than in *InSb*;

c) if we take into account the dependence of band parameters on temperature (according to (8) and (9)), then the distribution function of light (heavy) holes in *InSb* decreases by approximately 5.3 (2.5) times, and in *InAs* - by 5,2 (2) times.

The above cases certainly influence the spectral-temperature dependences $K^{(1)}(\omega, T)$, which are analyzed below.

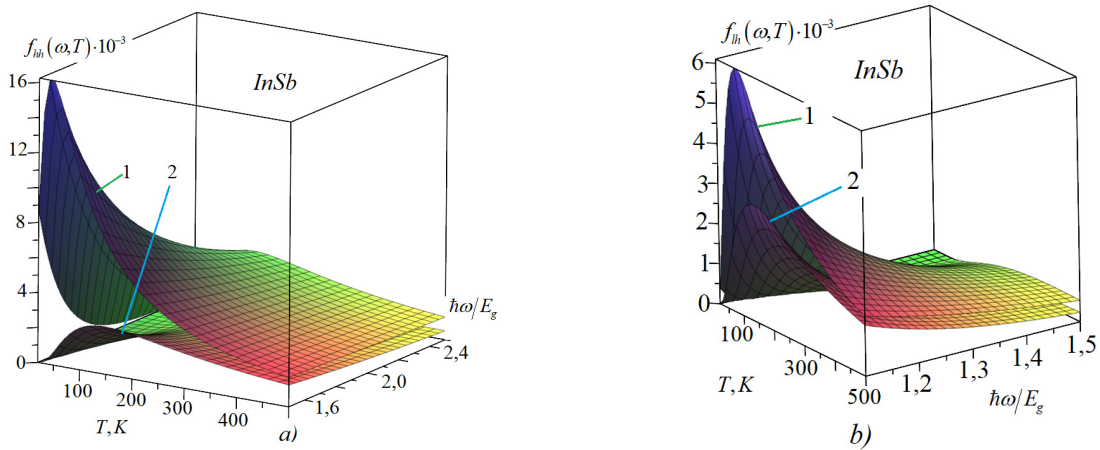


Figure 3. Spectral-temperature dependences of the distribution functions of heavy (a) and light (b) holes in *InSb*. 1 (2) – corresponds to $E_g = E_g(T = 0 \text{ K})(E_g(T))$

In Figure 4 shows spectral-temperature dependences $K^{(1)}(\omega, T)$ for optical transitions of subbands of light and heavy holes into the conduction band in *InSb* when illuminated with light of linear (1) and circular (2) polarization, where the temperature dependence of band parameters is not taken into account and the maximum value of coefficient $K_{c,\pm 1/2;hh,\pm 3/2}^{(1,linear)}(\omega, T)$ was taken as one unit, and the Rabi coefficient was chosen to be 0.5 [17, 18].

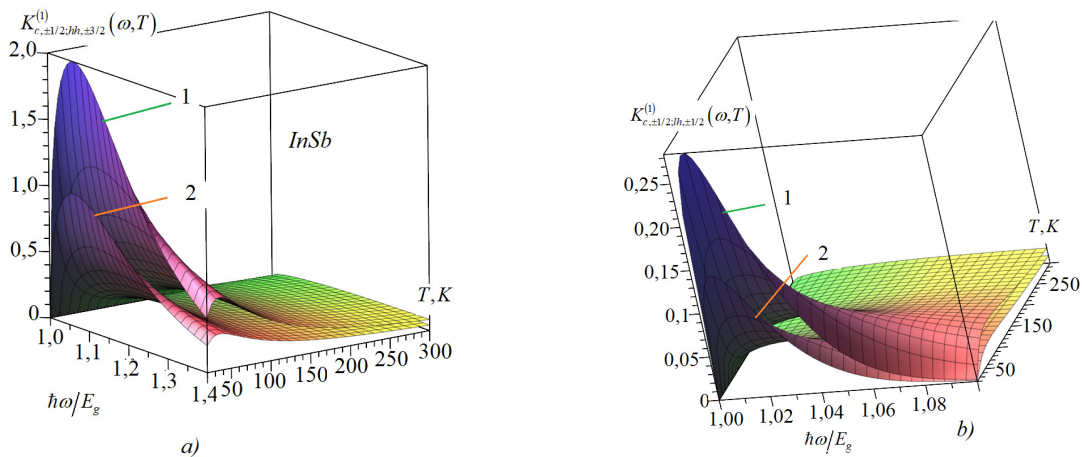


Figure 4. Spectral-temperature dependences of the 1FA coefficient of polarized light due to optical transitions from the subband of heavy $K_{c,\pm 1/2;hh,\pm 3/2}^{(1)}(\omega, T)$ (a) and light $K_{c,\pm 1/2;lh,\pm 1/2}^{(1)}(\omega, T)$ (b) holes to the conduction band of *InSb* (a), where 1 (2) corresponds to light of circular (linear) polarization. The calculations did not take into account the temperature dependence $E_g(T)$ and the maximum value of coefficient $K_{c,\pm 1/2;hh,\pm 3/2}^{(1,linear)}(\omega, T)$ was taken as one unit, and the Rabi coefficient was chosen equal to 0.5.

In this case, with increasing frequency and temperature, $K^{(1)}(\omega, T)$ increases (as do the hole distribution functions), reaches a maximum, and then decreases. In Figure 5 shows graphs of values $K_{c,\pm 1/2;hh,\pm 3/2}^{(1)}(\omega, T)$ and $K_{c,\pm 1/2;lh,\pm 1/2}^{(1)}(\omega, T)$ calculated taking into account the temperature dependence $E_g(T)$. Calculations show that the amplitude value of the 1FP coefficient in the region of low frequencies and temperatures sharply decreases with increasing temperature. This situation is explained by the temperature and spectral dependences of the hole distribution functions. We also note that the transition of value $K_{c,\pm 1/2;hh,\pm 3/2}^{(1)}(\omega, T)$ through a maximum in the temperature dependence is observed in the frequency range $\omega \approx 2E_g/\hbar$ for *InSb*, $\omega \approx 1E_g/\hbar$ for *InAs* and $\omega \approx 1,005E_g/\hbar$ 110 K GaAs for both linear and circular polarization, and the temperature corresponding to this maximum is higher, the higher bandgap width. In particular, this temperature is 45 K for *InSb* at $\omega = 1,3E_g/\hbar$, 80 K for *InAs* at $\omega = 1,4E_g/\hbar$ and 110 K for GaAs at $\omega = 1,02E_g/\hbar$.

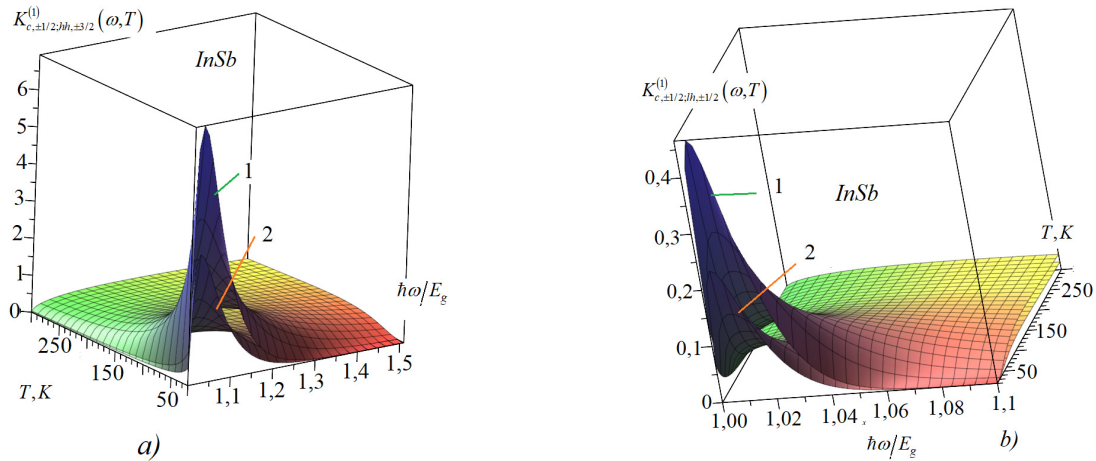


Figure 5. Spectral-temperature dependences of the 1PA coefficient caused by optical transitions from the subband of heavy holes $K_{c,\pm 1/2;hh,\pm 3/2}^{(1)}(\omega, T)$ (a) and light holes $K_{c,\pm 1/2;lh,\pm 1/2}^{(1)}(\omega, T)$ (b) to the conduction band in *InSb*, where 1 (2) corresponds to light of circular (linear) polarization. The calculations took into account the temperature dependence $E_g(T)$ and the maximum value of coefficient $K_{c,\pm 1/2;hh,\pm 3/2}^{(1,linear)}(\omega, T)$ was taken as one unit, and the Rabi coefficient was chosen equal to 0.5.

In Figure 6 shows the spectral-temperature dependences of the ratios $\tilde{K}_{c,\pm 1/2;lh,\pm 1/2}^{(1)}/K_{c,\pm 1/2;lh,\pm 1/2}^{(1)}$ and in *InSb* crystals. Here $\tilde{K}_{c,\pm 1/2;lh,\pm 1/2}^{(1)}$ and $K_{c,\pm 1/2;lh,\pm 1/2}^{(1)}$ the coefficients 1FP taking into account (Fig. 5 a) and without taking into account (Fig. 5 b) the temperature dependence of the band parameters, where the contribution of the coherent saturation effect is neglected (therefore $K_{c,\pm 1/2;hh,\pm 3/2}^{(1)}$ do not depend on the degree of polarization of light). From this figure it is clear that the contribution of optical transitions from the heavy hole subband is greater than the contribution of optical transitions from the light hole subband to the conduction band in *InSb*, and this contribution increases when taking into account $E_g(T)$.

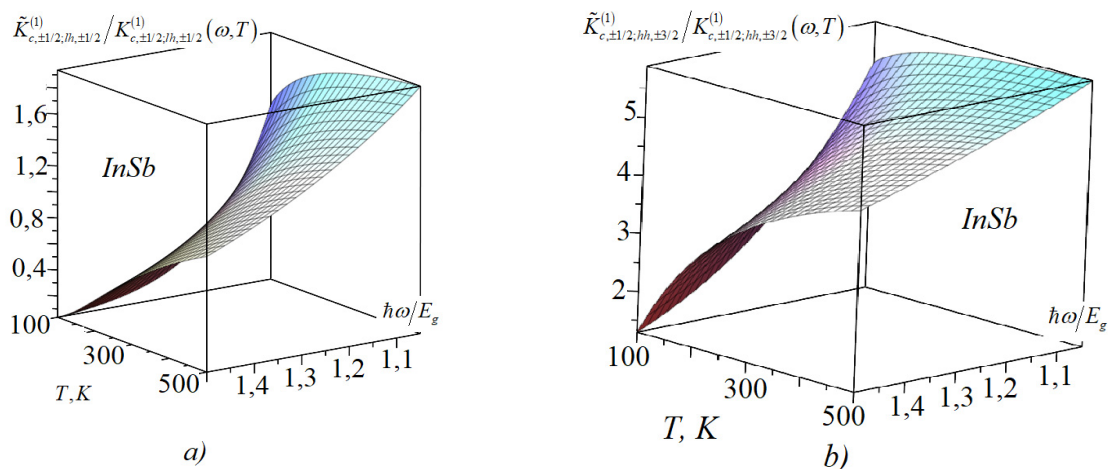


Figure 6. Spectral-temperature dependence of the ratio $\tilde{K}_{c,\pm 1/2;lh,\pm 1/2}^{(1)}/K_{c,\pm 1/2;lh,\pm 1/2}^{(1)}$ in *InSb*, where $\tilde{K}_{c,\pm 1/2;lh,\pm 1/2}^{(1)}$ ($K_{c,\pm 1/2;lh,\pm 1/2}^{(1)}$) is the coefficient 1PA taking into account (a) and without taking into account (b) the temperature dependence of band parameters, where the contribution of the coherent saturation effect is neglected.

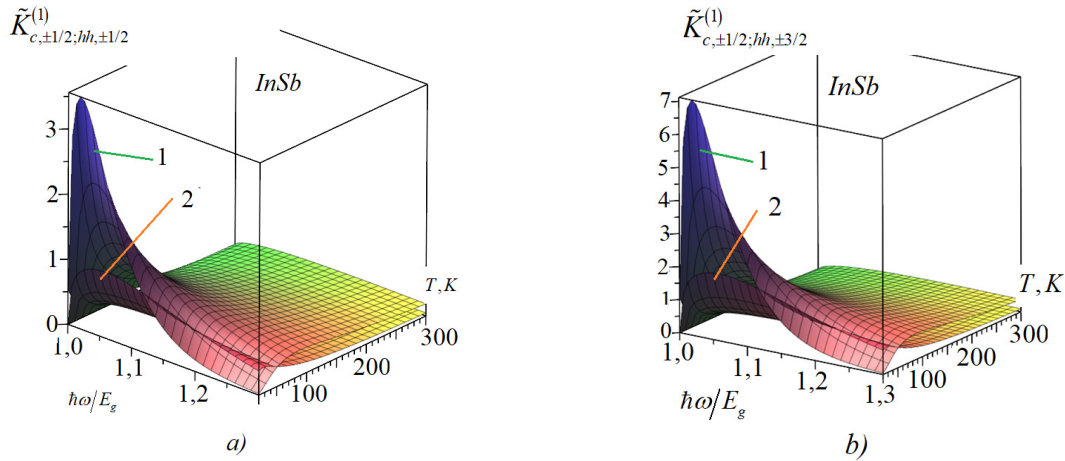


Figure 7. Spectral-temperature dependence of the ratio $\tilde{K}_{c,\pm 1/2;lh,\pm 1/2}^{(1)}/K_{c,\pm 1/2;lh,\pm 1/2}^{(1)}$ for light of linear (line 1) and circular (line 2) polarization, caused by optical transitions from the subband of light (a) and heavy (b) holes to the conduction band of *InSb*. In the calculations, the maximum value of the coefficient $K_{c,\pm 1/2;hh,\pm 3/2}^{(1,linear)}(\omega, T)$ was taken as one, and the Rabi coefficient was chosen equal to 0.5.

In Figure 7 shows the spectral-temperature dependences of the ratio $\tilde{K}_{c,\pm 1/2;lh,\pm 1/2}^{(1)}/K_{c,\pm 1/2;lh,\pm 1/2}^{(1)}$ for linearly (line 1) and circularly polarized light (line 2), caused by interband optical transitions from the light hole subband to the *InSb* conduction band, from where, that $\tilde{K}_{c,\pm 1/2;lh,\pm 1/2}^{(1)}/K_{c,\pm 1/2;lh,\pm 1/2}^{(1)}$ in a narrow-gap semiconductor for linear polarization in low-temperature regions is significantly greater than for circular polarization when taking into account the effect of coherent saturation. In this case, as calculations show, in the low-temperature region, the main contribution comes from optical transitions from the heavy hole subband, regardless of the degree of light polarization, both with and without taking into account the contribution of the coherent saturation effect.

According to (17), the spectral-temperature dependences $K^{(1)}(\omega, T)$ are determined by the distribution functions of heavy and light holes.

Consequently, taking into account relations (8) and (9) allows us to compare distribution functions both by temperature (at a fixed frequency) and by frequency (at a fixed temperature).

In Figure 8 shows the spectral-temperature dependence of the hole distribution functions $f(\omega, T)$, calculated taking into account the temperature dependence of the band gap and effective masses in *InSb*, where graphs 1(2) and 3(4) correspond to light (heavy) holes, calculated from (8) and (9).

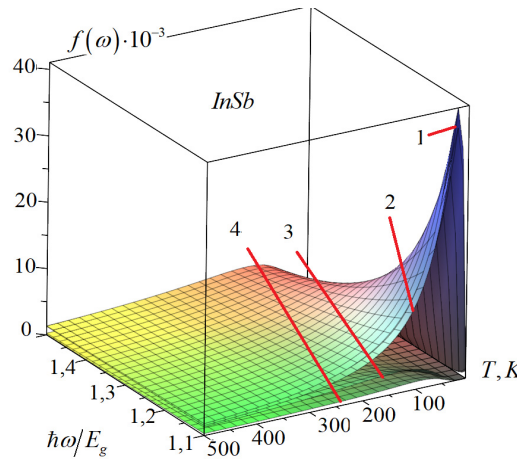


Figure 8. Spectral - temperature dependence of the hole distribution functions, calculated taking into account the temperature dependence of the band gap and effective masses in *InSb*, where graphs 1 (2) and 3 (4) correspond to light (heavy) holes, calculated from (8) and (9).

From these graphs it can be seen that in the region of low frequencies and high temperatures $f(\omega, T)$ decreases slightly (less than 5%) when moving from (8) to (9): the amplitude value of the distribution functions of heavy holes decreases by approximately 1.7 times in the low-frequency range. However, in the region of high frequencies and low temperatures the opposite is true.

Note that since the coefficient of single-photon interband absorption of light is proportional to the wave vector of photoexcited current carriers $k_{c,L}^{(\omega)} = [2m_c m_L \hbar^{-2} (\hbar\omega - E_g) / (m_c + m_L)]^{1/2}$, then under condition $\hbar\omega = E_g$ it becomes

zero, which means that light absorption satisfies condition $\hbar\omega \geq E_g$, where $E_g = E_g(T = 0)$. But if we take into account expressions (8) and (9), then $k_{c,L}^{(\omega)}(T) = \left\{ 2m_c(T)m_L\hbar^{-2} \left(\hbar\omega - E_g(T) \right) / [m_c(T) + m_L] \right\}^{1/2}$ increases with increasing temperature, since with increasing temperature $E_g(T)$ decreases. As a result, the light absorption edge satisfies condition $\hbar\omega \leq E_g(T = 0)$ (instead of $\hbar\omega \geq E_g$).

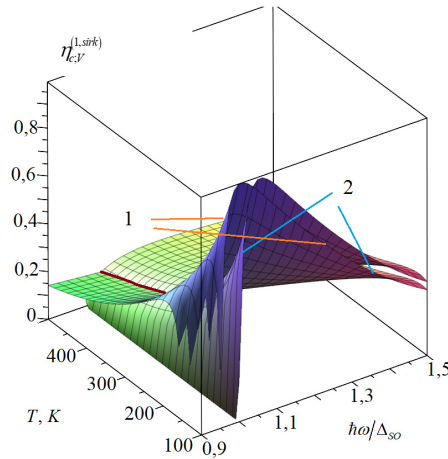


Figure 9. Spectral-temperature dependence of the relative total 1PA $\eta_{c,v}^{(1,circ)} = \left(\tilde{K}_{c,\pm 1/2;hh,\pm 1/2}^{(1,circ)} + \tilde{K}_{c,\pm 1/2;hh,\pm 3/2}^{(1,circ)} \right) / \left(K_{c,\pm 1/2;hh,\pm 3/2}^{(1,circ)} + K_{c,\pm 1/2;hh,\pm 3/2}^{(1,circ)} \right)$ for circularly polarized light in *InSb*. In the calculations, the maximum value of the coefficient $\tilde{K}_{c,\pm 1/2;lh,\pm 1/2}^{(1,linear)}$ was taken as one, and the Rabi coefficient was chosen equal to 0.5, where graphs 1 and 2 were calculated using formulas (8) and (9), respectively.

Calculations show that at room temperature the contribution of heavy holes to coefficient $\tilde{K}_{c,m;L,m'}^{(1)}(\omega, T)$ is approximately 10 times greater than the contribution of light holes in the frequency range satisfying condition $1.1E_g < \hbar\omega < 1.5E_g$. This situation also occurs in the spectral-temperature dependences of the resulting 1PA coefficient (see Fig. 9), and the physical nature of these dependences is explained by a similar frequency dependence of the nonequilibrium distribution functions of current carriers.

CONCLUSIONS

In conclusion, this study provides an in-depth theoretical framework to understand the mechanisms underlying single-photon interband absorption in semiconductors with diamond and zinc blende lattice structures. By incorporating temperature-dependent bandgap variations and the mixing of valence and conduction band states, the research highlights key factors that influence the absorption process. Heavy hole contributions were found to dominate over light hole contributions, with a significant enhancement of absorption coefficients in narrow-gap semiconductors at lower temperatures. The findings also reveal a pronounced dependence of linear-circular dichroism on light intensity, attributed to the coherent saturation effects.

The results underscore the critical role of temperature and band structure in determining optical absorption properties, offering valuable insights for applications in optoelectronic devices. However, the study also emphasizes the need for experimental validation to verify these theoretical predictions. Future work should focus on extending the analysis to a broader class of semiconductors and exploring the interplay of higher-order effects, such as spin-orbit coupling, to refine the understanding of optical absorption phenomena. These advancements will not only enhance the theoretical accuracy but also pave the way for practical implementations in advanced semiconductor technologies.

ORCID

✉ Rustam Y. Rasulov, <https://orcid.org/0000-0002-5512-0654>; ✉ Voxob R. Rasulov, <https://orcid.org/0000-0001-5255-5612>

REFERENCES

- [1] I.M. Tsidilkovski, *Band Structure of Semiconductors: International Series on the Science of the Solid State*, (Pergamon Press, 2016).
- [2] G.L. Bir, and G.E. Pikus, *Symmetry and Strain-induced Effects in Semiconductors*, (I.P.S.T., 1975).
- [3] E.L. Ivchenko, and R.Ya. Rasulov, *Symmetry and real band structure of semiconductors*, (FAN, Tashkent, 1992). (in Russian)
- [4] G.G. Zegrya, and V.I. Perel, *Fundamentals of semiconductor physics*, (Fizmatlit, 2009). (in Russian)
- [5] G. Pikus, and E.L. Ivchenko, *Superlattices and Other Heterostructures: Symmetry and Optical Phenomena*, *Springer Series in Solid-State Sciences*, Vol. 110, (Springer Verlag, 2nd edition, 1997).
- [6] E.L. Ivchenko, *Optical Spectroscopy of Semiconductor Nanostructures*, Vol. XII, (Alpha Science International Ltd., Harrow, UK, 2005).
- [7] M.M. Glazov, *Physics of low-dimensional systems. Course lecture*, (2022). (in Russian)

- [8] I. Vurgaftman, J.R. Meyer, and L.R. Ram-Mohan, "Band parameters for III–V compound semiconductors and their alloys," *Journal of Applied Physics*, **89**, 5815–5875 (2001). <https://doi.org/10.1063/1.1368156>
- [9] R. Päßler, "Parameter Sets Due to Fittings of the Temperature Dependencies of Fundamental Bandgaps in Semiconductors," *Phys. Stat. Sol. (b)*, **216**, 975–1007 (1999). [https://doi.org/10.1002/\(SICI\)1521-3951\(199912\)216:2<3.CO;2-E](https://doi.org/10.1002/(SICI)1521-3951(199912)216:2<3.CO;2-E)
- [10] E.L. Ivchenko, "Two-photon absorption of light and optical orientation of free carriers," *Physics*, **14**(12), 3489–3496 (1972). (in Russian)
- [11] R.Ya. Rasulov, "Linear-circular dichroism in multiphoton intersubband absorption in semiconductors," *Phys.* **35**(6), 1674–1678 (1993). <https://journals.ioffe.ru/articles/viewPDF/14966>
- [12] R.Ya. Rasulov, V.R. Rasulov, M.Kh. Kuchkarov, and I.M. Eshboltaev, "Interband multiphoton absorption of polarized radiation and its linear circular dichroism in semiconductors in the kane approximation." *Russian Physics Journal*, **65**(10), 1746–1754 (2023). <https://doi.org/10.1007/s11182-023-02825-3>
- [13] R.Ya. Rasulov, V.R. Rasulov, and I.M. Eshboltaev, "Linearly and circular dichroism in a semiconductor with a complex valence band with allowance for four-photon absorption of light," *Phys. Solid State*, **59**, 463–468 (2017). <https://doi.org/10.1134/S1063783417030283>
- [14] V.R. Rasulov, R.Ya. Rasulov, N.U. Kodirov, and U.M. Isomaddinova, "Interband single-photon absorption and its linear-circular dichroism in crystals taking into account the effect of coherent saturation," *Physics of the Solid State*, **65**(7), 1224–1230 (2023). <https://journals.ioffe.ru/articles/viewPDF/56410>
- [15] E.L. Ivchenko, *Physics of low-dimensional systems*, 2015. https://solid.phys.spbu.ru/images/Ivch_lec15.pdf (in Russian)
- [16] Y.U. Peter, and M. Cardona, *Fundamentals of Semiconductors: Physics and Materials Properties*, (Springer, 2010).
- [17] N.V. Leppenen, E.L. Ivchenko, and L.E. Golub, "Nonlinear optical absorption and photocurrents in topological insulators," *Phys. Rev. B*, **105**, 115306 (2022). <https://doi.org/10.1103/PhysRevB.105.115306>
- [18] D.A. Parshin, and A.R. Shabaev, "Theory of linear IR absorption by semiconductors with degenerate bands," *Zh. Exp. Teor. Fiz.* **92**(4), 1471–1484 (1987). http://jetp.ras.ru/cgi-bin/dn/e_065_04_0827.pdf (in Russian)

**ТЕОРЕТИЧНИЙ АНАЛІЗ МІЖЗОННОГО ОДНОФОТОННОГО ПОГЛИНАННЯ СВІТЛА В
НАПІВПРОВІДНИКАХ: ЕФЕКТИ ЗМІШУВАННЯ ЗОН ВАЛЕНТНОЇ ПРОВІДНОСТІ ТА
ТЕМПЕРАТУРНО-ЗАЛЕЖНОЇ ЗАБОРОНЕНОЇ ЗОНИ**

Рустам Я. Расулов^a, Вохоб Р. Расулов^a, Нурилло У. Кодіров^a, Мардон Х. Насіров^c, Ікбол М. Ешболтаєв^b

^a*Ферганський державний університет, Фергана, Узбекистан*



^b*Кокандський державний педагогічний інститут, Коканд, Узбекистан*

^c*Ферганський політехнічний інститут, Фергана, Узбекистан*

У цьому дослідженні представлено теоретичний аналіз спектральної та температурної залежності коефіцієнта однофотонного поглинання лінійно та циркулярно поляризованого світла в напівпровідниках із ґратковими структурами алмазу та цинкової обманки. Розглядаються оптичні переходи, що включають підзони легких і важких дірок і зону провідності, включаючи такі ефекти, як температурно-залежна заборонена зона, змішування станів валентної зони провідності та когерентне насичення. Отримані дані показують, що важкі діри сприяють однофотонному поглинанню приблизно в 10 разів більше, ніж легкі. Крім того, досліджується зв'язок між лінійно-круговим дихроїзмом та інтенсивністю світла, підкреслюючи роль когерентних ефектів насичення.

Ключові слова: напівпровідник; температурна залежність забороненої зони; змішування станів валентної зони зі станами зони провідності; однофотонне поглинання; спектрально-температурна залежність

ON THE THEORY OF TWO-PHOTON INTERSUBBAND ABSORPTION AND LINEAR-CIRCULAR DICHROISM IN SEMICONDUCTORS OF THE A_3B_5 TYPE

 Rustam Y. Rasulov^a,  Vokhob R. Rasulov^{a*}, Forrukh U. Kasimov^b, Mardonbek Kh. Nasirov^{a,c},
Islam E. Farmanov^a, Abay Z. Tursinbaev^d

^aFergana State University, Fergana, Uzbekistan

^bAndijan State University, Andijan, Uzbekistan

^cFergana State Technical University, Fergana, Uzbekistan

^dSouth Kazakhstan University of Muktar Auezov, Shymkent, Kazakhstan

*Corresponding Author e-mail: vrrasulov83@gmail.com

Received August 6, 2024; revised April 13, 2025; accepted April 23, 2025

The frequency-temperature dependences of the probability of two-photon absorption (2PA), caused by transitions from the branch of light holes to the subband of spin-orbit splitting and linear-circular dichroism (LCD) associated with 2PA, as well as the coefficient of two-photon light absorption in *GaAs* and *InAs*, where the contribution to the absorption of the effect of coherent saturation. The role of various types of transitions, differing from each other in virtual states and participating in the 2PT, is analyzed. In *GaAs* and *InAs*, the presence of several peaks in the frequency-temperature dependences of the 2PA coefficient was revealed; the appearance of the peaks is explained not only by a specific change in the distribution functions of photoexcited holes, but also by the fact that at certain frequency values, some denominators in the expressions of the composite matrix elements tend to zero.

Keywords: Two-photon optical transitions; Virtual states; Multiphoton optical transitions; Two-photon absorption coefficient; Coherent saturation effect; Semiconductor

PACS: 71.20. – b, 71.28. + d

INTRODUCTION

Nonlinear spectroscopy of solids has proven invaluable in determining their optical and electronic parameters. For instance, when single-photon absorption is forbidden by selection rules, multiphoton transitions may become allowed [1]. The processes of multiphoton absorption in crystals have been the subject of extensive theoretical and experimental studies since the advent of the laser (see, for example, [2–7]). This interest in multiphoton absorption has been driven by the significance of nonlinear absorption facilitated by powerful lasers and masers, as well as its role in numerous aspects of fundamental research in semiconductor physics. It should be noted that in the processes of electron-hole pair generation induced by intense optical radiation, both in bulk [2–13] and low-dimensional crystals, multiphoton interband and intraband transitions play a critical role [14–24].

Although [14–24] investigated optical phenomena in bulk and low-dimensional crystals, where either interband transitions or transitions between the branches of light and heavy holes are restricted, the question of single- and multiphoton absorption of linearly and circularly polarized light in narrow- and wide-bandgap semiconductors, driven by optical transitions from the branches of light and heavy holes to the spin-orbit split subband of the valence band, remains unresolved. This study is dedicated to addressing this issue.

Effective Luttinger–Kohn Hamiltonian for III–V Semiconductors (*GaAs*, *InAs*) Formulation of the Luttinger–Kohn Hamiltonian

In zincblende III–V semiconductors, the top valence bands (heavy-hole, light-hole, and split-off bands) are described by the Luttinger–Kohn (LK) Hamiltonian derived from $k \cdot p$ theory. This effective Hamiltonian acts on the Bloch states at the Brillouin-zone center with total angular momentum $j = 3/2$ (degenerate heavy-hole and light-hole, Γ_8 symmetry) and $j = 1/2$ (split-off band, Γ_7) due to the spin–orbit interaction. The LK Hamiltonian is a 6×6 matrix (or 4×4 if the split-off band is excluded) built from the angular momentum $J = 3/2$ matrices $\hat{J}_x, \hat{J}_y, \hat{J}_z$ and wavevector components k_x, k_y, k_z . To second order in \mathbf{k} , the general form can be written (in the $j = 3/2$ basis) as a quadratic form in $k_i k_j J_i J_j$ terms with three dimensionless Luttinger parameters $\gamma_1, \gamma_2, \gamma_3$. In an isotropic approximation (neglecting cubic anisotropy), the Hamiltonian simplifies to:

$$H_{LK} = \frac{\hbar^2}{2m_0} \left[\left(\gamma_1 + \frac{5}{2} \gamma_2 \right) k^2 - 2\gamma_2 (\mathbf{k} \cdot \mathbf{J})^2 \right],$$

where m_0 is the free electron mass, $k^2 = k_x^2 + k_y^2 + k_z^2$, and $\mathbf{k} \cdot \mathbf{J} = k_x \hat{J}_x + k_y \hat{J}_y + k_z \hat{J}_z$. This is the so-called spherical approximation ($\gamma_2 = \gamma_3$), which is often used for simplicity. In the general case for cubic crystals, $\gamma_2 \neq \gamma_3$, and one must

include distinct terms for $\hat{f}_i^2 k_i^2$ and the off-diagonal couplings $\hat{f}_i, \hat{f}_j k_i, k_j$ (which cause band warping). An explicit representation of the full 4×4 LK Hamiltonian (for the $j = 3/2$ subspace) in the Bloch basis $|3/2, m_j\rangle$ is

$$H_{LK}^{4 \times 4} = \frac{\hbar^2}{2m_0} \begin{pmatrix} A & -B & C & 0 \\ -B^* & D & 0 & C \\ C^* & 0 & D & B \\ 0 & C^* & B^* & A \end{pmatrix}$$

where (suppressing factor $\hbar^2/2m_0$) $A = \gamma_1 k^2 + (\gamma_2 + \gamma_3)(k_x^2 + k_y^2 - 2k_z^2)$, $D = \gamma_1 k^2 + (\gamma_2 + \gamma_3)(k_z^2 + k_y^2 - 2k_x^2)$ (cyclic permutations for D) and the off-diagonal couplings are $B = 2\sqrt{3}\gamma_3 k_z(k_x - ik_y)$, $C = -\sqrt{3}\gamma_2(k_x^2 - k_y^2) + 2i\sqrt{3}\gamma_3 k_x k_y$. (Here the basis is ordered as $|3/2, +3/2\rangle, |3/2, -1/2\rangle, |3/2, +1/2\rangle, |3/2, -3/2\rangle$ for this matrix.) The 6×6 Hamiltonian including the split-off $j = 1/2$ states is an extension of the above, with the spin-orbit energy Δ_{SO} separating the Γ_7 band on the diagonal and additional k -dependent coupling terms between $j = 3/2$ and $j = 1/2$ blocks. In the absence of inversion asymmetry (no bulk inversion asymmetry term $B = 0$ for centrosymmetric zincblende), the above H_{LK} is the standard effective Hamiltonian for holes in III-V compounds first formulated by Luttinger (1956). Eigenenergies and Eigenfunctions Zone-center basis: At $k = 0$ (the Γ point), the valence-band edges consist of a four-fold degenerate Γ_8 state (spin-orbit $j=3/2$ quartet) and a split-off Γ_7 doublet separated by Δ_{SO} . One convenient choice of orthonormal Bloch basis for the Γ_8 valence states is in terms of spin-orbit coupled atomic p -orbitals $|X\rangle, |Y\rangle, |Z\rangle$ and spin \uparrow, \downarrow . For example:

$$\begin{aligned} |3/2, +3/2\rangle &= \frac{-1}{\sqrt{2}}(|X + iY\rangle \uparrow), \\ |3/2, +1/2\rangle &= \frac{-1}{\sqrt{6}}(|X + iY\rangle \downarrow) + \sqrt{\frac{2}{3}}(|Z\rangle \uparrow), \\ |3/2, -1/2\rangle &= \frac{1}{\sqrt{6}}(|X - iY\rangle \uparrow) + \sqrt{\frac{2}{3}}(|Z\rangle \downarrow), \\ |3/2, -3/2\rangle &= \frac{1}{\sqrt{2}}(|X - iY\rangle \downarrow), \end{aligned}$$

up to overall phase factors. Here $|3/2, \pm 3/2\rangle$ are “heavy-hole” (HH) states with angular momentum projection $m_j = \pm 3/2$ (maximally aligned orbital and spin), and $|3/2, \pm 1/2\rangle$ are “light-hole” (LH) states ($m_j = \pm 1/2$) which are a mixture of spin-up and spin-down with the p_z -orbital character. The split-off $|1/2, \pm 1/2\rangle$ states (not written above) are primarily p_z -type with opposite spin mixture and lie Δ_{SO} lower in energy.

Dispersion and effective masses: For a given wavevector \mathbf{k} , one finds the band energies by diagonalizing H_{LK} . Along high-symmetry axes, the eigenstates can often be chosen as pure m_j states. For example, if \mathbf{k} is taken along the z -axis ($[001]$ direction), then \hat{J}_z commutes with H_{LK} , so m_j remains a good quantum number. In this case, the HH states ($m_j = \pm 3/2$) decouple from the LH states ($m_j = \pm 1/2$), yielding parabolic dispersions:

Heavy-hole band: $E_{hh}(k_{||}) = \frac{\hbar^2 k_{||}^2}{2m_0}(\gamma_1 - 2\gamma_2)$ for $\mathbf{k} = k_{||}\hat{z}$. This implies an effective mass $m_{hh}^{[001]} = \frac{m_0}{\gamma_1 - 2\gamma_2}$ along $[001]$.

Light-hole band: $E_{lh}(k_{||}) = \frac{\hbar^2 k_{||}^2}{2m_0}(\gamma_1 + 2\gamma_2)$ for $\mathbf{k} = k_{||}\hat{z}$, with effective mass $m_{lh}^{[001]} = \frac{m_0}{\gamma_1 + 2\gamma_2}$.

Twofold spin degeneracy is retained (e.g. $m_j = +3/2$ and $-3/2$ give the same E_{hh}). Because $\gamma_1 > \gamma_2$ for typical III-Vs, the HH band is “heavier” (larger effective mass, smaller curvature) than the LH band. For directions other than $[001]$, the angular momentum projection is not a conserved quantum number, and the HH-LH states mix under the influence of the γ_3 terms in the Hamiltonian. This mixing leads to anisotropic dispersion or warping. For instance, for motion along the $[111]$ direction one finds $E_{hh}(k_{[111]}) \propto (\gamma_1 - 2\gamma_3)k^2$ and $E_{lh}(k_{[111]}) \propto (\gamma_1 + 2\gamma_3)k^2$, which differ from the $[001]$ masses if $\gamma_3 \neq \gamma_2$. In GaAs and InAs, $\gamma_3 > \gamma_2$ (see values below), so the constant-energy surfaces of the HH band are non-spherical, with the dispersion being flatter (heavier mass) along $[111]$ than along $[001]$. The LK model thus captures the cubic anisotropy of the valence band, while still providing analytic eigenfunctions (four-component spinors) that are combinations of the Bloch basis states above. These LK eigenstates are used as envelope functions in envelope-function approximations for heterostructures and to calculate transition matrix elements for optical processes.

Standard Luttinger Parameters for GaAs and InAs

The Luttinger parameters ($\gamma_1, \gamma_2, \gamma_3$) are typically determined by fitting the model to experimentally measured band dispersions (effective masses) or derived from ab initio band structure calculations. Below we list representative room-temperature values for GaAs and InAs:

GaAs: $\gamma_1 \approx 6.98, \gamma_2 \approx 2.06, \gamma_3 \approx 2.93$; these differences are minor and reflect fit updates. $\Delta_{SO} \approx 0.341$ eV for GaAs.

InAs: $\gamma_1 \approx 20.0, \gamma_2 \approx 8.5, \gamma_3 \approx 9.2$ with $\Delta_{SO} \approx 0.39$ eV. These large parameter values indicate the strongly nonparabolic, highly anisotropic valence band in InAs (heavy holes in InAs have an especially large effective mass due to $\gamma_1 - 2\gamma_2$ being small).

Two-photon light absorption in A_3B_5 semiconductors

The two-photon absorption (2PA) coefficient is expressed in the following form [9–11]:

where: $f_{lh,\vec{k}}^{(2)}(f_{hh,\vec{k}}^{(2)})$ - is the distribution function of light (lh) and heavy (hh) holes, $M_{lh,m;hh,m'}^{(2)}(\vec{k})$ - is the matrix element (ME) of the transition $|hh, m\rangle \xrightarrow{2PA} |lh, m'\rangle$, $I(\omega)$ - represents the intensity (or frequency, ω) of light, the wave vector of holes participating in optical transitions $|hh, \pm 3/2\rangle \xrightarrow{2PA} |lh, \pm 1/2\rangle$, with the energy dispersion $E_{V_l}(\vec{k}) = (A - (-1)^l B)k^2 = \frac{\hbar^2}{2m_l}k^2$ ($l = 1, 2, l = 1(hh)$), is given as:

$l = 2(lh)$ -for heavy holes, the wave vector is expressed as: $k_{lh,hh}^{(2\omega)} = (2\mu_{lh,hh}\hbar^{-2}2\hbar\omega)^{1/2}$, where $\mu_{lh,hh} = \frac{m_{hh}m_{lh}}{m_{hh}-m_{lh}}$ is the reduced mass of the holes.

The energy of heavy holes with such a wave vector is equal to $E_{hh}(k_{lh,hh}^{(2\omega)}) = \frac{m_{lh}}{m_{hh}-m_{lh}}2\hbar\omega$, while the energy of light holes is $E_{lh}(k_{lh,hh}^{(2\omega)}) = \frac{m_{hh}}{m_{hh}-m_{lh}}2\hbar\omega$, and their distribution functions are determined respectively as:

$$f[E_{hh}(k_{lh,hh}^{(2\omega)})] = \exp\left(-\frac{2\hbar\omega}{k_B T} \frac{m_{lh}}{m_{hh}-m_{lh}}\right) \exp\left(\frac{E_F}{k_B T}\right) \quad (2)$$

and

$$f[E_{lh}(k_{lh,hh}^{(2\omega)})] = \exp\left(-\frac{2\hbar\omega}{k_B T} \frac{m_{hh}}{m_{hh}-m_{lh}}\right) \exp\left(\frac{E_F}{k_B T}\right). \quad (3)$$

Calculations show that if the temperature dependence of the bandgap width, the effective masses of charge carriers, and the effect of coherent saturation are not taken into account, the distribution functions increase with temperature at a fixed frequency, reach a maximum, and then decrease. At a fixed temperature, the distribution functions decrease with increasing frequency. This behavior of the distribution functions plays a key role in the frequency-temperature dependence of the 2PA coefficient.

Further, it should be noted that in subsequent calculations, unlike in [25], it is assumed that during multiphoton transitions, virtual states exist not only in the branches of heavy and light holes but also in the spin-orbit split subband.

Quantitative calculations show that the optical transitions considered in [25] for wide-bandgap semiconductors provide the main contribution to absorption in the low-frequency region, while the contribution in the high-frequency region ($\Delta_{SO} \leq 2\hbar\omega \leq E_g$) is less than 5%. Therefore, further analysis will focus on transitions between the light hole subband and the spin-orbit split subband, as these transitions make a significant contribution in the frequency region $\Delta_{SO} \leq 2\hbar\omega \leq E_g$ ($\Delta_{SO}, E_g \leq 2\hbar\omega$) for wide-bandgap (narrow-bandgap) semiconductors.

Matrix elements of two-photon transitions from the light hole branch to the spin-orbit split subband

When the photon energy satisfies the condition $\Delta_{SO} \leq 2\hbar\omega$, optical transitions occur from the heavy and light hole branches to the spin-orbit split subband. In particular, two-photon optical transitions from the light hole branch of the valence band to the spin-orbit split subband occur in two stages: in the first stage, i.e., during a transition of type $|lh, \pm 1/2\rangle \Rightarrow |SO, \pm 1/2\rangle$, the spin direction does not change during the optical transition, while in the second stage, $|lh, \pm 1/2\rangle \Rightarrow |SO, \mp 1/2\rangle$ (see Fig. 1), the spin direction reverses (see Table 1).

Table 1. Composite matrix elements of optical transitions from the light and heavy hole branches to the spin-orbit split subband (each multiplied by $\left(\frac{eA_0}{\hbar c}\right)^2$, $e'_\pm = e'_x \pm ie'_y$, $e'^2_\pm = e'^2_x + e'^2_y$).

Virtual state	Composite matrix elements of optical transitions	
	Type 1 optical transitions (spin direction does not change)	Type 2 optical transitions (spin direction reverses)
In the branches of the valence band	$\frac{B^2 k^2}{\hbar\omega\sqrt{2}} \left[\frac{3\hbar\omega}{E_{hh} - E_{lh} - \hbar\omega} e'^2_\pm + 4 \left(\frac{A}{B} + 1 \right) e'^2_z \right]$	$\frac{i}{\sqrt{6}} \frac{2(A+B)P_c k}{\hbar\omega} e'_+ e'_z$
In the spin-orbit split subband	$-\frac{P_c^2}{3\sqrt{2}} \frac{1}{E_{cond} - E_{lh} - \hbar\omega} (e'^2_\pm + 4e'^2_z)$	$\frac{1}{\sqrt{2}} \frac{P_c^2}{(E_{cond} - E_{lh} - \hbar\omega)} e'_+ e'_z$
In the conduction band	$2\sqrt{2} \frac{A}{B} \frac{B^2 k^2}{(E_{SO} - E_{lh} - \hbar\omega)} e'^2_z$	$\frac{3\sqrt{2}ABk^2}{E_{SO} - E_{lh} - \hbar\omega} e'_z e'_+$

In Table 1: A, B -band parameters of the semiconductor, $B = \frac{\hbar^2 m_{hh} - m_{lh}}{4 m_{lh} m_{hh}}$, bandgap parameters, P_c - Kane parameter [26, 27], $e'_\alpha (\alpha = x, y, z)$ - components of the light polarization vector, A_0 - amplitude of the electromagnetic wave vector potential.

In particular, for the optical transitions $|lh, \pm 1/2\rangle \xrightarrow{2PA} |SO, \pm 1/2\rangle$ shown in Fig. 1, the square of the modulus of the sum of the matrix elements (ME) is written as:

$$|M_{lh, \pm 1/2; SO, \pm 1/2}|^2 = \frac{1}{2} \left(\frac{eA_0}{\hbar c} \right)^4 \left(\frac{B^2 k^2}{\hbar \omega} \right)^2 (\Re_Z e'^4_z + \Re_\perp e'^4_\perp + \Re_{Z\perp} e'^2_z e'^2_\perp), \quad (4)$$

and for optical transitions of type $|lh, \pm 1/2\rangle \xrightarrow{2PA} |SO, \mp 1/2\rangle$:

$$|M_{lh, \pm 1/2; SO, \mp 1/2}|^2 = \left(\frac{eA_0}{\hbar c} \right)^4 \left(\frac{B k^2}{\hbar \omega} \right)^2 \Re'_{Z\perp} e'^2_z e'^2_\perp, \quad (5)$$

where:

$$\Re_Z = 16 \left[\left(\frac{A}{B} \frac{\hbar \omega}{E_{SO} - E_{lh} - \hbar \omega} \right)^2 + \left(\frac{A}{B} + 1 \right)^2 + \left(\frac{P_c^2}{3B^2 k^2} \frac{\hbar \omega}{E_{cond} - E_{lh} - \hbar \omega} \right)^2 \right], \quad (6a)$$

$$\Re_\perp = \left[\left(\frac{P_c^2}{3B^2 k^2} \frac{\hbar \omega}{E_{cond} - E_{lh} - \hbar \omega} \right)^2 + \left(\frac{3\hbar \omega}{E_{hh} - E_{lh} - \hbar \omega} \right)^2 \right], \quad (6b)$$

$$\Re_{Z\perp} = \left[8 \left(\frac{P_c^2}{3B^2 k^2} \frac{\hbar \omega}{E_{cond} - E_{lh} - \hbar \omega} \right)^2 + \frac{24\hbar \omega}{E_{hh} - E_{lh} - \hbar \omega} \left(\frac{A}{B} + 1 \right) \right], \quad (6c)$$

$$\Re'_{Z\perp} = \left[\frac{4}{6} \left(\frac{A}{B} + 1 \right)^2 \left(\frac{P_c}{Bk} \right)^2 + \frac{1}{2} \left(\frac{P_c^2 \hbar \omega}{Bk^2 (E_{cond} - E_{lh} - \hbar \omega)} \right)^2 + 18 \left(\frac{A}{B} \right)^2 \left(\frac{\hbar \omega}{E_{SO} - E_{lh} - \hbar \omega} \right)^2 \right]. \quad (6d)$$

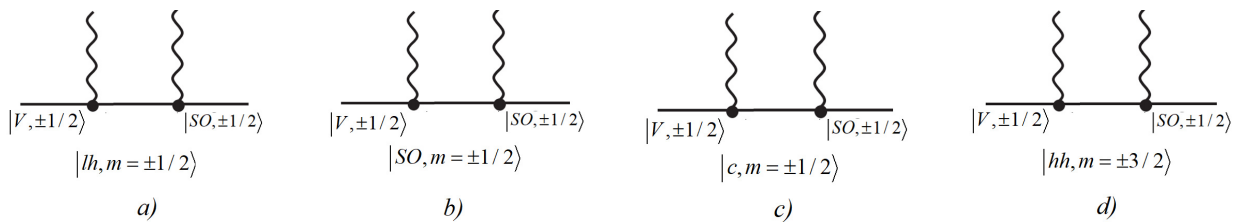


Figure 1. Types of two-photon transitions from the light hole branch of the valence band to the spin-orbit split subband $|V, \pm 1/2\rangle \xrightarrow{2PA} |SO, \pm 1/2\rangle$: a) Intermediate states are located in the light hole branch; b) In the spin-orbit split subband; c) In the heavy hole subband; d) In the heavy hole subband. In such optical transitions, the spin direction of charge carriers does not change. Optical transitions involving spin flip are determined in a similar manner, where the substitution $|SO, \pm 1/2\rangle \leftrightarrow |SO, \mp 1/2\rangle$ must be applied.

It should be noted that if the energy conservation law associated with TPA is taken into account, the energies of the holes involved in optical transitions from the light hole branch to the spin-orbit split subband are determined by the following expression

$$E_c(k_{SO, lh}^{(2\omega)}) = \frac{m_{SO} m_{lh}}{m_{cond}(m_{SO} - m_{lh})} (2\hbar \omega - \Delta_{SO}) + E_g, \quad (7)$$

$$E_{lh}(k_{SO, lh}^{(2\omega)}) = \frac{m_c}{m_c - m_{lh}} (2\hbar \omega - \Delta_{SO}), \quad E_{hh}(k_{SO, lh}^{(2\omega)}) = \frac{m_{SO} m_{lh}}{m_{hh}(m_{SO} - m_{lh})} (2\hbar \omega - \Delta_{SO}),$$

and their wave vector is given by: $k_{SO, lh}^{(2\omega)} = \sqrt{\frac{2\mu_{-}^{(SO, lh)}}{\hbar^2} (2\hbar \omega - \Delta_{SO})}$ where: $\mu_{-}^{(SO, lh)} = \frac{m_{SO} m_{lh}}{m_{SO} - m_{lh}}$ is the reduced mass of the holes, E_g (Δ_{SO}) - is the bandgap width (spin-orbit splitting), m_{SO} - is the effective mass of the holes, $E_{SO}(\vec{k}) = \Delta_{SO} + \frac{\hbar^2}{2m_{SO}} k^2$ - is the energy spectrum of the holes in the spin-orbit split subband.

It should be noted that we will conventionally classify semiconductors as wide-bandgap ($E_g \Delta_{SO}$), intermediate-bandgap ($E_g \approx \Delta_{SO}$), and narrow-bandgap ($E_g < \Delta_{SO}$). Now, let us analyze both interband and intraband optical transitions in these semiconductors. It is known that an optical transition between the conduction band and the valence band (interband optical transition) occurs when the condition $E_g(2\hbar \omega)$ is satisfied, while transitions from the light and heavy hole branches to the spin-orbit split subband (intraband optical transition) occur under the condition $\Delta_{SO}(2\hbar \omega)$. Thus, the order of interband and intraband optical transitions depends on the ratio $\frac{E_g}{\Delta_{SO}}$. From this, it can be seen that as the frequency increases in wide-bandgap (narrow-bandgap) semiconductors, intraband (interband) optical transitions occur first, followed by interband (intraband) optical transitions. In intermediate-bandgap semiconductors, both interband and intraband optical transitions occur (almost) simultaneously. This implies that when studying optical transitions, special

attention must be paid to the band structure of the semiconductor, which will be taken into account in subsequent calculations and in the analysis of results.

Since we will subsequently calculate the spectral, temperature, and polarization dependencies of optical properties, such as the light absorption coefficient and LCD, driven by two-photon transitions from the light and heavy hole branches to the spin-orbit split subband, it should be noted that in wide-bandgap (narrow-bandgap) semiconductors, such transitions are allowed in the frequency range $\Delta_{SO}(2\hbar\omega) \langle E_g \rangle (E_g, \Delta_{SO}(2\hbar\omega))$.

Linear-circular dichroism in two-photon transitions from the heavy and light hole branches to the spin-orbit split subband

Next, we will calculate the spectral and polarization dependencies of the LCD coefficient, determined by the probability of two-photon transitions, taking into account the phenomenon of coherent saturation [28, 29]:

$$W^{(2)} = \frac{2\pi}{\hbar} \frac{2\hbar\omega}{I} \left(\frac{eA_0}{m_0c} \right)^2 \left\langle \sum_{\vec{k}} \left| \sum_{m,m'=\pm 1/2; \vec{k}} M_{SO,m';lh,m}^{(2)}(\vec{k}) \right|^2 \left[1 + \sum_{\vec{k}} \frac{\alpha_{\omega}}{(\hbar\omega)^2} \left| \sum_{m,m'=\pm 1/2; \vec{k}} M_{SO,m';lh,m}^{(2)}(\vec{k}) \right|^2 \right]^{-1/2} \right\rangle \times (f_{lh,\vec{k}} - f_{SO,\vec{k}}) \delta(E_{SO}(\vec{k}) - E_{lh}(\vec{k}) - 2\hbar\omega), \quad (8)$$

Where the symbol $\langle \dots \rangle$ denotes averaging over the solid angles of the wave vector of the holes. Then, the square of the modulus of the two-photon matrix element (ME) is determined by the following relation: for optical transitions of type $|lh, \pm 1/2\rangle \xrightarrow{2PA} |SO, \pm 1/2\rangle$.

$$\Re_{SO,lh}^{(1)} = \frac{\frac{1}{2} \left(\frac{eA_0}{\hbar c} \right)^4 \left(\frac{B^2 k^2}{\hbar\omega} \right)^2 (\Re_Z e'^4_Z + \Re_{\perp} e'^4_{\perp} + \Re_{Z\perp} e'^2_Z e'^2_{\perp})}{\sqrt{1 + 4 \frac{\alpha_{\omega}}{\hbar^2 \omega^2} \left(\frac{eA_0}{\hbar c} \right)^4 \left(\frac{B^2 k^2}{\hbar\omega} \right)^2 (\Re_Z e'^4_Z + \Re_{\perp} e'^4_{\perp} + \Re_{Z\perp} e'^2_Z e'^2_{\perp})}}, \quad (9)$$

for optical transitions of type $|lh, \pm 1/2\rangle \xrightarrow{2PA} |SO, \mp 1/2\rangle$

$$\Re_{SO,lh}^{(2)} = \frac{\left(\frac{eA_0}{\hbar c} \right)^4 \left(\frac{B^2 k^2}{\hbar\omega} \right)^2 \Re'_{Z\perp} e'^2_Z e'^2_{\perp}}{\sqrt{1 + 4 \frac{\alpha_{\omega}}{\hbar^2 \omega^2} \left(\frac{eA_0}{\hbar c} \right)^4 \left(\frac{B^2 k^2}{\hbar\omega} \right)^2 \Re'_{Z\perp} e'^2_Z e'^2_{\perp}}}, \quad (10)$$

where

$$4 \frac{\alpha_{\omega}}{\hbar^2 \omega^2} \frac{1}{2} \left(\frac{eA_0}{\hbar c} \right)^4 \left(\frac{B^2 k^2}{\hbar\omega} \right)^2 = \xi_R \left(\frac{\Delta_{SO}}{\hbar\omega} \right)^6 \left[\frac{\mu_{SO,lh}}{4\mu_{hh,lh}} \left(2 \frac{\hbar\omega}{\Delta_{SO}} - 1 \right) \right]^2, \quad (11)$$

$\xi_R = 2\alpha_{\Delta} \left(\frac{I}{I_{\Delta}} \right)^3 \frac{e^4}{B^2 k_{\Delta}^2}$ - is the Rabi parameter, $k_{\Delta}^2 = \frac{2\mu_{hh,lh}}{\hbar^2} \Delta_{SO}$, $\alpha_{\Delta} = 6 \frac{\Delta_{SO}^2}{\hbar^2} T_n^{(1)} T_{n'}^{(1)}$, $I_{\Delta} = \frac{cn_{\omega} \Delta_{SO}^3}{(2\pi|B|^2 k_{\Delta})}$ - represent values in units of light intensity that depend on the band parameters of semiconductors, taking into account the energy conservation law describing two-photon transitions between the light and heavy hole subbands of the valence band. Since the value I_{Δ} depends on the effective mass of the holes in the spin-orbit split subband and its width, it is therefore influenced by the choice of Kane's model (three-band or four-band).

Thus, the coefficient of two-photon LCD light absorption depends not only on the band parameters of the semiconductor but also on the energy $E_c(k_{lh,SO}^{(2\omega)}) = \frac{m_{SO}m_{lh}}{m_c(m_{SO}-m_{lh})\hbar^2} (2\hbar\omega - \Delta_{SO}) + E_g$ of photoexcited electrons in the conduction band, $E_{hh}(k_{lh,SO}^{(2\omega)}) = \frac{m_{SO}m_{lh}}{m_{hh}(m_{SO}-m_{lh})\hbar^2} (2\hbar\omega - \Delta_{SO})$ of heavy holes, and $E_{SO}(k_{lh,SO}^{(2\omega)}) = -\frac{m_{lh}}{m_{SO}-m_{lh}} (2\hbar\omega - \Delta_{SO}) - \Delta_{SO}$ of holes in the spin-orbit split subband.

If the contribution of the coherent saturation effect is neglected (i.e., $\xi_R = 0$), then the average value of $\left\langle \sum_{m,m'=\pm 1/2; \vec{k}} \left| M_{SO,m';lh,m}^{(2)}(\vec{k}) \right|^2 \right\rangle$ is determined as follows: for linear polarization:

$$\left\langle \left| M_{lh,\pm 1/2;SO,\pm 1/2} \right|^2 \right\rangle = \frac{1}{2} \left(\frac{eA_0}{\hbar c} \right)^4 \left(\frac{B^2 k^2}{\hbar\omega} \right)^2 \frac{1}{15} (3\Re_Z + 8\Re_{\perp} + 2\Re_{Z\perp}), \quad (12)$$

$$\left\langle \left| M_{lh,\pm 1/2;SO,\mp 1/2} \right|^2 \right\rangle = \frac{2}{15} \left(\frac{eA_0}{\hbar c} \right)^4 \left(\frac{B^2 k^2}{\hbar\omega} \right)^2 \Re'_{Z\perp}; \quad (13)$$

for circular polarization

$$\left\langle \left| M_{lh,\pm 1/2;SO,\pm 1/2} \right|^2 \right\rangle = \left(\frac{eA_0}{\hbar c} \right)^4 \left(\frac{B^2 k^2}{\hbar\omega} \right)^2 \frac{1}{2} \frac{1}{15} (2\Re_Z + 7\Re_{\perp} + 3\Re_{Z\perp}), \quad (14)$$

$$\left\langle \left| M_{lh,\pm 1/2;SO,\mp 1/2} \right|^2 \right\rangle = \frac{1}{10} \left(\frac{eA_0}{\hbar c} \right)^4 \left(\frac{B^2 k^2}{\hbar\omega} \right)^2 \Re'_{Z\perp}. \quad (15)$$

Thus, the dependence of the probabilities of two-photon transitions from the light hole branch to the spin-orbit split subband, $|V, \pm 1/2\rangle \xrightarrow{2PA} |SO, \pm 1/2\rangle$ and $|V, \pm 1/2\rangle \xrightarrow{2PA} |SO, \mp 1/2\rangle$, for linearly polarized light is determined by the following relationships:

$$|M_{lh,\pm 1/2;SO,\pm 1/2}|^2 = \frac{1}{2} \left(\frac{eA_0}{ch} \right)^4 \left(\frac{B^2 k^2}{\hbar\omega} \right)^2 (\Re_Z e'^4_Z + \Re_{\perp} e'^4_{\perp} + \Re_{Z\perp} e'^2_Z e'^2_{\perp}), \quad (16)$$

$$|M_{lh,\pm 1/2;SO,\mp 1/2}|^2 = \left(\frac{eA_0}{ch} \right)^4 \left(\frac{B^2 k^2}{\hbar\omega} \right)^2 \Re'_{Z\perp} e'^2_Z e'^2_{\perp}. \quad (17)$$

Here, for linearly polarized light

$$|e'_Z|^2 = \frac{1}{2} s i n^2 \phi', |e'_{\perp}|^2 = 1 - |e'_Z|^2 \mp P_{circ} \cos \phi' = \frac{1}{2} (1 + \cos^2 \phi') \mp P_{circ} \cos \phi', \quad (18)$$

and for circularly polarized light

$$|e'_Z|^2 = \cos^2 \phi, |e'_{\perp}|^2 = \sin^2 \phi, |e'_{\pm}|^2 = \frac{1}{2} (1 + \cos^2 \phi') \mp P_{circ} \cos \phi', \quad (19)$$

where $\phi(\phi')$ — is the angle between the vectors $\vec{e}(\vec{q})$ and \vec{k} , \vec{e} — is the light polarization vector, $\vec{k}(\vec{q})$ is the wave vector of the hole (photon), P_{circ} — is the degree of circular polarization.

It should be noted that the polarization (angular) dependence, as well as the dependence on the Rabi factor for both the probability and the LCD coefficient, driven by two-photon optical transitions, are calculated according to relations (17) and (18). Initially, to simplify numerical calculations, we will ignore the contribution of the coherent saturation effect to the transition probabilities.

The spectral and angular dependence of the transition probabilities $|lh, \pm 1/2\rangle \xrightarrow{2PA} |SO, \pm 1/2\rangle$ ($W_{lh,\pm 1/2;SO,\pm 1/2}^{(linear)}$) and $|lh, \pm 1/2\rangle \xrightarrow{2PA} |SO, \mp 1/2\rangle$ ($W_{lh,\pm 1/2;SO,\mp 1/2}^{(linear)}$ for linear polarization in GaAs and InAs semiconductors, calculated according to equations (17) and (18), are shown in Fig. 2. The transition probabilities for $|lh, \pm 1/2\rangle \xrightarrow{2PA} |SO, \pm 1/2\rangle$, and $|lh, \pm 1/2\rangle \xrightarrow{2PA} |SO, \mp 1/2\rangle$ for circular polarization are also depicted in Fig. 2.

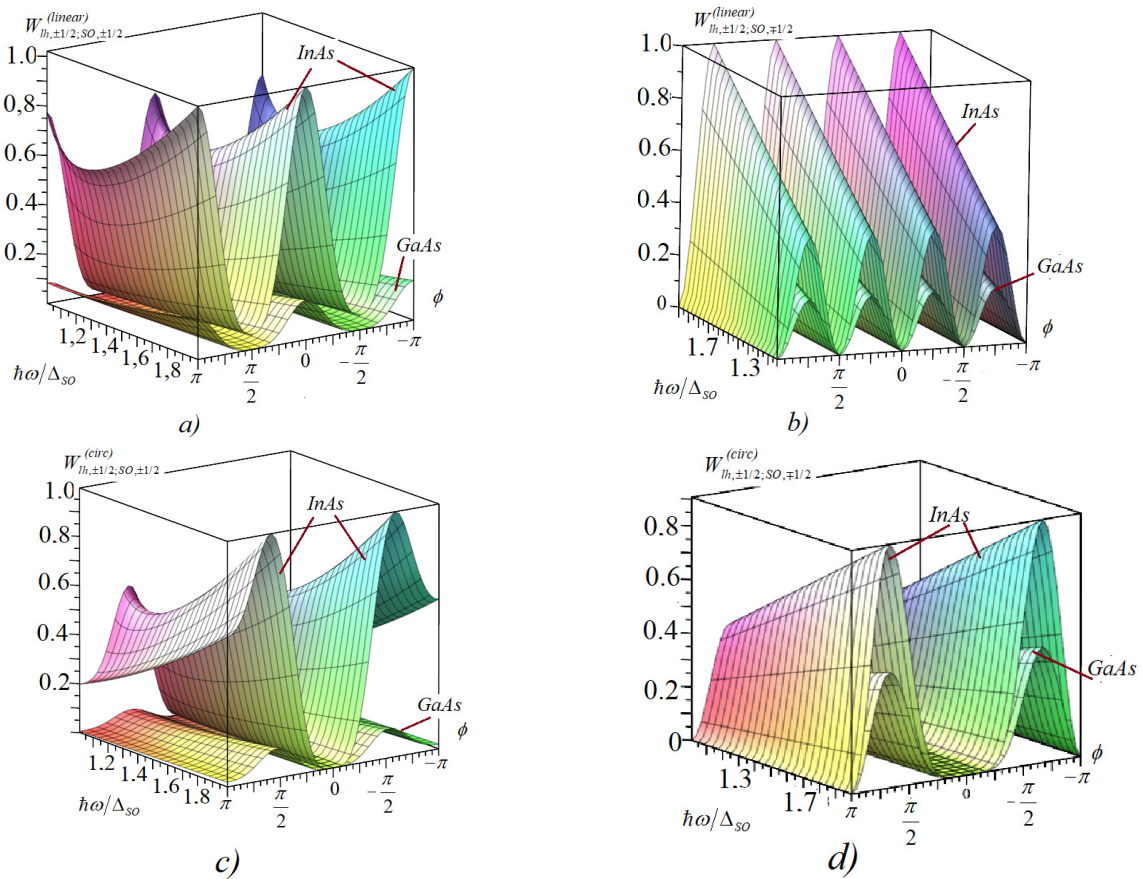


Figure 2. Spectral and angular dependencies of the transition probabilities of type $|lh, \pm 1/2\rangle \xrightarrow{2PA} |SO, \pm 1/2\rangle$ and $|lh, \pm 1/2\rangle \xrightarrow{2PA} |SO, \mp 1/2\rangle$ for linear polarization: (a, c) in InAs and (b, d) in GaAs

The spectral and angular dependence of the transition probabilities $|lh, \pm 1/2\rangle \xrightarrow{2PA} |SO, \pm 1/2\rangle$, $(W_{lh, \pm 1/2; SO, \pm 1/2}^{(linear)})$, and $|lh, \pm 1/2\rangle \xrightarrow{2PA} |SO, \mp 1/2\rangle$, $(W_{lh, \pm 1/2; SO, \mp 1/2}^{(linear)})$ for linear polarization in GaAs and InAs semiconductors, calculated according to equations (17) and (18), is shown in Fig. 2. For transitions of type $|lh, \pm 1/2\rangle \xrightarrow{2PA} |SO, \pm 1/2\rangle$ and $|lh, \pm 1/2\rangle \xrightarrow{2PA} |SO, \mp 1/2\rangle$ for circular polarization, the results are also presented in Fig. 2.

From Fig. 2, it can be seen that: a) The maximum values of the transition probabilities in InAs semiconductors are significantly higher than those in GaAs, while the oscillation of the angular dependence in InAs and GaAs is identical, i.e., the maximum and minimum oscillation values occur at the same angle in both materials. b) With increasing frequency, the maximum values of $W_{lh, \pm 1/2; SO, \pm 1/2}^{(linear)}$ and $W_{lh, \pm 1/2; SO, \pm 1/2}^{(circ)}$ decrease, passing through a minimum before increasing again, while $W_{lh, \pm 1/2; SO, \mp 1/2}^{(linear)}$ and $W_{lh, \pm 1/2; SO, \mp 1/2}^{(circ)}$ increase in both *InAs* and *GaAs* for both linear and circular polarization.

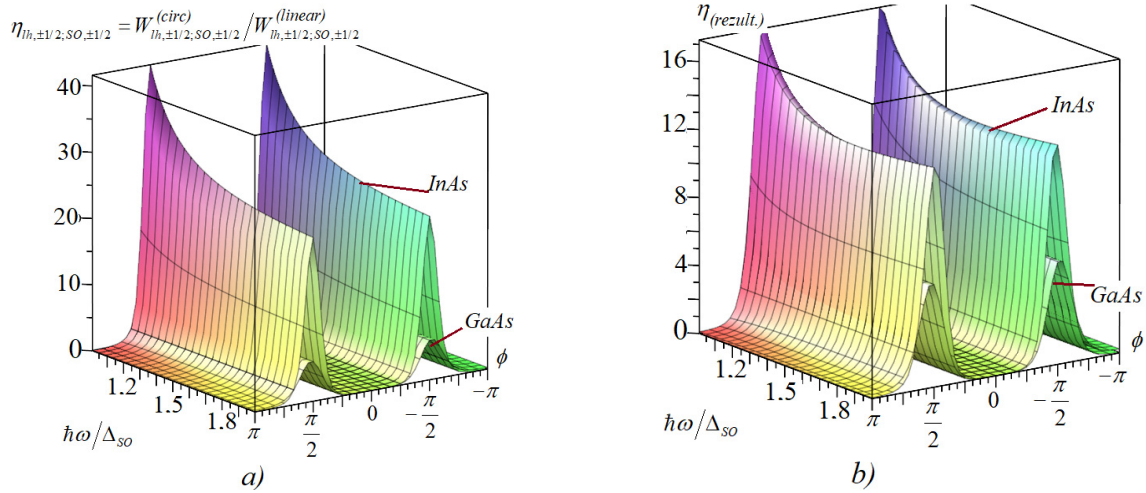


Figure 3. Spectral and angular dependencies of the two-photon LCD coefficient for optical transitions $|lh, \pm \frac{1}{2}\rangle \xrightarrow{2PA} |SO, \pm \frac{1}{2}\rangle$ (a) and the resulting LCD (b) in *GaAs* and *InAs*, where the contribution of the coherent saturation effect is neglected

Figure 3 shows the spectral and angular dependencies of the two-photon LCD coefficient for optical transitions $|lh, \pm 1/2\rangle \xrightarrow{2PA} |SO, \pm 1/2\rangle$ (Fig. 3a) and the resulting LCD (Fig. 3b) in *GaAs* and *InAs* semiconductors. From this figure, it is evident that the two-photon LCD exhibits the following characteristics: In narrow-bandgap semiconductors, it is greater than in wide-bandgap semiconductors. The polarization dependence has an oscillatory nature. With increasing frequency, the maximum value decreases for both semiconductors. It is more significant in the low-frequency region than in the high-frequency region and remains practically unchanged in the frequency range $\hbar\omega > 1.5\Delta_{SO}$. Peaks occur at angles $\pm\pi/2$ between the light polarization vector and the wave vector of charge carriers, and these peaks are independent of the type of semiconductor. Now, we proceed to analyze the calculation results considering the contribution of the coherent saturation effect to the probabilities of two-photon transitions. Calculations show that the two-photon LCD coefficient should be distinctly observable in the low-frequency region, as it is proportional to the value $\left(\frac{\Delta_{SO}}{\hbar\omega}\right)^6$. Therefore, we will further analyze the contribution of the coherent saturation effect in the frequency range $\frac{\approx \Delta_{SO}}{\hbar}$. First, we calculate the frequency-angular dependencies of the LCD coefficient for several values of the Rabi parameter $\xi_R = 2\alpha_{\Delta} \left(\frac{1}{I_{\Delta}}\right)^3 \frac{e^4}{B^2 k_A^2}$: $\xi_R = 0.1$ and $\xi_R = 1.5$

Figure 4 shows the frequency-angular dependencies of the probabilities $W_{lh, \pm 1/2; SO, \pm 1/2}^{(linear)}$ and $W_{lh, \pm 1/2; SO, \mp 1/2}^{(linear)}$ in *GaAs* and *InAs*, illuminated by both linearly and circularly polarized light for $\xi_R = 0.1$ and $\xi_R = 1.5$. It can be observed that the physical nature of the probabilities depends on the degree of light polarization, the types of transitions, and the band structure of the semiconductor: a) At a fixed frequency, the angular dependence $W_{lh, \pm 1/2; SO, \pm 1/2}^{(linear)}$ ($W_{lh, \pm 1/2; SO, \pm 1/2}^{(circ)}$) exhibits three (two) peaks for transitions $|lh, \pm 1/2\rangle \xrightarrow{2PA} |SO, \pm 1/2\rangle$, and four peaks for transitions $|lh, \pm 1/2\rangle \xrightarrow{2PA} |SO, \mp 1/2\rangle$.

From the latest results (see, for example, Fig. 4a, c, b, d), it is evident that the spectral dependence of the $\eta_{lh, SO} = \frac{W_{lh, SO}^{(circ)}}{W_{lh, SO}^{(chiz)}}$ two-photon LCD coefficient can only be calculated at certain angle values, since the probabilities of optical transitions for both linearly and circularly polarized light become zero at specific points.

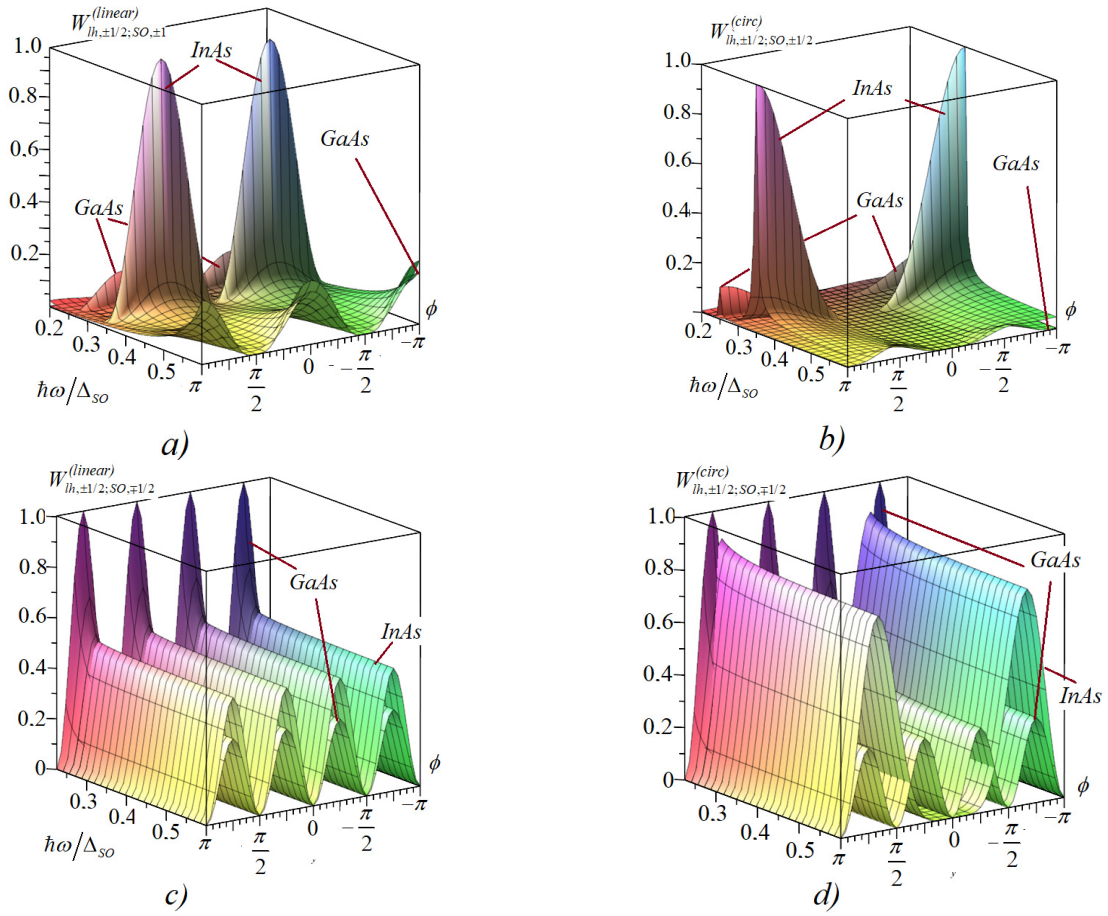


Figure 4. Spectral and angular dependencies of the transition probabilities of type $|lh, \pm 1/2\rangle \xrightarrow{2PA} |SO, \pm 1/2\rangle$ and $|lh, \pm 1/2\rangle \xrightarrow{2PA} |SO, \mp 1/2\rangle$ for linear (a, c) and circular (b, d) polarization in InAs and GaAs. The Rabi parameter is assumed to be 0.1

In such cases, the LCD coefficient remains undefined. Therefore, we will analyze the frequency-angular dependencies of $\eta_{lh, \pm 1/2; SO, \pm 1/2}$ in GaAs and InAs for two angle values between the light polarization vector and the photon wave vector: $\frac{\pi}{6}$ (a) and $\frac{\pi}{3}$ (b) (Fig. 5).

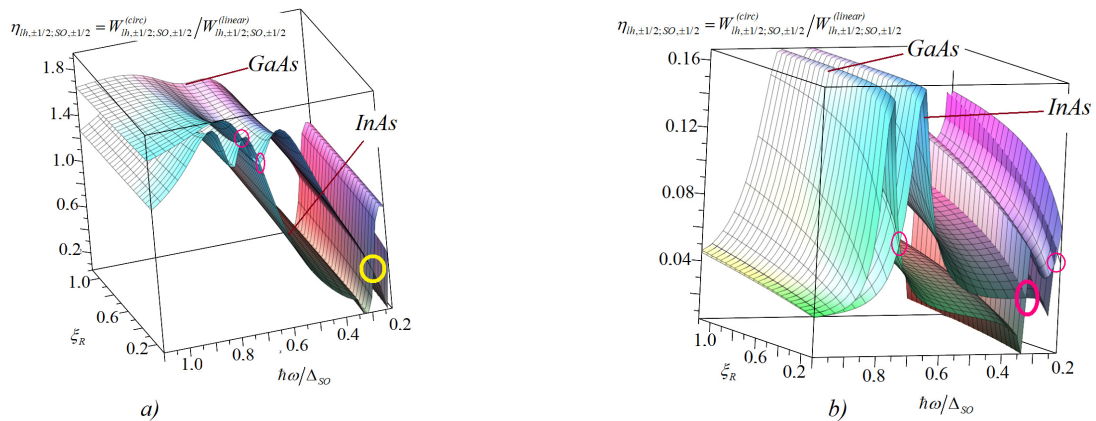


Figure 5. Frequency dependence and dependence on the Rabi parameter of the two-photon LCD coefficient for the angle between the light polarization vector and the photon wave vector equal to $\frac{\pi}{6}$ (a) and $\frac{\pi}{3}$ (b), calculated for optical transitions $|lh, \pm 1/2\rangle \xrightarrow{2PA} |SO, \pm 1/2\rangle$ in GaAs and InAs, where the intersections of the graphs are marked with circles

From Fig. 5, it is evident that the nature of the frequency dependence of the LCD coefficient: a) Depends on the band structure of the semiconductor; b) The amplitude value of $\eta_{lh, \pm 1/2; SO, \pm 1/2}$ is almost ten times greater than that of $\eta_{lh, \pm 1/2; SO, \mp 1/2}$ in both the high- and low-frequency regions for GaAs and InAs.

Fig. 6. Angular dependence and dependence on the Rabi parameter of the resulting two-photon LCD coefficient ($\eta_{\text{result}} = \eta_{lh, \pm 1/2; SO, \pm 1/2} + \eta_{lh, \pm 1/2; SO, \mp 1/2}$) in GaAs and InAs for two frequency values: $\hbar\omega = 0.25\text{eV}$ (a) and $\hbar\omega =$

0.5eV (b). It can be observed that the LCD is more noticeably observed in GaAs than in InAs, but the maximum LCD values in InAs occur at $\frac{\pm\pi}{2}$, and in GaAs at $\frac{3\pi}{4}$ when $\hbar\omega = 0.25\text{eV}$; in GaAs at $\frac{\pm 11\pi}{8}$, and in InAs at $\frac{\pm 3\pi}{2}$ when $\hbar\omega = 0.5\text{eV}$.

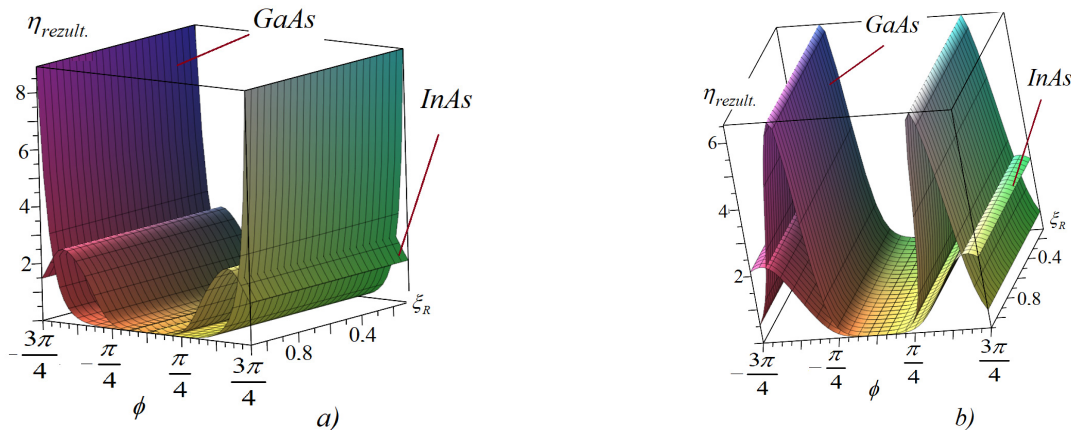


Figure 6. Angular dependence and dependence on the Rabi parameter of the resulting two-photon LCD coefficient ($\eta_{\text{rezult}} = \eta_{lh,\pm 1/2;SO,\pm 1/2} + \eta_{lh,\pm 1/2;SO,\mp 1/2}$) in GaAs and InAs for two frequency values: $\hbar\omega = 0.25\text{eV}$ (a) and $\hbar\omega = 0.5\text{eV}$ (b)

Calculations show that if the dependencies $E_g(T)$, $m_c(T)$, $m_{SO}(T)$, calculated using the three-band Kane model, are taken into account, the main contribution to the resulting two-photon LCD coefficient $\langle \eta^{(2)}(\omega, T) \rangle$, averaged over the solid angles of the hole wave vector, comes from transitions of type $|lh, \pm 1/2\rangle \xrightarrow{2\text{photonabsorption}} |SO, \pm 1/2\rangle$, while the contribution of transitions $|lh, \pm 1/2\rangle \xrightarrow{2\text{photonabsorption}} |SO, \mp 1/2\rangle$ is less than 3%. The calculations also indicate that, without considering the effect of coherent saturation, $\langle \eta^{(2)}(\omega, T) \rangle$ in GaAs and InAs is practically independent of temperature.

Light absorption due to two-photon transitions from the light hole branch of the valence band to the spin-orbit split subband

Thus, the coefficient of two-photon absorption caused by optical transitions between the light hole subband and the spin-orbit split subband is determined by the following relation

$$K^{(2)}(\omega, T) = \frac{2\hbar\omega}{I} \frac{2\pi m_{SO} m_{lh}}{(m_{SO} - m_{lh})\hbar^3} k_{lh,SO}^{(2\omega)} [f_{lh}(k_{lh,SO}^{(2\omega)}) - f_{SO}(k_{lh,SO}^{(2\omega)})] \times \int_0^\pi \sin\theta \cdot d\theta \int_0^{2\pi} d\varphi \left| \sum_{lh,m=\pm 1/2;SO,m'=\pm 1/2} M_{lh,m;SO,m'}^{(2)}(k_{lh,SO}^{(2\omega)}, \theta, \varphi) \right|^2 \quad (20)$$

where $k_{lh,SO}^{(2\omega)}$ is the wave vector of the photoexcited holes, and the matrix element (ME) of the transition $|lh, \pm 1/2\rangle \xrightarrow{2\text{photonliyutish}} |SO, \pm 1/2\rangle$ is:

$$M_{lh,\pm 1/2;SO,\pm 1/2} = \left(\frac{eA_0}{\hbar c} \right)^2 \frac{1}{2} \left(\frac{B^2 k^2}{\hbar\omega} \right)^2 \left\{ 4 \left[\frac{A}{B} \frac{\hbar\omega}{E_{SO} - E_{lh} - \hbar\omega} + 4 \left(\frac{A}{B} + 1 \right) \right] e_z'^2 - \frac{P_c^2}{B^2 k^2 3 E_{cond} - E_{lh} - \hbar\omega} (e_x'^2 + 4e_z'^2) + \frac{3\hbar\omega}{E_{hh} - E_{lh} - \hbar\omega} e_x'^2 \right\}, \quad (21)$$

for $|lh, \pm 1/2\rangle \xrightarrow{2PA} |SO, \mp 1/2\rangle$:

$$M_{lh,\pm 1/2;SO,\mp 1/2} = \left(\frac{eA_0}{\hbar c} \right)^2 \left[\frac{i}{\sqrt{6}} \frac{2(A+B)P_c k}{(\hbar\omega)} + \frac{1}{\sqrt{2}} \frac{P_c^2}{(E_{cond} - E_{lh} - \hbar\omega)_z} + \frac{3\sqrt{2}ABk^2}{E_{SO} - E_{lh} - \hbar\omega} \right] e_- e_+^*, \quad (22)$$

$f_{lh}(k_{lh,SO}^{(2\omega)})[f_{SO}(k_{lh,SO}^{(2\omega)})]$ - are the distribution functions of charge carriers in the light hole subband (spin-orbit split subband), $B^2(k_{lh,SO}^{(2\omega)})^2 = \frac{\hbar^2}{2} \left(\frac{m_{hh} - m_{lh}}{m_{lh} m_{hh}} \right)^2 \frac{m_{SO} m_{lh}}{(m_{SO} - m_{lh})} (2\hbar\omega - \Delta_{SO})$, $\theta(\varphi)$ -are the polar (azimuthal) angles of the hole wave vector. Calculations show that each term in equations (20) and (21) provides comparable contributions to the two-photon matrix element. This indicates that significant contributions are made not only by transitions where the intermediate states are located in the light and heavy hole branches but also in the spin-orbit split subband, as well as in the conduction band.

The average value of the matrix element (ME) (see formula (3.4.2)) is determined as:

$$\left\langle \left| M_{lh,m;SO,m'}^{(2)}(k_{lh,SO}^{(2\omega)}, \theta, \varphi) \right|^2 \right\rangle = \int_0^\pi \sin\theta \cdot d\theta \int_0^{2\pi} d\varphi \sum_{lh,m=\pm 1/2;SO,m'=\pm 1/2} \left| M_{lh,m;SO,m'}^{(2)}(k_{lh,SO}^{(2\omega)}, \theta, \varphi) \right|^2.$$

Then: for optical transitions of type: $|lh, \pm 1/2\rangle \xrightarrow{2\text{фотонноепоглощение}} |SO, \pm 1/2\rangle$:

$$\langle |M_{lh, \pm 1/2; SO, \pm 1/2}|^2 \rangle = \frac{1}{30} \left(\frac{I}{\hbar\omega} \frac{e^2}{c\hbar} \frac{2\pi}{n_\omega} \right)^2 \left(\frac{B^2 k^2}{\hbar\omega} \right)^2 \left(\Re_Z \{ \frac{3}{2} \} + \Re_\perp \{ \frac{8}{7} \} + \Re_{Z\perp} \{ \frac{2}{3} \} \right); \quad (23)$$

and for optical transitions of type: $|lh, \pm 1/2\rangle \xrightarrow{2PA} |SO, \mp 1/2\rangle$

$$\langle |M_{lh, \pm 1/2; SO, \pm 1/2}|^2 \rangle = \frac{1}{2} \left(\frac{I}{\hbar\omega} \frac{e^2}{c\hbar} \frac{2\pi}{n_\omega} \right)^2 \left(\frac{B^2 k^2}{\hbar\omega} \right)^2 \frac{1}{15} \left(\Re_Z \{ \frac{3}{2} \} + \Re_\perp \{ \frac{8}{7} \} + \Re_{Z\perp} \{ \frac{2}{3} \} \right). \quad (24)$$

The number indicated at the top (bottom) in expressions (22) and (23) refers to linear (circular) polarization. Thus, if in expression (19) the relations (20)–(23) are taken into account and the effect of coherent saturation is neglected, then:

a) For linearly polarized light:

$$K_{linear}^{(2)} = 2(2\pi)^3 \frac{I}{\hbar\omega} \left(f_{lh, \vec{k}}^{(2)} - f_{SO, \vec{k}}^{(2)} \right) \left(\frac{e^2}{c\hbar n_\omega} \right)^2 \left(\frac{B^2 k^2}{\hbar\omega} \right)^2 \frac{\mu_{-}^{(SO, lh)}}{\hbar^3} k_{SO, lh}^{(2\omega)} \times \\ \times \left\langle \left[3\Re'_{Z\perp} + \frac{1}{30} (2\Re_Z + 8\Re_\perp + 3\Re_{Z\perp}) \right] \right\rangle; \quad (25)$$

b) For circularly polarized light:

$$K_{circ}^{(2)} = 2(2\pi)^3 \frac{I}{\hbar\omega} \left(f_{lh, \vec{k}}^{(2)} - f_{SO, \vec{k}}^{(2)} \right) \left(\frac{e^2}{c\hbar n_\omega} \right)^2 \left(\frac{B^2 k^2}{\hbar\omega} \right)^2 \frac{\mu_{-}^{(SO, lh)}}{\hbar^3} k_{SO, lh}^{(2\omega)} \times \\ \times \left\langle \left[2\Re'_{Z\perp} + \frac{1}{30} (3\Re_Z + 7\Re_\perp + 2\Re_{Z\perp}) \right] \right\rangle. \quad (26)$$

The frequency-temperature dependencies of the absorption coefficient $K^{(2)}$, calculated using (24) and (25) for transitions $|lh, \pm 1/2\rangle \xrightarrow{2\text{фотонлиутилиш}} |SO, \pm 1/2\rangle$ and $|lh, \pm 1/2\rangle \xrightarrow{2\text{фотонлиутилиш}} |SO, \mp 1/2\rangle$ in GaAs (a, c) and InAs (b, d), are shown in Fig. 7. From this figure, it can be observed that: a) In GaAs, the consideration of $E_g(T)$ practically does not affect $K^{(2)}(\omega, T)$, whereas in InAs, it leads to an increase in $K^{(2)}(\omega, T)$. b) The amplitude value of $K_{circ}^{(2)}(\omega, T)$ is greater than the amplitude value of $K_{linear}^{(2)}(\omega, T)$. c) With increasing temperature in InAs, the maximum values of $K_{circ, linear}^{(2)}(\omega, T)$ decrease in the low-frequency region, while in the high-frequency region, they increase instead.

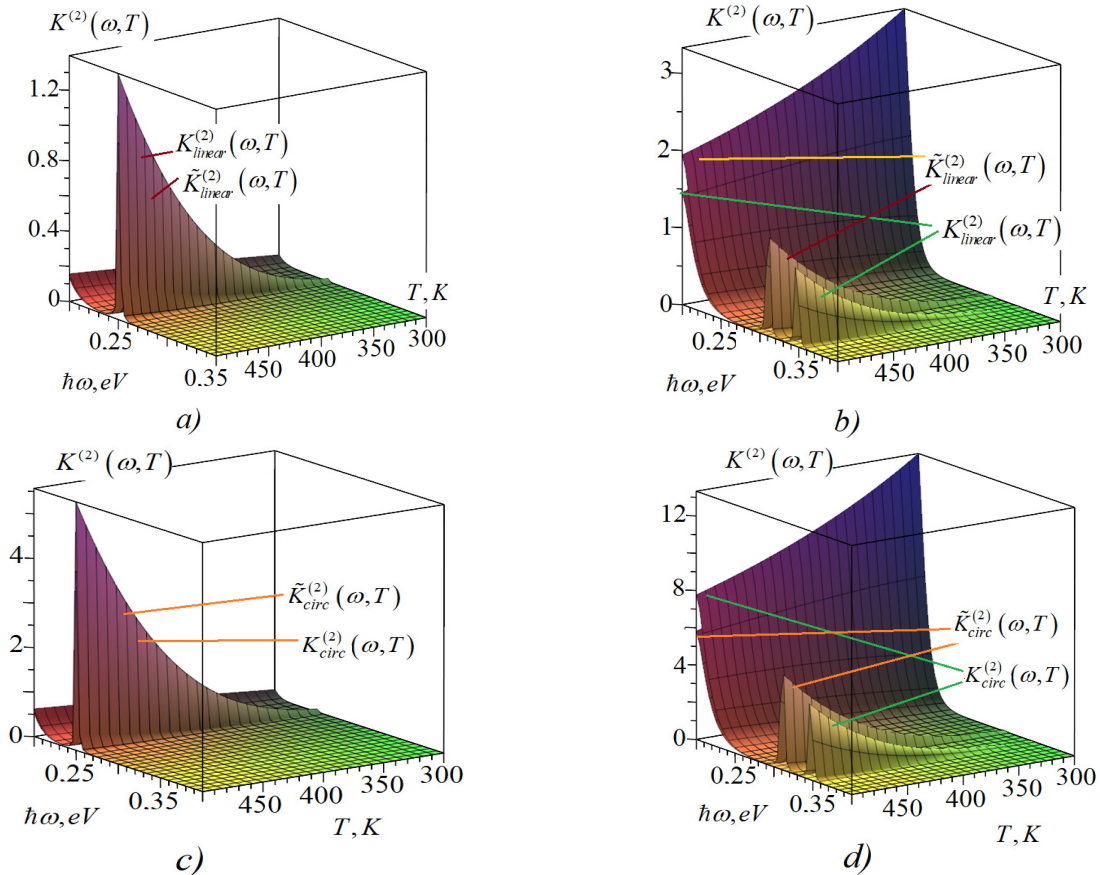


Figure 7. Frequency-temperature dependencies of the two-photon absorption coefficient $K^{(2)}(\omega, T)$ for linearly polarized light (a, b) and circularly polarized light (c, d) in semiconductors GaAs (a, c) and InAs (b, d)

This situation is explained by the ratio of the bandgap width to the spin-orbit splitting width, which is greater than one in GaAs and close to one in InAs.

In the study, the maximum value of $K^{(2)}(\omega, T)$ for linear polarization, calculated for in GaAs, was set equal to one, neglecting the contribution of the coherent saturation effect. $\left(\tilde{K}^{(2)}(\omega, T)\right)$ represents the 2PA coefficient in cases where the temperature dependence of the band parameters is considered (or not considered).

CONCLUSIONS

Thus, in this work:

1. Based on the multi-band Kane model, interband two-photon absorption (2PA) of light, caused by optical transitions from the light hole branch to the spin-orbit split subband in GaAs and InAs, has been theoretically investigated.
2. Two-photon interband optical transitions have been classified, with attention paid to the fact that virtual states of charge carriers are present not only in the light and heavy hole branches but also in the spin-orbit split subband and the conduction band.
3. In GaAs and InAs, the presence of several peaks in the frequency-temperature dependencies of the 2PA coefficient has been identified. The appearance of the peaks is explained not only by the specific change in the distribution functions of photoexcited holes but also by the fact that, at certain frequency values, some denominators in the expressions for the composite matrix elements tend toward zero.
4. It has been shown that all two-photon optical transitions, which differ by their virtual states, contribute comparably to the absorption.
5. It has been demonstrated that in the frequency regions where the spectral dependence of the probabilities of two-photon transitions changes sharply, two-photon linear-circular dichroism (LCD) can be clearly observed.

ORCID

✉ Rustam Y. Rasulov, <https://orcid.org/0000-0002-5512-0654>; ✉ Voxob R. Rasulov, <https://orcid.org/0000-0001-5255-5612>

REFERENCES

- [1] G.I. Stegeman, and R. A. Stegeman, *Nonlinear Optics: Phenomena, Materials and Devices*, (John Wiley & Sons, Inc., Hoboken, NJ, 2012).
- [2] E.L. Ivchenko, Sov. Phys. Semicond. **6**, 17 (1973). (in Russian)
- [3] V. Nathan, A.H. Guenther, and S.S. Mitra, J. Opt. Soc. Am. B, **2**(2), 294 (1985). <https://doi.org/10.1364/JOSAB.2.000294>
- [4] S.D. Ganichev, E.L. Ivchenko, R.Ya. Rasulov, I.D. Yaroshetskii, and B.Ya. Averbukh, Phys. Solid State, **35**(1), 104 (1993).
- [5] I.B. Zotova, and Y.J. Ding, Appl. Opt. **40**, 6654 (2001). <https://doi.org/10.1364/AO.40.006654>
- [6] P.D. Olszak, C.M. Cirloganu, S. Webster, L.A. Padilha, S. Guha, L.P. Gonzalez, S. Krishnamurthy, et al., Phys. Rev. B, **82**, 235207 (2010). <https://doi.org/10.1103/PhysRevB.82.235207>
- [7] S.B. Arifzhanov, A.M. Danishevskii, E.L. Ivchenko, S.F. Kochegarov, and V.K. Subashiev. Sov. Phys. JETP, **47**(1), 88 (1978). http://www.jetp.ras.ru/cgi-bin/dn/e_047_01_0088.pdf
- [8] R.Y. Rasulov, V.R. Rasulov, M.K. Nasirov, M.A. Mamatova, and I.A. Muminov, East European Journal of Physics, (3), 316 (2024). <https://doi.org/10.26565/2312-4334-2024-3-34>
- [9] V.R. Rasulov, R.Ya. Rasulov, N.U. Kodirov, and U.M. Isomaddinova, Physics of the Solid State, **65**(7), 92 (2023). <http://dx.doi.org/10.61011/PSS.2023.07.56410.77>
- [10] R.Ya. Rasulov, V.R. Rasulov, M.A. Mamatova, M.Kh. Nasirov, and U.M. Isomaddinova, East European Journal of Physics, (3), 310–315 (2024). <https://doi.org/10.26565/2312-4334-2024-3-33>
- [11] V.R. Rasulov, R.Ya. Rasulov, and I. Eshboltaev, Russ. Phys. J. **63**(11), 2025 (2015). <https://doi.org/10.1007/s11182-021-02265-x>
- [12] V.R. Rasulov, R.Ya. Rasulov, I.M. Eshboltaev, and M.X. Qo'chqorov, Semiconductors, **56**(10), 948 (2022). <http://dx.doi.org/10.21883/SC.2022.10.55023.9798>
- [13] D. Yu, Y.Y. Hu, G. Zhang, W. Li, and Y. Jiang, Scientific Reports, **12**(110), 1 (2022). <https://doi.org/10.1038/s41598-021-04203-w>
- [14] H.S. Pattanaik, M. Reichert, J.B. Khurgin, and D.J. Hagan, IEEE Journal of Quantum Electronics, **52**(3), 90000114 (2016). <https://doi.org/10.1109/JQE.2016.2526611>
- [15] E.L. Ivchenko, and G.E. Pikus, *Superlattices and other heterostructures. Symmetry and optical phenomena*, (Springer, Berlin, (1995).
- [16] E.L. Ivchenko, *Optical spectroscopy of semiconductor nanostructures*, Alpha Science, (Harrow, UK, 2005).
- [17] M.M. Glazov, E.L. Ivchenko, G. Wang, T. Amand, X. Marie, B. Urbaszek, and B.L. Liu, Physica Status Solidi (b), **252**(11), 2349 (2015). <https://doi.org/10.1002/pssb.201552211>
- [18] G. Wang, A. Chernikov, M.M. Glazov, and T.F. Heinz, arXiv:1707.05863v2 (2017). <https://doi.org/10.48550/arXiv.1707.05863>
- [19] S. Shree, I. Paradisanos, X. Marie, C. Robert, and B. Urbaszek, Nature Reviews Physics, **3**(1), 39 (2021). <https://doi.org/10.1038/s42254-020-00259-1>
- [20] R.Ya. Rasulov, V.R. Rasulov, N.U. Kodirov, M.Kh. Nasirov, I.M. Eshboltaev, East European Journal of Physics, (3), 303 (2024). <https://doi.org/10.26565/2312-4334-2024-3-32>
- [21] M. Lafrentz, D. Brunne, B. Kaminski, V.V. Pavlov, A.V. Rodina, R.V. Pisarev, D.R. Yakovlev, et al., Phys. Rev. Lett. **110**, 116402 (2013). <https://doi.org/10.1103/PhysRevLett.110.116402>
- [22] M.V. Durnev, and M.M. Glazov, Physics-Uspekhi, **188**(9), 913 (2018). <https://doi.org/10.3367/UFNe.2017.07.038172>
- [23] L.E. Golub, E.L. Ivchenko, and R.Ya. Rasulov, Physics and Technics of Semiconductors, **29**(6), 1093 (1995). (in Russian)
- [24] R.Ya. Rasulov, V.R. Rasulov, K.K. Urinova, M.A. Mamatova, and B.B. Akhmedov, East Eur. J. Phys. (1), 393 (2024). <https://doi.org/10.26565/2312-4334-2024-1-40>
- [25] U. Isomaddinova, PhD Thesis, Namangan, Republik of Uzbekistan, (2024). (in Russian)

- [26] V.R. Rasulov, R.Y. Rasulov, R.R. Sultonov, and B.B. Akhmedov, "Two- and Three-Photon Linear-Circular Dichroism in Cubic-Symmetry Semiconductors," *Semiconductors*, **54**(11), 1381–1387 (2020). <https://doi.org/10.1134/S1063782620110226>
- [27] V.R. Rasulov, R.Ya. Rasulov, I.M. Eshboltaev, and M.K. Nasirov, *Russian Physics Journal*, **58**(12), 1681–1686 (2015). <https://doi.org/10.1007/s11182-016-0702-2>
- [28] N.V. Leppen, E.L. Ivchenko, and L.E. Golub, *Phys. Rev. B*, **105**, 115306 (2022). <https://doi.org/10.1103/PhysRevB.105.115306>
- [29] D.A. Parshin, and A.R. Shabaev, *ZhETF*, **92**(4), 471 (1987). (in Russian)

ДО ТЕОРІЇ ДВОФОТОННОГО МІЖПІДЗОННОГО ПОГЛИНАННЯ ТА ЛІНІЙНО-ЦИРКУЛЯРНОГО ДИХРОЇЗМУ В НАПІВПРОВІДНИКАХ ТИПУ A_3B_5

Рустам Я. Расулов^a, Воксоб Р. Расулов^a, Фаррух У. Касимов^b, Мардонбек Х. Насіров^{a,c}, Іслам Е. Фарманов^a, Абай З. Турсінбаєв^d

^aФерганський державний університет, Фергана, Узбекистан

^bАндижанський державний університет, Андижан, Узбекистан



^cФерганський державний технічний університет, Фергана, Узбекистан

^dПівденно-Казахстанський університет Муктара Ауезова, Шимкент, Казахстан

У статті досліджуються частотно-температурні залежності ймовірності двофотонного поглинання ($2PA$), зумовленого переходами з гілки легких дірок до підзони спин-орбітального розщеплення, а також лінійно-циркулярного дихроїзму (LCD), пов'язаного з $2PA$, та коефіцієнта двофотонного поглинання світла в напівпровідниках $GaAs$ та $InAs$. Розглянуто вплив ефекту когерентного насичення на поглинання. Проаналізовано роль різних типів переходів, які відрізняються віртуальними станами та беруть участь у $2PA$. У $GaAs$ та $InAs$ виявлено наявність кількох піків у частотно-температурній залежності коефіцієнта $2PA$; поява цих піків пояснюється не лише специфічною зміною функцій розподілу фотоактивованих дірок, а й тим, що при певних значеннях частоти деякі знаменники у виразах для складених матричних елементів прямують до нуля.

Ключові слова: двофотонні оптичні переходи; віртуальні стани; багатифотонні оптичні переходи; коефіцієнт двофотонного поглинання; ефект когерентного насичення; напівпровідник

ON THE THEORY OF INTERBAND TWO-PHOTON ABSORPTION OF LIGHT IN SEMICONDUCTORS. ACCOUNTING ADMIXTURES TO THE STATES OF THE CONDUCTION BAND AND VALENCE STATES, THE RABI EFFECT

 Rustam Y. Rasulov^a,  Voxob R. Rasulov^{a*}, Forrukh U. Kasimov^b, Mardonbek Kh. Nasirov^c,
Islam E. Farmanov^a

^aFergana State University, Fergana, Uzbekistan

^bAndijan State University, Andijan, Uzbekistan

^cFergana State Technical University, Fergana, Uzbekistan

*Corresponding Author e-mail: vrrasulov83@gmail.com

Received January 15, 2024; revised April 10, 2025; accepted April 23, 2025

We present a theoretical study of interband two-photon (two-quantum) absorption of polarized light in semiconductors of cubic and tetrahedral symmetry. Our analysis is conducted within a multiband approximation, taking into account the admixture of valence states in the conduction-band states, as well as coherent saturation (Rabi) effects. We use simplified parabolic dispersion laws for both heavy- and light-hole subbands and for the conduction band, and compare two common temperature-dependent band-gap formulas (Varshni and Passler) to illustrate how they alter the spectral–temperature dependence of the total two-photon absorption coefficient. In particular, we show that the interband two-photon absorption first increases with photon frequency, reaches a maximum, and then decreases at a fixed temperature. The amplitude of the absorption for linearly polarized light is found to be larger than that for circularly polarized light, especially at lower temperatures. Our calculations reveal that the admixture of valence states significantly modifies the interband transitions, while the Rabi effect reduces the absorption in the high-intensity regime, especially at elevated temperatures. These findings may be useful for designing optoelectronic and photonic devices that rely on multiphoton interactions in narrow-gap semiconductors.

Keywords: Two-photon absorption; Rabi effect; Valence–conduction band mixing; Multiband approximation; Kane model; Temperature-dependent band gap; Varshni and Passler formulas; InSb and InAs semiconductors; Nonlinear optics

PACS: 42.65.–k, 78.20.Bh, 71.20.Nr

INTRODUCTION

In this paper, we analyze interband two-photon absorption in semiconductors of cubic and tetrahedral symmetry by employing a multiband $\mathbf{k} \cdot \mathbf{p}$ Kane-type Hamiltonian. Specifically, we consider the conduction band (Γ_6) and the valence bands ((Γ_8) heavy- and light-hole subbands, plus (Γ_7) for spin-orbit split-off). The complete 8×8 Kane model can, in principle, provide non-parabolic dispersion relations for electrons and holes. However, in the moderate energy range relevant to our two-photon absorption processes ($\hbar\omega \lesssim 0.8 E_g$), higher-order k^4 terms make only small corrections.

Therefore, for simplicity and analytic tractability, we adopt the following parabolic dispersions:

$$E_c(\mathbf{k}) = E_g + \frac{\hbar^2 k^2}{2m_c}, E_v(\mathbf{k}) = -\frac{\hbar^2 k^2}{2m_v},$$

where m_c and m_v are effective masses for electrons and holes, respectively. This approximation still incorporates conduction–valence admixture via Kane’s matrix elements (including Δ_{SO}), but neglects higher-order nonparabolic terms beyond k^2 . Extensive prior studies [see, for instance, Refs. 24–26] confirm that, under these conditions, the simpler parabolic form captures the essential physics of two-photon absorption in InSb and InAs.

The Hamiltonian thus includes admixture between Γ_6 , Γ_8 , and Γ_7 states, ensuring that valence-band mixing effects are accounted for. The spin-orbit interaction enters via the splitting Δ_{SO} , which modifies the band-coupling strengths and appears explicitly in our transition-matrix elements. In Section 3, we derive the two-photon absorption coefficients $K_{c,m;L,m'}^{(2)}$ under this model and discuss how the Rabi effect further alters the absorption in both low- and high-temperature regimes.

The discovery of powerful quantum generators of coherent laser electromagnetic waves stimulated the development of studies of optical phenomena in semiconductors that are nonlinear in illumination intensity [1–3]. In this aspect, it seems necessary to study the nonlinear optical parameters of both narrow- and wide-bandgap semiconductors. It is associated with the unusualness and complexity of the properties of the effect under consideration, the possibility of obtaining new information about the band parameters of the samples under study, and the prospect of application in optoelectronics and photonics.

Two-photon nonlinear optical phenomena caused by intraband transitions in semiconductors were carried out [1–3], where the calculation of two-photon matrix elements was carried out using perturbation theory for the field of an unpolarized electromagnetic wave in the two-band approximation [2, 3]. In [4–7], two- and three-photon linear-circular dichroism (LCD) were studied, and in [8–23], multiphoton intraband absorption of light of linear and circular polarization in semiconductors with a complex band structure was investigated. In [18], nonlinear single-photon absorption of polarized radiation in topological insulators was investigated.

In the above-mentioned works, the nonlinearity of the coefficient of single-photon absorption of light is described by the effect of coherent saturation (Rabi) [19] and it is determined both in intra-band [18] and interband [9, 10, 16, 17] optical transitions by the photoinduced addition to the distribution function of electrons, as well as light and heavy holes.

However, in the above-mentioned works, calculations were made of the spectral-polarization dependences of the intraband two-photon, i.e. two-quantum absorption of light (TQAL) and its LCD in semiconductors of tetrahedral symmetry. in Kane's three-zone model [24, 25], but not taken into account mixing of valence band states with conduction band states. This paper is devoted to filling this gap.

SPECTRAL-TEMPERATURE DEPENDENCES OF THE COEFFICIENT OF INTERBAND TWO-QUANTUM ABSORPTION OF LIGHT

Note that the coefficient of two-photon (quantum) absorption of light for optical transitions from the valence band to the conduction band is determined by the expression [23]

$$K^{(2)} = \sum_{\vec{k}, c, m=\pm 1/2; L, m'} K_{c, m; L, m'}^{(2)} = \sum_{\vec{k}, c, m=\pm 1/2; lh, m'=\pm 1/2} K_{c, m; lh, m'}^{(2)} + \sum_{\vec{k}, c, m=\pm 1/2; lh, m'=\pm 3/2} K_{c, m; hh, m'}^{(2)}. \quad (1)$$

Here

$$\sum_{\vec{k}, c, m=\pm 1/2; L, m'} K_{c, m; L, m'}^{(2)} = \frac{2\pi 2\hbar\omega}{\hbar} \sum_{\vec{k}, c, m=\pm 1/2; L, m'} \left(f_{c\vec{k}}^{(2)} - f_{L, \vec{k}}^{(2)} \right) \left| M_{c, m; L, m'}^{(2)}(\vec{k}) \right|^2 \delta(E_{c\vec{k}} - E_{L, \vec{k}} - 2\hbar\omega) \quad (2)$$

($L, m' = lh, m' = \pm 1/2$ ($hh, m' = \pm 3/2$)-for heavy (light) holes), where their energy spectrum has the form $E_{L, \vec{k}} = -\frac{\hbar^2 k^2}{(2m_L)}$, and the energy spectrum of electrons in the conduction band: $E_{c, \vec{k}} = E_g + \frac{\hbar^2 k^2}{(2m_c)}$.

If we take into account that the composite matrix of the two-quantum interband optical transition $M_{L, \vec{k}; SO, \vec{k}}^{(2)}$ in expression (2) depends on the inclusion of valence states $\Gamma 8$ (valence band) and $\Gamma 7$ (spin-orbit splitting band) in the states $\Gamma 6$ (conduction band), then we have the following expression

$$M_{lh, \vec{k}; c, \vec{k}}^{(2)} = \frac{1}{3} \left(\frac{eA_0}{\hbar} \right)^4 \frac{|p_{c, V}|^2 \hbar^2 k^2}{(\hbar\omega)^2} \left[\left(1 - \frac{4}{3} \zeta_g \right)^2 e_z'^4 - \left(\frac{\hbar\omega \zeta_g}{E_{hh} - E_{lh} - \hbar\omega} \right)^2 |e_{\perp}'|^4 \right], \quad (3)$$

$$M_{hh, \vec{k}; c, \vec{k}}^{(2)} = 3 \left(\frac{eA_0}{\hbar} \right)^4 \frac{|p_{c, V}|^2 \hbar^2 k^2}{(\hbar\omega)^2} \left(1 + \frac{2}{3} \frac{\hbar\omega \zeta_g}{E_{lh} - E_{hh} - \hbar\omega} \right)^2 e_z'^2 e_{\perp}'^2, \quad (4)$$

then the coefficient of two-quantum absorption of light caused by optical transitions from the subband of light holes to the conduction band is expressed as:

$$\sum_{\vec{k}, c, m=\pm 1/2; lh, m'=\pm 1/2} K_{c, m; lh, m'}^{(2)} = \frac{2}{3} C_I \left(f_{c, k_{cL}}^{(2)} - f_{lh, k_{cL}}^{(2)} \right) \frac{|p_{c, V}|^2 (k_{cL}^{(\omega)})^3}{(\hbar\omega)^5} \mu_+^{(c, lh)} \left[\left(1 - \frac{4}{3} \zeta_g \right)^2 e_z'^4 - \left(\frac{\hbar\omega \zeta_g}{E_{hh} - E_{lh} - \hbar\omega} \right)^2 |e_{\perp}'|^4 \right], \quad (5)$$

and for optical transitions from the heavy hole subband to the conduction band:

$$\sum_{\vec{k}, c, m=\pm 1/2; lh, m'=\pm 3/2} K_{c, m; hh, m'}^{(2)} = 6C_I \left(f_{c, k_{c, hh}}^{(2)} - f_{lh, k_{c, hh}}^{(2)} \right) \frac{|p_{c, V}|^2 (k_{c, hh}^{(\omega)})^3}{(\hbar\omega)^5} \mu_+^{(c, hh)} \left(1 + \frac{2}{3} \frac{\hbar\omega \zeta_g}{E_{lh} - E_{hh} - \hbar\omega} \right)^2, \quad (6)$$

Where $C_I = \frac{1}{\pi \hbar^3} \left(\frac{2\pi e^2}{\hbar n_{\omega} c} \right)^2 I \left(\frac{\hbar^2}{m_0} \right)^2$, $k_{c, L}^{(\omega)} = \sqrt{\frac{2\mu_+^{(c, L)}}{\hbar^2} (2\hbar\omega - E_g)}$, $L, m' = lh, m' = \pm 1/2$ ($hh, m' = \pm 3/2$)- for heavy (light) holes and took into account that $\left(\frac{eA_0}{\hbar} \right)^2 = \frac{2\pi e^2}{n_{\omega} c} \frac{I}{(\hbar\omega)^2}$, $I(\omega)$ is the intensity (frequency) of light, n_{ω} is the refractive index of light at frequency ω , $p_{c, V} = \left(\frac{3Bm_0^2 E_g}{\hbar^2} \right)^{1/2}$ is the Kane parameter, $B = \frac{\hbar^2 (m_{hh} - m_{lh})}{(4m_{hh} m_{lh})}$, m_{hh} (m_{lh}) is the effective mass of light (heavy) holes.

Note that if we take into account the contribution of the coherent saturation effect to $K_{c, m; L, m'}^{(2)}$, then it is necessary to replace in expression (2) $\left| M_{c, m; L, m'}^{(2)}(\vec{k}) \right|^2$ with $\sum_{nn' \vec{k}} \left| M_{n\vec{k}, n' \vec{k}}^{(N=2)} \right|^2 \sum_{nn' \vec{k}} \left[1 + \frac{\alpha_{\omega}}{\hbar^2 \omega^2} \left| M_{n\vec{k}, n' \vec{k}}^{(N=2)} \right| \right]^{-1/2}$. Then the square of the composite matrix element caused by two-photon optical transitions from the light hole subband to the conduction band consists of two terms, which are determined by the relations:

$$\frac{\alpha\omega}{\hbar^2\omega^2} \left| M_{lh,\vec{k};\vec{c}\vec{k}}^{(2)} \right|^2 = \xi^{(2)} \frac{|p_{c,v}^*|^2 k^2}{m_0 \Delta_{SO} k_A^2 \left(\frac{\hbar\omega}{\Delta_{SO}} \right)^6} \left[\left(1 - \frac{4}{3} \zeta_g \right)^2 e_z'^4 - \left(\frac{\hbar\omega \zeta_g}{E_{hh} - E_{lh} - \hbar\omega} \right)^2 |e_\perp'|^4 \right]. \quad (7)$$

$$\frac{\alpha\omega}{\hbar^2\omega^2} \left| M_{lh,\vec{k};\vec{c}\vec{k}}^{(2)} \right|^2 = 3\xi^{(2)} \frac{|p_{c,v}^*|^2 k^2}{m_0 \Delta_{SO} k_A^2 \left(\frac{\hbar\omega}{\Delta_{SO}} \right)^6} \left(1 + \frac{2}{3} \frac{\hbar\omega \zeta_g}{E_{lh} - E_{hh} - \hbar\omega} \right)^2 e_z'^2 e_\perp'^2. \quad (8)$$

Here $k_A^2 = \frac{2m_0}{\hbar^2} \Delta_{SO}$, $\xi^{(2)} = 2T_c^{(1)} T_{lh}^{(1)} \left(\frac{2\pi e^2}{n_0 c \hbar} \right)^2 \frac{\hbar^4 k_A^2}{m_0 \Delta_{SO}^5} I^2$, $T_c^{(1)} (T_{lh}^{(1)})$ is the time of exit from the final state of photoexcited electrons in the conduction band (light holes in the valence band).

Results of calculation of spectral and temperature dependence of the resulting absorption coefficient $K_{c,m;L,m'}^{(2)}$ of linear (line 1) and circular (line 2) polarization light produced according to (1) and (2) taking into account (3) and (4) and caused by vertical optical transitions from the subband of light and heavy holes of the valence band to the conduction band in InSb (a) and InAs (b) crystals are shown in (Fig. 1). In numerical calculations, the maximum value of the absorption coefficient of linearly polarized light was taken as unity, where the temperature dependence of the band gap and the contribution of the coherent saturation effect were not taken into account. Fig. 1 shows that in the region of low frequencies and temperatures, the value increases with increasing frequency and reaches a maximum, and then decreases. Also, the amplitude of the coefficient of two-quantum absorption of $K_{c,m;L,m'}^{(2)}(\omega, T)$ linearly polarized light is approximately 5 times greater than the amplitude of $K_{c,m;L,m'}^{(2)}(\omega, T)$ circular polarization both in InSb (a) and in InAs (b).

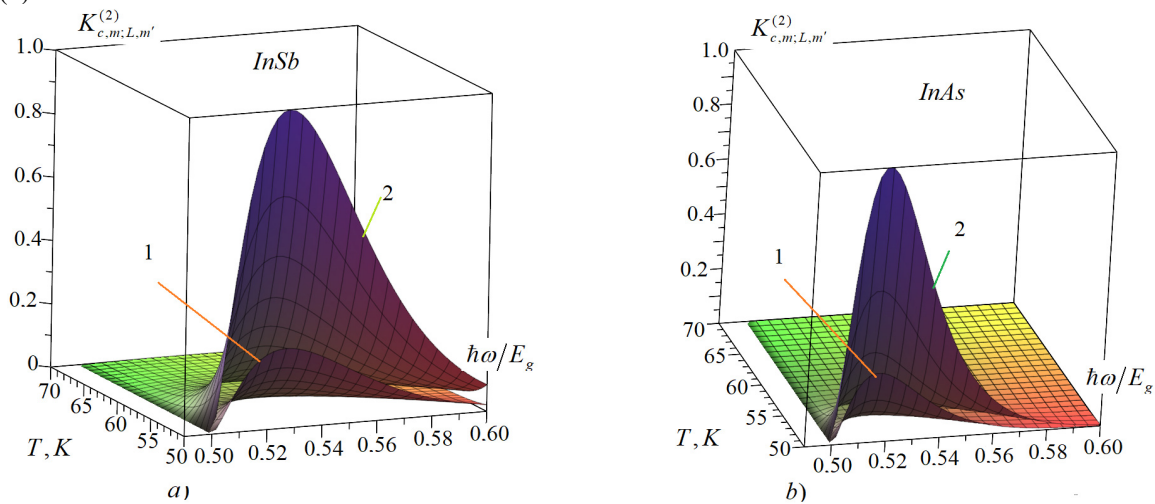


Figure 1. Spectral - temperature dependence $K_{c,m;L,m'}^{(2)}$ for light of linear (line 1) and circular (line 2) polarization in InSb (a) and InAs (b) crystals. In the calculations, the maximum value of the absorption coefficient of linearly polarized light $K_{c,m;L,m'}^{(2)}$ was taken as unity. In the numerical calculations, the temperature dependence of the band gap and the contribution of the coherent saturation effect were not taken into account.

In further calculations of the frequency-temperature dependence of the two-photon absorption coefficient, we assume that the temperature dependence of the band gap width is determined by the Varshni formula [26]

$$E_g(T) = E_g(T = 0) - \gamma_T \frac{T^2}{T + T_V} \quad (9)$$

here constants γ_T and T_V are material-dependent empirical parameters. Specifically, γ_T controls the rate at which the band gap decreases with increasing temperature, while T_V is a characteristic offset temperature that fine-tunes the shape of the denominator in the $T^2/(T + T_V)$ term. Passler's formula [27]

$$E_g(T) = E_g(T = 0) - \frac{\alpha\theta_p}{2} \left[\left(1 + \left(\frac{2T}{\theta_p} \right)^p \right)^{1/p} - 1 \right]. \quad (10)$$

Here, α is an empirical coefficient controlling the band-gap shrinkage rate, θ_p is a characteristic phonon-like temperature scale, and p is an exponent that shapes the functional form of the band-gap temperature dependence. Their values can be found through experimental data or taken from the literature for specific materials such as InSb and InAs [26,27]. The temperature dependences of the effective masses of electrons $m_c(T)$ in the conduction band and holes $m_{so}(T)$ in the spin-orbit splitting zone can be represented as [26]:

$$\frac{m_0}{m_{SO}(T)} = \gamma_1 - \frac{E_p \Delta_{SO}}{3E_g(E_g + \Delta_{SO})} \cdot \frac{m_0}{m_c(T)} = 1 + 2F + \frac{E_p(E_g + 2\Delta_{SO}/3)}{3E_g(E_g + \Delta_{SO})} \quad (11)$$

here F is a dimensionless parameter linked to higher-order non-parabolic corrections in the conduction band; it modifies the usual parabolic dispersion to more accurately reflect the influence of strong band coupling at higher energies. Along with these parameters, the Kane energy E_p and the spin-orbit splitting Δ_{SO} play central roles in describing the band structure within the Kane model. The Kane energy, E_p , originates from the momentum-matrix element between conduction and valence bands; it quantifies the degree of band mixing in narrow-gap semiconductors. A larger E_p generally signals stronger coupling between conduction and valence states, thereby affecting both the effective masses and optical transition probabilities. Meanwhile, the spin-orbit splitting Δ_{SO} represents the energy separation between the topmost valence-band states (often labeled Γ_8) and the spin-orbit split-off band (Γ_7), which arises from relativistic spin-orbit coupling in the crystal. In narrow-gap materials such as InSb and InAs, Δ_{SO} can significantly influence the valence-band structure and, consequently, the optical absorption processes. Numerical values for E_p , Δ_{SO} , F , γ_T and T_V relevant to InSb and InAs are provided in Refs. [25, 26].

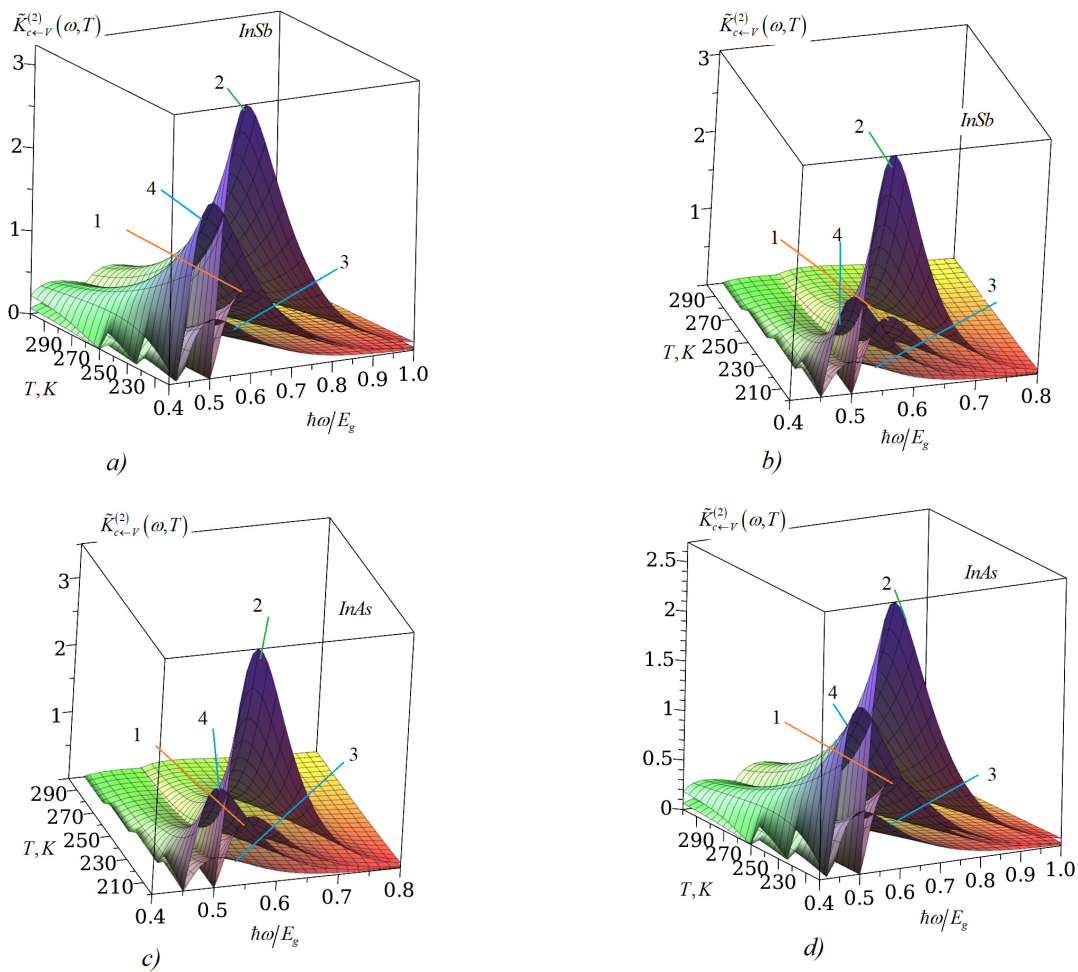


Figure 2. Spectral - temperature dependence of the total coefficient of two-quantum absorption $\tilde{K}_{c,\pm 1/2;hh,\pm 3/2}^{(2)}(\omega, T)$ of light of linear (lines 1 and 3) and circular (lines 2 and 4) polarization, caused by transitions of the heavy-hole subband of the valence band to the conduction band in In Sb (a, b) and InAs (c, d). In Fig. (a and c) the Rabi coefficient is 0.5, and in Fig. (b) and (d) is equal to 0.7

Figure 2 shows the spectral-temperature dependence of the total coefficient of two-quantum absorption of light $\tilde{K}_{c,\pm 1/2;hh,\pm 3/2}^{(2)}(\omega, T)$ of linear (lines 1 and 3) and circular (lines 2 and 4) polarization, caused by transitions from the subbands of light and heavy holes of the valence band to the conduction band in InAs (a,b) and InAs (c,d). Here $\tilde{K}_{c,\pm 1/2;hh,\pm 3/2}^{(2)}(\omega, T)$ ($K_{c,\pm 1/2;hh,\pm 3/2}^{(2)}(\omega, T)$) - the coefficient of two-photon absorption in the case when the temperature dependence of the band parameters is taken into account (not taken into account). In the calculations, the maximum value $\tilde{K}_{c,\pm 1/2;hh,\pm 3/2}^{(2)}(\omega, T)$ for linearly polarized light was taken as one unit. In Fig. 2 (a and c), the Rabi coefficient is equal to 0.5, and in Fig. 2 (b and d) is equal to 0.7. Graphs 1 and 2 are calculated using formula (9), and 3 and 4 using (10), respectively. From Fig. 2 it is evident that dependence (9) significantly affects the amplitude value of the temperature

dependence $\tilde{K}_{c,\pm 1/2;hh,\pm 3/2}^{(2)}(\omega, T)$ than (10), and the light absorption edge shifts by frequency $\omega_T^{(V)}(T) = \frac{\gamma T}{\hbar} \frac{T^2}{T+T_V}$ when choosing (9), by $\omega_T^{(P)}(T) = \frac{\alpha \theta_p}{2\hbar} \left[\left(1 + \left(\frac{2T}{\theta_p} \right)^p \right)^{1/p} - 1 \right]$ when choosing (10). Note also that regardless of the frequency of light, with an increase in the Rabi coefficient $\tilde{K}_{c,\pm 1/2;hh,\pm 3/2}^{(2)}(\omega, T)$ in InSb it is unnoticeable, but in InAs it decreases noticeably in the high temperature region, and in the low temperature region it is the opposite, which is associated with the complexity of the temperature dependence $\tilde{K}_{c,\pm 1/2;hh,\pm 3/2}^{(2)}(\omega, T)$.

CONCLUSIONS

We have presented a theoretical study of interband two-photon (two-quantum) absorption in cubic and tetrahedral semiconductors by incorporating valence-band admixture to conduction-band states and the coherent saturation (Rabi) effect within a multiband approximation. By employing parabolic dispersion laws that emerge from the full 8×8 Kane-type Hamiltonian (truncated to second order in \mathbf{k} for moderate photon energies $\hbar\omega \lesssim 0.8 E_g$), we have derived analytic expressions for the two-photon absorption coefficients of both linearly and circularly polarized light. To capture the material's temperature dependence, we have implemented both the Varshni and Passler formulas for the band-gap evolution, showing how these choices shift the absorption edges and alter amplitude values in InSb and InAs. The interplay between valence admixture and the spin-orbit-split Γ_7 band leads to nontrivial differences in the relative contributions from heavy- and light-hole subbands, while the Rabi effect suppresses absorption at high intensities, especially at elevated temperatures.

The novelty of this study lies in the combined treatment of valence-conduction admixture and coherent saturation in narrow-gap semiconductors, highlighting how each mechanism modifies the spectral-temperature dependence of two-photon absorption. Our results reveal that, under low-temperature conditions, the amplitude of two-photon absorption can be substantially enhanced for linearly polarized radiation compared to circular polarization, whereas at higher temperatures, the suppression from the Rabi effect becomes more pronounced. We further find that the choice of temperature-dependent gap formula (Varshni or Passler) significantly influences absorption peaks in the photon-frequency domain. These findings may guide future experimental work on multiphoton processes in narrow-gap materials and aid in the design of optoelectronic or photonic devices where higher-order absorption processes are crucial.

ORCID

✉ Rustam Y. Rasulov, <https://orcid.org/0000-0002-5512-0654>; ✉ Voxob R. Rasulov, <https://orcid.org/0000-0001-5255-5612>

REFERENCES

- [1] S. Krishnamurthy, Z.G. Yu, L.P. Gonzalez, and S. Guha, "Temperature and wavelength-dependent two-photon and free-carrier absorption in GaAs, InP, GaInAs, and InAsP," *J. Appl. Phys.* **109**, 033102 (2011). <https://doi.org/10.1063/1.3533775>
- [2] C.M. Cirloganu, L.A. Padilha, D.A. Fishman, S. Webster, D.J. Hagan, and E.W. Van Stryland, "Extremely nondegenerate two-photon absorption in direct-gap semiconductors [Invited]," *Opt. Express*, **19**, 22951-22960 (2011). <https://doi.org/10.1364/OE.19.022951>
- [3] C.M. Cirloganu, D.A. Fishman, S. Webster, L.A. Padilha, M. Monroe, D.J. Hagan, and E.W. Van Stryland, "Extremely Nondegenerate Two-Photon Detection of Sub-Bandgap Pulses," in: *Proceedings of the International Quantum Electronics Conference and Conference on Lasers and Electro-Optics Pacific Rim 2011*, (Optica Publishing Group, 2011), paper I1004.
- [4] R.Ya. Rasulov, V.R. Rasulov, and I. Eshboltaev, "On the theory of the ballistic linear photovoltaic effect in semiconductors of tetrahedral symmetry under two-photon absorption," *Russ. Phys. J.* **59**, 446-455 (2016). <https://doi.org/10.1007/s11182-016-0793-9>
- [5] S.B. Arifzhanov, A.M. Danishevsky, E.L. Ivchenko, S.F. Kochegarov, and V.K. Subashiev, "Role of the various types of transitions in three-photon absorption in InAs," *Sov. Phys. JETP*, **47**, 88 (1978). http://www.jetp.ras.ru/cgi-bin/dn/e_047_01_0088.pdf
- [6] R.Ya. Rasulov, Yu.E. Salenko, T. Éski, and A. Tukhtamatov, "Linear circular dichroism in nonlinear absorption of light in a quantum well," *Phys. Solid State* **40**, 1225-1227 (1998). <https://doi.org/10.1134/1.1130526>
- [7] S.B. Arifzhanov, A.M. Danishevsky, and E.L. Ivchenko, *Sov. Phys. JETP*, **74**, 172 (1978). http://www.jetp.ras.ru/cgi-bin/dn/e_047_01_0088.pdf
- [8] S. Benis, C.M. Cirloganu, N. Cox, T. Ensley, H. Hu, G. Nootz, P.D. Olszak, et al., "Three-photon absorption spectra and bandgap scaling in direct-gap semiconductors," *Optica*, **7**, 888-899 (2020). <https://doi.org/10.1364/OPTICA.396056>
- [9] D.C. Hutchings, and E.W. Van Stryland, "Nondegenerate two-photon absorption in zinc blende semiconductors," *J. Opt. Soc. Am. B*, **9**, 2065 (1992). <https://doi.org/10.1364/JOSAB.9.002065>
- [10] R.Ya. Rasulov, D.Sc. Thesis, "Polarization optical photovoltaic effects in semiconductors with linear and nonlinear absorption of light," Ioffe Institute, St. Petersburg, 1993. (in Russian)
- [11] A. Hayat, P. Ginzburg, and M. Orenstein, "Observation of two-photon emission from semiconductors," *Nat. Photonics*, **2**, 238-241 (2008). <https://doi.org/10.1038/nphoton.2008.28>
- [12] R.Ya. Rasulov, V.R. Rasulov, B.B. Akhmedov, I.A. Muminov, and K.K. Urinova, "Dimensional quantization in InSb and GaAs in three-zone model," *J. Phys. Conf. Ser.* **2697**, 012005 (2024). <https://doi.org/10.1088/1742-6596/2697/1/012005>
- [13] R.Ya. Rasulov, V.R. Rasulov, M.X. Nasirov, B.B. Akhmedov, and K.K. Urinova, "To the theory of multi-photon interband linear-circular dichroism in monoatomic layers of dichalcogenide metals," *AIP Conf. Proc.* **3268**, 030001 (2025). <https://doi.org/10.1063/5.0257255>

- [14] P.D. Olszak, C.M. Cirloganu, S. Webster, L.A. Padilha, S. Guha, L.P. Gonzalez, S. Krishnamurthy, *et al.*, "Spectral and temperature dependence of two-photon and free-carrier absorption in InSb," *Phys. Rev. B*, **82**, 235207 (2010). <https://doi.org/10.1103/PhysRevB.82.235207>
- [15] B.B. Akhmedov, "Nonlinear polarization optical phenomena and dimensional quantization in narrow-band crystals," Ph.D. Thesis, Fergana State University, Fergana, Republic of Uzbekistan, 2020. (in Russian)
- [16] I.M. Eshboltaev, "Theoretical studies of multiphoton absorption and shear photogalvanic effect in three- and two- dimensional electron systems," Ph.D. Thesis, Fergana State University, Fergana, Republic of Uzbekistan, 2018. (in Russian)
- [17] R.R. Sultonov, "Nonlinear absorption of light, two-photon ballistic current and size quantization in piezoelectrics," D.Sc. Thesis, Fergana State University, Fergana, Republic of Uzbekistan, 2020. (in Russian)
- [18] N.V. Leppen, E.L. Ivchenko, and L.E. Golub, "Spin noise spectroscopy of localized electrons and nuclei," *Phys. Rev. B*, **105**, 115306 (2022). <https://doi.org/10.1103/PhysRevB.105.115306>
- [19] D.A. Parshin, and A.R. Shabaev, "Theory of linear IR absorption by semiconductors with degenerate bands," *Sov. Phys. JETP* **65**, 827 (1987). http://jetp.ras.ru/cgi-bin/dn/e_065_04_0827.pdf
- [20] J.-Y. You, B. Gu, S. Maekawa, and G. Su, "Microscopic mechanism of high-temperature ferromagnetism in Fe, Mn, and Cr-doped InSb, InAs, and GaSb magnetic semiconductors," *Phys. Rev. B*, **102**, 094432 (2020). <https://doi.org/10.1103/PhysRevB.102.094432>
- [21] B.K. Hamed, "Multi photon absorption processes induced by ultra-fast light pulses," Ph.D. Thesis, Freie Universität Berlin, 2015.
- [22] V.R. Rasulov, R.Ya. Rasulov, N.U. Kodirov, and U.M. Isomaddinova, "Interband one photon absorption of light and its linear-circular dichroism in crystals with coherent saturation effect included," *Phys. Solid State*, **65**, 1173-1179 (2023). <https://doi.org/10.6101/PSS.2023.07.56410.77>
- [23] R.Y. Rasulov, V.R. Rasulov, M.K. Kuchkarov, *et al.*, "Interband Multiphoton Absorption of Polarized Radiation and Its Linear Circular Dichroism in Semiconductors in the Kane Approximation," *Russ. Phys. J.* **65**, 1746-1754 (2023). <https://doi.org/10.1007/s11182-023-02825-3>
- [24] G.L. Bir, and G.E. Pikus, *Symmetry and Strain-Induced Effects in Semiconductors* (Wiley, New York, 1974).
- [25] E.L. Ivchenko, and R.Ya. Rasulov, *Symmetry and Real Band Structure of Semiconductors* (Fan, Tashkent, 1989). (in Russian)
- [26] Vurgaftman, J.R. Meyer, and L.R. Ram-Mohan, "Band parameters for III-V compound semiconductors and their alloys," *J. Appl. Phys.* **89**, 5815-5875 (2001). <https://doi.org/10.1063/1.1368156>
- [27] R. Pässler, "Parameter Sets Due to Fittings of the Temperature Dependencies of Fundamental Bandgaps in Semiconductors," *Phys. Status Solidi B*, **216**, 975 (1999). [https://doi.org/10.1002/\(SICI\)1521-3951\(199912\)216:2%3C975::AID-PSSB975%3E3.0.CO;2-N](https://doi.org/10.1002/(SICI)1521-3951(199912)216:2%3C975::AID-PSSB975%3E3.0.CO;2-N)

**ДО ТЕОРІЇ МІЖЗОННОГО ДВОФОТОННОГО ПОГЛИНАННЯ СВІТЛА В НАПІВПРОВІДНИКАХ:
ВРАХУВАННЯ ЗМІШАННЯ СТАНІВ ПРОВІДНОСТІ ТА ВАЛЕНТНИХ СТАНІВ, ЕФЕКТ РАБІ**
Рустам Ю. Расулов^a, Воксоб Р. Расулов^{a*}, Фаррух У. Касимов^b, Мардонбек Х. Насіров^c, Іслам Е. Фарманов^a

^aФерганський державний університет, Фергана, Узбекистан

^bАндижанський державний університет, Андижан, Узбекистан

^cФерганський державний технічний університет, Фергана, Узбекистан

Ми представляємо теоретичне дослідження міжзонного двофотонного (двоквантового) поглинання поляризованого світла в напівпровідниках з кубічною та тетраедричною симетрією. Наш аналіз здійснюється в рамках багатозонного наближення з урахуванням змішування валентних станів у станах зони провідності, а також когерентних насичувальних (ефект Рабі) процесів. Ми використовуємо спрощені параболічні закони дисперсії для важких та легких дірок, а також для зони провідності, і порівнюємо дві поширені температурно-залежні формули ширини забороненої зони (Варшні та Песслера), щоб показати, як вони змінюють спектрально-температурну залежність загального коефіцієнта двофотонного поглинання. Зокрема, показано, що міжзонне двофотонне поглинання спочатку зростає з частотою фотона, досягає максимуму, а потім зменшується при фіксованій температурі. Встановлено, що амплітуда поглинання для лінійно поляризованого світла вища, ніж для кругової поляризації, особливо при низьких температурах. Наші розрахунки показують, що змішування валентних станів суттєво змінює міжзонні переходи, у той час як ефект Рабі зменшує поглинання в режимі високої інтенсивності, особливо при підвищених температурах. Отримані результати можуть бути корисними при проєктуванні оптоелектронних та фотонних пристроїв, що базуються на багатофотонній взаємодії в вузькозонних напівпровідниках.

Ключові слова: двофотонне поглинання; ефект Рабі; змішування валентної та провідної зон; багатозонне наближення; модель Кейна; температурно-залежна ширина забороненої зони; формули Варшні та Песслера; напівпровідники InSb та InAs; нелінійна оптика

INVESTIGATION OF Ar^+ IONS SCATTERING FROM THE SURFACE OF $\text{CdTe}(001) \langle 110 \rangle$ AT THE GLANCING INCIDENCE

Sh.R. Sadullaev^{a*}, Uchkun O. Kutliev^a, A.Yu. Saidova^a, G.O. Jumanazarov^a, R.R. Ruzmetov^b

^aUrgench State University named after Abu Raykhan Beruni, Department of Physics,
Khamid Olimjan street.14, Urgench 220100, Uzbekistan

^bMilitary-academically lyceum named after Jaloliddin Manguberdi, Urgench 220100, Uzbekistan

*Corresponding Author e-mail: sadullayev.sh.r@gmail.com

Received January 27, 2025; revised April 3, 2025; accepted April 28, 2025

This article presents the results of ion scattering from the surface of a thin film of $\text{CdTe}(001) \langle 110 \rangle$, obtained using ion stripping spectroscopy. The trajectories of scattered Ar^+ ions were obtained and analyzed, with an initial energy of 1 keV and at angles of incidence $\psi = 3^\circ$ and 7° . It is shown that the trajectories of scattered ions from the surface atomic row, from the wall of the semichannel and from the bottom of the semichannel differ from each other. The first trajectories of scattered ions from a surface semichannel consisting of five Cd and Te atoms arranged layer-by-layer in two layers were obtained. The shapes of these three types of trajectories are discussed and the energies, scattering coefficients, and inelastic energy losses of the scattered ions are calculated. It is shown that the energy values, scattering coefficient and inelastic energy losses of scattered ions from surface atomic rows differ little from each other. For ions scattered from the wall of the semichannel and from the bottom of the semichannel, the values of these parameters lie in the range.

Keywords: Computer simulation; Ion scattering; Semichannel; Trajectory scattered ions

PACS: 34.35.+a, 68.49.Sf, 79.20.Rf

INTRODUCTIONS

The use of ion probing is one of many available methods for studying surfaces. And it provides a wide range of energies and the ability to obtain information about composition and structure, using many equipment. One of the methods is the ion scattering spectroscopy method. The range of energies used in ion scattering is usually divided into three parts. Low energy ion scattering (LEIS, energies 500–10 keV), intermediate energy ion scattering (MEIS, 10–600 keV) and high energy ion scattering (HEIS, >1 MeV), these definitions have never been rigid. Ion scattering research did not become widespread until the early fifties of the last century and was concentrated mainly in the HEIS energy region. These studies tested the two-body collision model and found it to be applicable and ultimately led to the development of Rutherford backscattering (RBS). Lower energies were carried out in the late fifties of the last century [1–4], which found that the maximum energy of scattered ions corresponds to the prediction of the classical model of successive collisions. This was followed by the development of this line of research, which applied this method to the analysis of the elemental composition in the outermost monolayer, this led to a rapid increase in the number of studies on ion scattering. There is currently active research into many aspects of ion scattering, such as ion neutralization and the effects of different work functions or the determination of the universal scattering potential [5–9], and there is considerable interest in its application to the determination of surface structures.

It is known that CdTe thin films belong to $\text{A}^{\text{II}}\text{B}^{\text{VI}}$ semiconductor compounds, which. And also, CdTe -based solar cells attract attention because CdTe is characterized by direct energy band gap E_g and high absorption coefficient, which makes CdTe an excellent light-absorbing layer of solar cells. Therefore, obtaining and studying CdTe films is of great interest. And this work presents the results of studying the CdTe surface using the ion scattering spectroscopy method.

RESEARCH METHOD AND RESULTS

In the region of medium energies, the trajectories of colliding particles are determined to a first approximation by the forces of elastic interaction of atoms. These forces arise from the Coulomb forces of interaction between nuclei and electron atoms and, therefore, act at any distance between the interacting particles. Consequently, to calculate the trajectory of an incident ion, it is necessary to consider its interaction in the crystal lattice with all atoms simultaneously, which is very difficult. But at not very low energies, ion – atom collisions can be considered as isolated pair collisions of particles. Confirmation that the lattice atoms are free during collisions, i.e. behave like atoms of a dense gas, are the results of a study of the interaction time and energy of colliding particles [10–14].

In the pair collision approximation model, it appears that a particle of mass M_1 with atomic number Z_1 , with speed v_0 (and kinetic energy E_0), collides with a stationary target atom of mass M_2 and atomic number Z_2 . As a result of interaction, the incident particle is scattered in the laboratory coordinate system at an angle θ_{ofl} relative to the direction of its initial motion. In this case, the target atom as a result of the collision begins to move in a direction that makes an angle of θ_2 with

the initial direction of the incident particle. Applying the law of conservation of energy and momentum to an elementary act of interaction, we obtain for energy E_1 scattered particle the following relationship:

$$E_1 = (1 + \mu)^{-2} E_0 (\cos \theta_1 \pm \sqrt{(f\mu)^2 - \sin^2 \theta_1})^2$$

For the particles, interaction description the Ziegler – Biersack – Littmark (ZBL) potential [15] with regard to the time integral was used. The ZBL approximation for the screening function in the Thomas – Fermi potential takes into account the exchange and correlation energies and the so-called “universal” potential, obtained in this way shows good agreement with experiment over a wide range of interatomic separations. To estimate the in elastic energy loss in an elementary collision event, we used the Firsov formula modified by Kishinevsky [16].

In Fig.1. a semichannel formed on the surface of CdTe(001) <110> and a diagram of ion scattering from this semichannel are presented. The depth and width of the semichannel are 2.28Å and 4.64Å, respectively. Here ψ is the incidence angle, φ is the azimuthal scattering angle, and σ is the polar scattering angle. In our calculations, the aiming point is a is divided into coordinates I and J, which presented on the Fig.1. It should be noted that with increasing coordinates I we cover the entire width of the semichannel. Due to the symmetry of the semichannel, it is enough for us to use I/2 in our calculations, since we can symmetrically cover the entire width of the semichannel. Kinematics of the elementary act of collision of two particles within the framework of classical mechanics, making it possible to establish a connection between the characteristics of particles before and after the collision. Velocity (energy) of an incident ion with mass m_1 after the collision were determined by the laws of conservation of momentum and energy.

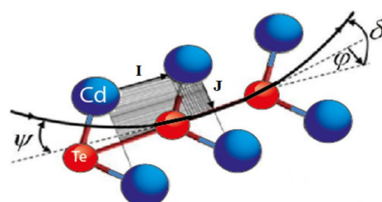


Figure 1. Semichannel and ion scattering scheme

In Fig. 2. a semichannel on the CdTe(001) <110> surface and the trajectories of scattered Ar⁺ ions after bombardment at grazing angles are presented. In the calculations, the angle of incidence was $\psi=3^\circ$ and 7° , and the initial energy was 1 keV. In Fig. 2. the trajectories of scattered ions at $\psi=3^\circ$ are presented. At first glance, one can see different trajectories of the scattered ion. Some of them end inside the semichannel and this shows that ions are implanted inside the crystal. It should be noted that reflections from the surface atom and the bottom atom of the semichannel are clearly visible. To understand the whole picture of the ion scattering process, we divide these trajectories into 3 groups. The first are the trajectories of scattered ions from the surface atomic row (1), second – from the wall of the surface atomic semichannel (2), and the third – from the bottom of the semichannel (3). The figure also shows that in these three areas there are stepped dense areas (7 pieces). Calculations have shown that dense areas are formed due to parallel trajectories, i.e., the trajectory incident and reflected particles do not diverge. Such trajectories can be observed in the three groups mentioned above. These three trajectory groups are shown separately in Fig. 3.

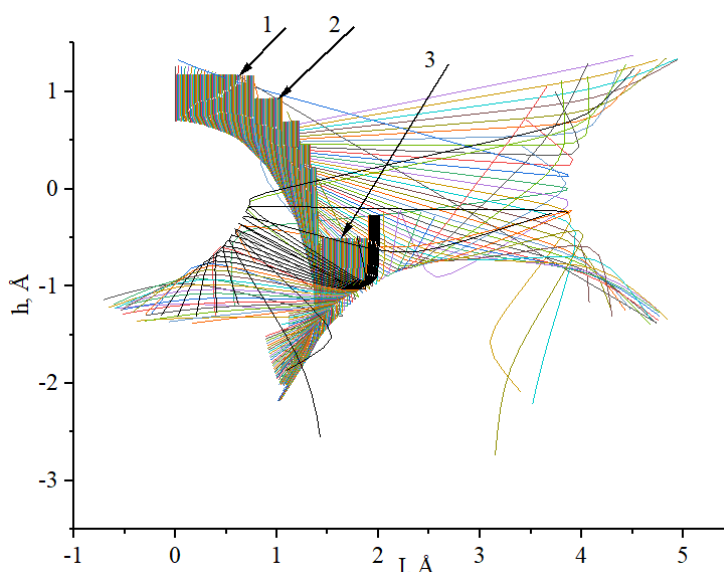


Figure 2. Trajectories of scattered Ar⁺ ions from the surface of CdTe(001) <110> at $\psi=3^\circ$ and $E_0=1$ keV.

Fig. 3a shows the trajectories of ions belonging to the first group, i.e. trajectories of ions scattered from the surface atomic row. It can be seen that at initial values of I , trajectories are observed whose projections of the incident and scattered parts are almost parallel. The parallelism is especially clearly visible when $I = 1$. And starting from $I = 2$, deviations from the original direction occur. It can be seen that further increases in the value of I lead to deviations from the initial direction towards the center of the semichannel. This is explained by the fact that as the value of I increases, the incident ions begin to collide with the edges of the surface atom and change their trajectories towards the center of the semichannel. Early calculations showed that the ions scattered from the surface atomic row have an energy of 991 eV, the scattering coefficient is -7, and the inelastic energy loss is -8 eV. This shows that the bombarding ions will lose about 10% of the initial energy at a grazing angle $\psi=3^\circ$.

In Fig. 3b. some trajectories belonging to group 2 are presented. These trajectories have different shapes. It can be seen that these trajectories also have trajectories in which the incident and reflected parts are similar. These trajectories are formed by scattering of ions from the surface atomic row and the bottom of the semichannel. Therefore, the projection trajectories are curves. And also, trajectories were observed that were not similar to the incident reflected part. This shows that the ion is first scattered from the surface atomic row, and then scattered from the atom located at the bottom of the semichannel and leaves this semichannel. There is also a trajectory similar to a loop (red trajectory). This trajectory is formed due to the scattering of the ion from the surface atomic row, then from the bottom of the hemichannel, and then again from the surface atomic row before exiting the hemichannel. Early calculations showed that ions scattered from the surface atomic row have an energy in the range of 968-980 eV, a scattering coefficient in the range of -14-30, and inelastic energy losses -15-29 eV.

In Fig. 3c. The trajectory of scattered ions belonging to group 3 is presented. It can be seen that the trajectory of the ions has an almost parallel shape to each other. And these ions remained (implanted) inside the crystal and before that were first scattered from the bottom of the semichannel, and then from the surface atom. They have the same physical parameters (energy 981-987 eV, dissipation coefficient -14-16, inelastic energy losses -12-17 eV).

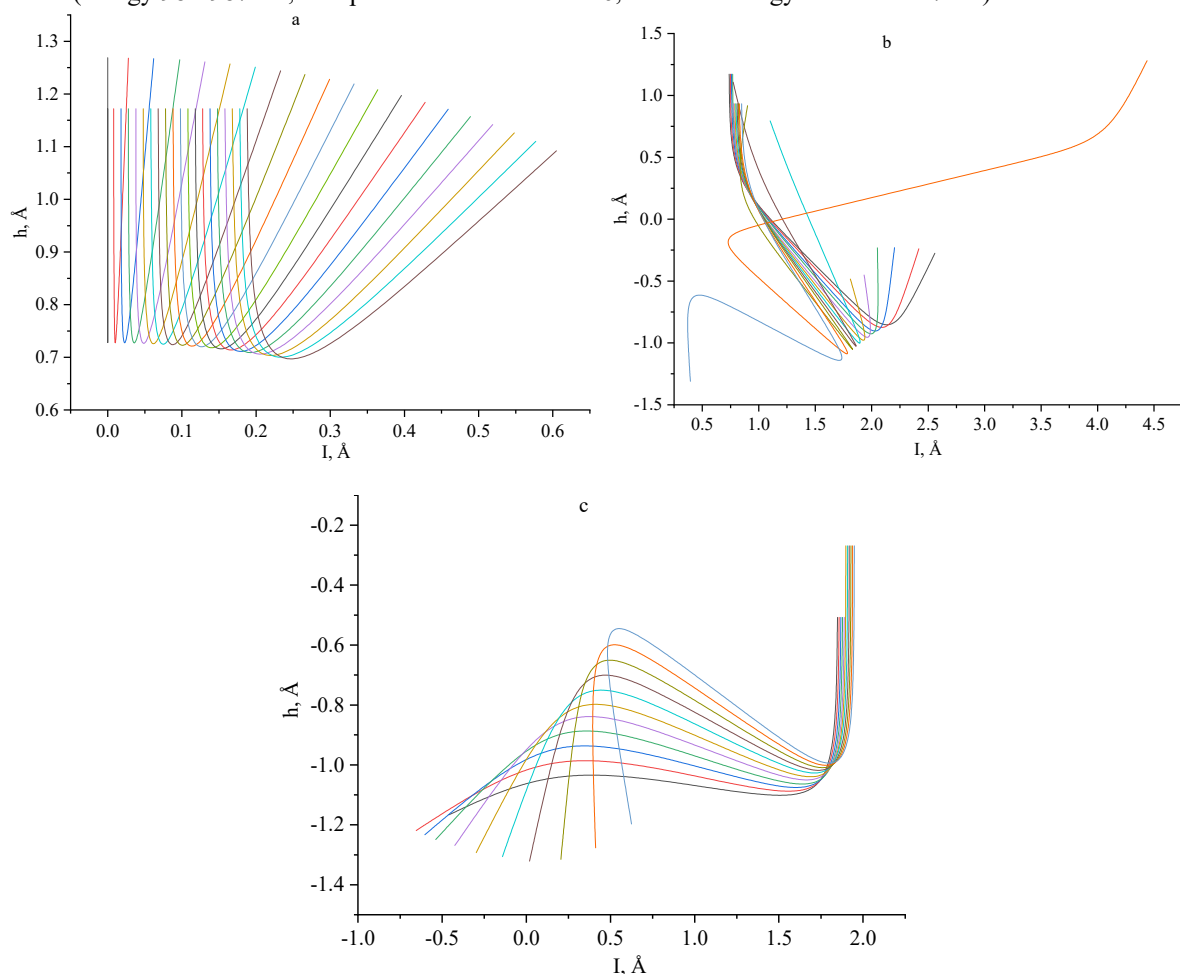


Figure 3. Trajectories of scattered ions from the surface atom (a), from the wall of the semichannel (b) and semichannel (c) of the CdTe(001) <110> surface at $\psi=3^\circ$ and $E_0=1$ keV

We also simulated the trajectory of Ar^+ ions scattered from the surface of CdTe(001) <110> at $\psi = 7^\circ$, with an initial energy of 1 keV (Fig. 4). It can be seen from the figure that the dense areas have become blurred and their step is equal to 3. This indicates that the changes in the reflected part from the incident one have increased. Note that reflections from

the surface atom and the bottom atom of the semichannel became more accurate. It is also clear that at this sliding angle the number of implanted ions has increased.

In Fig. 5a. the trajectories of scattered ions from a surface atom is presented. It can be seen that the steel trajectories were still moving towards the center of the semichannel than at the incidence angle $\psi=3^\circ$ and accordingly the energy of the scattered ions decreased to 959 eV, the collision coefficient was equal to 3, and the inelastic energy loss was -7 eV. In Fig. 5b. the trajectories of scattered ions from group 2 are presented. The difference between these trajectories and the case at $\psi=3^\circ$ is that the upper part narrowed and the lower part became wider. The energy of scattered ions is 935-984 eV, the collision coefficient is 7-12, inelastic energy losses are 15-23 eV. The trajectory of scattered ions from the bottom of the semichannel is shown in Fig. 5c. It can be seen that the ions, scattering from the bottom of the semichannel, were implanted into the crystal. The energy of these ions is -992-995 eV, collision coefficient is 4, inelastic energy losses are 4-6 eV.

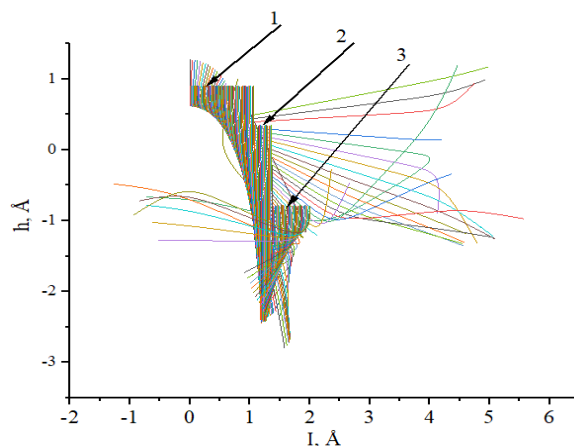


Figure 4. Trajectories of scattered ions from the surface of CdTe(001)<110> at $\psi=7^\circ$ and $E_0=1$ keV

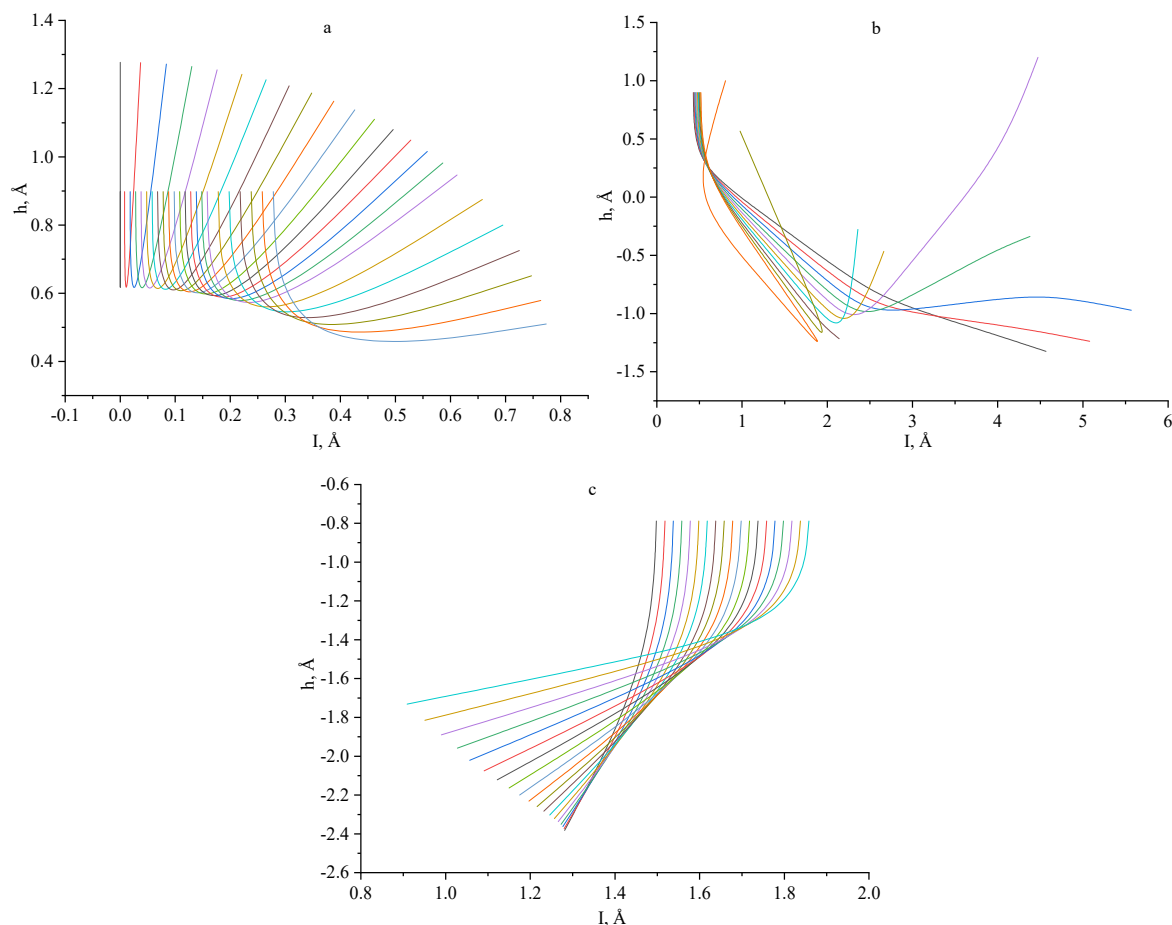


Figure 5. Trajectories of scattered ions from the surface atom (a), from the wall of the semichannel (b) and semichannel (c) of the CdTe(001)<110> surface at $\psi=7^\circ$ and $E_0=1$ keV

CONCLUSIONS

Ar⁺ ions from the surface semichannel formed on the surface of CdTe(001)<110>. Trajectories were obtained at the angle of incidence $\psi = 3^\circ$ and 7° , with an initial energy of 1 keV. The influence of increasing the grazing angle on the trajectory of scattered ions is shown. It has been established that an increase in the angle of incidence of bombarding particles leads to a change in the trajectory of scattered ions. With increasing angle of incidence of ions, the Ar⁺ part of the trajectory that is located inside the semichannel narrows and therefore it becomes clearer to obtain information about the location of the atoms on the surface and bottom of the semichannel. And the trajectories of scattered ions from the surface atom were not subject to change.

ORCID

Shuhrat R. Sadullaev, <https://orcid.org/0000-0002-1892-440X>; Uchkun O. Kutliev, <https://orcid.org/0000-0003-2241-2025>

REFERENCES

- [1] H. Brongersma, M. Draxler, M. Deridder, and P. Bauer, "Surface composition analysis by low-energy ion scattering," *Surf. Sci. Rep.* **62**, 63–109 (2007). <https://doi.org/10.1016/j.surfrep.2006.12.002>
- [2] D.R. Baer, and S. Thevuthasan, "Characterization of Thin Films and Coatings, in: Handbook of Deposition Technologies for Films and Coatings," (Third Edition), Chapter 16, edited by P.M. Martin, (William Andrew Publishing, Boston, 2010). pp. 749-864. <https://doi.org/10.1016/B978-0-8155-2031-3.00016-8>
- [3] T. Grehl, E. Niehuis, and H. H. Brongersma, "Surface Microanalysis by Low-Energy Ion Scattering," *Microscopy Today*, **19**(2), 34–38 (2011). <http://dx.doi.org/10.1017/s1551929511000095>.
- [4] D.N. Bernardo, W.A. Ausserer, Y.C. Ling, and G.H. Morrison, "Secondary ion scattering in dark field ion microscopy," *J. Appl. Phys.* **63**, 5638–5646 (1988). <https://doi.org/10.1063/1.340346>
- [5] F. Samavat, B.V. King, and D.J. O'Connor, "Low energy ion scattering," *Surface Review and Letters*, **14**, 31-41 (2007). <https://doi.org/10.1142/S0218625X07009001>
- [6] C.V. Cushman, P. Br ner, J. Zakel, G.H. Major, B.M. Lunt, N.J. Smith, T. Grehl, and M. R. Linford, "Low energy ion scattering (LEIS). A practical introduction to its theory, instrumentation, and applications," *Anal. Methods*, **8**, 3419 (2016). <https://doi.org/10.1039/C6AY00765A>
- [7] D. Primetzhofer, S.N. Markin, J.I. Juaristi, E. Taglauer, and P. Bauer, "Crystal effects in the neutralization of He⁺ ions in the low energy ion scattering regime," *Phys. Rev. Lett.* **100**(21), 213201 (2008). <https://doi.org/10.1103/PhysRevLett.100.213201>
- [8] F. Samavat, B.V. King, and D.J. O'Connor, "Low energy ion scattering," *Surface Review and Letters*, **14**, 31–41 (2007). <https://doi.org/10.1142/S0218625X07009001>
- [9] D.O. Boerma, "Surface physics with low-energy ion scattering," *Nuclear Instruments and Methods in Physics Research Section B: Beam Interactions with Materials and Atoms*, **183**, 73–87 (2001). [http://dx.doi.org/10.1016/S0168-583X\(01\)00311-1](http://dx.doi.org/10.1016/S0168-583X(01)00311-1)
- [10] J.J.C. Geerlings, L.F.Tz. Kwakman, and J. Los, "Local work function effects in the neutralization of alkali ions scattered from cesiated surfaces," *Surface Science*, **184**, 305-318 (1987). [https://doi.org/10.1016/S0039-6028\(87\)80359-X](https://doi.org/10.1016/S0039-6028(87)80359-X)
- [11] R.H. Bergmans, W.J. Huppertz, R.G. van Welzenis, and H.H. Brongersma, "Static low-energy ion scattering," *Nuclear Instruments and Methods in Physics Research Section B: Beam Interactions with Materials and Atoms*, **64**, 584–587 (1992). [http://dx.doi.org/10.1016/0168-583X\(92\)95538-3](http://dx.doi.org/10.1016/0168-583X(92)95538-3)
- [12] Z. Fateen, and I. Azhar, "Indium phosphide nanowires and their applications in optoelectronic devices," in: *2016 Proceedings: Mathematical, Physical and Engineering Sciences*, **472**, 2187 (2016). <https://doi.org/10.1098/rspa.2015.0804>
- [13] M.K. Karimov, U.O. Kutliev, and S.B. Bobojonova, "Investigation of angular spectrum of scattered inert gas ions from the InGaP (001) surface," *Phys. Chem. Solid State*, **22**, 742-745 (2021). <https://doi.org/10.15330/pcss.22.4.742-745>
- [14] U.O. Kutliev, M.U. Otabaev, M.K. Karimov, F.K. Masharipov, and I. Woiciechowski, "Scattering of low-energy Ne⁺ ions from the stepped surface of InGaP (001)<110> at the small angles of incidence," *Physics and Chemistry of Solid State*, **24**, 542-548 (2023). <https://doi.org/10.15330/pcss.24.3.542-548>
- [15] J.F. Ziegler, J.P. Biersack, and U. Littmark, *The stopping and range of ions in solids*, (Pergamon Press, NY, 1985)
- [16] L.M. Kishinevsky, *Izv. Acad. Nauk. Fiz.* **26**, 1410 (1962). (in Russian)

ДОСЛІДЖЕННЯ РОЗСПОВАННЯ ІОНІВ Ar⁺ ВІД ПОВЕРХНІ CdTe(001) <110> ПРИ КОВЗАЮЧОМУ ПАДІННІ

Ш.Р. Садулласв^а, У.О. Кутлієв^а, А.Ю. Саїдова^а, Г.О. Джуманазаров^а, Р.Р. Рузметов^б

^аУргенчський державний університет імені Абу Райхана Беруні, факультет фізики,
вул. Хаміда Олімджана, 14, Ургенч 220100, Узбекистан

^бВійськово-академічний ліцей імені Джалолідіна Мангуберді, Ургенч 220100, Узбекистан

У цій статті наведено результати розсіювання іонів на поверхні тонкої плівки CdTe (001) <110>, отримані за допомогою іонної стріп-спектроскопії. Отримано та проаналізовано траєкторії розсіювання іонів Ar⁺ з початковою енергією 1 кеВ і при кутах падіння $\psi = 3^\circ$ і 7° . Показано, що траєкторії розсіювання іонів від поверхневого ряду атомів, від стінки півканалу і від дна півканалу відрізняються одна від одної. Отримано перші траєкторії розсіювання іонів з поверхневого півканалу, що складається з п'яти атомів Cd і Te, розташованих пошарово в два шари. Обговорюються форми цих трьох типів траєкторій і розраховуються енергії, коефіцієнти розсіювання та непружні втрати енергії розсіювання іонів. Показано, що значення енергії, коефіцієнта розсіювання та непружних втрат енергії розсіювання іонів поверхневими атомними рядами мало відрізняються один від одного. Для іонів, розсіювання від стінки напівканалу та від дна напівканалу, значення цих параметрів лежать в межах діапазону.

Ключові слова: комп'ютерне моделювання; розсіювання іонів; півканальний; траєкторія розсіювання іонів

TUNABLE NEGATIVE DIFFERENTIAL RESISTANCE IN $\text{SnO}_2\text{:Co}$ MEMRISTORS ON p-Si

✉ Jamoliddin X. Murodov^{a,b,*}, ✉ Shavkat U. Yuldashev^b, ✉ Azamat O. Arslanov^c,
Marguba S. Mirkamilova^a, Utkur E. Jurayev^a

^aTashkent State Technical University named after Islam Karimov, Tashkent, Uzbekistan

^bCenter of Nanotechnology Development, National University of Uzbekistan, Tashkent, Uzbekistan

^cNational University of Uzbekistan named after Mirzo Ulugbek, Tashkent, Uzbekistan

*Corresponding Author e-mail: jamoliddinmilliy@gmail.com

Received January 16, 2025; revised March 11, 2025; accepted March 17, 2025

This study investigates the negative differential resistance (NDR) phenomenon in cobalt-doped tin dioxide ($\text{SnO}_2\text{:Co}$) memristors fabricated on p-type silicon substrates. Using ultrasonic spray pyrolysis (USP), crystalline $\text{SnO}_2\text{:Co}$ thin films were deposited on p-Si substrates with a thin native SiO_2 layer. The resulting memristor devices exhibit reproducible bipolar resistive switching between high-resistance (HRS) and low-resistance states (LRS). Key findings include the observation of a distinct NDR region in the current-voltage (I-V) characteristics, specifically in the positive voltage range from approximately +3V to +4V. Within this NDR region, current decreases despite increasing voltage, a characteristic hallmark of this effect. This behavior is attributed to the charge trapping and redistribution within the Co:SnO_2 material. The consistent and reproducible nature of the observed NDR effect suggests the potential of $\text{SnO}_2\text{:Co}$ memristors for applications in advanced memory and switching technologies. This work contributes to the understanding of resistive switching mechanisms in Co-doped SnO_2 thin films, which are promising materials for next-generation memory devices.

Keywords: SnO_2 doped by cobalt; Memristor; Negative differential resistance switching; USP

PACS: 85.50.-n

INTRODUCTION

Resistive switching phenomenon with different performance characteristics have been reported in various materials, including solid electrolyte [1], perovskites [2], organics [3] and binary transition metal oxides [4]. Among those materials, the metal oxides represent with many advantages of low cost, facile sample preparation. As one of the most studied wide bandgap semiconductors, ZnO thin films [5], Mg-ZnO films [6], CuO [7] and nanorods [8] as well as Mn-ZnO films [9] have been reported to shown stable resistive switching behavior.

However, study of the resistive switching property in cobalt-doped SnO_2 is few. It is well known that Co-doped SnO_2 is diluted magnetic semiconductor and is would be of great interesting to realized the resistive switching property. In this work, we demonstrate that 1%-5% cobalt-doped SnO_2 films-based metal-insulator-metal (MIM) structure exhibit reproducible bipolar resistive switching behavior. Building upon this foundation, our study delves deeper into the specific mechanisms and characteristics of resistive switching in cobalt-doped tin dioxide. While prior research has explored the potential of various materials for resistive memory applications, the unique combination of magnetic doping and semiconductor properties in Co-doped SnO_2 presents an opportunity to engineer novel functionalities beyond conventional resistive switching. This includes the potential for achieving tunable switching parameters, enhanced device performance, and even the integration of spin-based functionalities into memristive devices.

A critical aspect of this work is the exploration of the negative differential resistance (NDR) phenomenon exhibited by our Co-doped SnO_2 memristors. NDR, characterized by a decrease in current with an increase in voltage, holds significant promise for applications in low-power logic circuits, oscillators, and neuromorphic computing architectures. This study aims to precisely characterize the NDR behavior, identify the underlying physical processes driving it, and assess its impact on the overall performance of the fabricated devices. We aim to demonstrate that by carefully controlling the doping levels and material processing conditions, the NDR effect can be reliably harnessed for practical applications.

The insights gained from this investigation not only contribute to a better understanding of the fundamental properties of Co-doped SnO_2 but also pave the way for the development of innovative memory and switching devices with improved efficiency and novel functionalities. Our approach aims to bridge the gap between theoretical potential and practical realization, positioning Co-doped SnO_2 as a viable candidate for next-generation electronics.

METHODS

The cobalt doped SnO_2 films were deposited on heavily doped p-type silicon (100) substrates by ultrasonic spray pyrolysis method at ambient atmosphere, as described in details in [8]. All chemical reagents utilized in the present study were of analytical grade and used without further purification. The aqueous solution of tin acetate (0.5 mol/l) and cobalt acetate (0.005 mol/l and 0.001 mol/l) were used as the sources of Sn and Co, respectively. The substrate temperature was set at 450°C and the thickness of $\text{SnO}_2\text{:Co}$ film was about 200 nm. In order to measure the electrical properties of the

SnO₂:Co films, Ag top electrodes of 220 μm in diameter with 100nm thickness were thermally evaporated with a metal shadow mask. The current-voltage (I-V) characteristics of Ag/SnO₂:Co/SiO₂/p-type Si structure were measured by a Keithley 2460 source-measure unit. During the measurement in voltage sweeping mode, the positive bias was defined by the current flowing from the top electrode to bottom electrode, and the negative bias was defined by the opposite direction. To ensure the reliability and reproducibility of our measurements, several steps were taken to standardize the electrical characterization process. The Keithley 2460 source-measure unit was configured to perform voltage sweeps with a step size of 0.05V, while the compliance current limit was set at 10 mA to prevent any irreversible damage to the devices. Prior to each measurement, the system was calibrated to minimize any systematic errors, and the contact resistance between the probe tips and top electrodes was carefully verified. The measurements were conducted at room temperature under ambient atmospheric conditions, without any external illumination, unless stated otherwise. For each sample, I-V curves were recorded at multiple locations to assess the device-to-device variability. Furthermore, for detailed analysis of the switching behavior, including the endurance and retention characteristics of the devices, we performed repeated I-V cycling measurements and monitored the resistance state over time. Endurance tests were conducted by performing multiple voltage sweeps between the set and reset voltages, while retention tests were carried out by monitoring the change in the resistance at a fixed bias voltage. In order to establish the statistical significance of our results, we analyzed data from multiple devices and multiple measurement runs. The data processing and curve plotting were performed using OriginPro software, which allowed for precise determination of device parameters, such as switching thresholds and the negative differential resistance region. A schematic illustration of the device structure is included for clarity (Fig. 1).

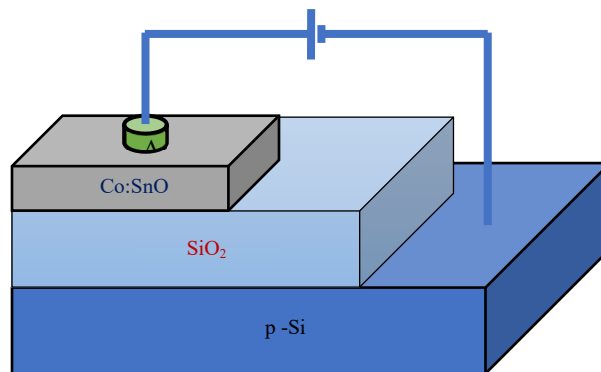


Figure 1. Schematic diagram of the Ag/Co:SnO₂/SiO₂/p-Si-based memristor structure. The top layer consists of a silver (Ag) contact, followed by a cobalt-doped tin oxide (Co:SnO₂) layer. This layer is deposited on a silicon dioxide (SiO₂) insulating layer, which is built on a p-type silicon (p-Si) substrate. The electrical properties of the memristor are studied by applying an external voltage

RESULTS

The current-voltage characteristic of a tin oxide material doped with 1% cobalt, typical of an RRAM device with an Ag/SnO₂:Co/SiO₂/p structure at room temperature (RT), is shown in Figure 2. Starting from 0V, as the voltage is increased in the positive direction, the current begins to increase non-linearly. It reaches a peak current value around 5V before dropping slightly as the voltage starts to decrease. This forms a clearly visible clockwise loop. The shape suggests that the device is switching between different resistance states, a common characteristic in memristive devices. As the voltage is swept negatively, a similar pattern is seen. The material initially has very low current, almost zero, until the voltage goes more negative than -3 V. At this point, the current suddenly increases sharply negatively. This abrupt change in current indicates that the device exhibits bipolar resistive switching behavior.

The Fig.3 shows the current-voltage characteristic of a tin oxide material that has been doped with 5% cobalt. The presence of a negative differential resistance (NDR) region is clearly evident in the graph depicted in the figure. In the positive voltage region, a portion of the graph shows a decrease in current with an increase in voltage (between +3V and +4V). This phenomenon is recognized as the Negative Differential Resistance (NDR) effect. Within this region, the material's resistance increases, leading to a temporary reduction in the current. An increase in voltage causes a change in the internal electric field of the material, thereby obstructing charge movement and consequently reducing the current. When the current decreases, the resistance of the material increases. This results in a temporary reduction of the material's ability to conduct electrical current. The current-voltage (I-V) graph illustrates how the current's direction and magnitude vary with both positive and negative applied voltages. The negative differential resistance (NDR) effect is seen solely within the positive voltage range. Following the negative differential resistance (NDR) region, the current rises again, suggesting that the device is capable of providing stable measurements. The consistent nature of the changes in the graph indicates the reproducibility of this characteristic. Beyond the qualitative observations described above, a detailed quantitative analysis was performed on the I-V characteristics presented in Figures 2 and 3. In the 1% Co-doped sample (Figure 2), while a hysteretic behavior indicative of resistive switching is apparent, the NDR effect is not prominent. The switching threshold voltages were measured to be approximately $\pm 2.5\text{V}$ for this device. However, a notable and robust NDR phenomenon is observed in the 5% Co-doped sample (Figure 3), with the NDR region occurring between approximately +3V and +4V, as previously mentioned. The peak current before the onset of NDR was recorded to be

around 15 mA, and a clear decrease in current is observed following the NDR region, eventually returning to higher current values upon further increase in voltage.

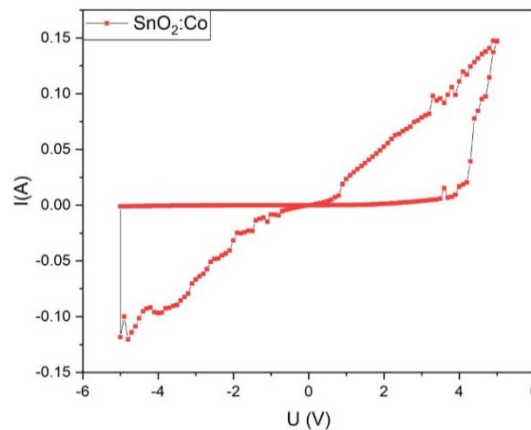


Figure 2. Current–voltage (I-V) curve of Ag/ $\text{SnO}_2\text{:Co}$ (1%)/ SiO_2 /p-Si resistive switching

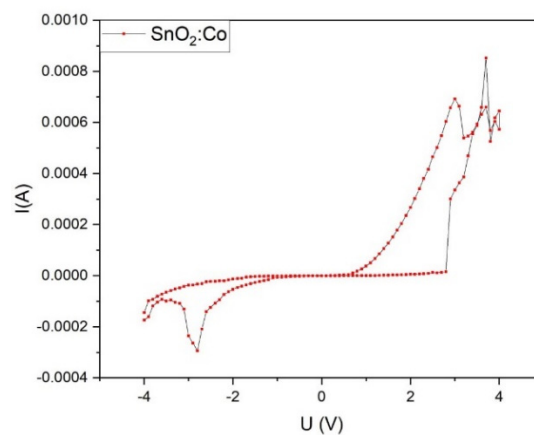


Figure 3. Current–voltage (I-V) curve of Ag/ $\text{SnO}_2\text{:Co}$ (5%)/ SiO_2 /p-Si resistive switching

CONCLUSION

This study successfully demonstrated a tunable negative differential resistance (NDR) effect in memristors based on cobalt-doped tin dioxide ($\text{SnO}_2\text{:Co}$). The $\text{SnO}_2\text{:Co}$ thin films, grown on p-type silicon substrates via ultrasonic spray pyrolysis (USP), exhibited unique electro-physical characteristics, demonstrating an unusual decrease in current within a specific voltage range. The identified NDR region, particularly within the positive voltage range (approximately +3V to +4V), highlights the promising potential of the devices studied. This behavior is attributed to the trapping of charge carriers and the redistribution of the electric field within the material.

The observed resistive switching properties, especially the stable transitions between high and low resistance states, indicate the suitability of these materials for memory applications. The presence of the NDR effect further creates new possibilities for these devices to be used in dynamic switching technologies, including low-power logic circuits and oscillation generators. The results position the Co:SnO_2 system as a promising candidate for controlled memory elements and future generation electronics.

Building upon the findings, further research is warranted to optimize the NDR effect and the device performance parameters. This includes fine-tuning the doping levels, film thickness, and the selection of electrode materials, as well as enhancing the device structure. Additionally, exploring the underlying mechanisms more deeply to stabilize the fabrication process and broaden the scope of applications is also crucial. These research directions could lead to finding new solutions for high-performance and low-power electronics. Our work provides a solid foundation for the future application of the Co:SnO_2 material in electronic devices, especially in memory and switching components.

ORCID

©Jamoliddin X. Murodov, <https://orcid.org/0009-0006-3088-4881>; ©Shavkat U. Yuldashev, <https://orcid.org/0000-0002-2187-5960>
©Azamat O. Arslanov, <https://orcid.org/0009-0000-4817-8770>

REFERENCES

- [1] X.B. Yan, *et al.*, “Bipolar Resistive Switching Performance of The Nonvolatile Memory Cells Based on $(\text{AgI})_{0.2}(\text{Ag}_2\text{MoO}_4)_{0.8}$ Solid Electrolyte Films,” *J. Appl. Phys.* **106**, 054501 (2009). <https://doi.org/10.1063/1.3211293>

- [2] K. Kang, W. Hu, and X. Tang, "Halide Perovskites for Resistive Switching Memory," J. Phys. Chem. Lett. **12**, 48, 11673-11682 (2021). <https://doi.org/10.1021/acs.jpcclett.1c03408>
- [3] W. Li, et al., "High On/Off Ratio Organic Resistive Switching Memory Based on Carbazolyl Dicyanobenzene and a Polymer Composit: The Journal of Phys. Chem. C, **126**(30), 12897–12905 (2022). <http://dx.doi.org/10.1021/acs.jpcc.2c03641>
- [4] D. Ielmini, "Resistive Switching Memories Based on Metal Oxides: Mechanisms, Reliability and Scaling," Semicond. Sci. Technol. **31**, 063002 (2016). <http://dx.doi.org/10.1088/0268-1242/31/6/063002>
- [5] F.M. Simanjuntak, D. Panda, K.H. Wei, and T.Y. Tseng, "Status and Prospects of ZnO-Based Resistive Switching Memory Devices," Nanoscale Research Letters, **11**, 368 (2016). <http://dx.doi.org/10.1186/s11671-016-1570-y>
- [6] Sh. Abdullaev, D.J. Lee, Sh. Rano, and Sh.U. Yuldashev, "Negative Differential Resistance Effect in ZnMgO Memristor with SiO₂ Thin Oxide Layer on p-Type Silicon," Semiconductors Physics and Microelectronics, (2020). https://uzjournals.edu.uz/semiconductors/vol2/issue_2.html
- [7] P.D. Walke, et al., "Memristive Devices from CuO Nanoparticles," Nanomaterials, **10**(9), 1677 (2020). <https://doi.org/10.3390/nano10091677>
- [8] K. Bandopadhyay, K.N. Prajapati, and J. Mitra, "Resistive Switching in Individual ZnO Nanorods: Delineating The Ionic Current By Photo-Stimulation," Nanotechnology, **29**, 105701 (2018). <https://doi.org/10.1088/1361-6528/aaa63f>
- [9] S.S. Li, and Y.K. Su, "Oxygen-Vacancy Induced Resistive Switching Effect In Mn-Doped ZnO Memory Devices," Physica Status Solidi rrl, **13**(2), 1800453 (2019). <http://dx.doi.org/10.1002/pssr.201800453>

РЕГУЛЬОВАНИЙ ВІД'ЄМНИЙ ДИФЕРЕНЦІАЛЬНИЙ ОПІР У МЕМРИСТОРАХ SnO₂:Co НА p-Si

Джамолдін Х. Муродов^{a,b}, Шавкат У. Юлдашев^b, Азамат О. Арсланов^c, Маргуба С. Міркамілова^a, Уткур Е. Джураєв^a

^aТашкентський державний технічний університет імені Іслама Карімова, Ташкент, Узбекистан

^bЦентр розвитку нанотехнологій, Національний університет Узбекистану, Ташкент, Узбекистан

^cНаціональний університет Узбекистану імені Мірзо Улугбека, Ташкент, Узбекистан

У цьому дослідженні досліджується явище від'ємного диференціального опору (ОДО) у мемристорах на основі діоксиду олова (SnO₂:Co), легованого кобальтом, виготовлених на кремнієвих підкладках р-типу. За допомогою ультразвукового розпилювального піролізу (USP) тонкі кристалічні плівки SnO₂:Co були нанесені на підкладки p-Si з тонким шаром рідного SiO₂. Отримані мемристорні пристрої демонструють відтворюване біполярне резистивне перемикавання між високоомним (HRS) та низькоомним (LRS) станами. Ключові висновки включають спостереження чіткої області NDR (від'ємного диференціального опору) на вольт-амперних (ВАХ), зокрема в діапазоні позитивної напруги приблизно від +3 В до +4 В. У цій області NDR струм зменшується, незважаючи на збільшення напруги, що є характерною ознакою цього ефекту. Така поведінка пояснюється захопленням та перерозподілом заряду в матеріалі Co:SnO₂. Постійна та відтворювана природа спостережуваного ефекту NDR свідчить про потенціал мемристорів SnO₂:Co для застосування в передових технологіях пам'яті та комутації. Ця робота сприяє розумінню механізмів резистивного перемикавання в тонких плівках SnO₂, легованих кобальтом, які є перспективними матеріалами для пристроїв пам'яті наступного покоління.

Ключові слова: легування кобальтом SnO₂; мемристор; комутація з негативним диференціальним опором; USP

EFFECTIVE CHARGE OF Mn AND Ni IMPURITY ATOMS IN SILICON UNDER THE INFLUENCE OF AN EXTERNAL ELECTRIC FIELD

 **Bobir O. Isakov***, **Xalmurat M. Iliyev**, **Zafar B. Khudoynazarov**,  **Giyosiddin A. Kushiev**

Tashkent state technical university, University St., 2, 100095, Tashkent, Uzbekistan

**Corresponding Author e-mail: bobir6422isakov@gmail.com*

Received January 13, 2025; revised March 19, 2025; accepted March 24, 2025

In this work, the diffusion of Mn and Ni impurity atoms to *p*-Si and *n*-Si samples under the influence of an external electric field was investigated in the temperature range $T \sim 800 \div 1300^\circ\text{C}$. The research results show that at temperatures above 1000°C , the effective charge of manganese ion has a negative value, and at temperatures below 900°C , the effective charge has a positive value. In the temperature range $T = 800 \div 1250^\circ\text{C}$, nickel ions move in the opposite direction to the current direction of the electric field. The increase in the effective charge with the increase in temperature was explained by the attraction of neutral nickel atoms by electrons.

Keywords: *Silicon; Impurity atoms; Diffusion; Effective charge; External electric field*

PACS: 61.72.uf, 68.43.Jk

1. INTRODUCTION

The external electric field causes the movement of the impurity particles in the semiconductor and the interaction between the diffusion particles and the free charge carriers of the semiconductor. In a number of cases, this interaction significantly affects the migration of these particles [1,2].

Formation of III-V and II-VI binary compounds in Si crystal lattice and surface is one of the most promising directions. But when forming III-V and II-VI group compounds in the silicon crystal lattice, the diffusion coefficient of III and V group elements in Si material is small ($\sim 10^{-14} \div 10^{-11} \text{ cm}^2/(\text{V}\cdot\text{s})$) [3,4,5,6,7,8,9], due to the low solubility of group II and VI elements in Si material ($\sim 10^{15} \div 10^{18} \text{ cm}^{-3}$) [10,11,12,13,14,15], it is not possible to detect the change in the functional parameters of the Si semiconductor using existing devices. For this reason, the interest in increasing the diffusion coefficient and solubility of impurity atoms in crystals of Si and Ge [16,17,18,19] is of great scientific and practical importance.

Until now, there are very few articles devoted to the effect of external electric field on the diffusion of impurity in semiconductors. This article provides information on the electromigration of nickel (Ni) (a Ni acceptor in silicon [20,21,22]) and manganese (Mn) (a Mn donor in silicon [23,24,25]) in silicon.

2. MATERIALS AND METHODS

For the study, *p*-Si ($n_B \approx 5 \times 10^{15} \text{ cm}^{-3}$) and *n*-Si ($n_P \approx 5 \times 10^{13} \text{ cm}^{-3}$) brands of silicon were selected. The samples were cut in dimensions of $5 \times 10 \times 1 \text{ mm}^3$ (all samples have the same size) using a STX-402 diamond wire cutter, and the surface of the samples was mechanically and chemically treated.

After that, using the VUP4 device, a thin metal layer of Mn (the purity of manganese was 99.998%) on the surface of *p*-Si and Ni (the purity of nickel was 99.997%) on the surface of *n*-Si was formed (Fig. 1).

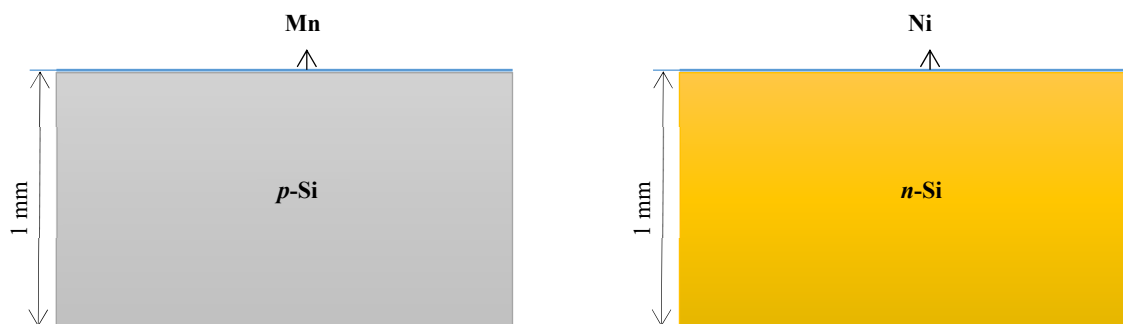


Figure 1. Si samples with a thin metal layer formed on the surface

Two grains of Si samples with a thin metal layer of Mn on the surface, were placed in an electro-diffusion device for the purpose of diffusion. In this case, the positive pole of the electro-diffusion device was connected to one of the samples and the negative pole to the other. The same process was repeated for Si samples on which a thin metal layer of Ni was formed on the surface (Fig. 2). In the process of electro-diffusion, a constant current with a current density of $J = 20 \div 260 \text{ A/cm}^2$ was passed through the samples for 20 minutes, during which the samples were heated to a temperature

of 800÷1300°C. After the end of the electro-diffusion process, the samples were quickly cooled using a special oil and subjected to chemical and mechanical processing. After electro-diffusion, the distance between the contact boundaries of the samples and the depth of the p-n transition in the cathode and anode samples was measured using an optical comparator with an accuracy of ±1 μm.



Figure 2. Placement of samples in an electro-diffusion device

3. RESULTS AND DISCUSSION

By studying the distribution of the impurity concentration in the samples, the mobility of ions can be determined from the following equation:

$$\mu = \frac{Q_+ - Q_-}{N_0 Et}, \quad (1)$$

where Q_+ and Q_- are the amount of impurity diffused in the direct current E electric field to the anode and cathode samples, N_0 is the impurity concentration in the $x = 0$ plane, t is the duration of electrical migration. On the other hand, if you know the concentration distribution in the studied samples, you can determine the ratio of the mobility to the diffusion coefficient:

$$\frac{\mu}{D} = \frac{1}{E} \frac{d}{dx} \ln \frac{N_-(x,t)}{N_+(x,t)}. \quad (2)$$

where $N_-(x,t)$ and $N_+(x,t)$ are the impurity concentration distributions in the cathode and anode samples, respectively.

Diffusion of impurities to silicon under the influence of an external electric field, analysis of the concentration profile of impurities was supplemented by the p - n junction technique. In this case, the mobility of ions is determined by the following formula:

$$\mu = \frac{x_- - x_+}{2Et}, \quad (3)$$

where x_- and x_+ are the p - n junction depths of the cathode and anode samples, respectively. The surfaces of the samples were chemically cleaned from the oxide layer, and the p - n junction depth was determined using a thermoprobe and layer-by-layer chemical decomposition method.

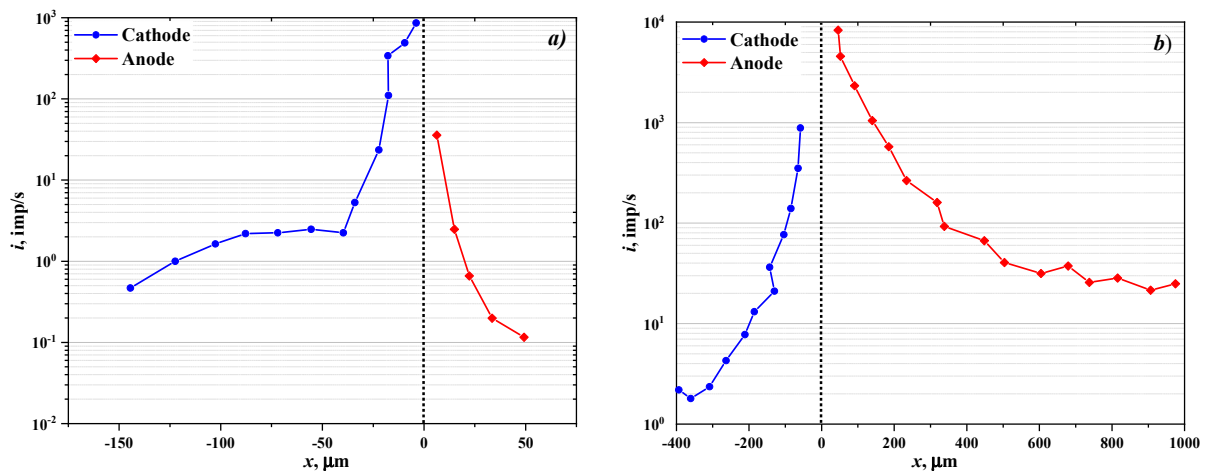


Figure 3. Distribution of impurities in silicon doped with Mn atoms under the influence of an external electric field: a) $T=830^\circ\text{C}$; b) $T=1200^\circ\text{C}$.

Figure 3 shows that manganese ions move in the same direction as the external electric current at temperatures $T = 830^\circ\text{C}$ (at temperatures below $T = 950^\circ\text{C}$), that is, manganese ions are connected to the cathode moves towards the sample. Manganese ions at temperature $T = 1200^\circ\text{C}$ (at temperatures higher than $T = 1000^\circ\text{C}$) move mainly towards the anode (Fig. 3 b).

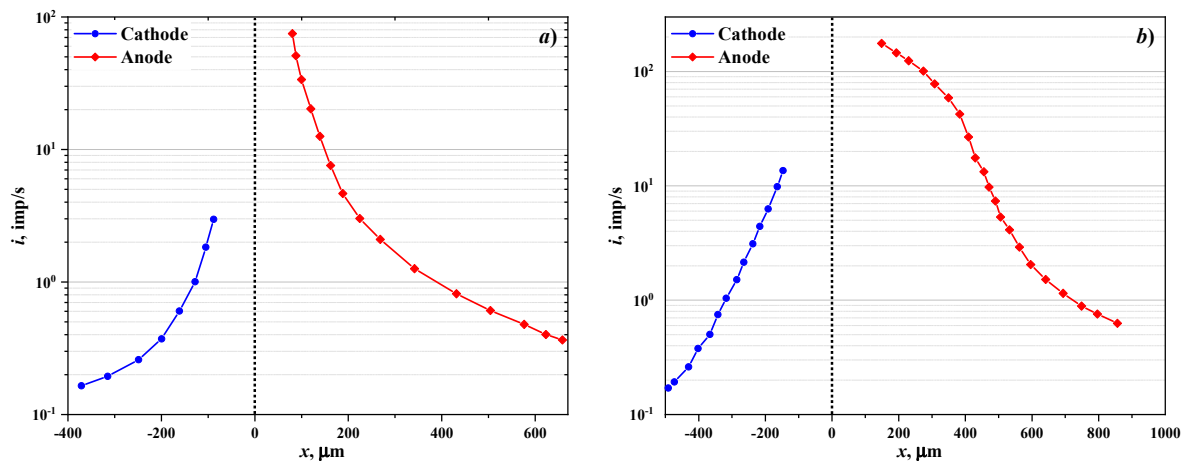


Figure 4. Distribution of diffusion of Ni atoms in silicon under the influence of an external electric field:
a) $T=813^\circ\text{C}$; b) $T=1200^\circ\text{C}$.

Figure 4 shows the graphs for electromigration of nickel in silicon in anode and cathode samples at temperatures $T = 813^\circ\text{C}$ and $T = 1200^\circ\text{C}$. As can be seen from the figure, in this case, unlike Mn, it is not observed to move in the same direction as the direction of the external electric current in the entire temperature range, and in the studied temperature range, the ions of Ni atoms $q = 0.3 \div 2$ moves towards the anode in the form of an effective charge. In the temperature range $T = 800 \div 1250^\circ\text{C}$, the lack of inversion of the mobility of nickel ions and the increase of the effective charge with increasing temperature indicate that the results of the electromigration study can be explained by the attraction of neutral nickel atoms by electrons is necessary, because the movement of neutral atoms in electromigration is determined only by the attraction effect.

Knowing μ/D and using Einstein's relation (4), the charge of the input ions can be calculated (Fig. 5).

$$\frac{\mu}{D} = \frac{q}{kT}, \quad (4)$$

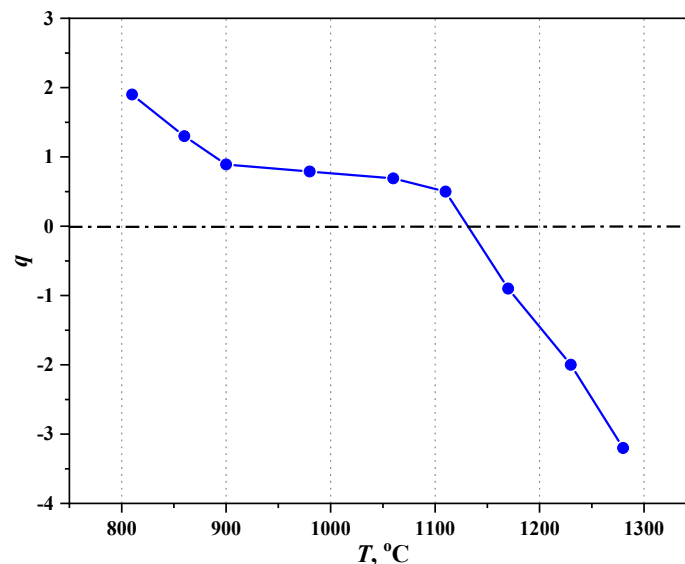


Figure 5. Dependence of effective charge of Mn ions doped on silicon by electro-diffusion method on diffusion temperature

4. CONCLUSION

Values of manganese ion mobility and their effective charge calculated from experimental data as a function of diffusion temperature are shown in Fig. 5. It can be seen that at temperatures above 1000°C , the effective charge of manganese ion has a negative value and the transmission increases rapidly with increasing temperature, and at temperatures below 900°C , the effective charge has a positive value and changes in the range of 1:2. The movement of manganese ions to the cathode at temperatures below 900°C can be explained by the diffusion of manganese in the form of Mn^{++} , which has a large diffusion coefficient in silicon, between the nodes. However, in this case, the reason for the change in direction of movement of Mn ions at $T=950^\circ\text{C}$ remains unclear. This anomalous phenomenon may be a consequence of a change in the diffusion mechanism of manganese or a manifestation of the attraction effect of manganese ions with electrons.

The results of the experiment show that the solubility and diffusion coefficient of silicon-doped impurities can be increased under the influence of a constant external electric field. Proving this assumption requires large-scale experiments on the doped of silicon impurities under the influence of an external electric field.

ORCID

Bobir O. Isakov, <https://orcid.org/0000-0002-6072-3695>; Giyosiddin A. Kushiev, <https://orcid.org/0000-0002-5158-8997>

REFERENCES

- [1] B.I. Boltaks and T.D. Dzhaferov, “The Effect of Applied Electric Field on Diffusion of Impurities in Gallium Arsenide”, *Phys. Stat. Sol.* **19**, 705 (1967). <https://doi.org/10.1002/pssb.19670190221>
- [2] X.M. Iliyev, Z.B. Khudoynazarov, B.O. Isakov, M.X. Madjitov, and A.A. Ganiyev, “Electrodiffusion of manganese atoms in silicon”, *East European journal of physics*, (2), 384-387 (2024). <https://doi.org/10.26565/2312-4334-2024-2-48>
- [3] N.F. Zikrillayev, S.B. Isamov, B.O. Isakov, T. Wumaier, Li wen Liang, J.X. Zhan, and T. Xiayimulati, “New Technological Solution for the Tailoring of Multilayer Silicon-based Systems with Binary Nanoclusters Involving Elements of Groups III and V”, *Journal of nano- and electronic physics*, **15**(6), 06024 (2023). [https://doi.org/10.21272/jnep.15\(6\).06024](https://doi.org/10.21272/jnep.15(6).06024)
- [4] X.M. Iliyev, V.B. Odzhaev, S.B. Isamov, B.O. Isakov, B.K. Ismaylov, K.S. Ayupov, Sh.I. Hamrokulov, and S.O. Khasanbaeva, “X-ray diffraction and Raman spectroscopy analyses of GaSb-enriched Si surface formed by applying diffusion doping technique”, *East European journal of physics*, (3), 363-369 (2023). <https://doi.org/10.26565/2312-4334-2023-3-38>
- [5] X.M. Iliyev, S.B. Isamov, B.O. Isakov, U.X. Qurbonova, and S.A. Abduraxmonov, “A surface study of Si doped simultaneously with Ga and Sb”, *East European journal of physics*, (3), 303-307 (2023). <https://doi.org/10.26565/2312-4334-2023-3-29>
- [6] Kh.M. Iliev, N.F. Zikrillayev, K.S. Ayupov, B.O. Isakov, B.A. Abdurakhmanov, Z.N. Umarchodjaeva, and L.I. Isamiddinova, “Effect of GaSb Compound on Silicon Bandgap Energy”, *Journal of nano- and electronic physics*, **16**(2), 02004 (2024). [https://doi.org/10.21272/jnep.16\(2\).02004](https://doi.org/10.21272/jnep.16(2).02004)
- [7] Kh.M. Iliev, S.V. Koveshnikov, B.O. Isakov, E.Zh. Kosbergenov, G.A. Kushiev, and Z.B. Khudoynazarov, “The Elemental Composition Investigation of Silicon Doped with Gallium and Antimony Atoms”, *Surface Engineering and Applied Electrochemistry*, **60**(4), 633–639 (2024). <https://doi.org/10.3103/S106837552470025X>
- [8] W. Yang, Y. Li, F. Meng, H. Yu, M. Wang, P. Wang, G. Luo, *et al.*, “III–V compound materials and lasers on silicon,” *Journal of Semiconductors*, **40**, 101305 (2019). <http://doi.org/10.1088/1674-4926/40/10/101305>
- [9] M. Levinshstein, S. Rumyantsev, and M. Shur, editors, *Semiconductor parameters. Handbook series on semiconductor parameters*, vol. 1, (World Scientific Publishing, 1996).
- [10] N.F. Zikrillayev, M.K. Khakkulov, B.O. Isakov, “The mechanism of the formation of binary compounds between Zn and S impurity atoms in Si crystal lattice”, *East European journal of physics*, (4), 177-181 (2023). <https://doi.org/10.26565/2312-4334-2023-4-20>
- [11] J. Liu, and S. Yue, “Fabrication of ZnS layer on silicon nanopillars surface for photoresistor application,” *Chemical Physics Letters*, **801**, 139716 (2022). <https://doi.org/10.1016/j.cplett.2022.139716>
- [12] J. Kang, J.-S. Park, P. Stradins, and S.-H. Wei, “Nonisovalent Si-III-V and Si-II-VI alloys: Covalent, ionic, and mixed phases,” *Physical Review B*, **96**, 045203 (2017). <https://doi.org/10.1103/PhysRevB.96.045203>
- [13] H.J. Xu, H.S. Jia, Z.T. Yao, and X.J. Lia, “Photoluminescence and I–V characteristics of ZnS grown on silicon nanoporous pillar array,” *J. Mater. Res.* **23**(1), 121–126 (2008). <https://doi.org/10.1557/JMR.2008.0005>
- [14] M. Özkan, N. Ekem, S. Pat, M.Z. and Balbağ, “ZnS thin film deposition on Silicon and glass substrates by Thermionic vacuum Arc,” *Materials Science in Semiconductor Processing*, **15**, 113–119 (2012). <https://doi.org/10.1016/j.mssp.2011.07.004>
- [15] N.F. Zikrillayev, O.B. Tursunov, and G.A. Kushiev, “Development and Creation of a New Class of Graded-Gap Structures Based on Silicon with the Participation of Zn and Se Atoms”, *Surface Engineering and Applied Electrochemistry*, **59**(5), 670–673 (2023). <https://doi.org/10.3103/S1068375523050198>
- [16] N.F. Zikrillayev, G.A. Kushiev, S.V. Koveshnikov, B.A. Abdurakhmanov, U.K. Qurbonova, and A.A. Sattorov, “Current status of silicon studies with GexSi1-x binary compounds and possibilities of their applications in electronics”, *East European journal of physics*, (3), 334-339 (2023). <https://doi.org/10.26565/2312-4334-2023-3-34>
- [17] N.F. Zikrillayev, G.A. Kushiev, Sh.I. Hamrokulov, and Y.A. Abduganiev, “Optical Properties of GexSi1-x Binary Compounds in Silicon”, *Journal of nano- and electronic physics*, **15**(3), 03024 (2023). [https://doi.org/10.21272/jnep.15\(3\).03024](https://doi.org/10.21272/jnep.15(3).03024)
- [18] N.F. Zikrillayev, S.V. Koveshnikov, S.B. Isamov, B.A. Abdurakhmonov, and G.A. Kushiev, “Spectral Dependence of the Photoconductivity of GexSi1-x Type Graded-Gap Structures Obtained by Diffusion Technology”, *Semiconductors*, **56**(1), 29-31 (2022). <https://doi.org/10.1134/S1063782622020191>
- [19] G.A. Kushiev, B.O. Isakov, and U.X. Mukhammadjonov, “The Prospects of Obtaining a New Material with a Hetero-Baric Structure GexSi1-x-Si Based on Silicon for Photo Energy Applications”, *Journal of nano- and electronic physics*, **16**(3), 03003 (2024). [https://doi.org/10.21272/jnep.16\(3\).03003](https://doi.org/10.21272/jnep.16(3).03003)
- [20] M.K. Bakhadirkanov, Z.T. Kenzhaev, Kh.S. Turekeev, B.O. Isakov, and A.A. Usmonov, “Gettering properties of nickel in silicon photocells”, *Technical Physics*, **67**(14), (2022). <https://doi.org/10.21883/TP.2022.14.55221.99-21>
- [21] N. Zikrillayev, Z. Kenzhaev, T. Ismailov, U. Kurbanova, B. Aliyev, “Effect of nickel doping on the spectral sensitivity of silicon solar cells”, *E3S Web of Conferences*, **434**, 01036 (2023). <https://doi.org/10.1051/e3sconf/202343401036>
- [22] Z.T. Kenzhaev, N.F. Zikrillayev, K.S. Ayupov, K.A. Ismailov, S.V. Koveshnikov, and T.B. Ismailov, “Enhancing the Efficiency of Silicon Solar Cells through Nickel Doping”, *Surface Engineering and Applied Electrochemistry*, **59**(6), 858–866 (2023). <https://doi.org/10.3103/S1068375523060108>
- [23] N.F. Zikrillayev, G.A. Kushiev, S.B. Isamov, B.A. Abdurakhmanov, O.B. Tursunov, “Photovoltaic Properties of Silicon Doped with Manganese and Germanium”, *Journal of nano- and electronic physics*, **15**(1), 01021 (2023). [https://doi.org/10.21272/jnep.15\(1\).01021](https://doi.org/10.21272/jnep.15(1).01021)
- [24] M.O. Tursunov, K.M. Iliev, and B.K. Ismaylov, “High-temperature analysis of silicon properties with manganese-oxygen binary complexes”, *Physical Sciences and Technology*, **11**(1-2), 4 (2024). <https://doi.org/10.26577/phst2024v11i1a1>

- [25] N.F. Zikrillae, Kh.M. Iliev, G.Kh. Mavlonov, S.B. Isamov and M.Kh. Madjitov, "Negative magnetoresistance in silicon doped with manganese", E3S Web of Conferences, **401**, 05094 (2023). <https://doi.org/10.1051/e3sconf/202340105094>

ЕФЕКТИВНИЙ ЗАРЯД ДОМІШКОВИХ АТОМІВ Mn ТА Ni В КРЕМНІ ПІД ВПЛИВОМ ЗОВНІШНЬОГО ЕЛЕКТРИЧНОГО ПОЛЯ

Бобір О. Ісаков, Халмурат М. Ілієв, Зафар Б. Худойназаров, Гійосіддін А. Кушієв

Ташкентський державний технічний університет, вул. Університетська, 2. 100095, Ташкент, Узбекистан

У даній роботі досліджено дифузію домішкових атомів Mn та Ni до зразків p-Si та n-Si під дією зовнішнього електричного поля в інтервалі температур $T \sim 800 \div 1300^\circ\text{C}$. Результати досліджень показують, що при температурах вище 1000°C ефективний заряд іона марганцю має негативне значення, а при температурах нижче 900°C ефективний заряд має позитивне значення. В інтервалі температур $T = 800 \div 1250^\circ\text{C}$ іони нікелю рухаються в протилежному напрямку до поточного напрямку електричного поля. Збільшення ефективного заряду з підвищенням температури пояснювали притяганням електронами нейтральних атомів нікелю.

Ключові слова: кремній, домішкові атоми, дифузія, ефективний заряд, зовнішнє електричне поле

MATHEMATICAL ANALYSIS OF THE FEATURES OF RADIAL p-n JUNCTION: INFLUENCE OF TEMPERATURE AND CONCENTRATION

 J.Sh. Abdullayev^{a*},  I.B. Sapaev^{a,b}, N.Sh. Esanmuradova^{a,b,e}, S.R. Kadirov^c, Sh.M. Kuliye^d

^aNational Research University TIAME, Department of Physics and Chemistry, Tashkent, Uzbekistan

^bWestern Caspian University, Baku, Azerbaijan

^cUrgench State University, Urgench, Uzbekistan

^dPhysical-Technical Institute of Uzbekistan Academy of Sciences, 100084 Tashkent, Uzbekistan

^eKimyo International University in Tashkent, Uzbekistan

*Corresponding Author e-mail: j.sh.abdullayev6@gmail.com

Received November 11, 2025; revised January 7, 2025; in final form March 23, 2025; accepted April 1, 2025

In this article, the electrophysical characteristics of GaAs/Si radial heterojunctions are studied analytically over a temperature range of 50 K to 500 K in increments of 50 K, considering various doping concentrations. The analysis encompasses band gap narrowing (BGN), built-in potential, the difference in band gap between GaAs and Si, and capacitance-voltage (C-V) characteristics. In particular, we focus on shell radii of 0.5 μm and 1 μm within the structure. We found that the thickness of the depletion region of the GaAs/Si radial heterojunction increases with rising temperature. When the doping concentration changes from $2 \cdot 10^{15}$ to $2 \cdot 10^{18}$ BGN decreases by 2 meV. The charge capacity of the GaAs/Si radial heterojunction increases by 3 nF as the temperature rises from 50 K to 500 K. Additionally, the built-in potential of the GaAs/Si radial heterojunction decreases by 1.5 volts with increasing temperature.

Keywords: Radial p-n and p-i-n junction; Light trap; External factors; Volt-farad; Volt-amper; Cryogenic temperatures

PACS: 73.40. Lq, 73.61.Cw, 73.61.Ey, 72.20.Jv

INTRODUCTION

Over time, the ongoing surge in research on semiconductor electronic devices has led to significant advancements in their design, unique materials, optimization, and functionality. Key developments include two-dimensional transistors [1-4], nanowires [5], and notably, radial p-n and p-i-n junction structures [6,7]. Radial p-n junctions offer several advantages over traditional planar junctions, especially in submicron nanowire applications [8-11], including high internal and external quantum efficiency [12], low recombination due to short diffusion length [13], and a high surface-to-volume ratio [14]. Over the past two decades, these radial junctions have gained popularity for their enhanced optical and electronic properties, making them ideal for applications such as photodiodes, optical sensors [15], thermal and photovoltaic detectors [16], and solar cells [17]. Their design minimizes optical losses through efficient light absorption and charge carrier collection, thereby enhancing energy conversion efficiency. Additionally, the perpendicular alignment of light absorption and carrier transport in radial p-n junctions supports high-frequency performance, making them suitable for high-speed electronics and wireless communication systems.

Furthermore, radial junctions are integral to high-speed photodetectors [18], avalanche photodiodes [19], photovoltaic devices, gamma-ray detectors [20], and infrared sensors [21,22]. Their unique structural design provides superior efficiency, speed, and sensitivity [23], essential for various modern semiconductor applications [24]. Given their broad applications, it is crucial to investigate the electrophysical properties of these junctions, particularly ionization processes and their behavior across a wide temperature range. Both theoretical modeling and experimental validation are essential to ensure the reliability and accuracy of these semiconductor devices.

While radial p-n and p-i-n junctions have been extensively studied, research on heterojunction structures remains comparatively limited. In this work, we have focused on the GaAs/Si heterojunction structure, analyzing its electrophysical features theoretically and analytically. Using mathematical modeling, we have analyzed the electrophysical characteristics of the n-GaAs/p-Si heterojunction structure to gain insights into its performance under varying temperatures and applied voltages.

METHODS AND MATERIAL

2.1 Material and Geometric Parameters

Despite the development of new semiconductor materials, GaAs remains the primary material for optoelectronic devices, while Si continues to be the most widely used material due to its advanced development technology and abundance on the Earth's surface. Based on this perspective, Si and GaAs were selected for this study. Figure 1 shows the cross-sectional view of the selected radial p-n junction sample, cut along the Z-axis. We derived solutions for radial p-n junction structures with a p-type core radius of 0.5 μm and an n-type shell radius of 1 μm . Where r denotes the radial

dimension, $\circ e^+$ and $\bullet e^-$ represents the densities of ionized N_D^+ donor and N_A^- acceptor atoms respectively, at the interface of the radial p-n heterojunction within the depletion region. If full ionization case $N_D^+ = N_D$, $N_A^- = N_A$. In Figure 1, the interval $0 < r < r_p$ represents the p-type quasi-neutral region (QNR), the interval $r_p < r < r_n$ represents the depletion region in the radial p-n heterojunction junction, the interval $r_n < r < 2R$ represents the n-type quasi-neutral region (QNR).

$$d_{p-n} = \sqrt{\frac{2(\epsilon_{GaAs} N_A + \epsilon_{Si} N_D)(\phi_{bi}(T) - U)}{q \epsilon_{Si} \epsilon_{GaAs} \epsilon_0 N_A \cdot N_D}}. \quad (1)$$

The interval $d_{p-n} = r_p < r < r_n$ represents the depletion region and this depends on temperature and external voltage and is represented by the expression (1): Where, $\phi_{bi}(T)$ is the built-in potential of the radial p-n junction which is defined by the expression (3), ϵ_{Si} , and ϵ_{GaAs} are dielectric constant of the Si and GaAs respectively, $\epsilon_0 = 8.85 \cdot 10^{-12} \text{ F} \cdot \text{m}^{-1}$ electrical constant. Heterojunction p-n structures are essential for advanced semiconductor devices, as they enhance performance through optimized band alignment and reduced recombination. The depletion region width plays a crucial role in determining device efficiency by influencing charge carrier distribution, breakdown voltage, and overall performance, particularly in high-frequency and high-power applications.

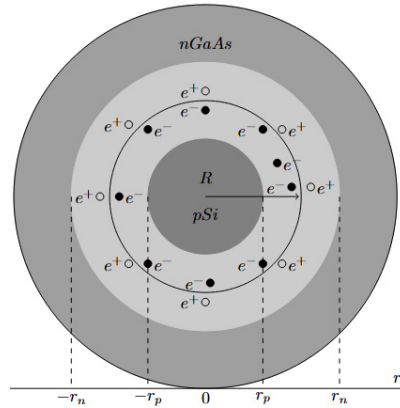


Figure 1. This figure illustrates a 2D cross-section of submicron radial p-n junction structures. The n-type GaAs region is represented by the light gray area, the p-type Si region by the dark gray area, and the depletion region is shown in very light gray

Precisely understanding and controlling this width is critical for improving the functionality and reliability of heterojunction-based devices. Figure 2 illustrates how the depletion region varies with external voltage at different temperatures, based on the results derived from Equation (1).

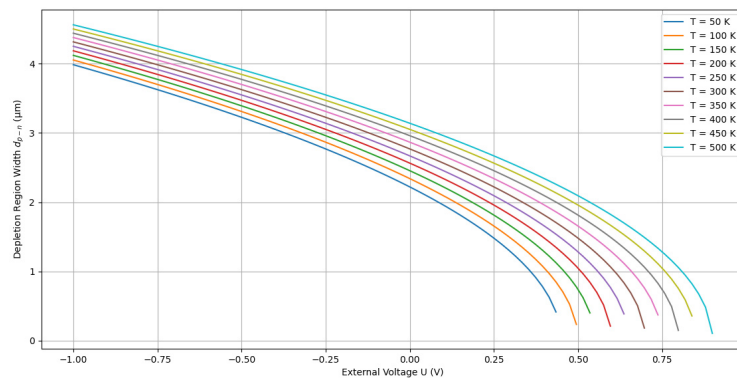


Figure 2. Temperature dependence of the depletion region thickness differences in the p-GaAs/n-Si heterojunction

The band gap is indeed one of the most critical parameters in semiconductor materials, especially for heterojunctions like p-GaAs/n-Si. In such heterojunctions, the difference in band gaps between GaAs (about 1.43 eV) and Si (about 1.12 eV) at 300K, plays a significant role in their behavior and performance, particularly affecting charge carrier dynamics, recombination, and junction properties. This balance of properties in GaAs/Si heterojunctions supports a wide range of applications in high-speed electronics and optoelectronic devices. The (2) expression represents the change in the width of the band gap with temperature variation.

$$\Delta E_g(T) = \Delta E_g(0) - T^2 \cdot \left(\frac{\alpha_{GaAs}}{T + \theta_{GaAs}} - \frac{\alpha_{Si}}{T + \theta_{Si}} \right). \quad (2)$$

Where, $\Delta E_g(0)$ is differences of the band gap Si and GaAs at 0 K. θ_{GaAs} and θ_{Si} are Debye temperature GaAs and Si respectively. The Debye temperature can be calculated using the material's properties, but empirical values are often referenced.

$$\phi_{bi}(T) = \Delta E_g(T) - \frac{kT}{q} \cdot \ln\left(\frac{N_A \cdot N_D}{n_{iGaAs} \cdot n_{iSi}}\right). \quad (3)$$

Here, k is the Boltzmann constant, T is the absolute temperature in Kelvin, q is the charge of an electron, N_A and N_D are acceptor and donor concentration respectively, n_{iSi} and n_{iGaAs} are intrinsic carrier concentrations of Si and GaAs respectively. The electrostatic potential difference in the radial p-GaAs/n-Si heterojunction varies with changes in the external source voltage, which can be expressed as follows:

$$\Delta\phi_{p-n} = \phi_{bi}(T) - U. \quad (4)$$

The charge capacity of the GaAs/Si radial heterojunction depends on the differences in electrostatic potential. The negative charge of the p-type acceptors is balanced by the positive charge of the n-type donors $Q = Q^+ = Q^-$. which is equal to the differential electric capacity derived from the change in charge with respect to voltage. The results of the analytical and mathematical expressions derived above are analyzed in the following section, along with proposed future expectations. Additionally, the obtained results have been calibrated. The charge capacity of the p-GaAs/n-Si heterojunction is expressed by equation (5)

$$C_{p-n} = S \sqrt{\frac{q\epsilon_{Si}\epsilon_{GaAs}\epsilon_0 N_A \cdot N_D}{2(\epsilon_{GaAs} N_A + \epsilon_{Si} N_D)(\phi_{bi}(T) - U)}}. \quad (5)$$

RESULTS AND DISCUSSION

In this section, the results are presented and analyzed. The analytical study of GaAs/Si radial heterojunctions over a temperature range of 50 K to 500 K provides significant insights into their electrophysical characteristics. One key finding is the observed increase in the depletion region thickness with rising temperature, while it decreases with increasing external voltage, as shown in Figure 2. This behavior is attributed to the intrinsic properties of the semiconductor materials involved. As temperature increases, thermal energy enhances charge carrier movement, effectively reducing the doping concentration within the depletion region. Consequently, a wider depletion width is required to maintain charge neutrality across the junction, which is critical for the heterojunction's operation.

The depletion region thickness in p-GaAs/n-Si heterojunctions is analyzed at various voltages, specifically -1 V and 1 V, across different temperatures ranging from 50 K to 500 K in 50 K increments, as depicted in Figure 2. The results indicate that the depletion region thickness decreases with increasing voltage and temperature. Additionally, the potential barrier of the p-n junction is directly influenced by the depletion region thickness, leading to observable variations in the potential barrier. This dependence plays a crucial role in the functionality of devices such as thermosensors, photosensors, and solar cells.

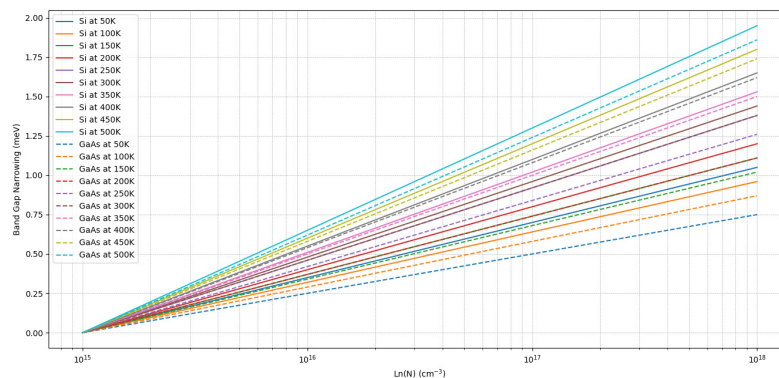


Figure 3. Bandgap narrowing as a function of logarithmic doping concentration in both n-Si and p-GaAs

Another noteworthy result is the decrease in band gap narrowing (BGN) by 2 meV as the doping concentration increases from changes from $2 \cdot 10^{15}$ to $2 \cdot 10^{18}$. This trend indicates that higher doping levels enhance the screening of ionized impurities, effectively reducing the interactions responsible for BGN. The implications of BGN on device performance are significant, as a narrower band gap can lead to increased leakage currents, potentially degrading the efficiency of heterojunction-based devices such as solar cells and light-emitting diodes, as shown in Figure 3. Understanding the interplay between temperature, doping concentration, and band gap narrowing is crucial for designing high-performance GaAs/Si radial heterojunctions. The results of this study highlight the potential of GaAs/Si heterojunctions in advancing semiconductor technology. By leveraging insights into BGN and temperature effects,

manufacturers can design devices with improved performance, enhanced efficiency, and an extended operational range across various applications.

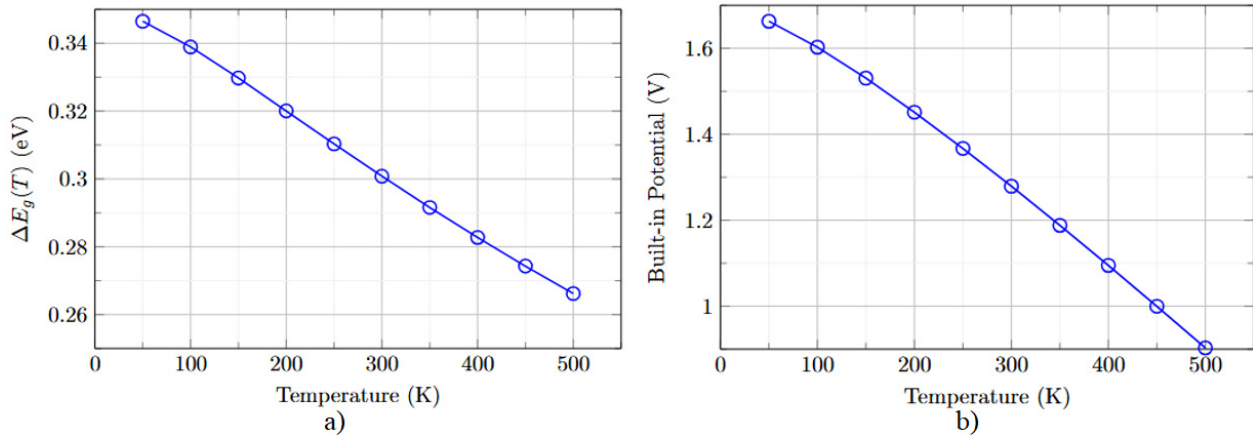


Figure 4. a) Temperature dependence of the band gap differences in the p-GaAs/n-Si heterojunction, b) The built-in potential of the p-GaAs/n-Si heterojunction varies with temperature from 50 K to 500 K

Moreover, the decrease in built-in potential by 1.5 volts with increasing temperature provides crucial insights into the stability of the junction. The built-in potential is vital for determining the electric field strength within the depletion region, which influences carrier recombination and overall junction performance.

The temperature dependence of the bandgap energy difference is also significant, as the bandgap decreases from 3.2 eV at 200K to 3.0 eV at 300K, suggesting a bandgap narrowing effect. This phenomenon, commonly observed in semiconductors, results from increased lattice vibrations, as shown in Figure 4.

As temperature rises, the reduced built-in potential may lead to increased thermal generation of electron-hole pairs, potentially elevating the reverse saturation current. This observation highlights the need for robust thermal management in device design, particularly for applications operating under varying thermal conditions.

The results of this study emphasize the intricate relationship between temperature, doping concentration, and the electrophysical characteristics of GaAs/Si radial heterojunctions. The increase in depletion width, the reduction in bandgap narrowing, the enhancement of charge capacity, and the decrease in built-in potential collectively provide valuable insights into optimizing device performance across different thermal environments.

Future work should focus on the experimental validation of these findings and exploring strategies to mitigate the adverse effects of temperature on the electrical characteristics of GaAs/Si radial heterojunctions, particularly for applications in high-performance semiconductor devices.

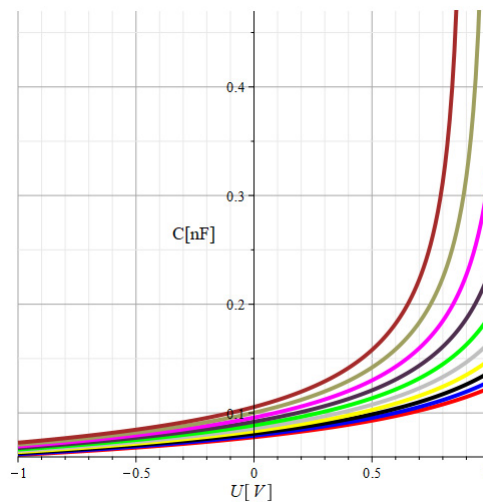




Figure 5. The charge capacity of the p-GaAs/n-Si heterojunction varies with external voltage over a temperature range from 50 K to 500 K, with the red line representing 50 K and the brown line representing 500 K

The observed increase in charge capacity by 3 nF with rising temperature from 50 K to 500 K reflects the temperature dependence of the capacitance-voltage (C-V) characteristics in Figure 5. As temperature increases, carriers are thermally excited, increasing their availability for conduction and, subsequently, enhancing the overall capacitance of the device. This behavior is particularly significant in high-frequency applications where capacitance stability is essential. It suggests that GaAs/Si radial heterojunctions could be designed to operate effectively across a broad temperature range, although careful consideration must be given to temperature effects on other parameters such as leakage current and noise.

CONCLUSIONS

In conclusion, this study provides a comprehensive analysis of the electrophysical characteristics of GaAs/Si radial heterojunctions across a temperature range of 50 K to 500 K, focusing on the effects of various doping concentrations and shell radii of 0.5 μm and 1 μm . Our findings reveal that the depletion region thickness increases with temperature, indicating enhanced charge distribution within the junction. Notably, the band gap narrowing (BGN) was found to decrease by 2 meV as the doping concentration varied from $2 \cdot 10^{15}$ to $2 \cdot 10^{18}$, highlighting the influence of doping on electronic properties. Furthermore, we observed an increase in charge capacity by 3 nF with temperature elevation, which signifies improved device performance at higher thermal conditions. Conversely, the built-in potential experienced a notable decrease of 1.5 volts as temperature increased, suggesting a reduction in the energy barrier for charge carriers. These insights into the temperature-dependent behavior of GaAs/Si radial heterojunctions contribute valuable knowledge for the design and optimization of semiconductor devices operating in varying thermal environments.

ORCID

 Jo'shqin Sh. Abdullayev, <https://orcid.org/0000-0001-6110-6616>;  Ibrokhim B. Sapaev, <https://orcid.org/0000-0003-2365-1554>

REFERENCES

- [1] R. Elbersen, R.M. Tiggelaar, A. Milbrat, G. Mul, H. Gardeniers, and J. Huskens, "Controlled Doping Methods for Radial p/n Junctions in Silicon," *Advanced Energy Materials*, **5**(6), 1401745 (2014). <https://doi.org/10.1002/aenm.201401745>
- [2] E. Gnani, A. Gnudi, S. Reggiani, and G. Baccarani, "Theory of the Junctionless Nanowire FET," *IEEE Trans. Electron Devices*, **58**(9), 2903 (2011). <https://doi.org/10.1109/TED.2011.2159608>
- [3] J.Sh. Abdullayev, and I.B. Sapaev, "Optimization of The Influence of Temperature on The Electrical Distribution of Structures with Radial p-n Junction Structures," *East Eur. J. Physics*, (3), 344-349 (2024). <https://doi.org/10.26565/2312-4334-2024-3-39>
- [4] J.Sh. Abdullayev, and I.B. Sapaev, "Optimizing the Influence of Doping and Temperature on The Electrophysical Features of p-n and p-i-n Junction Structures," *Eurasian Physical Technical Journal*, **21**(3/49), 21–28 (2024). <https://doi.org/10.31489/2024No3/21-28>
- [5] J.Sh. Abdullayev, "Influence of Linear Doping Profiles on the Electrophysical Features of p-n Junctions," *East Eur. J. Phys.* (1), 245-249 (2025). <https://doi.org/10.26565/2312-4334-2025-1-26>
- [6] O.V. Pylypova, A.A. Evtukh, P.V. Parfenyuk, I.I. Ivanov, I.M. Korobchuk, O.O. Havryliuk, and O.Yu. Semchuk, "Electrical and optical properties of nanowires based solar cell with radial p-n junction," *Opto-Electronics Review*, **27**(2), 143 (2019). <https://doi.org/10.1016/j.opelre.2019.05.003>
- [7] R. Ragi, R.V.T. da Nobrega, U.R. Duarte, and M.A. Romero, "An Explicit Quantum-Mechanical Compact Model for the I-V Characteristics of Cylindrical Nanowire MOSFETs," *IEEE Trans. Nanotechnol.* **15**(4), 627 (2016). <https://doi.org/10.1109/TNANO.2016.2567323>
- [8] R.D. Trevisoli, R.T. Doria, M. de Souza, S. Das, I. Ferain, and M.A. Pavanello, "Surface-Potential-Based Drain Current Analytical Model for Triple-Gate Junctionless Nanowire Transistors," *IEEE Trans. Electron Devices*, **59**(12), 3510 (2012). <https://doi.org/10.1109/TED.2012.2219055>
- [9] N.D. Akhavan, I. Ferain, P. Razavi, R. Yu, and J.-P. Colinge, "Improvement of carrier ballisticity in junctionless nanowire transistors," *Appl. Phys. Lett.* **98**(10), 103510 (2011). <https://doi.org/10.1063/1.3559625>
- [10] J.Sh. Abdullayev, and I.B. Sapaev, "Modeling and calibration of electrical features of p-n junctions based on Si and GaAs," *Physical Sciences and Technology*, **11**, 3-4 39–48 (2024). <https://doi.org/10.26577/phst2024v11i2b05>
- [11] J.Sh. Abdullayev, and I.B. Sapaev, "Factors Influencing the Ideality Factor of Semiconductor p-n and p-i-n Junction Structures at Cryogenic Temperatures," *East Eur. J. Phys.* (4), 329-333 (2024). <https://doi.org/10.26565/2312-4334-2024-4-37>
- [12] A.V. Babichev, H. Zhang, P. Lavenus, F.H. Julien, A.Y. Egorov, Y.T. Lin, and M. Tchernycheva, "GaN nanowire ultraviolet photodetector with a graphene transparent contact," *Applied Physics Letters*, **103**(20), 201103 (2013). <https://doi.org/10.1063/1.4829756>
- [13] D.H.K. Murthy, T. Xu, W.H. Chen, A.J. Houtepen, T.J. Savenije, L.D.A. Siebbeles, *et al.*, "Efficient photogeneration of charge carriers in silicon nanowires with a radial doping gradient," *Nanotechnology*, **22**(31), 315710 (2011). <https://doi.org/10.1088/0957-4484/22/31/315710>
- [14] B. Pal, K.J. Sarkar, and P. Banerji, "Fabrication and studies on Si/InP core-shell nanowire based solar cell using etched Si nanowire arrays," *Solar Energy Materials and Solar Cells*, **204**, 110217 (2020). <https://doi.org/10.1016/j.solmat.2019.110217>
- [15] I. Aberg, G. Vescovi, D. Asoli, U. Naseem, J.P. Gilboy, C. Sundvall, and L. Samuelson, "A GaAs Nanowire Array Solar Cell With 15.3% Efficiency at 1 Sun," *IEEE Journal of Photovoltaics*, **6**(1), 185 (2016). <https://doi.org/10.1109/JPHOTOV.2015.2484967>
- [16] J. Sh. Abdullayev, I. B. Sapaev, Kh. N. Juraev, "Theoretical analysis of incomplete ionization on the electrical behavior of radial p-n junction structures," *Low Temp. Phys.* **51**, 60–64 (2025). <https://doi.org/10.1063/10.0034646>
- [17] J.Sh. Abdullayev, and I.B. Sapaev, "Analytic Analysis of the Features of GaAs/Si Radial Heterojunctions: Influence of Temperature and Concentration," *East Eur. J. Phys.* (1), 204-210 (2025). <https://doi.org/10.26565/2312-4334-2025-1-21>
- [18] O. Toktarbaiuly, M. Baisariyev, A. Kaisha, T. Duisebayev, N. Ibrayev, T. Serikov, M. Ibraimov, *et al.*, "Enhancement of Power Conversion Efficiency of Dye-Sensitized Solar Cells Via Incorporation of Gan Semiconductor Material Synthesized in Hot-Wall Chemical Vapor Deposition Furnace," *Eurasian Physical Technical Journal*, **21**(4/50), 131–139 (2024). <https://doi.org/10.31489/2024No4/131-139>
- [19] M.Sh. Isaev, A.I. Khudayberdieva, M.N. Mamatkulov, U.T. Asatov, and S.R. Kodirov, "The Surface Layer Morphology of Si<Cr> Samples," *East Eur. J. Phys.* (4), 297–300 (2024). <https://doi.org/10.26565/2312-4334-2024-4-32>
- [20] L. Olimov, and I. Anarboyev, "Some Electrophysical Properties of Polycrystalline Silicon Obtained in a Solar Oven," *Silicon*, **14**, 3817–3822 (2022). <https://doi.org/10.1007/s12633-021-01596-1>

- [21] L. Olimov, and I. Anarboyev, "Mechanism of thermoelectric material efficiency increase," AIP Conf. Proc. **3244**, 060015 (2024). <https://doi.org/10.1063/5.0242092>
- [22] I. Sapaev, I.B. Sapaev, *et. al.*, "Influence of the parameters to transition capacitance at NCDS-PSI heterostructure," E3S Web Conf., **383**, 04022 (2023). <https://doi.org/10.1051/e3sconf/202338304022>
- [23] A.T. Mamadalimov, M.Sh. Isaev, M.N. Mamatkulov, S.R. Kodirov, and J.T. Abdurazzokov, "Study of Silicide Formation in Large Diameter Monocrystalline Silicon," East Eur. J. Phys. (2), 366-371 (2024). <https://doi.org/10.26565/2312-4334-2024-2-45>
- [24] M.S. Isaev, U.T. Asatov, M.A. Tulametov, S.R. Kodirov, and A.E. Rajabov, "Study of the Inhomogeneities of Overcompensated Silicon Samples Doped with Manganese," East Eur. J. Phys. (2), 341-344 (2024). <https://doi.org/10.26565/2312-4334-2024-2-40>

**МАТЕМАТИЧНИЙ АНАЛІЗ ОСОБЛИВОСТЕЙ РАДІАЛЬНОГО p-n ПЕРЕХОДУ:
ВПЛИВ ТЕМПЕРАТУРИ ТА КОНЦЕНТРАЦІЇ**

Й.Ш. Абдуллаєв^a, І.Б. Сапаєв^{a,b}, Н.Ш. Есанмурадова^{a,b,e}, С.Р. Кадиров^c, Ш.М. Кулієв^d

^aНаціональний дослідницький університет ТПAME, фізико-хімічний факультет, Ташкент, Узбекистан

^bЗахідно-Каспійський університет, Баку, Азербайджан




^cУргенський державний університет, Ургенч, Узбекистан

^dФізико-технічний інститут Академії наук Узбекистану, Ташкент, Узбекистан

^eМіжнародний університет Кіміо в Ташкенті, Узбекистан

У цій статті аналітично досліджуються електрофізичні характеристики радіальних гетеропереходів GaAs/Si в діапазоні температур від 50 K до 500 K з кроком 50 K, з урахуванням різних концентрацій домішок. Аналіз охоплює звуження зони провідності (BGN), вбудований потенціал, різницю в ширині забороненої зони між GaAs та Si, а також характеристики ємності-напруги (C-V). Особливу увагу приділено оболонковим радіусам 0,5 мкм та 1 мкм у цій структурі. Було виявлено, що товщина збідненої області радіального гетеропереходу GaAs/Si збільшується з підвищенням температури. Коли концентрація домішок змінюється з $2 \cdot 10^{15}$ до $2 \cdot 10^{18}$, BGN зменшується на 2 meV. Ємність радіального гетеропереходу GaAs/Si збільшується на 3 pF при підвищенні температури з 50 K до 500 K. Крім того, вбудований потенціал радіального гетеропереходу GaAs/Si зменшується на 1,5 вольтів з підвищенням температури. Отримані аналітичні результати були порівняні з експериментальними даними та відкалібровані.

Ключові слова: радіальні p-n та p-i-n переходи; світлова пастка; зовнішні фактори; вольт-фарад; вольт-ампер; криогенні температури

CHARACTERISTICS OF ELECTRICAL CURRENT RELAXATION IN MONOCRYSTAL TlInSe_2 R.S. Madatov^a, A.I. Najafov^b, M.A. Mammadov^a, A.S. Alekperov^{c,d},  Z.I. Asadova^a,  F.G. Asadov^{a,e},
 R.E. Huseynov^{b,*}^a*Institute of Radiation Problems, Ministry of Science and Education Republic of Azerbaijan, Baku, AZ-1143, Azerbaijan*^b*Institute of Physics, Ministry of Science and Education Republic of Azerbaijan, Baku, AZ-1143, Azerbaijan*^c*Azerbaijan State Pedagogical University, Baku, AZ-1000, Azerbaijan*^d*Western Caspian University, Baku, AZ-1001, Azerbaijan*^e*Azerbaijan State Oil and Industry University, Baku, AZ-1010, Azerbaijan**Corresponding Author e-mail: r.e.huseynov@gmail.com

Received January 21, 2025; revised March 31, 2024; accepted April 14, 2025

This study investigates the volt-ampere characteristic of the TlInSe_2 compound at various temperatures, as well as the relaxation of electric current across different voltages (corresponding to varying electric field intensities) at a temperature of 300 K. From the volt-ampere characteristic analysis, we calculated the concentration of free charge carriers, mobility, and trap concentration, yielding values of $n_0 = 5.45 \cdot 10^{18} \text{ cm}^{-3}$, $\mu = 3.03 \cdot 10^{-3} \text{ cm}^2/\text{V}\cdot\text{s}$, and $N_t = 5.2 \cdot 10^{10} \text{ cm}^{-3}$, respectively. The dependence of electrical conductivity on temperature revealed local energy levels with activation energies of 0.2 eV and 0.53 eV in the TlInSe_2 crystal. It was found that at low, constant voltages (where the electric field intensity $E < 25 \text{ V/m}$), relaxation processes occur within the TlInSe_2 compound, leading to a decrease in current due to charge accumulation. An increase in current was observed at higher voltages (where $E > 25 \text{ V/m}$). This increase was attributed to the injection of charge carriers from the contacts, the discharge of charges accumulated near the contact under the influence of the electric field, and the partial discharge of electron centres.

Keywords: Volt-ampere characteristics; Current relaxation; Current intensity; Electric field intensity; Charge carriers; Local energy levels

PACS: 72.20.-i; 71.20.Nr

1. INTRODUCTION

Studying the structure and physical properties of materials used in electronics and spintronics under external influences is essential. These external factors, which include conditions experienced during the use of these materials in various fields like space technologies, have prompted extensive recent research. This research focuses on understanding functional materials that are subjected to various conditions, such as temperature, pressure, and radiation [1-6]. Chalcogenide semiconductors play a significant role among functional semiconductors. Investigating their structure and physical properties is critical for developing converters that can operate effectively under diverse conditions. Consequently, both the structural components and electronic processes of these materials are being explored. It has been established that physical properties are influenced by the type, stoichiometric amounts, and valence of the anions and cations present [7-11]. The generation and capture of charge carriers occurring at local levels within the forbidden zone of semiconductor materials significantly influence the performance of devices built from these materials, including their electrical characteristics. As a result, the dark current can vary over time based on the voltage applied to the crystal. In some instances, even with a constant voltage, the current may either increase or decrease, a phenomenon known as current relaxation. This relaxation depends on the nature, concentration, and energy state of the local energy levels within the studied crystals. The changes in the charges accumulated in these local levels, which are created by various structural defects within the forbidden zone of the crystal, lead to current relaxation. Additionally, the nature of this relaxation is influenced by the voltage applied to the system. Current relaxation and the accumulation of electric charge occur due to the presence of local levels in the forbidden zone, which are caused by inhomogeneities, mixtures, and other factors in semiconductor materials. Investigating current relaxation in semiconductor materials offers valuable insights into the kinetics of the local levels situated in the forbidden zone.

The semiconductor compound TlInSe_2 belongs to the group of ternary $\text{A}^{\text{III}}\text{B}^{\text{III}}\text{C}_2^{\text{VI}}$ compounds and has a chain-like defective structure [12,13]. According to electronographic and X-ray crystallographic analyses, the TlInSe_2 compound is a structural-coordinated analogue of TlSe , obtained by substituting Tl^{3+} ions with In^{3+} ions [14]. The interest in these compounds is due to their small crystal structure size, high concentration of defects (10^{17} cm^{-3}), distinct electrical and photoelectric properties, and sharp anisotropy of physical properties in various crystallographic directions [15-17]. TlInSe_2 crystals are applied in various electronic technology fields, such as in X-ray detectors, tensor resistors, and more. Despite the available information about the electrical and photoelectric properties of TlInSe_2 crystals, as well as the effect of radiation on their physical properties, the kinetics of current flow in chain-like crystals and the kinetic parameters of trapping centres have not been thoroughly studied [18]. Therefore, studying the current relaxation in TlInSe_2 crystals, which affects their electrical and photoelectric properties, is of particular interest.

Cite as: R.S. Madatov, A.I. Najafov, M.A. Mammadov, A.S. Alekperov, Z.I. Asadova, F.G. Asadov, R.E. Huseynov, East Eur. J. Phys. 2, 226 (2025), <https://doi.org/10.26565/2312-4334-2025-2-25>

© R.S. Madatov, A.I. Najafov, M.A. Mammadov, A.S. Alekperov, Z.I. Asadova, F.G. Asadov, R.E. Huseynov, 2025; CC BY 4.0 license

This work aims to investigate the relaxation processes in TlInSe₂ crystals, to study the relationship between electrical conductivity and accumulated charges in the semiconductor, and to clarify the causes of the occurring physical processes. The volt-ampere characteristics of TlInSe₂ compounds and the current relaxation at various constant voltages were studied to achieve this.

2. EXPERIMENT

TlInSe₂ single crystals were grown using the directed crystallisation method as described in [12]. These crystals exhibit a tetragonal structure, with the following lattice parameters: $a = 8.06 \text{ \AA}$, $c = 6.822 \text{ \AA}$. Parallelepiped-shaped samples with dimensions of $6.66 \times 0.84 \times 0.43 \text{ mm}$ (Sample No. 1) and $5.2 \times 1.56 \times 0.53 \text{ mm}$ (Sample No. 2) were prepared from the obtained crystals. The silver paste was used as the contact material. After making the contacts, the samples were kept at room temperature for 24 hours to dry. The contacts were found to be ohmic.

During the experiments, the samples were placed in a cryostat, and the air inside the cryostat was evacuated to a pressure of 10^{-2} Pa . The width of the forbidden band of the sample was determined from the temperature-dependent graph of electrical conductivity at a constant voltage in the TlInSe₂ crystal, yielding a value of 1.23 eV.

In the study of current relaxation at a constant voltage, the ends of the sample were short-circuited after each measurement, and measurements were taken after 1 hour.

3. RESULTS AND DISCUSSIONS

Several theories explain how charge carriers injected from contacts in semiconductor materials contribute to electrical conductivity. According to these theories, charge carriers generate current in semiconductors either through the conduction band or via a hopping mechanism involving deep energy levels within the forbidden band. Consequently, the band structure of semiconductor materials is studied both theoretically and experimentally [19-23]. The physical properties of semiconductors are largely determined by the energy levels of electrons and ions. Therefore, understanding the formation of electronic processes and the electrical properties in these materials is essential [24-27].

Figure 1 illustrates the volt-ampere characteristic for the TlInSe₂ compound at a temperature of 300 K, displaying both the increasing voltage (curve 1) and decreasing voltage (curve 2) directions. From the graph (curve 1 in Fig. 1), it is evident that at very low voltages (300 K), the current intensity shows a sublinear dependence on voltage. This is followed by a linear region, after which a quadratic dependence is observed. When the voltage is increased to 25 V (electric field intensity of $3.75 \times 10^3 \text{ V/m}$) and then reduced, the graph exhibits slight deviations above the initial curve, resulting in hysteresis-like behaviour. When the voltage is lowered to 10 V, the curve obtained during the decreasing voltage measurement closely resembles that of the increasing voltage direction, indicating that the hysteresis effect is practically negligible.

In subsequent measurements, raising the voltage to higher levels reached the point of complete trap filling, causing both the sample and contacts to heat up and leading to failure. Consequently, studies at high voltages were not conducted. Figure 2 presents the voltage-current characteristic obtained at various temperatures for the TlInSe₂ compound. As the temperature decreases, the sublinear region expands, the linear portion shortens, and the transition voltage from the linear to quadratic part shifts toward higher voltage values. At relatively high voltage levels, the exponent n varies between 2 and 5, indicating that the current intensity follows the relation $I \sim (U^n)$.

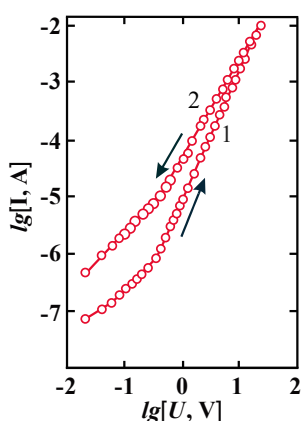


Figure 1. Volt-ampere characteristics in the direction of increasing (curve 1) and decreasing (curve 2) voltage in a TlInSe₂ single crystal at a temperature of 300 K

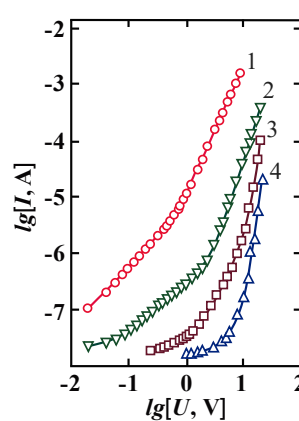


Figure 2. Volt-ampere characteristics of the TlInSe₂ compound at different temperatures. 1-300 K, 2- 250 K, 3- 198 K, 4-132 K

The graph depicting the temperature dependence of current intensity at a constant voltage in the TlInSe₂ crystal reveals local energy levels with activation energies of 0.2 eV and 0.53 eV within the forbidden zone. Based on these results and existing literature, the conductivity mechanism in the TlInSe₂ crystal can be explained as follows:

According to the theory of space charge-limited currents, in semiconductors with trapped charge carriers, the current flows through the semiconductor primarily due to the equilibrium charge carriers when the electric field is small. As the applied electric field increases, the number of charge carriers entering the semiconductor from the contacts also rises. If

the time ($t = L/v$) that equilibrium charge carriers spend travelling through the semiconductor (where L is the distance between contacts and v is the drift velocity of these carriers) exceeds the lifetime of the charge carriers entering from the contacts, then the current flowing through the sample behaves in an ohmic manner.

$$j = en_0\mu \frac{U}{L}. \quad (1)$$

In this context, j represents the current density, n_0 is the equilibrium charge carrier concentration, μ denotes carrier mobility, U is the applied voltage, and L is the distance between the contacts.

As the applied voltage (or external field intensity) increases, the number of charge carriers injected from the metal contacts into the semiconductor also increases. These carriers gradually penetrate a larger area of the semiconductor. Once the charge carriers have filled the entire area of the semiconductor sample, the lifetime of the equilibrium charge carriers becomes shorter than that of the injected charge carriers. Consequently, the amount of current flowing through the semiconductor becomes limited by these charges. In this scenario, the current density can be expressed as follows:

$$j = \frac{9}{32\pi} \epsilon \mu \frac{U^2}{L^3}. \quad (2)$$

Based on the transition voltage (U') value from the ohmic to the quadratic part:

$$n_0 = \frac{9\epsilon U'}{32\pi e L^2}. \quad (3)$$

The equilibrium charge carrier concentration in the sample was determined using formula (3). From this calculation, we found that the equilibrium charge carrier concentration in the TlInSe₂ crystal is $n_0 = 5.45 \cdot 10^{18} \text{ cm}^{-3}$. We can now use this value in formula (1).

$$\mu = \frac{jL}{en_0U} = \frac{IL}{Sen_0U}. \quad (4)$$

The mobility value of the load carriers was calculated using formula (4), resulting in a value of $\mu = 3.03 \cdot 10^{-3} \frac{\text{cm}^2}{\text{V}\cdot\text{s}}$.

The volt-ampere characteristic provides information about the concentration of traps in the crystal by determining the transition voltage (U') from the ohmic region to the quadratic part:

$$N_t = \frac{CU'}{eLS}. \quad (5)$$

Using the formula (5), the calculated value of $N_t = 5.2 \cdot 10^{10} \text{ cm}^{-3}$ (where e is the elemental charge, L is the distance between contacts, S is the contact area, and C is the electric capacity of the sample).

When studying the electrical properties of the TlInSe₂ compound, it was observed that the electric current relaxes at a constant voltage. Unlike other similar compounds, samples of TlInSe₂ do not always show a decrease in current intensity over time at low constant voltage values.

At an electric field intensity of $E = 1.92 \text{ V/m}$ ($U = 0.1 \text{ V}$), the current intensity initially increases over 120 seconds, then decreases for 60 seconds, before consistently rising again. At $E = 3.83 \text{ V/m}$ ($U = 0.2 \text{ V}$), the current intensity decreases for the first 60 seconds, followed by a steady increase. At $E = 19.2 \text{ V/m}$ ($U = 1 \text{ V}$), the current intensity decreases for the first 120 seconds, then increases briefly for 60 seconds, changes slowly for a while, and ultimately increases at a steady rate (see Fig. 3.a).

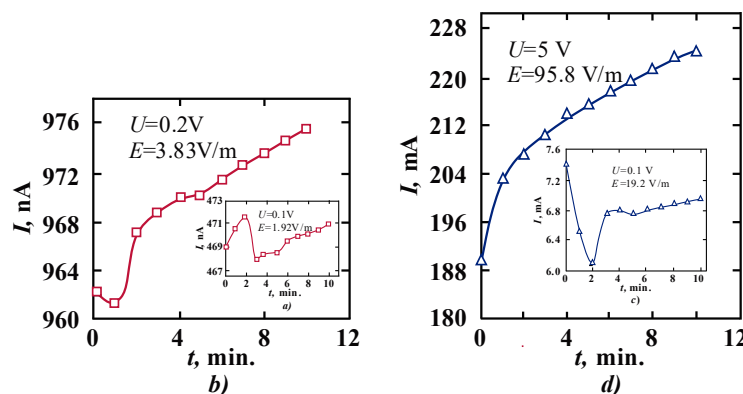


Figure 3. Relaxation of the electric current at different voltages (at different values of the electric field intensity) in the TlInSe₂ compound at a temperature of 300 K. a) $E = 1.92 \text{ V/m}$, b) $E = 3.83 \text{ V/m}$, c) $E = 19.2 \text{ V/m}$, d) $E = 95.8 \text{ V/m}$.

When the electric field intensity exceeds 25 V/m at constant voltage, only an increase in current intensity is observed over time. Initially, the rate of this increase is significant, but it gradually slows down, indicating that the current rises

more slowly as time goes on (see Fig. 3.b). As the electric field intensity increases, the rate of increase in current intensity also rises.

Figure 4 illustrates the time dependence of the electric charge accumulated in the TlInSe_2 crystal at a voltage of 1 V ($E = 19.2 \text{ V/m}$). The graph indicates that the rate of charge accumulation gradually decreases as the duration of the constant electric field applied to the sample increases.

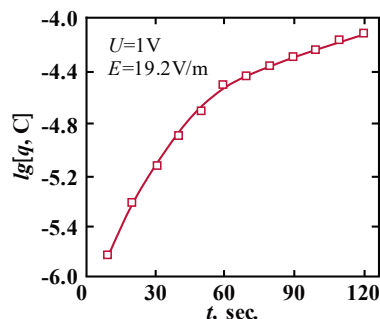


Figure 4. Time dependence of the electric charge accumulated in a TlInSe_2 crystal under a constant voltage of 1 V.

The presence of a sublinear portion in the volt-ampere characteristic at low values of electric field intensity at a temperature of 300 K—namely, a decrease in electrical conductivity—can be attributed to small energy (shallow) traps located in the forbidden zone close to the conduction band. The existence of these shallow traps is further confirmed by the observed decrease in current intensity over time when a constant small voltage is applied. Moreover, at low voltages (where electric field intensity $E < 25 \text{ V/m}$), most of the charge carriers injected from the contacts are captured by these traps. Consequently, both the concentration of injected additional charge carriers decreases, and the electric field created by the trapped electrons hinders the movement of electrons involved in conduction. This leads to a reduction in current intensity over time at the applied constant voltage. In such a case, the current limit by space charges within the sample is significantly lower than in the absence of traps.

Simultaneously, electrons can escape from the traps to the conduction band due to thermal excitation. When the rate at which electrons are excited from the traps equals the rate at which they are captured, the quasi-Fermi level rises, the concentration of free electrons increases, and a stationary state is established. One reason for the increase in current intensity after a decrease in constant voltage in the TlInSe_2 compound could be related to the effective filling of the traps.

Additionally, the presence of a barrier at the boundary with the anode causes the accumulation of volume charges near the anode when current flows through the sample. This accumulation makes it difficult for electrons to pass through this region, increasing resistance. Consequently, the voltage applied to that section also rises. An increase in the voltage drop near the anode enhances the electric field intensity in that region, which lowers the height of the barrier. As a result, current intensity increases again due to both the discharge of charges accumulated near the contact under the influence of the field and the partial release of the centres that capture electrons.

At relatively high voltages (where electric field intensity $E > 25 \text{ V/m}$), the effects of thermal excitation and the filling of traps by captured electrons overshadow the decrease in current due to the trapping of injected electrons. Thus, instead of decreasing, the current shows an increase. The upward shift of the graph obtained during the voltage decrease in Fig. 1, compared to the graph obtained during the voltage increase, further suggests that current intensity increases due to the filling of traps during current flow through the crystal. Notably, the current intensity does not decrease during the first 60 seconds at a constant voltage of $U = 0.1 \text{ V}$; instead, it increases, potentially due to the transfer of charge carriers from shallow levels in the forbidden zone to the conduction band.

CONCLUSIONS

In the studied TlInSe_2 compound, it was determined that electronic relaxation processes occur at a stable voltage (or electric field intensity). The crystals of the TlInSe_2 compound exhibit defects, which contribute to current relaxation in their electrical conductivity. Consequently, electric charge accumulates in the shallow energy levels present within the crystal structure. At relatively high electric field values, the current intensity increases again due to the discharge of charges that had accumulated near the contact, the partial discharge of centres that capture electrons, and the injection of charge carriers from the contacts. Since the measurements were conducted at a temperature of 300 K, the influence of charge carriers on electrical conductivity through a jump mechanism, involving deep levels within the forbidden zone, can be considered negligible at this temperature.

ORCID

©F.G. Asadov, <https://orcid.org/0009-0005-0258-485X>; ©Z.I. Asadova, <https://orcid.org/0009-0004-4295-3165>

©R.E. Huseynov, <https://orcid.org/0000-0003-0636-3948>

REFERENCES

- [1] H.J. Alasali, U. Rilwan, K.A. Mahmoud, T.A. Hanafy, and M.I. Sayyed, Nuclear Engineering and Technology, **56**(10), 4050 (2024). <https://doi.org/10.1016/j.net.2024.05.006>

- [2] E.M. Mahrous, A.M. Al-Baradi, Kh.S. Shaaban, A. Ashour, Sh.A.M. Issa, and H.M.H. Zakaly, *Optical Materials*, **157**(1), 116057 (2024). <https://doi.org/10.1016/j.optmat.2024.116057>
- [3] M. Papailiou, S. Dimitrova, E.S. Babayev, and H. Mavromichalaki, *AIP Conference Proceedings*, **1203**, 748 (2010). <https://doi.org/10.1063/1.3322548>
- [4] E.S. Babayev, in: *Proceedings of the 3rd International Conference on Recent Advances in Space Technologies, RAST 2007*, 4284095 (Istanbul, Turkey, 2007). pp.760-767. <https://doi.org/10.1109/RAST.2007.4284095>
- [5] S.G. Asadullayeva, N.A. Ismayilova, and T.G. Naghiyev, *Modern Physics Letters B*, **37**(34), 2350166 (2023). <https://doi.org/10.1142/S021798492350166X>
- [6] Sh.A.M. Issa, A.M. Hassan, M. Algethami, and H.M.H. Zakaly, *Ceramics International*, **50**(20), 38281 (2024). <https://doi.org/10.1016/j.ceramint.2024.07.192>
- [7] Y.I. Aliyev, Y.G. Asadov, A.O. Dashdemirov, R.D. Aliyeva, T.G. Naghiyev, and S.H. Jabarov, *International Journal of Modern Physics B*, **33**(23), 1950271 (2019). <https://doi.org/10.1142/S0217979219502710>
- [8] G.M. Agamirzayeva, G.G. Huseynov, Y.I. Aliyev, T.T. Abdullayeva, and R.F. Novruzov, *Advanced Physical Research*, **5**(1), 19 (2023). https://jomardpublishing.com/UploadFiles/Files/journals/APR/V5N1/Agamirzayeva_et_al.pdf
- [9] S.G. Asadullayeva, N.A. Ismayilova, M.A. Musayev, and I.I. Abbasov, *International Journal of Modern Physics B*, **38**(01), 2450007 (2024). <https://doi.org/10.1142/S0217979224500073>
- [10] Y.I. Aliyev, N.A. Ismayilova, R.F. Novruzov, A.O. Dashdamirov, H.J. Huseynov, S.H. Jabarov, and A.A. Ayubov, *Modern Physics Letters B*, **33**(21), 1950242 (2019). <https://doi.org/10.1142/S0217984919502427>
- [11] R.S. Madatov, A.S. Alekperov, F.N. Nurmammadova, N.A. Ismayilova, and S.H. Jabarov, *East European Journal of Physics*, (1), 322 (2024). <https://doi.org/10.26565/2312-4334-2024-1-29>
- [12] S.H. Jabarov, N.A. Ismayilova, D.P. Kozlenko, T.G. Mammadov, N.T. Mamedov, H.S. Orudzhiev, S.E. Kichanov, *et al.*, *Solid State Sciences*, **111**, 106343 (2021). <https://doi.org/10.1016/j.solidstatesciences.2020.106343>
- [13] N.T. Mamedov, S.H. Jabarov, D.P. Kozlenko, N.A. Ismayilova, M.Yu. Seyidov, T.G. Mammadov, and N.T. Dang, *International Journal of Modern Physics B*, **33**(15), 1950149 (2019). <https://doi.org/10.1142/S0217979219501492>
- [14] A.F. Qasrawi, F.G. Aljammal, N.M. Taleb, and N.M. Gasanly, *Physica B: Condensed Matter*, **406**(14), 2740 (2011). <https://doi.org/10.1016/j.physb.2011.04.018>
- [15] R.S. Madatov, A.I. Nadzhafov, V.S. Mamedov, and M.A. Mamedov, *Surface Engineering and Applied Electrochemistry*, **46**, 154 (2010). <https://doi.org/10.3103/S1068375510020122>
- [16] R.S. Madatov, A.I. Nadzhafov, T.B. Tagiev, M.R. Gazanfarov, and M.A. Mekhrabova, *Physics of the Solid State*, **53**, 2205 (2011). <https://doi.org/10.1134/S1063783411110151>
- [17] R.S. Madatov, A.I. Najafov, Yu.M. Mustafayev, M.R. Gazanfarov, and I.M. Movsumova, *Semiconductors*, **49**, 1166 (2015). <https://doi.org/10.1134/S1063782615090195>
- [18] M. Ishikawa, T. Nakayama, K. Wakita, Y.G. Shim, and N. Mamedov, *Journal of Applied Physics*, **123**, 161575 (2018). <https://doi.org/10.1063/1.5011337>
- [19] N. Ismayilova, and S. Asadullayeva, *Indian Journal of Physics*, **98**, 1103 (2024). <https://doi.org/10.1007/s12648-023-02858-x>
- [20] S.G. Asadullayeva, A.O. Dashdemirov, A.S. Alekperov, N.A. Ismayilova, A.A. Hadieva, A.N. Cafarova, and A.S. Abiyev, *Advanced Physical Research*, **5**(1), 12 (2023). https://jomardpublishing.com/UploadFiles/Files/journals/APR/V5N1/Asadullayeva_et_al.pdf
- [21] T.G. Naghiyev, R.F. Babayeva, Y.I. Aliyev, *European Physical Journal B*, **97**(6), 86 (2024). <https://doi.org/10.1140/epjb/s10051-024-00731-2>
- [22] A.K. Nabiyeva, S.H. Jabarov, N.A. Ismayilova, and H.J. Huseynov, *Ferroelectrics Letters Section*, **51**(1-3), 9 (2024). <https://doi.org/10.1080/07315171.2023.2300594>
- [23] N. Iram, R. Sharma, J. Ahmed, R. Almeer, A. Kumar, and Z. Abbas, *Journal of Physics and Chemistry of Solids*, **196**, 112368 (2025). <https://doi.org/10.1016/j.jpcs.2024.112368>
- [24] N.S. Ezra, I.S. Mustafa, M.I. Sayyed, K.K. Dakok, I.M. Fadhirlul, T.H. Khazaalah, G.I. Efenji, *et al.*, *Optical Materials*, **155**, 115907 (2024). <https://doi.org/10.1016/j.optmat.2024.115907>
- [25] G.B. Ibragimov, R.Z. Ibaeva, A.S. Alekperov, and B.G. Ibragimov, *Advanced Physical Research*, **6**(1), 56 <https://doi.org/10.62476/apr61.62>
- [26] H.F. Khalil, S.A.M. Issa, S.G. Elsharkawy, R.B. Malidarreh, S. Gad, A. Badawi, F. Fakhry, and H.M.H. Zakaly, *Journal of Sol-Gel Science and Technology*, **112**, 898 (2024). <https://doi.org/10.1007/s10971-024-06520-8>
- [27] T.A. Darziyeva, E.S. Alekperov, S.H. Jabarov, M.N. Mirzayev, *Integrated Ferroelectrics*, **232**(1), 127 (2023). <https://doi.org/10.1080/10584587.2023.2173447>

ХАРАКТЕРИСТИКИ РЕЛАКСАЦІЇ ЕЛЕКТРИЧНОГО СТРУМУ В МОНОКРИСТАЛІ TlInSe₂

Р.С. Мадатов^a, А.І. Наджафов^b, М.А. Мамедов^a, А.С. Алекперов^{c,d}, З.І. Асадова^a, Ф.Г. Асадов^a, Р.Е. Гусейнов^b

^aІнститут радіаційних проблем Міністерства науки і освіти Азербайджанської Республіки, Баку, AZ-1143, Азербайджан

^bІнститут фізики Міністерства науки і освіти Азербайджанської Республіки, Баку, AZ-1143, Азербайджан

^cАзербайджанський державний педагогічний університет, Баку, AZ-1000, Азербайджан

^dБакинський інженерний університет, Хирдалан, AZ-0101, Азербайджан

У цьому дослідженні досліджується вольт-амперна характеристика сполуки TlInSe₂ при різних температурах, а також релаксація електричного струму при різних напругах (що відповідають різним інтенсивностям електричного поля) при температурі 300 К. З аналізу вольт-амперної характеристики ми розрахували концентрацію вільних носіїв заряду, рухливість і концентрацію пастки, що дало значення $n_0 = 5.45 \cdot 10^{18} \text{ cm}^{-3}$, $\mu = 3.03 \cdot 10^{-3} \text{ cm}^2/\text{V} \cdot \text{s}$ і $N_t = 5.2 \cdot 10^{10} \text{ cm}^{-3}$ відповідно. Залежність електропровідності від температури виявила в кристалі TlInSe₂ локальні енергетичні рівні з енергією активації 0,2 еВ і 0,53 еВ. Виявлено, що при низьких постійних напругах (де напруженість електричного поля $E < 25 \text{ В/м}$) у сполуці TlInSe₂ відбуваються релаксаційні процеси, що призводять до зменшення струму внаслідок накопичення заряду. Збільшення струму спостерігалось при вищих напругах (де $E > 25 \text{ В/м}$). Це збільшення пояснюється інжекцією носіїв заряду з контактів, розрядом зарядів, накопичених поблизу контакту під дією електричного поля, і частковим розрядом електронних центрів.

Ключові слова: вольт-амперна характеристика; поточне розслаблення; сила струму; напруженість електричного поля; носії заряду; місцеві рівні енергії

SPECTRAL AND TEMPERATURE DYNAMICS OF PHOTON ABSORPTION IN MONATOMIC TRANSITION METAL DICHALCOGENIDES

 **Rustam Y. Rasulov^a**,  **Voxob R. Rasulov^{a*}**, **Mardonbek Kh. Nasirov^c**,
Mavzurbek Kh. Kuchkarov^b, **Kamola K. Urinova^b**

^a*Fergana State University, Fergana, Uzbekistan*

^b*Kokand State pedagogical Institute, Kokand, Uzbekistan*

^c*Fergana State Technical University, Fergana, Uzbekistan*

*Corresponding Author e-mail: vrrasulov83@gmail.com

Received December 31, 2024; revised April 9, 2025; accepted April 16, 2025

This study delves into the interband absorption dynamics of polarized radiation in monatomic layers of transition metal dichalcogenides (TMDs), a field critical to advancing nano- and optoelectronics. Using theoretical modeling and computational analysis, the spectral and temperature dependencies of one- and two-photon absorption coefficients were examined for linearly and circularly polarized light. Results reveal a pronounced increase in absorption coefficients with frequency, reaching a peak before declining, a behavior modulated by the material's bandgap and temperature. The analysis further highlights the substantial impact of light polarization on absorption characteristics, with temperature-dependent shifts in the maximum absorption frequency. These findings contribute to a deeper understanding of the optical properties of 2D TMD materials and pave the way for their application in designing efficient photodetectors, light-emitting diodes, and other next-generation optoelectronic devices.

Keywords: *Monoatomic layers; Transition metal dichalcogenides; Photon absorption; Spectral dependency; Temperature influence; Polarization effects*

PACS: 78.67.-n, 78.20.Bh, 42.65.-k

INTRODUCTION

Although transition metal dichalcogenides have been studied for more than 50 years [1–3], scientific interest in two-dimensional (2D) structures, in particular monoatomic layers of transition metal dichalcogenides (TMDs), has increased even more since the creation of graphene [4, 5]. Monoatomic layers of TMD represent weakly (van der Waals) and strongly (covalently) bonded atoms, which makes it possible to isolate from a sample a 2D layer with a thickness equal to the size of one elementary lattice. The development of such technologies and recent advances in the production of new types of devices based on them [6] have opened up new possibilities for the use of 2D TMD layers in the field of nanoelectronics and optoelectronics [7].

One of the unique properties of TMDs such as MoS₂, MoSe₂, WS₂ and WSe₂ is that when two-dimensional monoatomic layers are produced from a bulk sample, they become a direct gap material as the number of layers is reduced. In particular, monoatomic single-layer transition metal dichalcogenides have the nature of direct-gap semiconductors [8]. Monoatomic layers of such TMDs are today widely used in the field of nano-, optoelectronics and photonics [9–12].

It should be noted that the excitonic optical properties of monoatomic layers of TMD have been widely studied in both experimental and theoretical aspects (see, for example, [13–19] and references therein). However, single- and multiphoton absorption of interband or single-band polarized light in semiconductors and its linear circular dichroism [20–23] have been theoretically poorly studied. Therefore, in this work, the frequency and temperature dependence of the interband single- and multiphoton absorption coefficient of linearly and circularly polarized light in monatomic TMD layers was studied.

METHODS

The investigation of interband photon absorption in monatomic layers of transition metal dichalcogenides (TMDs) was carried out using a combination of theoretical modeling and computational analysis. The study focused on the spectral and temperature-dependent behavior of one- and two-photon absorption coefficients under polarized radiation.

The optical transitions were analyzed using models designed for semiconductors with diamond and zinc blende lattice structures, adapted for the unique properties of 2D monoatomic layers. The single-photon absorption coefficient was derived using the equilibrium distribution function of charge carriers and the composite matrix element for interband transitions. For two-photon absorption, the squared modulus of the composite matrix element was incorporated alongside the law of energy conservation for multiphoton transitions.

The temperature dependency of the bandgap energy was modeled using the Varshni and Passler formulas, which account for thermal effects specific to the materials studied. Effective masses of electrons and holes were treated as functions of temperature to reflect their sensitivity to thermal variations. The Hamiltonian was formulated to include terms representing the mixing of light and heavy hole states with conduction band states. This formulation ensured accurate incorporation of spin-orbit coupling effects, particularly relevant for narrow-gap TMD semiconductors.

Cite as: R.Y. Rasulov, V.R. Rasulov, M.Kh. Nasirov, M.Kh. Kuchkarov, K.K. Urinova, East Eur. J. Phys. 2, 231 (2025), <https://doi.org/10.26565/2312-4334-2025-2-26>

© R.Y. Rasulov, V.R. Rasulov, M.Kh. Nasirov, M.Kh. Kuchkarov, K.K. Urinova, 2025; CC BY 4.0 license

Polarization effects were considered by defining the polarization vector relative to the monatomic layer plane. Coherent saturation effects were analyzed using the Rabi parameter to evaluate the nonlinear optical response under varying light intensities. Calculations were conducted using the computational software “Maple,” leveraging constants and material-specific parameters sourced from established databases and prior studies to ensure precision and reliability.

The absorption coefficients were analyzed for trends and validated by comparing the results with existing theoretical and experimental data. Spectral and temperature dependencies were visualized through graphs to illustrate key trends, such as peak absorption frequencies and their shifts with temperature and bandgap width. This methodological framework provided a comprehensive understanding of the optical properties of monatomic TMD layers and their behavior under polarized radiation.

SPECTRAL AND TEMPERATURE DEPENDENCES OF THE COEFFICIENT OF ONE- AND TWO-PHOTON LIGHT ABSORPTION

The spectral and temperature dependences of the coefficient of interband single-photon light absorption ($K_{c;V}^{(1)}$) in a monatomic TMD layer are determined by the relation [20, 25]

$$K_{c;V}^{(1)} = \frac{2\pi \hbar \omega}{\hbar} \sum_{\vec{k}_\perp} \left| M_{c;V}^{(1)}(\vec{k}) \right|^2 \cdot [f_c(\vec{k}_\perp) - f_v(\vec{k}_\perp)] \delta(E_c(\vec{k}_\perp) - E_v(\vec{k}_\perp) - \hbar \omega) \quad (1)$$

where $M_{c;V}^{(1)}(\vec{k})$ - is the composite matrix element of the interband optical transition, $f_c(\vec{k}_\perp)$ ($f_v(\vec{k}_\perp)$) - is the distribution function of electrons (holes) in the conduction band (valence band), $\omega(I)$ - is the frequency (intensity) of light, $E_c(\vec{k}_\perp) = (\tilde{E}_g^2 + \gamma^2 k_\perp^2)^{1/2}$, $E_v(\vec{k}_\perp) = -(\tilde{E}_g^2 + \gamma^2 k_\perp^2)^{1/2}$ - is the energy dispersion of electrons (holes), \vec{k}_\perp - is the two-dimensional wave vector of current carriers, directed in the plane of the TMD layer, $\gamma = \hbar(\tilde{E}_g/m^*)^{1/2}$, $\tilde{E}_g = E_g/2$, E_g - is the bandgap width, m^* - is the effective mass of current carriers, the sign $\langle \dots \rangle$ means angular averaging over the solid angles of the two-dimensional wave vector, the rest are well-known quantities.

Following [24] and taking into account the law of conservation of energy, it is not difficult to obtain that the square of the modulus of the composite matrix element of a single-photon optical transition we obtain:

$$|M_{c;V}^{(1)}(k_\omega)|^2 = \left(\frac{eA_0}{\hbar c} \right)^2 \frac{\tilde{E}_g^2 + 2\gamma^2 k_\omega^2}{\tilde{E}_g^2 + 4\gamma^2 k_\omega^2} p_0^2 \left[e'^2_\perp - 2 \frac{\gamma^2 k_\omega^2}{\tilde{E}_g^2 + 2\gamma^2 k_\omega^2} (e'^2_x - e'^2_y) \right], \quad (2)$$

where $\vec{e}'_\perp = (e'_x, e'_y)$ - is the two-dimensional light polarization vector directed along the plane of the layer, $k_\omega = \sqrt{(\hbar\omega)^2 - \tilde{E}_g^2}/\gamma$ - is the wave vector of current carriers participating in a single-photon optical transition and is determined using the δ - function in (1). Then $K_{c;V}^{(1)}$ becomes

$$K_{c;V}^{(1)} = \frac{\pi^2 e^2}{\hbar n_\omega c} \frac{p_0^2 \gamma n^{(2)}}{m_0 \tilde{E}_g^2} \frac{(\xi_1^2 - 1)^{1/2}}{\xi_1} \cdot e^{E_g(1-\xi_1)/(2k_B T)} \left\langle \frac{7+\xi_1^2}{3+\xi_1^2} \left[\frac{1}{2\pi} \left[e'^2_\perp + \frac{1-\xi_1^2}{7+\xi_1^2} (e'^2_x - e'^2_y) \right] \right] \right\rangle, \quad (3)$$

here $e^{E_F/k_B T} = \pi \gamma^2 n^{(2)} / [k_B T (\tilde{E}_g + k_B T)]^{-1} e^{\tilde{E}_g/k_B T}$, $\xi_1 = \hbar\omega/E_g$, with the help of which the Fermi energy is determined depending on temperature, two-dimensional concentration $n^{(2)}$ and band parameters¹.

Figure 1 shows the spectral and temperature relationships of the inter-zone one-photon absorption coefficient $K_{c;V}^{(1)}(\omega, T)$ of light in monoatomic layers of metal dichalcogenides: the 1st line in the picture corresponds to $E_g = 0.3$ eV, the 2nd line corresponds to $E_g = 0.5$ eV quantities and $500 \text{ K} < T < 600 \text{ K}$ to the temperature range. $E_g = 0.3$ eV and 200 K of $K_{c;V}^{(1)}(\omega, T)$ were calculated. It can be seen from this figure that the spectral and temperature coupling of $K_{c;V}^{(1)}(\omega, T)$ increases with the width of the forbidden zone, and as the temperature decreases, the one-photon absorption $K_{c;V}^{(1)}(\omega, T)$ coefficient of light in monoatomic layers of metal dichalcogenides increases significantly: in particular, the value of $K_{c;V}^{(1)}(\omega, T = 200 \text{ K})$ calculated for the $E_g = 0.3$ eV forbidden zone is greater than the value calculated for the $E_g = 1$ eV forbidden zone will be several thousand times larger. This is because $e^{E_F/k_B T}$ takes large values in small temperature fields and large bandgap values (such temperature coupling is suitable for 2D current carrier systems).

In particular, in monoatomic layers of dichalcogenides of transition metals with $E_g = 0.3$ eV forbidden zone, the magnitude of $e^{E_F/k_B T}$ decreases 10 times when the temperature increases from 200 K to 270 K. For this reason, we recorded the spectral and temperature relationship of $K_{c;V}^{(1)}(\omega, T)$ with respect to the field of $500 \text{ K} < T < 600 \text{ K}$

¹ In what follows we use the following notations for the N photon optical transition: $\xi_N = N\xi_1$ and $k_{N\omega} = [(N\hbar\omega)^2 - E_g^2]^{1/2}/(2\gamma) = E_g [N^2 \xi_1^2 - 1]^{1/2}/(2\gamma)$.

temperatures in Fig. 2 b). It can be seen from this figure that at a certain temperature value, the magnitude of $K_{c;V}^{(1)}(\omega, T)$ increases with increasing frequency, reaches a maximum, and then decreases. However, at a specific value of $\hbar\omega$, $K_{c;V}^{(1)}(\omega, T)$ decreases with increasing temperature, and this nature of temperature dependence is explained by temperature dependence of magnitude $\zeta(T) = 4 e^{E_F/k_B T} / (\gamma^2 \pi n^{(2)} E_g)$.

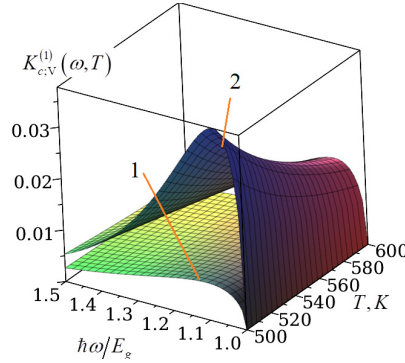


Figure 1. Spectral and temperature correlations of interband one-photon absorption coefficient $K_{c;V}^{(1)}(\omega, T)$ of linearly polarized light in monoatomic layers of transition metal dichalcogenides: 1st line $E_g = 0.3$ eV, 2nd line $E_g = 0.5$ eV in the figure correspond to quantities. In the calculations, the calculated maximum value of $K_{c;V}^{(1)}(\omega, T = 200$ K) for $E_g = 0.3$ eV was taken as one unit.

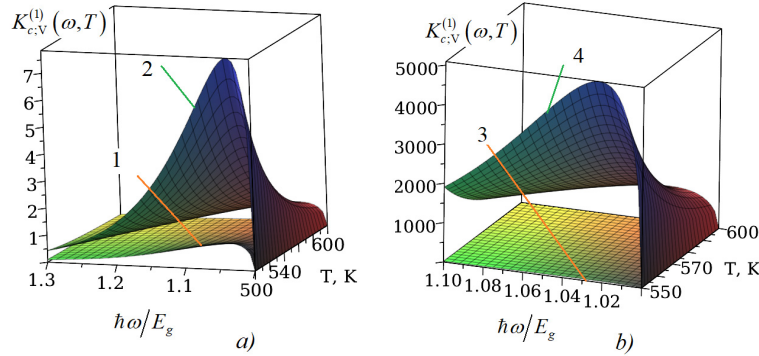


Figure 2. Spectral and temperature correlations of interband one-photon absorption coefficient $K_{c;V}^{(1)}(\omega, T)$ of linearly polarized light in monoatomic layers of transition metal dichalcogenides: a) in the figure, line 1 corresponds to the quantity $E_g = 1.0$ eV, line 2 corresponds to the quantity $E_g = 1.2$ eV, b) line 3 corresponds to the quantity $E_g = 1.5$ eV, line 4 corresponds to the quantity $E_g = 2.0$ eV will come. In the calculations, the maximum value of $K_{c;V}^{(1)}(E_g = 1$ eV, $\omega, T)$ was taken as a unit.

The $K_{c;V}^{(1)}(\omega, T)$ bond reaches a maximum of $K_{c;V}^{(1, \max)}(\omega_{\max}, T)$ at frequencies $\omega_{\max} \approx 1.072E_g/\hbar$ and $\omega_{\max} \approx 1.125E_g/\hbar$ at temperatures $T = 300$ K and $T = 600$ K, respectively, that is, $K_{c;V}^{(1, \max)}(\omega_{\max}, T)$ increases with increasing temperature (see Table 1).

Table 1. This table presents the mathematical relationship between the band gap energy E_g of semiconductor materials, the temperature T , and the peak absorption frequency ω_{\max} in the optical domain

	$T = 300$ K	$T = 600$ K
$E_g = 0.3$ eV	$\omega_{\max} \approx 1.072E_g/\hbar$	$\omega_{\max} \approx 1.125E_g/\hbar$
$E_g = 0.5$ eV	$\omega_{\max} \approx 1.058E_g/\hbar$	$\omega_{\max} \approx 1.10E_g/\hbar$
$E_g = 1$ eV	$\omega_{\max} \approx 1.03E_g/\hbar$	$\omega_{\max} \approx 1.058E_g/\hbar$

In the calculations, the calculated maximum value of $K_{c;V}^{(1)}(\omega, T = 500$ K) for $E_g = 1.0$ eV was taken as one unit. $K_{c;V}^{(1)}(\omega, T)$ bonds $T = 550$ K, $T = 600$ K and $T = 700$ K correspondingly at temperatures $K_{c;V}^{(1)}(E_g = 1$ eV, $\omega, T)$ reach the maximum value of magnitude $\omega_{\max} \approx 1.043E_g/\hbar$, $\omega_{\max} \approx 1.046E_g/\hbar$ and $\omega_{\max} \approx 1.053E_g/\hbar$ frequencies, $K_{c;V}^{(1)}(E_g = 1.2$ eV, $\omega, T)$ reach the maximum value of magnitude $\omega_{\max} \approx 1.036E_g/\hbar$, $\omega_{\max} \approx 1.041E_g/\hbar$ and $\omega_{\max} \approx 1.045E_g/\hbar$ frequencies, $K_{c;V}^{(1)}(E_g = 1.5$ eV, $\omega, T)$ reach the maximum value of magnitude $\omega_{\max} \approx 1.029E_g/\hbar$, $\omega_{\max} \approx 1.032E_g/\hbar$, and $\omega_{\max} \approx 1.037E_g/\hbar$ frequencies, $K_{c;V}^{(1)}(E_g = 2$ eV, $\omega, T)$ reach the maximum value of magnitude $\omega_{\max} \approx 1.022E_g/\hbar$, $\omega_{\max} \approx 1.024E_g/\hbar$, and $\omega_{\max} \approx 1.02E_g/\hbar$ frequencies, i.e. with an increase in temperature, the frequency corresponding to the maximum values of the $K_{c;V}^{(1,2,3,4)}(\omega, T)$ quantities increases somewhat, although not significantly, but this maximum frequency decreases with an increase in the width of the forbidden zone.

The coefficient of two-photon interband absorption of light is defined as

$$K_{c;V}^{(2)} = \frac{2\pi}{\hbar} \frac{2\hbar\omega}{I} \left| M_{c;V}^{(2)}(\vec{k}) \right|^2 \cdot [f_c(k) - f_v(k)] \delta(E_c(k) - E_v(k) - 2\hbar\omega), \quad (4)$$

Then, given the expression for the squared modulus of a composite matrix element:

$$\left| M_{c;V}^{(2)}(\vec{k}_1, \vec{e}) \right|^2 = \left(\frac{eA_0}{m_0c} \right)^4 p_0^4 \frac{32}{3E_g^2} \xi^4 \frac{(4\xi_2^2 - 1)}{(3 + 4\xi_2^2)} [4e_\perp^2 + (4\xi_2^2 - 1)e_y'^2] e_x'^2, \quad (5)$$

we find that the coefficient of two-photon light absorption has the form:

$$K_{c;V}^{(2)} = K_{c;V}^{(2)}(0) e^{\tilde{E}_g/k_B T} e^{-E_V(k_2\omega)/k_B T} \frac{k_2\omega\xi_1}{\frac{k_B T}{E_g} \left(1 + \frac{2k_B T}{E_g} \right)} \frac{(4\xi_1^2 - 1)}{(3 + 4\xi_1^2)} \left\langle \frac{1}{2\pi} [4e_\perp^2 + (4\xi_1^2 - 1)e_y'^2] e_x'^2 \right\rangle, \quad (6)$$

where $K_{c;V}^{(2)}(0) = \frac{256}{3} \pi \left(\frac{2\pi e^2}{\hbar n_{\omega} c} \right)^2 \frac{\hbar I \gamma^6 n^{(2)}}{E_g^8}$, $\xi = \hbar\omega/E_g$ and took into account that the law of conservation of energy for a two-photon optical transition.

Fig. 3 shows the spectral and temperature relationships of the interband two-photon absorption coefficient $K_{c;V}^{(2)}(\omega, T)$ of light in monoatomic layers of transition metal dichalcogenides: a), b), c) pictures show the relationships related to monoatomic layers with forbidden band width $E_g = 0.3 \text{ eV}$, $E_g = 0.6 \text{ eV}$ and $E_g = 1.0 \text{ eV}$ of $K_{c;V}^{(2)}(\omega, T)$. Lines 1 in the images correspond to linear, and lines 2 correspond to circularly polarized light. In the calculations, the calculated maximum value of $K_{c;V}^{(2)}(\omega, T = 200 \text{ K})$ for $E_g = 0.3 \text{ eV}$ was taken as one unit. It can be seen from Figure 3 that both in the spectral connection of the quantity $K_{c;V}^{(2)}(\omega, T)$ and in the temperature connection, it gradually reaches a maximum with the increase of ω, T , and then decreases. Tables 2 (3) for the exact value of the forbidden zone width of the temperature (frequency) corresponding to the maximum value of $K_{c;V}^{(2)}(\omega, T)$ at the selected value of the frequency (temperature). Numerical calculations show that: a) the frequency corresponding to the maximum value of $K_{c;V}^{(2)}(\omega, T)$ at a specific value of the temperature decreases with an increase in the width of the forbidden zone (see Table 2), that is, it reaches a significant value in monoatomic layers with a narrow zone; b) the temperature corresponding to the maximum value of $K_{c;V}^{(2)}(\omega, T)$ at a specific value of the frequency increases significantly with an increase in the width of the forbidden zone (T_{\max}) (see Table 3), that is, in monoatomic layers with a wide zone, it is greater than 1000 K by T_{\max} ; c) As the bandgap width increases, the maximum value of $K_{c;V}^{(2)}(\omega, T)$ decreases for both linearly polarized light and circularly polarized light.

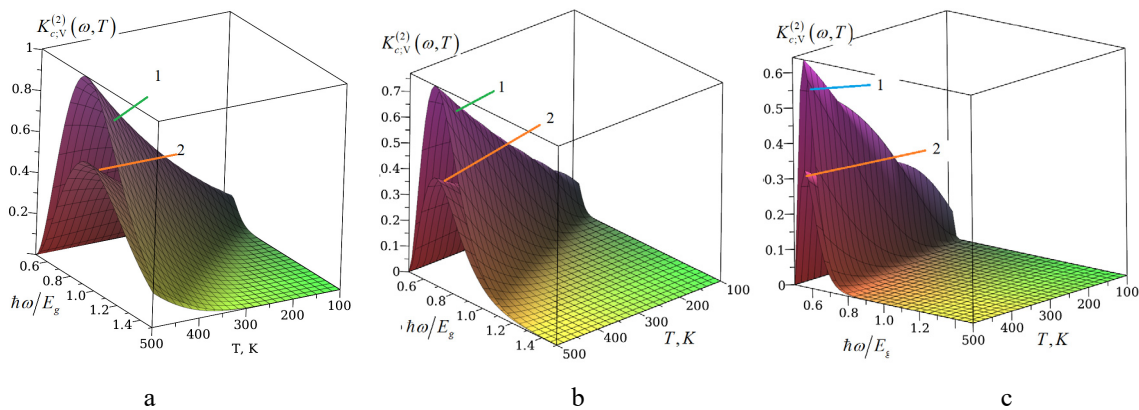


Figure 3. Spectral and temperature correlations of interband two-photon absorption coefficient $K_{c;V}^{(2)}(\omega, T)$ of light in monoatomic layers of transition metal dichalcogenides: a), b), c) pictures show the correlations $K_{c;V}^{(2)}(\omega, T)$ of monoatomic layers with forbidden band width $E_g = 0.3 \text{ eV}$, $E_g = 0.6 \text{ eV}$, and $E_g = 1.0 \text{ eV}$. Lines 1 in the figure correspond to linear, and lines 2 correspond to circularly polarized light. In the calculations, the calculated maximum value of $K_{c;V}^{(2)}(\omega, T = 200 \text{ K})$ for $E_g = 0.3 \text{ eV}$ was taken as one unit

Table 2. Calculated results of the frequency corresponding to the maximum values of the two-photon absorption coefficient of light in monoatomic layers of transition metal dichalcogenides versus temperature and bandgap width.

$E_g, \text{ eV}$	ω_{\max} frequencies corresponding to the maximum values of the two-photon absorption coefficient (calculated in units of E_g/\hbar)					
	$T = 100 \text{ K}$		$T = 300 \text{ K}$		$T = 500 \text{ K}$	
	Lin. pol.	Cir. pol.	Lin. pol.	Cir. pol.	Lin. pol.	Cir. pol.
1.5	0.514	0.514	0.536	0.557	0.563	0.564

Table 3. Calculated results of the temperature corresponding to the maximum values of the two-photon absorption coefficient of light in monoatomic layers of transition metal dichalcogenides versus frequency and bandgap width.

E_g, eV	T_{max}, K temperature corresponding to the maximum values of the two-photon absorption coefficient					
	$\hbar\omega = 0.6E_g$		$\hbar\omega = 0.7E_g$		$\hbar\omega = 0.8E_g$	
	Lin. pol.	Cir. pol.	Lin. pol.	Cir. pol.	Lin. pol.	Cir. pol.
1.5	1000	1000	> 1000	> 1000	> 1000	> 1000

CONCLUSIONS

This study presents a theoretical framework for understanding the interband absorption of polarized radiation in monatomic layers of transition metal dichalcogenides (TMDs). Through comprehensive modeling and computational analysis, the spectral and temperature dependencies of one- and two-photon absorption coefficients were examined under linearly and circularly polarized light. The findings reveal that absorption coefficients increase with frequency up to a peak value and then decrease, with the behavior significantly influenced by the material's bandgap width, temperature, and polarization of the incident radiation.

The analysis demonstrated that for a fixed temperature, the frequency corresponding to maximum absorption decreases with increasing bandgap width, suggesting enhanced absorption in narrow-gap TMD layers. Conversely, at a fixed frequency, the temperature corresponding to maximum absorption increases with larger bandgap widths. The results also highlight that the maximum absorption coefficients are more pronounced in narrow-gap TMDs at lower temperatures, emphasizing the role of thermal effects in tailoring optical properties.

These insights contribute to a deeper understanding of the optical transitions in 2D TMD semiconductors and their potential applications in nanoelectronics and optoelectronics. The study provides a foundation for designing advanced photodetectors, light-emitting diodes, and other devices utilizing the unique optical characteristics of monatomic TMD layers. Future work could extend these findings through experimental validation and explore their implications for device optimization under various operational conditions.

ORCID

✉Rustam Y. Rasulov, <https://orcid.org/0000-0002-5512-0654>; ✉Voxob R. Rasulov, <https://orcid.org/0000-0001-5255-5612>

REFERENCES

- [1] J. Wilson, and A. Yoffe, "The Transition Metal Dichalcogenides Discussion, and interpretation of the observed optical, electrical and structural properties" *Adv. Phys.* **18**(73), 193–335 (1969). <https://doi.org/10.1080/00018736900101307>
- [2] V.L. Kalikhman, and Ya.S. Umanskii, "Features of Layered Crystals," *Phys.–Usp.* **15**(6), 728–742 (1973). (in Russian)
- [3] R.A. Bromley, R.B. Murray, and A.D. Yoffe, "Electronic Properties of MoS₂," *J. Phys. C: Solid State Phys.* **5**(7), 759–785 (1973).
- [4] K.S. Novoselov, *et al.*, "Electric Field Effect in Atomically Thin Carbon Films," *Science*, **306**(5696), 666–669 (2003). <https://doi.org/10.1126/science.1102896>
- [5] K.S. Novoselov, A.K. Geim, S.V. Morozov, D. Jiang, Y. Zhang, S.V. Dubonos, I.V. Grigorieva, *et al.*, "Two-dimensional Atomic Crystals," *PNAS*, **102**(30), 10451–10454 (2005). <https://doi.org/10.1073/pnas.0502848102>
- [6] L.A. Chernozatonskii, and A.A. Artyukh, "Graphene Nanoribbons and Their Prospects," *Phys.–Usp.* **61**(1), 2–23 (2018).
- [7] Q.H. Wang, *et al.*, "Electronics and Optoelectronics of Two-dimensional Transition Metal Dichalcogenides," *Nat. Nanotechnol.* **7**(11), 699–712 (2012). <https://doi.org/10.1038/nnano.2012.193>
- [8] K.F. Mak, *et al.*, "Atomically Thin MoS₂: A New Direct-gap Semiconductor," *Phys. Rev. Lett.* **105**(13), 136805 (2010). <https://doi.org/10.1103/physrevlett.105.136805>
- [9] A. Wee, X. Yin, and C.S. Tang, *Two-Dimensional Transition-Metal Dichalcogenides: Phase Engineering and Applications in Electronics and Optoelectronics*, (Addison-Wesley Publishing, 2023).
- [10] Q.H. Wang, *et al.*, "Applications of Transition Metal Dichalcogenides," *Nat. Nanotechnol.* **7**(11), 699–712 (2012). <https://doi.org/10.1038/nnano.2012.193>
- [11] A. Krasnok, S. Lepeshov, and A. Alú, "Nanophotonics with 2D transition metal dichalcogenides [Invited]," *Opt. Express*, **26**, 15972–15994 (2018).
- [12] K.F. Mak, and J. Shan, "Photonics and optoelectronics of 2D semiconductor transition metal dichalcogenides," *Nat. Photonics* **10**, 216–225 (2016). <https://doi.org/10.1038/nphoton.2015.282>
- [13] G. Wang, *et al.*, "Colloquium: Excitons in Atomically Thin Transition Metal Dichalcogenides," *Rev. Mod. Phys.* **90**(2), 021001 (2018). <https://doi.org/10.1103/RevModPhys.90.021001>
- [14] M.M. Glazov, *et al.*, "Spin and valley dynamics of excitons in transition metal dichalcogenide monolayers," *Phys. Status Solidi B*, **252**(11), 2349–2360 (2015). <https://doi.org/10.1002/pssb.201552211>
- [15] G. Wang, *et al.*, "Excitons in atomically thin transition metal dichalcogenides," *arXiv:1707.05863* (2017). <https://arxiv.org/abs/1707.05863>
- [16] S.Shree, *et al.*, "Guide to optical spectroscopy of layered semiconductors," *Nat. Rev. Phys.* **3**, 39–54 (2021). <https://doi.org/10.1038/s42254-020-00259-1>
- [17] M.M. Glazov, and E.L. Ivchenko, "Valley Orientation of Electrons and Excitons in Atomically Thin Transition Metal Dichalcogenide Monolayers (Brief Review)." *JETP Lett.* **113**, 7–17 (2021). <https://doi.org/10.1134/S0021364021010033>
- [18] L.M. Malar, T.V. Alencar, *et al.*, "Observation of intense second harmonic generation from MoS₂ atomic crystals," *Phys. Rev. B*, **87**, 201401(R) (13.05.2013). <https://doi.org/10.1103/PhysRevB.87.201401>
- [19] M.V. Durnev, and M.M. Glazov, "Excitons and trions in two-dimensional semiconductors based on transition metal dichalcogenides," *Phys. Usp.* **61**, 825–845 (2018).

- [20] V.R. Rasulov, *et al.*, “Linear-Circular Dichroism of Four-Photon Absorption of Light in Semiconductors with a Complex Valence Band,” *Russian Physics Journal*, **58**(12), 1681-1686 (2016). <https://doi.org/10.1007/s11182-016-0702-2>
- [21] V.R. Rasulov, R.Y. Rasulov, R.R. Sultonov, and B.B. Akhmedov, “Two- and Three-Photon Linear-Circular Dichroism in Cubic-Symmetry Semiconductors,” *Semiconductors* **54**(11), 1381–1387 (2020). <https://doi.org/10.1134/S1063782620110226>
- [22] R.Ya. Rasulov, *et al.*, “On the theory of the shift linear photovoltaic effect in semiconductors of tetrahedral symmetry under two photon absorption,” *Russian Physics Journal*, **59**(1), 92-98 (2016). <https://doi.org/10.1007/s11182-016-0742-7>
- [23] R.Y. Rasulov, V.R. Rasulov, K.K. Urinova, M.A. Mamatova, and B.B. Akhmedov, “Single and Multiphoton Optical Transitions in Atomically Thin Layers of Transition Metal Dichalcogenides,” *East European Journal of Physics*, (1), 393-397 (2024). <https://doi.org/10.26565/2312-4334-2024-1-40>
- [24] R. Rasulov, *et al.*, “To the Theory of Multi-Photon Interband Linear-Circular Dichroism in Monoatomic Layers of Dichalcogenide Metals,” *AIP Conference Proceedings*, **3268**, 030001 (2025). <https://doi.org/10.1063/5.0257255>

СПЕКТРАЛЬНА ТА ТЕМПЕРАТУРНА ДИНАМІКА ПОГЛИНАННЯ ФОТОНІВ В ОДНОАТОМНИХ ДИХАЛЬКОГЕНІДАХ ПЕРЕХІДНИХ МЕТАЛІВ

Рустам Ю. Расулов^а, Воксоб Р. Расулов^а, Мардонбек Х. Насіров^с, Мавзурбек Х. Кучкаров^б, Камола К. Урінова^б

^аФерганський державний університет, Фергана, Узбекистан

^бКокандський державний педагогічний інститут, Коканд, Узбекистан

^сФерганський державний технічний університет, Фергана, Узбекистан

У цьому дослідженні розглядається динаміка міжзонного поглинання поляризованого випромінювання в одноатомних шарах дихалькогенідів перехідних металів (ТМД), що є критично важливим для розвитку нано- та оптоелектроніки. Використовуючи теоретичне моделювання та обчислювальний аналіз, були досліджені спектральні та температурні залежності коефіцієнтів одно- та двофотонного поглинання для лінійно та циркулярно поляризованого світла. Результати показують виражене збільшення коефіцієнтів поглинання з частотою, досягаючи піку перед зниженням, поведінка, що модулюється шириною забороненої зони матеріалу та температурою. Аналіз також підкреслює істотний вплив поляризації світла на характеристики поглинання із залежними від температури зрушеннями максимальної частоти поглинання. Ці знахідки сприяють глибшому розумінню оптичних властивостей матеріалів 2D TMD і відкривають шлях для їх застосування в розробці ефективних фотодетекторів, світлодіодів та інших оптоелектронних пристроїв наступного покоління.

Ключові слова: одноатомні шари; дихалькогеніди перехідних металів; поглинання фотонів; спектральна залежність; вплив температури; ефекти поляризації